Stable Quantum Information in Topological Systems

INAUGURALDISSERTATION

zur

Erlangung der Würde eines Doktors der Philosophie

vorgelegt der

Philosophisch-Naturwissenschaftlichen Fakultät

der Universität Basel

von

Adrian Hutter
aus Oberriet (SG), Schweiz

Basel, 2015

Namensnennung-Keine kommerzielle Nutzung-Keine Bearbeitung 2.5 Schweiz

Sie dürfen:

das Werk vervielfältigen, verbreiten und öffentlich zugänglich machen

Zu den folgenden Bedingungen:

Namensnennung. Sie müssen den Namen des Autors/Rechteinhabers in der von ihm festgelegten Weise nennen (wodurch aber nicht der Eindruck entstehen darf, Sie oder die Nutzung des Werkes durch Sie würden entlohnt).

Keine kommerzielle Nutzung. Dieses Werk darf nicht für kommerzielle Zwecke verwendet werden.

Keine Bearbeitung. Dieses Werk darf nicht bearbeitet oder in anderer Weise verändert werden.

- Im Falle einer Verbreitung müssen Sie anderen die Lizenzbedingungen, unter welche dieses Werk fällt, mitteilen. Am Einfachsten ist es, einen Link auf diese Seite einzubinden.
- Jede der vorgenannten Bedingungen kann aufgehoben werden, sofern Sie die Einwilligung des Rechteinhabers dazu erhalten.
- Diese Lizenz lässt die Urheberpersönlichkeitsrechte unberührt.

Die gesetzlichen Schranken des Urheberrechts bleiben hiervon unberührt.

Die Commons Deed ist eine Zusammenfassung des Lizenzvertrags in allgemeinverständlicher Sprache: http://creativecommons.org/licenses/by-nc-nd/2.5/ch/legalcode.de

Haftungsausschluss:
Die Commons Deed ist kein Lizenzvertrag. Sie ist lediglich ein Referenztext, der den zugrundeliegenden Lizenzvertrag übersichtlich und in allgemeinverständlicher Sprache wiedergibt. Die Deed selbst entfaltet keine juristische Wirkung und erscheint im eigentlichen Lizenzvertrag nicht. Creative Commons ist keine Rechtsanwaltsgesellschaft und leistet keine Rechtsberatung. Die Weitergabe und Verlinkung des Commons Deeds führt zu keinem Mandatsverhältnis.

Quelle: http://creativecommons.org/licenses/by-nc-nd/2.5/ch/ Datum: 3.4.2009

Genehmigt von der Philosophisch-Naturwissenschaftlichen Fakultät auf Antrag von

Prof. Dr. Daniel Loss

Prof. Dr. Jiannis Pachos

Basel, den 15. September 2015

Prof. Dr. Jörg Schibler
Dekan

Acknowledgments

I would like to start by thanking my advisor Prof. Daniel Loss who accepted me as a PhD student in his group and who gave me the opportunity to work on many different and exciting research projects. His enthusiasm for Physics was contagious and I am very grateful for his guidance, help, and support during the four years of my PhD studies. His door was always open for me to discuss with him and he shared his ideas with the greatest generosity. His constant encouragements and his positive attitude towards my work have been of inestimable value.

My deepest gratitude goes to Dr. James R. Wootton with whom I shared my office and collaborated on most of my projects. Most of this thesis would not have been possible without James' unique expertise in anyonic systems and my day-to-day work in the office would have been very different without his British sense of humor. I would also like to thank Dr. Fabio Pedrocchi for extensive collaborations, for always being open to share his expertise with me, and for many a lunch break spent together.

Further, I am grateful to Prof. Jiannis Pachos who kindly accepted to co-referee my thesis and to Prof. Christoph Bruder who chaired my PhD defense exam.

Many thanks to Prof. Jens Eisert for inviting me to a one-week research visit at the FU Berlin, and to all of the AG Eisert for their openness and hospitality.

During my time as a PhD student, I was fortunate enough to meet many talented researchers, all willing to share their enthusiasm, knowledge, and insights with me. For stimulating scientific exchange, I would like to thank Hussain Anwar, Daniel Becker, Courtney Brell, Benjamin Brown, Christoph Bruder, Earl Campbell, Claudio Chamon, Jens Eisert, Steven Flammia, Christian Gogolin, Jeongwang Haah, Michael Herold, Arthur Jaffe, Michael Kastoryano, Christoph Klöffel, Andrew Landahl, Olivier Landon-Cardinal, Anthony Leggett, Axel Lode, Naomi Nicker-

son, Jiannis Pachos, David Poulin, Beat Röthlisberger, Constantin Schrade, Chris Self, Oleg Szehr, Luka Trifunovic, Beni Yoshida, and many others.

I enjoyed the many discussions and social interactions with my colleagues and frequent visitors at the condensed matter theory group in Basel. For the enjoyable and stimulating time I spent with them, I would like to thank Samuel Aldana, Mohammad Alidoust, Ehud Amitai Christoph Bruder, Daniel Becker, Stefano Chesi, Carlos Egues, Gerson Ferreira, Suhas Gangadharaiah, Silas Hoffman, Kevin van Hoogdalem, Arthur Jaffe, Jelena Klinovaja, Christoph Klöffel, Viktoriia Kornich, Axel Lode, Daniel Loss, Franziska Maier, Tobias Meng, Kouki Nakata, Simon Nigg, Andreas Nunnenkamp, Christoph Orth, Fabio Pedrocchi, Christina Psaroudaki, Diego Rainis, Hugo Ribeiro, Beat Röthlisberger, Arijit Saha, Thomas Schmidt, Constantin Schrade, Tibor Sekera, Marcel Serina, Peter Stano, Dimitrije Stepanenko, Vladimir Stojanović, Grégory Strübi, Pawel Szumniak, Rakesh Tiwari, Luka Trifunovic, Andreas Wagner, Stefan Walter, James Wootton, Robert Zielke, and Alexander Zyuzin.

Last but not least, I would like to thank my friends and family for their love and wholehearted support.

Summary

The superposition principle of quantum mechanics implies that the amount of classical (i.e., non-quantum) information needed to describe a quantum system is in general exponentially large in the size of the system. This makes simulating quantum physics on a classical computer quickly infeasible, even for moderately-sized systems and using the best present-day supercomputers in the world. This is unfortunate, since systems for which quantum effects are relevant are of interest in many areas of science and engineering, ranging from drug design to materials research. In 1982, Richard Feynman gave birth to the idea of a *quantum computer*, when he realized that simulating quantum physics could be achieved much more efficiently with a computer that was *itself* a quantum system. Since then, the number of problems for which a quantum computer is known to enjoy an advantage over a classical computer has steadily increased, ranging now far beyond the task of simulating quantum physics.

A quantum computation of any interest will need to create complicated superposition states, for otherwise it would not achieve anything that could not be simulated on a classical computer. These superposition states, however, are highly fragile, and this fragility is the main obstacle that the scientific community faces on the road towards a useful quantum computer. Quantum computing will only be possible if it can be performed in a fault-tolerant way. It is due to seminal work by Alexei Kitaev from 1997 that the modern theory of quantum fault-tolerance is closely related to the term *topology*. Topology, as a sub-field of mathematics, is concerned with the properties of space that are preserved under continuous deformations. Topological order, a purely quantum phenomenon, refers to states which cannot be distinguished or evolved into each other locally, yet are globally distinct. The information that distinguishes between these states is stored in non-local degrees of freedom. If it is possible to store quantum information in these non-local degrees of freedom, this would be hugely attractive from a practical perspective, as

it would mean that the information stored this way is immune to many forms of local errors.

Two-dimensional topologically ordered states support excitations known as *anyons*. These are exotic quasi-particles that defy the dichotomy between fermions and bosons that applies to quantum particles in three spatial dimensions. In a *topological quantum computer*, the non-locally stored quantum information is processed by braiding these anyons around each other. Such a computation would be insensitive to small perturbations of the path along which anyons are braided, but would only depend on its topological properties. An open problem is whether topological order can persist at finite temperature.

Equivalently, one can ask whether it is possible to build a system in which quantum information can be stored in a stable manner for arbitrarily long times, without performing active error correction and despite constant influence of a thermal environment. Such a system would constitute a *self-correcting quantum memory* and would extend the concept of a hard disk drive to the quantum realm. Whether nature allows for such a system to be built is of tremendous interest from both a fundamental and a practical perspective.

Two-dimensional topologically ordered systems – those hosting anyons – do not qualify as self-correcting quantum memories; any finite temperature corrupts them in a time that is independent of the size of the system. In the present thesis, we propose and study systems in which the thermal stability of a simple toy model of an anyonic system, Kitaev's toric code, is enhanced in various ways. We consider coupling it to optical cavity modes, to bosonic particles, or to a ferromagnet. These auxiliary systems then induce long-ranged interactions between the anyons, which allow to increase the finite-temperature lifetime of the stored quantum information arbitrarily by increasing the size of the system.

While a topological quantum computer is naturally immune to many forms of imperfections and perturbations, accidental creation of anyonic quasi-particles due to coupling to an external environment is a form of error that requires active correction. This problem has seen surprisingly little attention until recently and is still poorly understood. In this thesis, we develop algorithms that are able to perform this task and provide the first proofs of its in-principle feasibility. Furthermore, we develop a system with the rare property that it both supports anyons that can be used for topological quantum computing, and allows for error correction with well-established techniques.

Historically, the first proposals for building a fault-tolerant quantum computer involved an array of *qubits* (quantum bits) and a set of elementary operations that can be performed on individual and pairs of qubits. Fault-tolerant qubit-based quantum computing has been inspired tremendously from the insights gained in the study of topological quantum information processing. The *surface code*, which combines a qubit-based architecture with topological methods, is now at the forefront of the quest towards a fault-tolerant, scalable quantum computer. In the surface code, a large number of measurements are performed on a continuous basis to get some information about what errors have occurred. This information then needs to be converted by a classical algorithm into a prescription for performing error correction. In this thesis, we develop such an algorithm that, at the time of its publication, was the best efficient algorithm known for the surface code. Error correction for qubit-based quantum computers is typically studied with simplistic error models in which the errors on each qubit are independent from each other. We study what kinds of spatial and temporal correlations between the errors arise when a surface code is coupled to a typical model of an environment, and how they affect its correctability.

Contents

I Self-Correctiong Quantum Memories

II Quantum Error Correction and Non-Abelian Anyons

CHAPTER 1

Introduction

In this first chapter, we provide some background and motivation for the contents of the rest of the present thesis. Furthermore, the contents of each of the remaining chapters are briefly summarized in the appropriate context. The order in which topics are discussed in this introduction does not follow the order in which they appear in the rest of the thesis, but is guided by pedagogical concerns and roughly follows the historical development.

Sec. 1.1 starts with some historical background and also provides some motivation for building a quantum computer, the overarching goal to which this thesis is devoted. In Sec. 1.2 we introduce the concept of fault-tolerance and argue for its necessity when performing quantum computation. We then introduce *anyons* in Sec. 1.3, exotic quasi-particles that are related in some way or another to virtually every modern approach to quantum fault-tolerance and appear in every subsequent chapter of this thesis. Sec. 1.4 introduces Alexei Kitaev's intriguing proposal to use anyons to perform quantum computation. In Sec. 1.5 we describe the quest for a self-correcting quantum memory, a quantum system that suppresses errors through its own dynamics, i.e. without external control and thus allows for *passive* storage of quantum information. Finally, Sec. 1.6 introduces surface code quantum computing, the currently leading approach towards scalable (fault-tolerant) quantum computing. It involves *active* error correction, meaning that traces of the errors are detected, a hypothesis about what errors might have occurred is formed, and a corresponding correction operation is actively performed.

The rest of this thesis is partitioned into Part I with four chapters about self-correcting quantum memories, and Part II with six chapters concerning quantum error correction and non-Abelian anyons. Within each part, the chapters are ordered chronologically.

1.1 Historical background

The beginning of the twentieth century saw turmoil and revolutions in the fields of politics, warfare, economics, and culture. It was in the midst of this period that physics went through one of its largest crises ever.

The physics of that time (nowadays dubbed *classical physics*) predicted absurdities such as electrons falling into the atomic nucleus or black bodies emitting radiation with infinite power. This crisis could only be overcome with the creation of the modern theory of *quantum mechanics*. It soon became apparent, however, that quantum physics is not only able to overcome the absurdities of classical physics, but in fact entails its own set of conclusions that are in stark contrast to how our intuition tells us the world should work. "Anyone who is not shocked by quantum theory has not understood it," exclaimed Niels Bohr. Most of the counter-intuitive implications of quantum physics are related to the so-called *superposition principle*, which allows quantum systems to simultaneously be in different classical states. The most famous critic of quantum mechanics, Albert Einstein, argued for its incompleteness [1] and could not accept its predictions for all of his life.

In the end, however, it is the experimentalist's task to decide the fate of competing theories. When it comes to experimental verifications, the history of quantum physics has been an unparalleled success story. As an example, the deviation of quantum electrodynamics' prediction of the electron g-factor from experimental values is smaller than one part in a trillion – which is sometimes referred to as the most precise prediction in all of science. The experimental verifications of quantum physics have at times been spectacular. For instance, in 2012 a group led by Anton Zeilinger reported teleportation of a quantum state over a distance of 143 kilometres between the two Canary Islands of La Palma and Tenerife [2].

Quantum physics allows for a vastly larger set of possible states of a physical system than classical physics does. While the number of variables needed to describe the state of a classical system grows *linearly* with the size of the system, it does so *exponentially* for a quantum mechanical one.[1] This makes describing the state and predicting the time-evolution of a quantum mechanical system in general much more computationally costly than for a classical one. While a classical computer can simulate an arbitrary quantum system, it can in general only do so with an exponential overhead. This makes the task quickly infeasible even for moderately-sized systems and using the best present-day supercomputers in the world.

It was in 1982 when Richard Feynman realized that simulating a quantum mechanical system with a computer that was *itself* a quantum system would be much more efficient [3]. The idea of a *quantum computer* was born. The most obvious application of a quantum computer – simulating other quantum systems – has promising applications in numerous fields such as drug design, materials research, and nanotechnology. Indeed, a large fraction of currently existing (classical) supercomputers are occupied with simulating systems in which quantum effects are relevant.

Over the past three decades, the set of problems for which quantum computers are known to enjoy an advantage over classical computers has steadily increased. Most prominently, in 1994 Peter Shor discovered that a quantum computer could be used to factorize large integers into their prime factors in sub-exponential time [4], while the most efficient (publicly) known classical algorithms take exponential time. The relevance of the problem of prime-factorization is due to the widely-used RSA public key cryptosystem (employed for example in credit card transactions) relying on its supposed computational hardness. A practically useful large-scale quantum computer would thus shatter the safety of many present-day encryption schemes. Further tasks for which quantum computers would be useful include searching large unstructured databases [5], solving large systems of linear equations (ubiquitous in many areas of science and engineering) [6], machine learning problems [7], and – most importantly – those applications which no one in our classical era has the prescience to foresee.

1.2 Quantum fault-tolerance

Storage and processing of information always need to be carried out by a physical system, and every physical system has its imperfections. "In-

---

[1] This is true for *pure* states, i.e. those which are not a probabilistic mixtures of others. When probabilistic mixtures are considered, the necessary number of variables for a classical system may also be exponentially large.

formation is physical," as Rolf Landauer succinctly put it, and quantum is no different from classical in this regard. The concept of performing computations in a fault-tolerant way, i.e. one that can be done reliably despite such imperfections, is well-known from classical computing. It is used for computations which are of utmost sensitivity, such as guiding moon rockets or steering nuclear power plants. The basic idea behind fault-tolerance is to introduce some redundancy into the computation, such that a small number of virtually faultless components can be distilled from a large number of faulty ones. Hardware errors in modern microprocessors and hard disks are so rare, however, that fault-tolerance is not required for most every-day applications. In the language of information theory, we can say that is possible to create classical hardware which allows to store and process a large number of *bits* (each carrying the information '0' or '1') with very low error rates.

This is in stark contrast to the quantum realm. Quantum information is, as a rule, fragile and elusive. The quantum analog of the classical bit is the quantum-bit, or *qubit* for short. At its core, quantum mechanics is not a theory that describes specific interactions (like Netwon's theory of gravitation), but rather a mathematical framework for the construction of such physical theories. Analogously, a qubit does not describe a particular physical system. Rather, any quantum mechanical system with at least two distinguishable states does, in principle, qualify as a qubit. However, a practically useful qubit is distinguished by the ease of manipulating it and the long-livedness of its superposition states (what is known as *coherence*).

Each known elementary particle carries with it an internal degree of freedom known as *spin*. Constituents of matter, such as electrons, neutrons, and protons are particles with spin $\frac{1}{2}$, meaning that they have two distinguishable internal states ("spin up" and "spin down"). They are thus natural candidates for qubits. In 1997, Loss and DiVincenzo proposed to use the spin of a single electron in a gate-defined semiconductor quantum dot as a qubit [8]. This proposal has guided the research on spin qubits over the past two decades [9]. Spin qubits in quantum dots are attractive because they offer the prospect of ultra-fast gates, miniaturization, and scalability. Furthermore, the achievable decoherence times are long compared with the typical gate operation times, which is an important requirement for implementing quantum gates with high fidelities. Not too long ago, the phase information of the spin was lost after a few nanoseconds only, primarily because of dephasing due to the interaction with nuclear spins of the host lattice. By now, decoherence times

T_2 on the order of hundreds of microseconds [10] are routinely achieved in the laboratory. While this is a prolongation by several orders of magnitude compared with the initially achieved coherence times, it is still rather short compared to typical human time-scales.

However, most of the errors in a future spin-based quantum computer will not be due to decoherence (*accidental* interaction of a qubit with its environment), but due to *intentional* interactions between different qubits, which are necessary to process the information stored in them. Performing a quantum computation of any interest requires to construct superposition states involving multiple qubits. These are referred to as *entangled* states and responsible for one of the deepest puzzles that nature poses to mankind – the *non-locality* of quantum mechanics [12, 13]. In order to entangle two qubits, one uses a physical interaction between their carrier systems. In the Loss-DiVincenzo proposal, this is the Heisenberg exchange coupling between the two electrons [8]. Small imperfections in the performance of these operations lead to error rates that typically far exceed those which are due to the natural decoherence of the qubit. A truly large-scale quantum computation, as would be necessary to find the prime factors of an integer which is too large to be factorized on a classical computer, will involve such a large number of elementary operations that errors are virtually guaranteed to happen before the computation is complete. This is true even if we grant the prospect of significant further decreases in experimentally achievable error rates. A spin-based quantum computer will thus, unlike a modern desktop computer, necessarily resort to fault-tolerance. The remaining sections of this chapter introduce concepts that are relevant in the modern theory of quantum fault-tolerance and for the projects that constitute the present thesis.

1.3 Anyons

The fundamental difference between classical and quantum particles is that each of the former has its own identity, while the latter do not. In a collection of a large number of identical classical particles, such as a gas, it is possible to follow the trajectory of each of them through space and time. By way of contrast, the wave function describing the state of even a single quantum particle is spread out over space. The position of a quantum particle can in general not be used to identify it and distinguish it from another particle of the same kind. For two particles, there is a single wave function describing the joint spatial distribution of both of them.

How the wave function of a number of particles gets transformed when they are exchanged is described by their *exchange statistics*. The indistinguishability of quantum particles such as electrons puts severe constraints on the exchange statistics. The effect of exchanging two particles cannot depend on small local changes of the path along which they are moved but only on its *topological* properties, such as how many times the path of one particle winds around another. In particular, the exchange statistics should be independent under continuous deformations of the exchange path.

This apparently innocuous fact has far-reaching implications for the types of particles that can exist in nature. We can give a sketch of a much more rigorous argument to this effect.[2] Consider a clockwise exchange of two indistinguishable particles. Given their indistinguishability, this exchange has no locally detectable effects, but may transform their joint wave function in ways that are not locally detectable. If this exchange is performed twice, it is easy to see that it can be deformed to a process in which one of the two particles is moved clockwise around the other, following path B in Fig. 1.1. Path B in Fig. 1.1, however, can be continuously deformed to path A, by lifting it across the right particle. Path A in turn can be continuously deformed to a trivial path, meaning that none of the two particles are moved.

We conclude from this that performing two successive clockwise exchanges of two indistinguishable particles should not affect their wave function in any way. A *single* exchange can thus only multiply their wave function by a factor $+1$ or -1. These two possible values correspond to particles called bosons and fermions, respectively. A direct implication of the -1 factor for fermions is Pauli's exclusion principle: two fermions cannot occupy the same state. All elementary particles are fermions or

---

[2] A mathematically more rigorous version of the result is as follows. While the state space of N classical particles in d-dimensional space is given by $(\mathbb{R}^d)^{\times N} \simeq R^{dN}$, the configuration space for N *indistinguishable* particles is given by $\mathcal{C}_N(d)$. This space is obtained from R^{dN} by removing all states in which multiple particles occupy the same location, and identifying all points which are identical up to a permutation of the particles. One can then show that the first homotopy group of $\mathcal{C}_N(d)$ is isomorphic to the symmetric group S_N if $d \geq 3$, and isomorphic to the braid group B_N if $d = 2$ [11]. The groups S_N and B_N differ exactly in the fact that the generators (transpositions) of S_N are involutions (square to the identity) while those of B_N are not. The symmetric group S_N has exactly two one-dimensional representations: the trivial one and the alternating or sign representation. These two representations correspond to bosons and fermions, respectively.

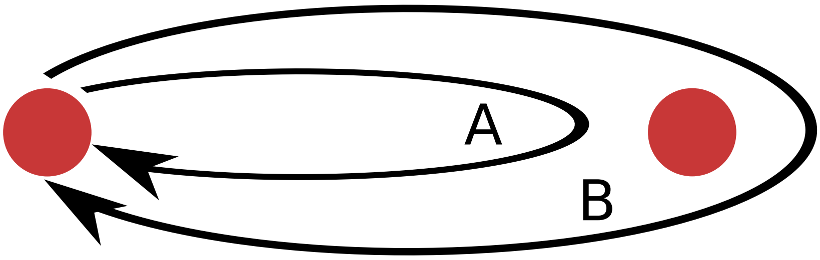

Figure 1.1: The left particle is moved along path A or path B while the right particle is kept at its position. Path B can be continuously deformed to path A in three and more spatial dimensions, but not in two.

bosons, and composite particles are fermions if and only if they contain an odd number of fermions. For example, ^{3}He is a fermion while ^{4}He is a boson, leading to very different behavior of the two isotopes at low temperature.

However, the argument presented above made an implicit assumption regarding the dimensionality of space. In Fig. 1.1, path B can only be continuously deformed to path A if there is at least one additional spatial dimension available to the two dimensions in which the loops A and B are formed. The fermion-boson dichotomy falls apart in two spatial dimensions, and particles are possible whose wave function acquires a phase other than $+1$ or -1 upon exchange. “Since interchange of two of these particles can give *any* phase, I will call them generically anyons,” explained Frank Wilczek in 1982 [14]. In fact, braiding anyons around each other can not only multiply their wave function by phase factors, but can actually apply unitaries to their wave function that may not commute with each other. Anyons with this property are called *non-Abelian*, as opposed to the *Abelian* ones, for which only phases can be obtained by braiding them.

It is noteworthy that two-dimensional space offering *less* freedom than three-dimensional space leads to a *richer* zoo of possible particles. Of course, restricting the movement of a number of elementary particles to two dimensions will not affect their exchange statistics. Rather, one can only hope to find anyons by creating *quasi*-particle excitations that live in a truly two-dimensional world. Historically, the first physical system argued to host non-Abelian anyons were fractional quantum Hall states [15], which arise when a two-dimensional electron gas at sufficiently low temperatures is subject to sufficiently strong magnetic fields.

By now, the range of physical systems which were proposed as potential hosts for non-Abelian anyons has been widely expanded.

1.4 Topological quantum computation

In 1997, Alexei Kitaev proposed to employ anyons in order to build a quantum computer [16]. Every project in this thesis traces its way back, in one way or another, to Kitaev's seminal work. It is Kitaev's merit that the modern theory of fault-tolerant quantum computing is tightly connected with the term *topology*. Indeed, a quantum computer using anyons is called a *topological quantum computer* [17,18]. Topology, as a subfield of mathematics, is concerned with the properties of space that are preserved under continuous deformations.[3] If two paths describing how anyons are braided around each other can be continuously deformed into each other (if they belong to the same *homology class*), moving the anyons along these paths will indeed apply the same unitary to their wave function. From a practical perspective, this is very attractive. Performing a quantum computation is, in principle, nothing than applying a unitary to a certain input state. If we can perform such a unitary by braiding anyons around each other, they offer some inherent fault-tolerance: the unitary is independent under small deformations of the path. While the slightest interaction with its environment can decohere a (say, spin-) qubit, a small perturbation to the anyonic braiding path will not affect the outcome of a computation performed with a topological quantum computer.

For a long time, physicists believed that all phases of matter and their phase transitions can be described within the paradigm of spontaneous symmetry breaking. If a ferromagnet is cooled below its critical temperature, magnetization arises from a previously unordered state. The magnet "spontaneously chooses" the direction in which its magnetization points and thereby breaks the rotational symmetry of space, which is not broken at the level of its microscopic interactions. Similarly, the translational symmetry of space is spontaneously broken when a crystal is formed. It was only the discovery of the aforementioned fractional quantum Hall effect that defied this paradigm. While the different groundstates of a ferromagnet can be distinguished *locally*, by probing the local magnetization, systems with topological order are defined as those whose groundstates cannot be distinguished locally. As it turns out, two-

---

[3] It is an oft-told joke that a topologist is a person who cannot tell the difference between a donut and a coffee cup.

dimensional topologically-ordered systems are exactly those which host anyons.

For pure states (those which are not a probabilistic mixture of other states), topological order is a purely quantum phenomenon. Two pure classical states are identical if an only if they are locally identical. By contrast, quantum physics allows states to be *locally indistinguishable yet globally orthogonal* (that is, distinguishable with probability 1). We can say that the information that distinguishes between two such states is stored in non-local degrees of freedom.

It is not only impossible to distinguish topologically ordered states by any local means, it is also impossible to induce transitions between them with local perturbations. Again, this is very attractive for the task of storing quantum information. It has been shown that the presence of topological order implies that the detrimental effect of static local perturbations is exponentially suppressed in the size of the system [19]. Quantum information stored topologically, in non-local degrees of freedom, is immune to many forms of local "attacks". It can then be processed by braiding anyons around each other.

A natural question is how powerful this computational model is. That is, what set of unitaries can be generated through braiding of non-Abelian anyons? (For Abelian anyons, only phases can be generated, which does not allow for any interesting computations.) The answer depends on the type of non-Abelian anyon. One of the key properties of an anyon model are its fusion rules. The fusion rule $a \times b = c + d + e$, for instance, tells us that fusing two anyons of type a and b with each other can result in an anyon of type c, d, or e. It is precisely the information about this kind of fusion outcome that is stored and processed non-locally during topological quantum computation, and which is inaccessible by any local means. For non-trivial information processing to be possible, there needs thus to be at least one pair of (possibly identical) anyon types a and b with at least two possible fusion outcomes. Anyon models with this property are, by definition, the non-Abelian ones.

Each anyon model contains one particle type 1, which denotes the "anyonic vacuum", i.e., the presence of no anyon. Clearly, $a \times 1 = a$ for any a. It follows from the above that the simplest possible non-Abelian anyon model has two particle species, 1 and σ, and a unique non-trivial fusion rule

$$\sigma \times \sigma = 1 + \sigma \,. \tag{1.1}$$

The unique anyon model defined through this fusion rule is called the *Fibonacci anyon*. As it turns out, this anyon model allows for *universal quantum computation* by purely topological means [20], despite its simplicity. This means the following. The possible quantum states of a number of Fibonacci anyons, which all have fixed locations, span a Hilbert space whose dimension is exponentially large in the number of anyons. Measurements of these states can be performed by fusing the anyons in pairs, and the states can be evolved by braiding the anyons around each other and thereby making use of their exchange statistics. The Fibonacci anyons being universal means that any unitary on this Hilbert space can be approximated to arbitrary accuracy by braiding the anyons. The computational model whose basic operations involve creating and fusing pairs of anyons and braiding them thus allows to perform any quantum computation in a fault-tolerant manner.

Unfortunately, simplicity of the fusion rules is not a good predictor for the difficulty of creating a given anyon model, and Fibonacci anyons remain elusive to the present day. Current experimental research focuses on generating so-called Majorana fermions, exotic quasi-particles that are their own anti-particles, in nanowire hybrid systems (e.g. [21–23]). The anyon model that describes the braiding of localized Majorana fermions is known as *Ising anyons*. Unfortunately, Ising anyons are not universal for quantum computation by braiding alone. However, it is in principle possible to combine topological operations (which have intrinsically very low error rates) with faulty non-topological operations to obtain a universal quantum computer [24].

In the present thesis, non-Abelian anyons will appear in two contexts. Firstly, we propose in Chapter 9 a model involving a lattice of qubits, each of which interacts with its nearest neighbors. If defect lines are introduced into this lattice, non-Abelian anyons appear at their endpoints. These are known as *parafermions* and generalize Majorana fermions. When it comes to quantum computing, they enjoy a crucial advantage over Majorana fermions, in that they allow to perform an entangling gate by braiding them. This means that a much smaller number of non-topological operations (which imply a huge overhead) will be necessary.

Secondly, we study the problem of performing error correction for non-Abelian anyons. We have elaborated on the inherent fault-tolerance that quantum processing by means of non-Abelian anyons enjoys. Unitaries that are performed through braiding of anyons are insensitive to small deformations of the path along which anyons are moved, and topologically ordered systems are immune to local perturbations. However, other possibilities for the introduction of errors exist, such as the (unavoidable) coupling to an external system, that can act as a thermal heat bath. In a truly-large scale computation, errors are virtually guaranteed to happen. Non-Abelian anyons are thus only a viable platform for *scalable* quantum computing if errors can be corrected. The field of error correction for non-Abelian anyons is still relatively young, and half of the publications in this field are contained as Chapters 8, 10, and 11 in the present thesis. These chapters are agnostic with respect to the physical system supporting the anyons, and are only concerned with the algorithmic aspects of the problem.

1.5 Self-correcting quantum memories

The capability to store information in a reliable way is indispensable not only for the possibility of human civilization, but of life itself. Indeed, DNA, the repository of genetic information, is under constant attack from environmental agents like skin cancer-causing UV rays, which makes DNA repair processes indispensable [25]. These repair processes constitute a form of *active error correction*: traces of errors are detected and a physically implemented algorithm performs an appropriate correction. We can contrast active error correction with *self-correcting* memories. These perform *passive error correction*, i.e., take care of errors without active intervention of external agents, such as the aforementioned DNA repair processes.

The author is not aware of a rigorous distinction between *active* error correction (requiring external intervention) and *passive* error correction (self-correcting behavior without external intervention). Suppose that there is an unstable system A (say, a noisy quantum computer) and an external system B that performs active error correction on A. Then, one could argue that the joint system AB is self-correcting, since it does not require any interventions from the outside. However, active error correction requires a constant supply of energy from the outside. The information that details the traces of errors that have been detected needs to be physically stored. Given a finite memory size of the system that performs correction, this information needs to be erased after a finite amount of time. Landauer's principle [26] implies that erasing classical information at finite temperature necessarily has an energy cost, which gets dissipated into a thermal heat bath. Defining a system that performs active error correction as one which has a constant inflow of energy would miss the point, however. Energy by itself is generally abundant, and it is exactly the transfer of thermal energy from the environment to the system that one seeks to combat. Rather, the signature of active error correction is converting *low-entropic* energy from an external source into *high-entropic* (thermal) energy. With other words, a tentative definition of active error correction would thus be that, in contrast to passive error correction, it requires a constant supply of *free energy*.

Ancient Egyptian hieroglyphs have outlasted millennia, and quantum information stored in the non-local degrees of freedom of a number of Majorana fermions would hopefully remain uncorrupted for times which are significantly longer than those achieved by present-day technologies. However, for a system to qualify as a self-correcting memory, it needs to pass a higher threshold than merely allowing for *long* storage times. Instead, we demand that it be possible to increase the lifetime of the stored information *arbitrarily* by increasing the size of the system. Ideally, the lifetime of the stored information would grow *exponentially* with the system size. While we often take the ability to store classical information robustly for long periods of time for granted, it is a non-trivial fact that nature allows for self-correcting classical memories according to this strong definition. The simplest example of such a memory is the 2D ferromagnetic Ising model on a square lattice, a two-dimensional array of spins (which can only point "up" or "down"), and in which each spin energetically prefers to point in the same direction as its four nearest neighbors. At sufficiently high temperatures, the ferromagnet is unordered and, up to fluctuations, half of the spins point "up" and half of them point "down". However, when the temperature is sufficiently small compared to the energy scale of the interactions, a phase transition occurs and magnetization spontaneously arises [27]. A significant majority of the spins will now point "up" or "down". This is in contrast to the one-dimensional ferromagnetic Ising model, which does not exhibit a finite-temperature phase transition [28]. If we define any state with a majority of "up" spins as "0" and any state with a majority of "down" spins as "1", the lifetime of the bit defined this way will indeed be exponentially large in the size of the system. Magnetic components, which rely on similar principles, are the essential building blocks of modern computer hard drives, and allow for very reliable storage of classical information without any supply of (free) energy.

It is an intriguing question, and indeed one of the major open problems in theoretical physics, whether nature also allows to build a self-correcting *quantum* memory (SCQM) – can one build a "quantum hard drive"? As a matter of fact, there are sceptics arguing on grounds of principle against the very possibility of stable storage of quantum information [29]. There are different conceptions as to exactly what kind of system would qualify as an SCQM. Recall that for the 2D Ising model we have defined a "0" state as one with a *majority* of "up" spins. Determining the majority orientation of the spins is a non-trivial task that needs to be performed by the user of the memory; it defies "passiveness" in a stricter sense. Correspondingly, we allow a non-trivial read-out or "decoding" step for an SCQM. While no intervention is allowed during storage, the user may perform measurements, run a non-trivial classical decoding algorithm, and perform correction operations before read-out.

One set of requirements for an SCQM has become known as the "Caltech rules" in the community. A model is a D-dimensional SCQM under the Caltech rules if the following conditions are satisfied [30].

1. (finite spins) It consists of finite dimensional spins embedded in $\mathbb{R}^D$ with finite density.
2. (bounded local interactions) It evolves under a Hamiltonian comprised of a finite density of interactions of bounded strength and bounded range.
3. (nontrivial codespace) It encodes at least one qubit in its degenerate ground space.
4. (perturbative stability) The logical space associated with at least one encoded qubit must be perturbatively stable in the thermodynamic limit.
5. (efficient decoding) This encoded qubit allows for a polynomial time decoding algorithm.
6. (exponential lifetime) Under coupling to a thermal bath at some non-zero temperature in the weak-coupling Markovian limit, the lifetime of this encoded qubit asymptotically scales exponentially in the number of spins.

An alternative set of requirements is given by Brown *et al.* [31]. They distinguish between *required conditions* and *desirable features*.

It is noteworthy that the requirement of perturbative stability is *not* satisfied for the 2D Ising model, the archetypical example of a self-correcting *classical* memory: a finite magnetic field strength puts an upper bound on the lifetime of a bit stored in the Ising ferromagnet. If an SCQM with $D \leq 3$ is possible, this would mean that it is stable in a stronger sense than the 2D Ising model is. The requirement of perturbative stability also naturally builds a link to topological order. Indeed, the question of whether a SCQM exists is equivalent to the question of whether topological order can exist at finite temperature [32].

Alexei Kitaev has proposed a model for a two-dimensional quantum memory that has become widely known as the "toric code" [16] and is well-nigh omnipresent in the present thesis. It involves a square lattice of qubits which are coupled through local four-qubit interaction terms. The toric code is the simplest toy model of a system with topological quantum order. It hosts a relatively simple (Abelian) anyon model and it fulfills all of the Caltech rules except for the crucial one – the last. At any non-zero temperature, the lifetime of quantum information stored in the degenerate ground space of the toric code is upper-bounded by a constant which is independent of the system size [33].

While classical bits can only suffer bit-flips ($0 \leftrightarrow 1$), qubits can suffer both bit-flips ($|0\rangle \leftrightarrow |1\rangle$) and phase-flips ($|0\rangle \rightarrow |0\rangle$ and $|1\rangle \rightarrow -|1\rangle$).[4] The toric code offers a finite degree of protection but no stability against both bit- and phase-flips in much the same way as the 1D Ising model offers a finite degree of protection but no stability against bit-flips. The 2D Ising model, on the other hand, offers stability against bit-flips but no protection whatsoever against phase-flips. The pattern that emerges here is that one spatial dimension can be used to offer finite protection (but no stability) against one type of errors, while two spatial dimensions are sufficient for stability against one type of errors (bit-flips *or* phase-flips). There are generalizations of the toric code to 3D and 4D, and the pattern continues as one would expect, see Table 1.1.

The 4D toric code is an SCQM under the Caltech rules [34], and it is the only one known so far. Unfortunately, nature has only three spatial dimensions to offer. Bravyi and Terhal have shown that no 2D SCQM can exist under the Caltech rules [35]. The reason for this can be understood intuitively. Perturbatively stable systems are topologically ordered, and 2D topologically ordered systems host a non-trivial anyon model. Given the finite strength and range of the interactions, creating an anyon has a finite energy cost, meaning that the thermal bath creates

---

[4] More generally, rotations around arbitrary axes and by arbitrary angles are possible for a qubit. However, stability against bit- and phase-flips implies stability against arbitrary error types.

1D	Finite protection against one type of errors.
2D	Finite protection against both types of errors *or* stability against one type of errors and no protection against the other.
3D	Stability against one type of errors and finite protection against the other.
4D	Stability against both types of errors.

Table 1.1: Degree of protection against bit- and phase-flip errors that different spatial dimensions offer when using an Ising model or toric code.

anyons at a rate which is proportional to the size of the system. Any finite density of anyons is thus surpassed in a system-size independent time. For sufficiently short times, a decoding algorithm can recognize clusters of anyons that presumably have been created together and fuse them accordingly. However, once the density of anyons becomes too high, finding these clusters becomes ambiguous and error correction breaks down. Yoshida has shown a similar result for 3D when assuming translational invariance [32]. Given these no-go results, the only hope for an SCQM under the Caltech rules in less than four dimensions would be a three-dimensional system without translational invariance. Currently, the most promising candidate for such a system is due to Brell [30]. Brell's ingenious proposal considers fractal subsets of a 4D toric code whose fractal (Hausdorff) dimension is less than 3, and which can be embedded into $\mathbb{R}^3$. However, as of the writing of this thesis, no consensus with regards to the perturbative stability of the model has been reached, nor is an efficient decoding algorithm known.

The whole Part I of the present thesis is devoted to the study of SCQM's. We propose and study models of SCQM in two or three dimensions that abandon one or more of the Caltech rules. Of course, there should be a physical rationale behind the violation of these rules. For example, the first of the rules demands that all involved subsystems be finite-dimensional spins. However, real particles not only possess their spin but also motional degrees of freedom and there is no reason not to involve these for the purposes of constructing an SCQM. The second rule demands that all interactions be of finite range. However, photon-mediated interactions are naturally of infinite range. Indeed, cavity quantum electrodynamics is a well-established technology [36] that allows for fast long-distance interactions between electron spins. Accordingly, it has been proposed to couple spin qubits through microcavities for quantum information processing [37].

Models for an SCQM based on long-range (e.g. cavity-mediated) interactions have been proposed and analyzed in the Loss group at the University of Basel [38–40]. Like the standard toric code, these models assume periodic boundary conditions. For models with short-ranged interactions, the choice of boundary conditions (open or periodic) is typically considered a technicality and becomes irrelevant for large enough systems. However, in Chapter 2 we analyze the effect of the boundaries on these memories with long-range interactions, and show that it becomes in fact *dominant*. In Chapter 3 we propose to dynamically (i.e. not on the level of physical interactions) realize an SCQM Hamiltonian with long-range interactions and open boundaries by applying NMR-like pulse sequences to an array of qubits with typical two-body interactions. Next, we propose in Chapter 4 a system in which a toric code is coupled to a bath of thermal bosons through local interactions and with finite interaction strengths. So, in contrast to the cavity-based proposals, no non-local terms are put in "by hand". This model indeed leads to a lifetime that grows exponentially with the size of the system. However, a perturbation that led to a mass gap for the bosons would imply an upper bound on the lifetime that can be achieved, so the model is not perturbatively stable in a strict sense, as pointed out in Ref. [41]. Finally, we study in Chapter 5 a Hamiltonian involving only local two-spin interactions for which the model in Chapter 4 emerges as a low-energy effective Hamiltonian. This system will then exhibit self-correcting behavior, as long as the perturbative expansion remains valid.

1.6 Surface code quantum computing

A fundamental difference between bits and qubits is that the former have only two possible states while even a single qubit has an infinity of possible states. This means in particular that errors can distort a qubit in arbitrarily small ways. Given this inherent non-discreteness of quantum information, it is not at all obvious that qubit-based computations can be performed fault-tolerantly. When Knill, Laflamme, and Zurek [42], and Aharonov and Ben-Or [43] in 1996 established the feasibility of fault-tolerant quantum computing by *threshold theorems*, this constituted one of the biggest advances in the history of quantum computing.

Proposals for fault-tolerant quantum computing with qubits are based on *quantum error correction* (QEC). In any scheme for QEC, *logical* qubits are encoded into a subspace of a larger number of *physical* qubits. One assumes that elementary operations which can be performed by use of the physical qubits suffer from some error rate p. Interactions between the physical qubits and measurements on them are then performed continuously in a way that is specified by the QEC scheme. This serves both to process the logical qubits and to detect traces of errors that have occurred. These traces are called the *error syndrome*. Transforming the syndrome measurement outcomes into a hypothesis about what errors have occurred may necessitate a non-trivial classical computation. One then seeks to establish, either analytically or through numerical simulations, a *threshold error rate* p_c which has the property that for $p < p_c$ the probability of an error on the logical qubits is exponentially small in the overhead, that is, the ratio of physical to logical qubits. The threshold error rate p_c in general depends on both the QEC scheme and the classical algorithm that processes the error syndrome. The more effort one is able and willing to invest into the classical computation, the higher will the threshold p_c in general be, although a certain maximal value can of course not be surpassed.

Unfortunately, the thresholds established in Refs. [42,43] were on the order of $p_c \approx 10^{-6}$, which is much lower than what can be achieved in the foreseeable future. Furthermore, these results required the ability to perform gates between arbitrary pairs and triples of qubits, with error rates independent of their spatial distance, which is experimentally daunting, too.

Kitaev's toric code Hamiltonian is a sum of local four-qubit terms. These terms energetically enforce parity constraints on the four involved qubits. Instead of enforcing these parity constraints energetically, one could alternatively repeatedly perform measurements to check whether they are satisfied, and apply correction operations if they are not. The simplest way to measure these four-qubit operators is to have an ancillary qubit in the middle of the four involved qubits, perform appropriate entangling gates between the ancillary and its four surrounding qubits, and finally measure the ancilla qubit. This variant of the toric code is known as the *surface code*. It is very attractive from an experimental perspective in that it requires only the ability to perform single-qubit gates and entangling gates between pairs of nearest neighbors. These requirements are as low as one could hope.

The central place that the surface code has in today's theory of fault-tolerant quantum computing is due to a number of crucial results by

Raussendorf and Harrington [44]. First of all, they demonstrated numerically that the surface code has an exceptionally large threshold error rate on the order of $p_c \approx 10^{-2}$, which is right at the brink of what can be achieved with state-of-the-art superconducting qubits [45]. The number of logical qubits that can be stored in a (large enough) surface code can be increased arbitrarily by inserting "holes" into it. It is then possible to entangle these logical qubits by braiding the corresponding holes around each other, much in the same way as anyons are braided in topological quantum computing. The surface code allows fault-tolerant performance of an entangling gate, and of a limited number of single-qubit gates. Unfortunately, this gate set does not allow for universal quantum computation.

Universality can be achieved if ancilla states which can *not* be generated by the surface code gates are available. Of course, these ancilla states should be fault-tolerant, too. Bravyi and Kitaev showed that certain states, known as "magic states", have the property that a purer copy of them can be distilled from a larger number of noisy copies [46]. Defect braiding in the surface code, together with the ability to distill magic states, allows for fault-tolerant and scalable universal quantum computation and is currently the clearest visible path towards this goal. From an historical perspective, it is ironic that while topological quantum computing was originally introduced as an alternative to qubit-based quantum computing, it has in fact inspired tremendous progress in the field of fault-tolerant qubit-based quantum computing, which has profited enormously from the insights gained in the study of topological quantum information processing and is now again at the forefront of the quest towards a fault-tolerant quantum computer.

Fig. 1.2 provides an overview over a layered architecture for a fault-tolerant quantum computer based on the surface code. It is inspired by the discussion in Ref. [49]. The bottom layer deals with with those operations that are actually performed on the physical level. This includes entangling gates through direct physical interactions and a limited set of single-qubit operations, including preparation and measurement. All operations at this level are imperfect. The second layer is concerned with QEC. Its task is to extract virtually error-free components from the noisy substrate. To do this, it applies a classical error correction algorithm to the syndrome measurement results, from which a prescription for how to perform error correction is obtained. This layer also includes the production of magic states, and it is this second layer that we are concerned with in this thesis. At the third layer, the error-free components from the

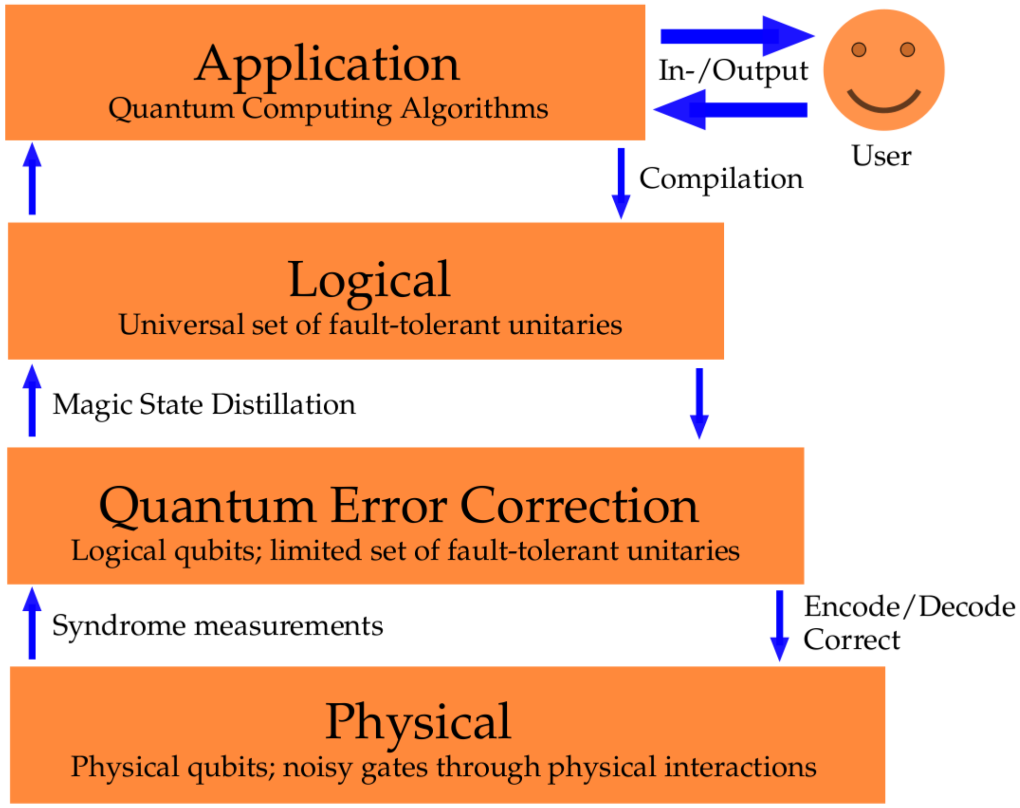

Figure 1.2: Layered architecture for a surface code based quantum computer, inspired by Ref. [49].

second layer are combined to form arbitrary fault-tolerant unitaries. The topmost layer includes the interaction with the user of the quantum computer. He or she specifies the quantum algorithm that is to be performed. This algorithm is then compiled by the computer; that is, a way is found to perform it with the universal set of fault-tolerant gates that the logical layer provides.

The results of Raussendorf and Harrington have been further developed and popularized by Austin Fowler [47, 48]. One of the biggest drawbacks of the surface code architecture is that most qubits in it are occupied not with performing the actual computation, but with distilling magic states, which has a huge overhead [48]. Finding ways to mitigate this is an active are of research. Possible alternatives to the approach outlined above include the use of “lattice surgery” instead of defect braiding in the surface code [50], or to employ “color codes” [51], close relatives of toric/surface codes. A recent study suggests that the combination of these alternatives may actually constitute the most efficient possibility to perform fault-tolerant qubit-based quantum computing [52]. Proof-of-principle experiments for a minimal color code have already been performed with 7 trapped-ion qubits [53].

In Chapter 6 we present a classical algorithm for error correction in the surface code that, at the time of its publication, was the best known efficent algorithm for the surface code. In the meantime, Bravyi, Suchara, and Vargo have developed a nigh-optimal efficient algorithm for the same noise model [54]. Error correction algorithms for the surface code are typically bench-marked with simplistic error models, in which the error events on different qubits are independent from each other. However, if different qubits couple to the same environmental modes, this can lead to correlations in the errors. In Chapter 7, we study what kinds of temporal and spatial correlations between the errors arise when a surface code is coupled to a standard model of an environment, a bath of freely propagating modes. For most bath types that we consider, we find that the time-window available before error correction becomes unfeasible stays finite in the thermodynamic limit. Chapters 8 and 10 study not only error correction for non-Abelian anyons, but also for generalizations of the surface code to *qudits*, that is, quantum systems with more than two distinguishable states.

Part I

Self-Correctiong Quantum Memories

CHAPTER 2

Self-Correcting Quantum Memory with a Boundary

Adapted from:
Adrian Hutter, James R. Wootton, Beat Röthlisberger, and Daniel Loss
"Self-correcting quantum memory with a boundary",
Phys. Rev. A **86**, 052340 (2012)

We study the two-dimensional toric code Hamiltonian with effective long-range interactions between its anyonic excitations induced by coupling the toric code to external fields. It has been shown that such interactions allow to increase the lifetime of the stored quantum information arbitrarily by making L, the linear size of the memory, larger [Phys. Rev. A **82** 022305 (2010)]. We show that for these systems the choice of boundary conditions (open boundaries as opposed to periodic boundary conditions) is not a mere technicality; the influence of anyons produced at the boundaries becomes in fact *dominant* for large enough L. This influence can be both beneficial or detrimental. In particular, we study an effective Hamiltonian proposed in [Phys. Rev. B **83** 115415 (2011)] that describes repulsion between anyons and anyon holes. For this system, we find a lifetime of the stored quantum information that grows exponentially in L^2 for both periodic and open boundary conditions, though the exponent in the later case is found to be less favourable. However, L is upper-bounded through the breakdown of the perturbative treatment of the underlying Hamiltonian.

2.1 Introduction

An important open problem in quantum information concerns the feasibility of a *self-correcting quantum memory*. Finding a system that protects a quantum state from decoherence induced by a thermal bath, without the need for active monitoring and error-correction, proves much more difficult than in the classical case. On the most basic level, this is due to the fact that a classical bit only needs protection against logical X operations while a qubit needs protection against a logical X and Z. If a state is stored in a many-qubit system, a desirable feature is *topological protection* of the stored (qu-)bit: we want a logical error X (or Z in the quantum case) to necessitate a number of single-qubit errors σ_x (or σ_z) that scales with L, the linear size of the memory. The simplest model that energetically penalizes σ_x errors and offers topological protection of a stored classical bit is the 1D ferromagnetic Ising model. The simplest model that penalizes σ_x and σ_z errors and topologically protects a qubit is given by Kitaev's 2D toric code Hamiltonian [16]. In fact, the latter can be mapped exactly to two independent copies of the former [33, 55]. Unfortunately, both of these systems are not thermally stable. Once a topological defect (a pair of domain walls in the 1D Ising model or a pair of anyons in the 2D toric code) has been created, it can spread and lead to a logical error without any further energy cost. The lifetime of a qubit stored in the degenerate ground states of the 2D toric code is thus for any finite temperature upper-bounded by a constant independent of L [33,38,56]. The 2D toric code can therefore not serve as a 'quantum hard drive'. These difficulties can be overcome if the dimensionality of the systems is increased. In the 2D Ising model and the 4D toric code, any sequence of single-qubit Pauli operators that leads to a logical error has to surpass an energy barrier whose size scales with L. Since the number of error paths connecting two distinct ground states is exponentially large in L, these systems are thermally stable below some critical temperature T_c, meaning that the lifetime of the stored information grows exponentially with L [33,34,57].

Whether a similar degree of protection for a quantum state can be achieved in less than four dimensions is not clear. One can show that for *every* 2D local stabilizer Hamiltonian the height of the energy barrier separating orthogonal states stored in a degenerate ground state is upper bounded by a constant independent of L [35,58,59], ruling out the possibility of using such systems for the fault-tolerant storage of quantum information by self-correction. In principle, these no-go results leave two ways out: Either one abandons the locality of the terms in the Hamiltonian or one goes to dimension 3. Indeed, both of these routes have been followed in the recent literature. While the 3D toric code is not thermally stable, Haah showed in a recent breakthrough the existence of 3D Hamiltonians with local interactions that have no string-like logical operators [60]. Unlike anyons in the 2D toric code, defects cannot move further than a certain constant distance away without creating other defects. This property implies a logarithmically growing energy barrier between orthogonal ground states, leading one to expect a lifetime that grows polynomially with L [61]. However, the best known lower bound on the memory lifetime of Haah's Hamiltonian is upper-bounded by a constant independent of L [62] and further improvement is not expected [63]. Furthermore, a 3D architecture may lead to practical difficulties when accessing the physical qubits for syndrome measurement and error correction.

We therefore believe that the most promising route to follow in search for a realistic proposal for a quantum memory is to start from the 2D toric code Hamiltonian and add terms to it that

- can be physically motivated, and
- lead to a memory lifetime that becomes arbitrarily large as $L \to \infty$.

Long-range repulsive interactions ($1/r^{\alpha}$-potential with $0 \leq \alpha < 2$) between the anyons lead to a logarithmically-growing self-consistent mean field gap for anyon creation, yielding a polynomially increasing lifetime [38], see Sec. 2.3 below. So rather than trying to find a Hamiltonian with a macroscopic energy barrier between orthogonal ground states, this approach seeks to suppress the anyon creation rate. The toric code Hamiltonian (involving local *four*-qubit couplings) with non-interacting anyons can be obtained as an effective Hamiltonian of the Kitaev honeycomb model, which involves nearest-neighbor *two*-qubit Ising couplings [64]. How an $\alpha = 0$ interaction between the anyons can be obtained through such a honeycomb model coupled to electromagnetic modes has been studied in detail in [39], see Sec. 2.4 below.

In an alternative approach it was shown that coupling the toric code to a bosonic field leads to an effective gravitational potential between the anyonic defects [65]. Below some critical temperature, all anyons coalesce to a single point. However, the time the system needs to approach this metastable state and how to best perform error correction in this system have not been investigated so far.

Self-correcting quantum memories are usually discussed with periodic boundary conditions, giving the toric code its name. This way, the complications that arise with the possibility of creating unpaired topological defects at the boundaries can be avoided. One expects that the influence of the boundaries becomes negligible if L becomes large enough, which is certainly correct for Hamiltonians with local interactions. However, here we study memories with long-range interactions between the anyons as proposed in [38, 39] and show that for these systems the influence of the boundary becomes in fact *dominant* for large enough L. It can be beneficial and detrimental. Specifically, unpaired anyons from the boundary lead to an effective bias for anyons from the bulk to move to the closest boundary, thus prolonging the time until error correction becomes ambiguous (see Sec. 2.3). On the other hand, the ability to create unpaired anyons at the boundaries halves the energetic gap above the anyonic vacuum. This becomes especially relevant if this gap is so strong that the anyonic system is basically restricted to its ground state and first excited state (see Sec. 2.4).

The paper is structured as follows. In Section 2.2 we discuss how error correction can be performed in the planar code (a toric code with open boundaries) in contact with a thermal environment. In Section 2.3 we study the influence of the boundaries for a Hamiltonian with spatially constant repulsion between the anyons, while in Section 2.4 an effective Hamiltonian that describes repulsion between anyons and anyon holes is investigated.

2.2 Error correction in the planar code

The planar code

A self-correcting quantum memory is supposed to protect a quantum state from a thermal environment by means of its internal dynamics and without need for active error-correction. A single error correction step may be performed before the stored state is read out. We shall use here a version of the toric code first introduced in [66], which, contrary to what the name suggests, is not periodic but does have a boundary. We will refer to this as the *planar code*. Consider a grid with quadratic cells and physical qubits placed on the edges, as depicted in Figure 2.1. We call the four qubits around one unit cell a 'plaquette' and the four qubits around a vertex a 'star'. We define plaquette operators $A_p = (\sigma_z)^{\otimes 4}$, where the tensor product runs over the four qubits around some plaquette p and star operators $B_s = (\sigma_x)^{\otimes 4}$, where the tensor product runs over the four qubits around some vertex s. Plaquette operators on the left and right boundary and star operators on the top an bottom boundary are tensor products of three Pauli operators only. All of these operators are commuting since they overlap at zero or two qubits. Let the space $\mathcal{K}_0 \subset \mathcal{H} = (\mathbb{C}^2)^{\otimes N}$ (N is the total number of qubits) be defined as the space stabilized by all plaquette and star operators. That is, $\mathcal{K}_0$ is the space of all states $|\psi\rangle$ such that for each three- or four-qubit plaquette or star operator A_p or B_s we have $A_p|\psi\rangle = |\psi\rangle$ and $B_s|\psi\rangle = |\psi\rangle$. Since all the plaquette and star operators are independent (unlike in the toric code where the product of all plaquette and star stabilizer operators is the identity), one easily verifies that $\dim \mathcal{K}_0 = 2$, independent of the height and width of the grid,[1] such that one logical qubit can be stored in this space. States in $\mathcal{K}_0$ are *topologically protected*. They cannot be distinguished by any local observable and not be evolved into each other by any local unitary.

We then define a Hamiltonian that imposes an energy penalty for the violation of every stabilizer condition. Let $n_p = (1 - (\sigma_z)^{\otimes 4})/2$, $n_{p'} = (1 - (\sigma_z)^{\otimes 3})/2$, $n_s = (1 - (\sigma_x)^{\otimes 4})/2$, and $n_{s'} = (1 - (\sigma_x)^{\otimes 3})/2$. The tensor products run over the qubits depicted in Figure 2.1. These operators have eigenvalue 0 for states that satisfy the corresponding stabilizer conditions and eigenvalue 1 for states that violate it. For some state $|\psi\rangle \in \mathcal{H}$ we say that an anyon is present at plaquette p (vertex s) if $n_p|\psi\rangle = |\psi\rangle$ ($n_s|\psi\rangle = |\psi\rangle$) and that no anyon is present if $n_p|\psi\rangle = 0$ ($n_s|\psi\rangle = 0$), i.e. we interpret stabilizer violations as the presence of anyons. We then use the well-known toric code Hamiltonian

$$H_{\mathrm{Kitaev}} = \Delta \left(\sum_p n_p + \sum_s n_s \right) , \tag{2.1}$$

which simply counts the total number of anyons. The code subspace $\mathcal{K}_0$, which is the degenerate ground state of this Hamiltonian, corresponds to the anyonic vacuum. This Hamiltonian is stable against weak local

---

[1] Let the 'height' h be given by the number of plaquette operators from top to bottom and the 'width' w by the number of star operators from left to right. The total number of qubits is then given by $2hw + h + w + 1$, the number of plaquette operators by $h(w+1)$ and the number of star operators by $(h+1)w$. Since each stabilizer condition eliminates half of all $2^{2hw+h+w+1}$ degrees of freedom, we are left with 2 of them.

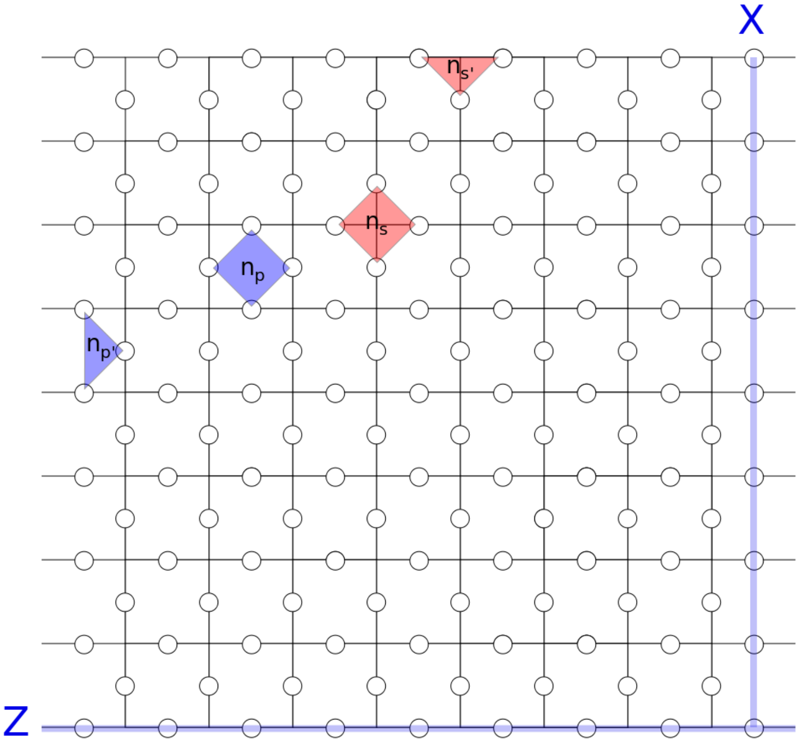

Figure 2.1: A planar code of size $L = 8$. Depicted are a four-qubit plaquette operator n_p, a three-qubit plaquette operator $n_{p'}$, a four-qubit star operator n_s, and a three-qubit star operator $n_{s'}$. The logical operator X (Z) is given by any chain of Pauli operators σ_x (σ_z) connecting the top and bottom (left and right) boundary.

perturbations in the sense that the lifting of the ground state degeneracy through such a perturbation is exponentially small in L [16].

Starting from the anyonic vacuum, if a qubit suffers a spin-flip error σ_x (phase-flip error σ_z), two plaquette (star) anyons are created on the two adjacent plaquettes (vertices). Once an anyon exists, it can move on the surface without any further energy cost, whereby creating further spin- or phase-flip errors along its path. Two anyons of the same kind can fuse to the vacuum. On the two horizontal (vertical) boundaries of the grid in Figure 2.1 a single plaquette (star) anyon can be created. Similarly, the boundaries can absorb single anyons. If two anyons are jointly created from the vacuum, move around and then fuse to the vacuum, the produced error path can be expressed as a product of stabilizers and therefore acts trivially on the code subspace $\mathcal{K}_0$. The same holds if a single anyon is created on a boundary and then is absorbed by the same boundary again. The only possibility to act non-trivially on the state stored in $\mathcal{K}_0$ is if an error path connects the two opposite boundaries. We therefore define the logical operators $X = \bigotimes \sigma_x$ and $Z = \bigotimes \sigma_z$ acting on all qubits along the paths depicted in Figure 2.1. Since all such products that connect the two opposite boundaries are identical up to multiplication with stabilizers, the precise form of the path does not matter. These operators commute with all the stabilizers (i.e. they are elements of the centralizer of the stabilizer group) though are not products of stabilizers. They allow thus to act non-trivially on the state stored in $\mathcal{K}_0$ without leaving any smoking guns in the form of anyons. They satisfy $X^2 = Z^2 = \mathbb{1}$ and $XZ = -ZX$ and may therefore be seen as Pauli operators acting on the encoded qubit.

At the read-out step, all the operators n_s and n_p are measured and the presence of anyons (the *syndrome*) is detected. The goal is then to annihilate all anyons (either by fusing them to the vacuum or by moving them to a boundary that can absorb them) and thereby to undo the errors caused by the diffusion of the anyons. More precisely, the goal is that the total unitary formed by the natural anyon dynamics (creation, diffusion, and annihilation) plus the error correction procedure is equal to a product of stabilizers and thus acts trivially on the code space. Even more precisely, the dynamics induced by the thermal environment are in fact a probabilistic mixture of different unitary evolutions, this will be discussed in more detail later on.

Error correction

We will study planar codes of different sizes L, by which we mean that the number of plaquette operators from top to bottom as well as the number of star operators from left to right is given by L. Consequently, there are $L - 1$ four-qubit plaquettes and 2 three-qubit plaquettes from left to right and thus a total of $L \cdot (L+1)$ plaquettes. The total number of qubits is then given by $N = 2L^2 + 2L + 1$. It is well-known that in the limit of large L error correction in the toric code is unambiguously possible if less than 11% of the physical qubits are subject to uncorrelated bit- and phase-flip errors [57]. However, qubit errors induced by a thermal environment *are* correlated due to the diffusion of the anyons. Error correction therefore typically becomes impossible if a few percent of the qubits have suffered errors [38].

The error correction step consists of three substeps. In a first step, the anyon configuration or syndrome is determined by measuring all the operators n_s and n_p. This means that we project to the subspaces $\mathcal{K}_i$ with a given anyon configuration. Since there are $L \cdot (L+1)$ potential locations for anyons of each kind, there are $2^{2L\cdot(L+1)}$ such spaces, each of which has dimension 2 (they can be obtained from $\mathcal{K}_0$ by applying single-qubit errors), so

$$\mathcal{H} = \bigoplus_{i=0}^{2^{2L\cdot(L+1)}-1} \mathcal{K}_i \,. \tag{2.2}$$

Indeed, one verifies that $2 \cdot 2^{2L\cdot(L+1)}$ equals $\dim \mathcal{H} = 2^N = 2^{2L^2+2L+1}$. In a second step, a classical computation is performed on the error syndrome whose output tells how to best annihilate the anyons by fusing them with each other or moving them to a boundary of the type that can absorb them, which is then done in a third step.

In a more formal language, let ρ_0 denote the initial state stored in the memory with $\operatorname{supp} \rho_0 \subseteq \mathcal{K}_0$. The influence of errors on this state is then captured by a quantum channel (CPTPM) Φ_{err}. The goal of the classical computation is then, given knowledge about the error model Φ_{err} and the syndrome (the space $\mathcal{K}_i$, that is), to find a sequence of single-qubit Pauli operators U_i which corrects the errors. In other words, we want U_i to map $\mathcal{K}_i$ to $\mathcal{K}_0$. Now let P_i denote the projector onto $\mathcal{K}_i$. Formally, we can write the error-correction procedure performed on the corrupted state $\rho_t = \Phi_{\text{err}}^t(\rho_0)$ as $\Phi_{\text{corr}}(\rho_t) = \sum_i U_i P_i \rho_t P_i U_i^\dagger$. At the end of the day, we want the error

$$\delta(t) := \left\| \rho_0 - \left(\Phi_{\text{corr}} \circ \Phi_{\text{err}}^t\right)(\rho_0) \right\|_1 \tag{2.3}$$

to be as small as possible for any given encoded state ρ_0. In the corrected state $\left(\Phi_{\text{corr}} \circ \Phi_{\text{err}}^t\right)(\rho_0)$ no anyons are left. We therefore either have successfully corrected all errors, performed a logical X, a logical Z or both, thus

$$\begin{aligned} \left(\Phi_{\text{corr}} \circ \Phi_{\text{err}}^t\right)(\rho_0) = {} & (1-p_X)(1-p_Z) \times \rho_0 \\ & + p_X(1-p_Z) \times X\rho_0 X \\ & + (1-p_X)p_Z \times Z\rho_0 Z \\ & + p_X p_Z \times XZ\rho_0 ZX \end{aligned} \tag{2.4}$$

(assuming that the error correction procedure treats plaquette- and star-anyons independently). We therefore have

$$\delta(t) \leq 2 \cdot (p_X(1-p_Z) + (1-p_X)p_Z + p_X p_Z) \leq 2(p_X + p_Z) \,. \tag{2.5}$$

In order to obtain simple scalar functions that characterize the decay of the stored quantum information, we study the autocorrelation functions

$$C^X_{\mathrm{corr}}(t) := 2^{-N} \operatorname{tr}\left[X \cdot \left(\Phi_{\mathrm{corr}} \circ \Phi^t_{\mathrm{err}}\right)^\dagger (X)\right] \tag{2.6}$$

$$C^Z_{\mathrm{corr}}(t) := 2^{-N} \operatorname{tr}\left[Z \cdot \left(\Phi_{\mathrm{corr}} \circ \Phi^t_{\mathrm{err}}\right)^\dagger (Z)\right] \,. \tag{2.7}$$

The prefactor is such that $C^X_{\mathrm{corr}}(0) = C^Z_{\mathrm{corr}}(0) = 1$, assuming that no operation is performed on the stored information if no anyons are measured.

This assumption is in fact less trivial than it may seem. Performing a logical operation in the error correction step is beneficial if an odd number of logical operators have been performed by the bath. Assume that the bath induces logical errors that leave no anyons with rate r. Then, the probability that no logical error has been performed is in fact small for times $t \gg r^{-1}$. The probability that after time t k logical errors have been performed is given by the Poisson distribution,

$$P(k, rt) = \frac{(rt)^k e^{-rt}}{k!} \,. \tag{2.8}$$

The Poisson distribution is peaked around rt, which may be an odd integer. However, the probability

$$\sum_{k \text{ even}} P(k, rt) = \frac{1}{2}\left(1 + e^{-2rt}\right) \tag{2.9}$$

of an even number of errors is greater than $\frac{1}{2}$ for any rt, such that the optimal strategy is, indeed, not to do anything if no anyon is detected.

$C^X_{\mathrm{corr}}(t)$ is 1 if after error correction at time t no logical Z-operator has been applied and -1 if one has been applied (i.e. an odd number of σ_z-operators has been applied to any line connecting the left and right boundary). Therefore, $C^X_{\mathrm{corr}}(t) = 1 - 2p_Z$ and analogously $C^Z_{\mathrm{corr}}(t) = 1 - 2p_X$. In conclusion we have

$$\left\|\rho_0 - \left(\Phi_{\mathrm{corr}} \circ \Phi^t_{\mathrm{err}}\right)(\rho_0)\right\|_1 \leq \left(1 - C^X_{\mathrm{corr}}(t)\right) + \left(1 - C^Z_{\mathrm{corr}}(t)\right) \,. \tag{2.10}$$

We define the lifetime $\tau(\varepsilon)$ of the memory as the maximal time such that $\min\left\{C^X_{\mathrm{corr}}(t), C^Z_{\mathrm{corr}}(t)\right\} \geq 1-\varepsilon$ for all $t \leq \tau(\varepsilon)$, implying that $\delta(t) \leq 2\varepsilon$ for $t \leq \tau(\varepsilon)$.

The total evolution $\Phi_{\mathrm{corr}} \circ \Phi^t_{\mathrm{err}}$ is a statistical mixture of different unitary evolutions. In the numerical simulations, we will in each run follow a definite unitary evolution, such that $C^Z_{\mathrm{corr}}(t)$ is at any time given by ± 1. The probability of a certain unitary is thereby determined by the error model Φ_{err}. Sampling over a large number of runs, we obtain a smooth function $C^Z_{\mathrm{corr}}(t)$.

We say that two sequences of single-qubit Pauli operators are equivalent if they are identical up to multiplication with stabilizers. For every given anyon configuration, there are four equivalence classes of errors that produce it from the vacuum. These equivalence classes can be mapped onto each other by application of the logical operators I, X, Z, XZ. Given a syndrome, the goal is to guess the most likely equivalence class of errors that has produced it, which one allows to remove the anyons without disturbing the stored quantum information. Calculating the probabilities of the four equivalence classes is numerically too costly to be performed with current technology. We thus make the simplifying assumption that the most likely error path that has led to the given syndrome is an element of the most likely equivalence class. This may not be true for every possible anyon configuration but seems a reasonable approximation. Applying stabilizers to the most likely error path will produce further error paths with identical or slightly lower probabilities that are elements of the same equivalence class. Rather than finding the error path with maximal probability, we may equivalently find the error path with *minimal weight*, if we define the weight to be the negative logarithm of the probability that a certain error chain has occurred. Taking the negative logarithm ensures that the weight is additive for independent error chains. This is known as the Shannon information content of an event in classical information theory [67] and up to a constant factor the only function having the additivity property.

To illustrate this, let us consider a concrete simple error model. We assume that each physical qubit suffers a spin-flip error with probability p_x and a phase-flip error with probability p_z,

$$\begin{aligned}&\Phi_{\mathrm{err}} = \Phi^{\otimes N}_{\mathrm{single-qubit}} \quad , \\ &\Phi_{\mathrm{single-qubit}}(\omega) = \\ &(1-p_x)(1-p_z)\cdot\omega + p_x(1-p_z)\cdot\sigma_x\omega\sigma_x + (1-p_x)p_z\cdot\sigma_z\omega\sigma_z + p_xp_z\cdot\sigma_y\omega\sigma_y \ .\end{aligned} \tag{2.11}$$

The weight of an error chain involving ℓ_x spin-flips and ℓ_z phase-flips is then

$$\ell_x \cdot \ln \frac{1-p_x}{p_x} + \ell_z \cdot \ln \frac{1-p_z}{p_z} + \text{const} \,, \tag{2.12}$$

allowing us to minimize (for $p_x, p_z < \frac{1}{2}$) ℓ_x and ℓ_x independently. The number of single-qubit Pauli operators necessary to connect two anyons with each other is given by the so-called 'Manhattan distance' of the anyons, i.e. the sum of the horizontal and the vertical coordinate difference of two anyons. Similarly, the weight of a chain connecting an anyon to a boundary is given by the horizontal or vertical distance. In detail, our minimal weight matching of n anyons (of one kind) then works as follows.

1. Perform a Delaunay triangulation on the set of anyon coordinates, thereby restricting the full graph of $\frac{n(n-1)}{2}$ edges between anyons to $O(n)$ edges. Calculate the Manhattan weights of all edges in the restricted graph.
2. For every anyon, add a 'virtual' partner on the closer boundary able to absorb it and add an edge to the graph with weight given by the distance to the boundary.
3. Connect all virtual anyons with zero-weight edges.
4. Perform a minimum-weight matching of the graph obtained this way.

Points 1. and 4. are identical to the methods used in [38, 40]. We perform the Delaunay triangulation using the library `Triangle` [68] while for the minimal-weight perfect matching we employ the library `Blossom V` [69] implementing the 'blossom' algorithm due to Edmond's [70]. The numerical cost of this procedure is strongly dominated by the last step. Adding the virtual anyons ensures that each real anyon can be connected to the closest edge able to absorb it and that there is always an even number of points in the graph entering the perfect matching algorithm. Giving the edges between virtual anyons weight zero ensures that those virtual anyons that are not connected to a real one can be removed at no cost.

Employing this algorithm, we obtain the decay of the autocorrelation function C^Z_{corr} as a function of p_x illustrated for different lattice sizes in

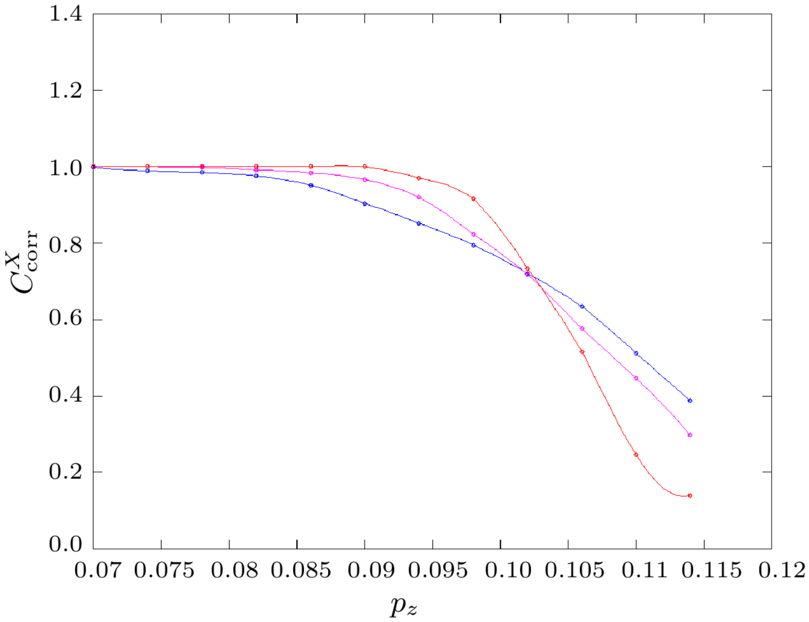

Figure 2.2: The plot shows the autocorrelation function C^X_{corr} as a function of the fraction of physical spins p_z that have suffered spin-flip errors. Circles give the numerical results, the lines are guides to the eye. The curves correspond to different lattice sizes $L = 32$ (blue), $L = 64$ (magenta) and $L = 128$ (red). We anticipate that in the limit $L \to \infty$ error correction is unambiguously possible for any $p_z < p_c$, with $p_c \gtrsim 0.102$.

Figure 2.2. The curves for different lattice sizes intersect for $p_c \gtrsim 0.102$, so that in the limit of $L \to \infty$ error correction is possible for $p_x, p_y < p_c$. Our numerically obtained value is only slightly smaller than the theoretical value $p_c \simeq 0.1094 \pm 0.0002$ [57]. For the uncorrected or 'bare' autocorrelation functions we have $2^{-N}\,\mathrm{tr}\left[X \cdot \Phi^{\dagger}_{\mathrm{err}}(X)\right] \approx 0$ in the whole parameter regime depicted in Figure 2.2, so there is a regime where our error-correction procedure is maximally beneficial, bringing the autocorrelation function from 0 to 1.

Error model

We now turn to the situation we are actually physically interested in, namely where Φ^t_{err} is induced by the memory Hamiltonian H and coupling of the memory to a thermal environment. We consider a Davies weak-coupling limit [71] and briefly summarize its discussion in [38, 40, 62]. In this limit, the evolution of the memory is described by a Markovian Master equation

$$\dot{\rho}_t = -i\,[H, \rho_t] + \mathcal{L}(\rho_t) \tag{2.13}$$

where the interaction between the memory and the bath is captured in the unitarity-breaking Lindblad operator $\mathcal{L}$. We assume that the environment is weakly coupled to the bath through single-qubit Pauli operators and thus is able to induce spin- and phase-flip errors, leading to transitions between eigenstates of H that differ only by the application of a single-qubit Pauli operator. Processes in which an energy ω is transferred from the anyonic system to the bath happen with rate $\gamma(\omega)$, which depends on how the bath is modeled. An expression for $\gamma(\omega)$ often found in the literature is given by

$$\gamma(\omega) = 2\kappa_n \left|\frac{\omega^n}{1 - e^{-\beta\omega}}\right| e^{-|\omega|/\omega_c} \tag{2.14}$$

and can be derived from a spin-boson model [72,73]. In the following, we set the cutoff frequency of the bath $\omega_c \to \infty$ for simplicity. A bath with $n = 1$ is called 'Ohmic', whereas one with $n \geq 2$ is called 'super-Ohmic'. Only the former case is considered in the numerical simulations.[2] To summarize, we will use

$$\gamma(\omega) = \gamma(0) \cdot \left|\frac{\beta\omega}{1 - e^{-\beta\omega}}\right| \tag{2.15}$$

where we think of $1/\gamma(0) = (2\kappa_1 T)^{-1}$ as the relevant microscopic timescale, since the diffusion of anyons is widely determined by $\gamma(0)$. Note that Eq. (2.14) and Eq. (2.15) fulfill the detailed balance condition $\gamma(-\omega) = \gamma(\omega) \cdot e^{-\beta\omega}$, guaranteeing that the Gibbs state is the fixed point of the Markovian dynamics, $\mathcal{L}\left(e^{-\beta H}\right) = 0$.

In such a physical model, the weight of a hypothetical error chain is not simply given by its Manhattan length, as it was the case in Eq. (2.12). It is in general not true that the most likely error chain is the one with the smallest number of spin flips. The number of hoppings some time Δt

---

[2] Note that for a super-Ohmic bath we have $\gamma(0) = 0$, forbidding the direct hopping of anyons and heavily suppressing their diffusion. In this case, only 'indirect hopping' [38] is possible, in which a new pair of anyons is created next to an existing one and the existing one fuses with one of them, leading to an effective movement of the already existing anyon.

after the creation of an anyon or a pair of anyons is Poisson-distributed and for large $\gamma(0)\cdot\Delta t$ there is in fact a *small* probability that the number of spin flips is still small. Using the Manhattan distance as the weight of an error chain connecting two anyons (as done in [38,40]) seems thus hard to justify. Rather than trying to find the most likely error chain, we therefore try to find the most likely *pairing* of the defects (a pairing may either be between two anyons or between an anyon and a boundary). This is not exactly equivalent to finding the most likely equivalence class of errors but should not make a relevant difference in practice and is numerically feasible.

The random walk of an anyon on the grid leads to a diffusive spreading of the probability distribution. The probability of finding it at time t at a position $\vec{r}$ relative to its position at time t' is

$$\frac{1}{4\pi D(t-t')}\cdot e^{-\vec{r}^2/4D(t-t')}\,. \tag{2.16}$$

In the case of an Ohmic bath, the diffusion constant D is basically given by the hopping rate $\gamma(0)$ [38]. Similarly, the distance vector of two anyons that have been jointly created diffuses with a constant $2D$ since both of its ends are moving. A sensible choice for the weight of an edge between two anyons is therefore the square of their Euclidean distance, while for an edge connecting an anyon to its closer boundary we take the weight to be *twice* the square of the Euclidean distance. A more thorough justification of this choice can be found in Appendix 2.A. An example for the application of the error correction algorithm is given in Figure 2.3.

2.3 Long-range repulsion between anyons

A $1/r^\alpha$ repulsive potential with $0\leq\alpha<2$ between the anyons allows one to increase the lifetime of the toric code arbitrarily by increasing L [38]. We study the $\alpha=0$ case here, since for this case proposals of its physical implementation exist [38, 39]. Furthermore, this case can be analyzed analytically without need for a mean-field approximation and provides the best scaling of the lifetime with L. Since the repulsive potential is independent of the anyon distances r, its numerical simulation has the lowest cost.

We study a system with a repulsion between the anyons which is spa-

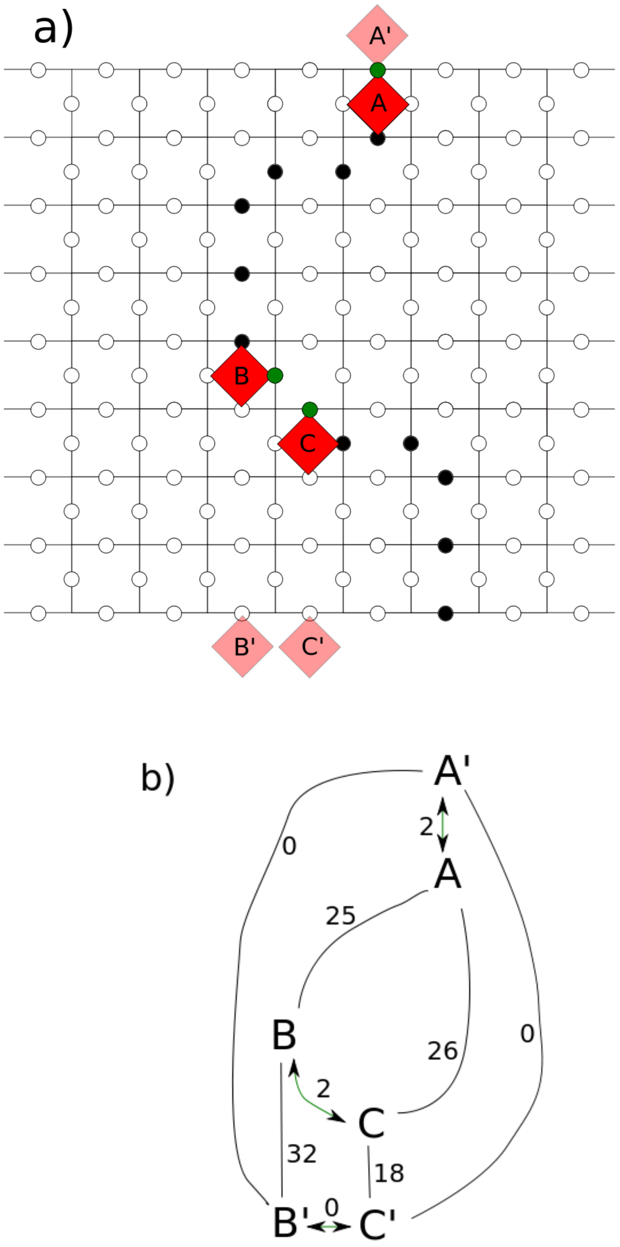

Figure 2.3: The code has suffered σ_x errors at the black qubits in a). The syndrome measurement detects plaquette anyons A, B, and C. For the error correction procedure, we first perform a Delaunay triangulation of the full graph with edges connecting all real anyons (in the case of only three real anyons, the full graph and the triangulation coincide). Then, virtual anyons A', B', and C' are added. The graph b) is then used for the perfect matching algorithm, where the obtained matching is highlighted with arrows. Error correction fails, because anyons B and C are fused and anyon A is moved to the upper boundary, thereby performing a logical X operator on the qubit stored in $\mathcal{K}_0$.

tially constant, so the total Hamiltonian is

$$H = H_{\text{Kitaev}} + \frac{A}{2} \cdot \left(\sum_{p \neq p'} n_p n_{p'} + \sum_{s \neq s'} n_s n_{s'} \right) , \tag{2.17}$$

where H_{Kitaev} is as in Eq. (2.1).[3] Let us first discuss the toric code, i.e. a memory with periodic boundary conditions. The lifetime of the memory is given by the time when finding the most likely anyon pairing becomes ambiguous. After a time t, the distance between the two anyons of a pair is of order $\sqrt{Dt}$, with a diffusion constant D. Let n_{eq} be the equilibrium density of anyons, such that their average separation is $\sim 1/\sqrt{n_{\text{eq}}}$. We may then estimate the lifetime of the memory as the time when the anyons have diffused over their average distance and error correction becomes ambiguous,

$$\tau(\varepsilon) = \frac{c(\varepsilon)}{D \cdot n_{\text{eq}}} . \tag{2.18}$$

We use $c(\varepsilon)$ as a single fitting parameter, which can be thought of as a critical fraction of spins affected by errors and will be of order of a few percents [38].

Let

$$e_{\text{eq}} = \Delta + A(L^2 n_{\text{eq}} - 1) \tag{2.19}$$

denote energy per anyon in equilibrium. Since there is either one or no anyon at each position, the equilibrium anyon density can be determined self-consistently from

$$n_{\text{eq}} = [\exp(\beta e_{\text{eq}}) + 1]^{-1} . \tag{2.20}$$

The diffusion constant is $D = \gamma(0) + 4\gamma(-2e_{\text{eq}})$, which for an Ohmic bath is widely dominated by the first summand [38].

---

[3] We assume in this section that the energy penalty for both three- and four-qubit stabilizer violations have the same strength Δ. This can be achieved by appropriately desigend perturbative gadgets [74]. However, we will see that the stability of the memory for large L is due to the second term in Eq. (2.17), i.e. the inter-anyonic interaction, and that the bare anyon energy cost Δ becomes in fact irrelevant. In contrast, in Sec. 2.4, we will assume that the stabilizer operators are obtained from the honeycomb model such that there is no energy penalty associated with three-qubit stabilizer operators. Basically, the total energy is now parabolically rather than linearly increasing in the anyon numbers. The physical realization of such an interaction and its effect on the lifetime of the toric code have been studied in detail in [38–40].

Straightforward algebra (c.f. Appendix 2.B) gives two simple bounds on n_{eq} for large enough L. We have that

$$n_{\text{eq}} > \frac{1}{L^2} \quad \text{if} \quad L^2 > \exp(\beta\Delta) + 1 \tag{2.21}$$

and

$$n_{\text{eq}} < \frac{1}{L^{2-\varepsilon}} \quad \text{if} \quad \frac{\ln L}{L^{\varepsilon} - 1} < \frac{\beta A}{2-\varepsilon} \; . \tag{2.22}$$

Putting these bounds into Eq. (2.20) we also find

$$L^{2-\varepsilon} < \exp(\beta e_{\text{eq}}) + 1 < L^2 \tag{2.23}$$

for large enough L. The lifetime Eq. (2.18) is inverse in n_{eq} and will thus for any $\varepsilon > 0$ grow faster than $L^{2-\varepsilon}$ as $L \to \infty$.

In the case of the planar code, single anyons can be created at and absorbed by the boundaries. The anyon production rate per boundary spin is $\gamma(-e_{\text{eq}})$ (if the anyon density approaches the equilibrium density), while it is $2\gamma(-2e_{\text{eq}} - A)$ for spins in the bulk. Again, e_{eq} can be determined self-consistently from Eq. (2.19) and Eq. (2.20), where we replace L^2 by $L(L+1)$ in Eq. (2.19) for the planar code. In order to find the total creation rates, these single-spin production rates have to be multiplied by $2(L+1)$ and $2L^2 - 1$, the number of spins on the boundary and in the bulk, respectively. The total rate for production of anyons on the boundaries is then, using the bath Eq. (2.15),

$$2(L+1) \cdot \gamma(-e_{\text{eq}}) \simeq 2(L+1)\frac{\beta e_{\text{eq}}}{\exp(\beta e_{\text{eq}})}\gamma(0) \; , \tag{2.24}$$

while the total rate for the production of anyons in the bulk is

$$(2L^2 - 1) \cdot 2\gamma(-2e_{\text{eq}} - A) \simeq (2L^2 - 1)\frac{4\beta e_{\text{eq}}}{\exp(2\beta e_{\text{eq}})}\gamma(0) \; . \tag{2.25}$$

Since the anyon density vanishes for large enough L, we neglected for these estimates that in fact only those spins that have no adjacent anyons should be considered for the anyon production rate. Using Eq. (2.23) with $\varepsilon = \frac{1}{2}$, we see that both the anyon production rate on the boundaries and in the bulk go to 0 as $L \to \infty$. But which of the two will dominate for large L? Applying again Eq. (2.23), it is clear that the ratio $\simeq \frac{\exp(\beta e_{\text{eq}})}{4L}$ of the boundary to the bulk rate is in fact *diverging* with L. The analytics

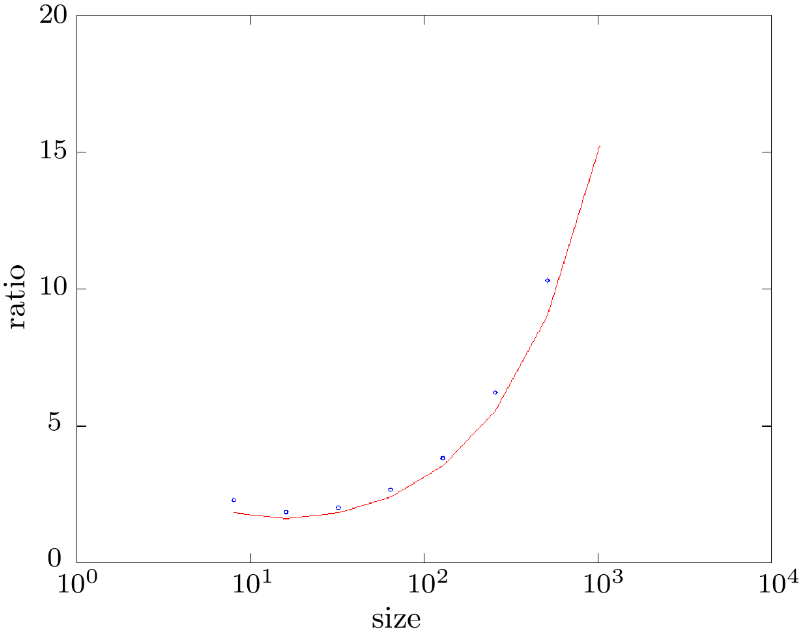

Figure 2.4: Ratio of the number of anyons created on the boundary to the number of anyons created in the bulk if the anyon population approaches its equilibrium value. The blue circles show numerical results sampled over a time $10^5 \cdot (\kappa_1 \Delta)^{-1}$. The red curve shows the analytical prediction $\exp(\beta e_{\mathrm{eq}})/4L$. We have used parameters $\beta\Delta = 1/0.3$ and $A/\Delta = 0.1$ and a bath $\gamma(\omega)$ as in Eq. (2.15).

are in excellent agreement with numerical simulations (Figure 2.4) that show an increasing ratio after a slight minimum at $L \simeq 16$.

Let us note that the ratio of "active" anyons is in fact slightly different than what the above analysis suggests. The probability that an anyon created at the boundary is not reabsorbed before it gets to the second row is $\frac{\gamma(0)}{\gamma(0)+\gamma(+e_{\mathrm{eq}})} \simeq \frac{\gamma(0)}{\gamma(+e_{\mathrm{eq}})}$. Similarly, the probability that a newly created pair is not immediately re-annihilated is $\simeq \frac{6\gamma(0)}{\gamma(2e_{\mathrm{eq}}+A)}$. If we are only interested in the ratio of boundary to bulk anyons that ever get away from their place of creation, we thus obtain a further factor $\frac{\gamma(2e_{\mathrm{eq}}+A)}{6\gamma(+e_{\mathrm{eq}})}$. For the bath Eq. (2.15), this factor converges to $\frac{1}{3}$ for large enough L. The ratio of "active" anyons created at the boundaries to "active" anyons created in the bulk is thus finally $\frac{\exp(\beta e_{\mathrm{eq}})}{12L}$.

An anyon created at the boundary has three possible fates.

1. It can be reabsorbed by the same boundary (which will happen to most of them) or fuse with an anyon created at the same boundary, leading to a trivial operation performed on the degenerate ground space.
2. It can fuse with an anyon created at the opposite boundary or be absorbed by the opposite boundary, leading to a logical error.
3. It can fuse with an anyon created in the bulk.

We will argue that the time it takes to create a logical error via possibility 2 is larger than the lifetime of the memory in the toric case and that possibility 3 has a beneficial effect on the lifetime of the memory. Combining these arguments with the fact that anyon production on the boundary surpasses the anyon production in the bulk, we conclude that the boundary has a positive net effect on the lifetime of the memory.

Let us study the time it takes to create a logical error through possibility 2. There are two time-scales involved in the creation of such an error: The time it takes to create an anyon that walks during its lifetime at least once to the opposite half of the grid and the time it takes to do this walk. What is the probability that an anyon created at a boundary ever moves to the opposite half of the grid and what is the expected number of hoppings necessary for this? Up to the boundary conditions, this problem is exactly equivalent to a well-known mathematical problem called The Gambler's Ruin. If a newly created anyon is to ever reach the opposite half, it first has to avoid immediate reabsorbtion. The probability of ever getting to the second row is $\simeq \frac{\gamma(0)}{\gamma(+e_{\mathrm{eq}})}$. Now imagine that the distance of the anyon to the boundary that has created it represents a gambler's bankroll. He starts with one unit of money (the anyon starts at the first row) and then does a series of fair coin flips for one unit of money each. He ends when either he gets broke (the anyon gets reabsorbed by the same boundary that has created it) or his bankroll reaches $L/2$ units of money (the anyon reaches the opposite half of the grid). Since the gambler starts with one unit of money and he does a series of games with zero expectation value, his probability of ever reaching $L/2$ has to be $2/L$, which also answers the corresponding question for the anyon. Note that movements of the anyon parallel to the boundary that has created it are irrelevant for the production of logical errors, which is why the problem can be mapped to such a one-dimensional one. Note that in the case of anyons this probability provides in fact an upper bound, since we neglected the possibility that the anyon fuses with another one before reaching the opposite half of the grid. A formally correct treatment of the problem can be found in Appendix 2.C. There, we also show that the average number of coin flips (hoppings perpendicular to the creating boundary) needed to reach $L/2$ is $(L/2)^2$.

To summarize, anyons are created at the boundaries with rate $2(L+1)\gamma(-e_{\mathrm{eq}})$, only a fraction $\frac{\gamma(0)}{\gamma(+e_{\mathrm{eq}})}$ do not immediately get reabsorbed and only a fraction of at most $\frac{2}{L}$ ever reaches the opposite half of the grid. If an anyon does reach the opposite grid, this takes on average a time $\frac{1}{\gamma(0)} \cdot 2 \cdot \left(\frac{L}{2}\right)^2$ (the factor 2 takes hoppings parallel to the creating boundary into account). The total lifetime of a memory in which anyons are only created at the boundaries may therefore be estimated as

$$\frac{1}{2(L+1)\gamma(-e_{\mathrm{eq}})} \cdot \frac{\gamma(+e_{\mathrm{eq}})}{\gamma(0)} \cdot \frac{L}{2} + \frac{1}{\gamma(0)} \cdot \frac{L^2}{2} \simeq \frac{1}{4\gamma(0)} \cdot \left(e^{\beta e_{\mathrm{eq}}} + 2L^2\right) \quad (2.26)$$

where we used detailed balance. Note that the only time-scale that entered the first summand was the anyon creation time $1/\gamma(-e_{\mathrm{eq}})$. However, this cancels exactly with $\gamma(+e_{\mathrm{eq}})$: the higher the anyon production rate, the higher is (by detailed balance) the probability that an anyon is immediately reabsorbed, such that the only remaining time-scale is $1/\gamma(0)$.

The only property of the bath $\gamma(\omega)$ we used was the detailed balance property, so this scaling behavior is independent of the particulars of the bath and not specific for Eq. (2.15). However, in the case of a super-Ohmic bath with $\gamma(0) = 0$ the analysis of the Gambler's Ruin problem has to be redone with an effective hopping rate emerging from indirect hopping processes that scale with $\gamma(-2e_{\mathrm{eq}} - A)$ [38]. Since e_{eq} diverges logarithmically with L (2.23), the effective hopping rate becomes vanishing for large L, leading to an improved scaling of the memory lifetime with L [38].

Using Eq. (2.20) we see that the first summand in Eq. (2.26), i.e. the timescale needed for the creation of an anyon that walks to the opposite half, is for large enough L identical to the lifetime of the toric code Eq. (2.18). Furthermore, we know from Eq. (2.23) that the second summand grows faster than the first one. We conclude that the time needed for anyons created on the boundaries to produce a logical error grows faster with L than the time before the matching of anyons produced in the bulk becomes ambiguous.

In the limit of very large L, anyons are created almost exclusively on the boundary, once the anyon production rates have approached their equilibrium values. However, as long as the anyon population is small enough anyon production in the bulk will outweigh anyon production on the boundaries, so that possibility 3 is non-negligible even for large L.

Possibility 3 has the same effect as if the bulk anyon with which the boundary anyon fused had moved to and been absorbed by the creating boundary. The effect of possibility 3 is therefore to cause an effective bias of bulk anyons to move to the closer boundary. We saw that the probability that a boundary anyon gets a certain distance away from its creating boundary decreases at least inversely with that distance. This effect is thus the stronger, the closer the bulk anyons are to the boundary. We saw in the discussion of the toric case that error correction breaks down if the anyons that have been created as parts of the same pair have moved sufficiently far away from each other such that the pair-matching becomes ambiguous. If two such anyons, however distant they are, now move to the same boundary this ambiguity is resolved without a logical error.

In conclusion, the equilibrium density of anyons n_{eq} is not affected by the boundary conditions, but the fraction of anyons created on the boundary becomes dominant for large enough L. The time it takes for boundary anyons to create a logical error grows faster with L than the lifetime of the toric code. We expect a beneficial effect from the possibility of boundary anyons fusing with bulk anyons. We conclude that for large enough L a planar code of size L has a larger lifetime than a toric code of size L.

This is indeed confirmed by our numerical simulations. Already for $L \gtrsim 32$ the lifetime $\tau(0.1)$ of the planar code exceeds the one of the toric code. For very small memories ($L < 10$) the toric code is superior, which may be attributed to logical errors caused by single anyons. In the planar code in Figure 2.1, for example, an anyon created at a boundary needs to perform only 4 hoppings to cause a logical error when error correction is performed. Figure 2.5 illustrates the temporal decay of the stored quantum information by depicting the autocorrelation functions $C^Z_{\text{corr}}(t)$ for different lattice sizes and for both planar and toric grids. The obtained lifetimes are illustrated in Figure 2.6.

While we included the analytical prediction Eq. (2.18) for the lifetime of the toric code in Figure 2.6, we cannot give such a simple expression for the lifetime of the planar code. When L is increased, the effect of the boundary changes from adversarial to beneficial.

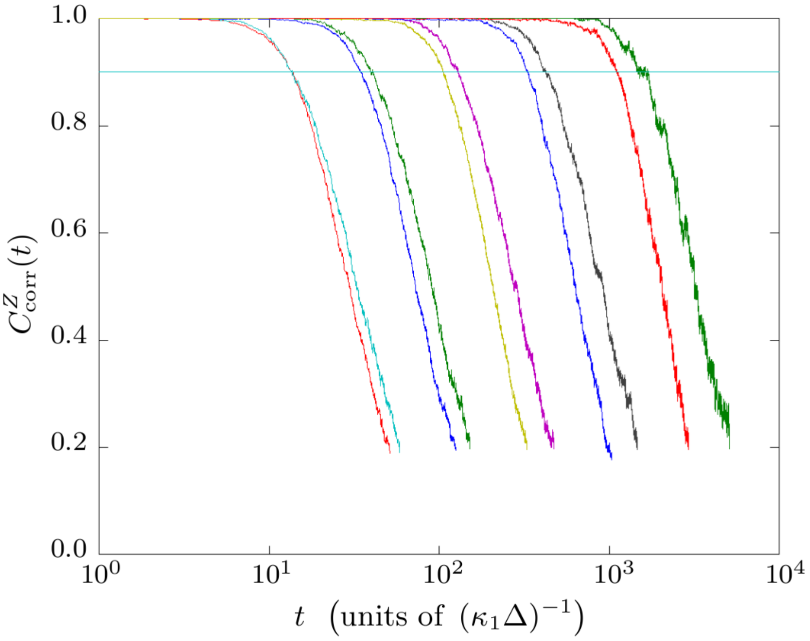

Figure 2.5: Temporal decay of the autocorrelation functions $C^Z_{\rm corr}(t)$ for different lattice sizes and boundary conditions, for the Hamiltonian Eq. (2.17) and the bath Eq. (2.15). Times are in units of $(\kappa_1\Delta)^{-1}$ and the physical parameters are $\beta\Delta = 1/0.3$ and $A/\Delta = 0.1$. From left to right (at height 0.6, say) we have (grid type – size L) toric 32, planar 32, toric 64, planar 64, toric 128, planar 128, toric 256, planar 256, toric 512, and planar 512. The intersection of $C^Z_{\rm corr}(t)$ with the horizontal line at height 0.9 is used to determine the lifetimes $\tau(0.1)$ given in Figure 2.6.

2.4 The honeycomb model as a quantum memory

From the honeycomb to the planar code

The toric code Hamiltonian Eq. (2.1) (involving local *four*-qubit couplings) can be realized as a low-energy effective Hamiltonian of the Kitaev honeycomb model, which involves only local *two*-qubit couplings [39,64,75]. The Hamiltonian of the honeycomb model can be simplified through a spin to hard-core boson transformation [75]. In this new language, the toric code Hamiltonian Eq. (2.1) emerges as a low-energy (no hard-core bosons present) fourth-order effective Hamiltonian. The qubits of the

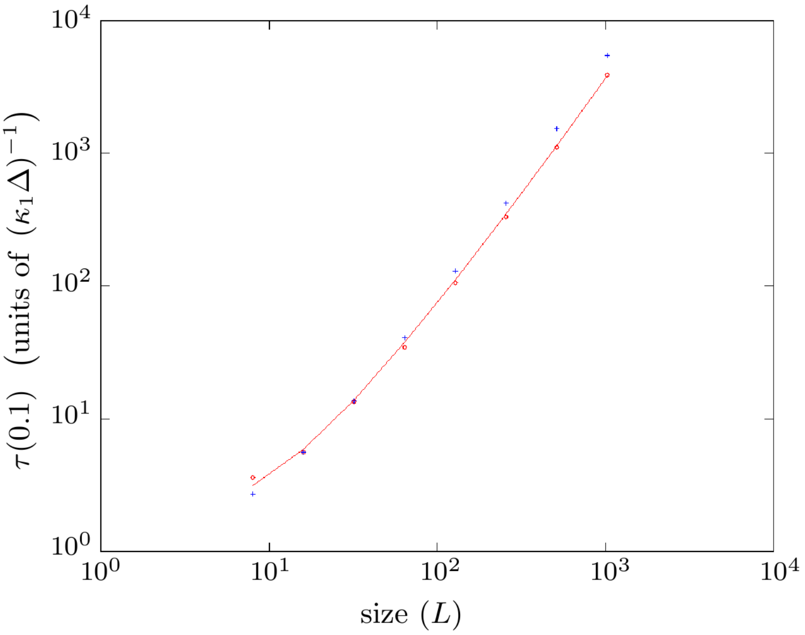

Figure 2.6: Lifetimes $\tau(0.1)$ of the quantum information stored in the systems described in the caption of Figure 2.5. The blue crosses represent planar codes, the red circles toric codes. The sizes L of the codes are 8, 16, 32, 64, 128, 256, 512, and 1024. The red line shows the analytical prediction for the lifetime in the toric case obtained from Eq. (2.18) with $c(0.1) = 5.1\%$. [38] find with an analogous plot [Fig. 6] $c(0.1) = 4.4\%$. The increased lifetime is due the choice of the square of the Euclidean distance rather than the Manhattan length as the weight of an error chain.

toric code obtained this way are not identical to the physical qubits of the underlying honeycomb lattice, but are *effective* qubits. The interactions of Eq. (2.1) between four of these effective qubits are mediated through processes in which two pairs of virtual hard-core bosons are created and then fuse again to the vacuum. An interaction involving three effective qubits would correspond to a process in which a pair of virtual hard-core bosons is created from the vacuum, followed by a hopping and an annihilation process. Clearly, such processes give no contribution to the effective Hamiltonian and the third-order effective Hamiltonian vanishes. There is no way of obtaining from the honeycomb model the three-qubit boundary terms introduced in [66] and used so far in this paper.

Figure 2.7 schematically shows a planar code obtained from the hon-

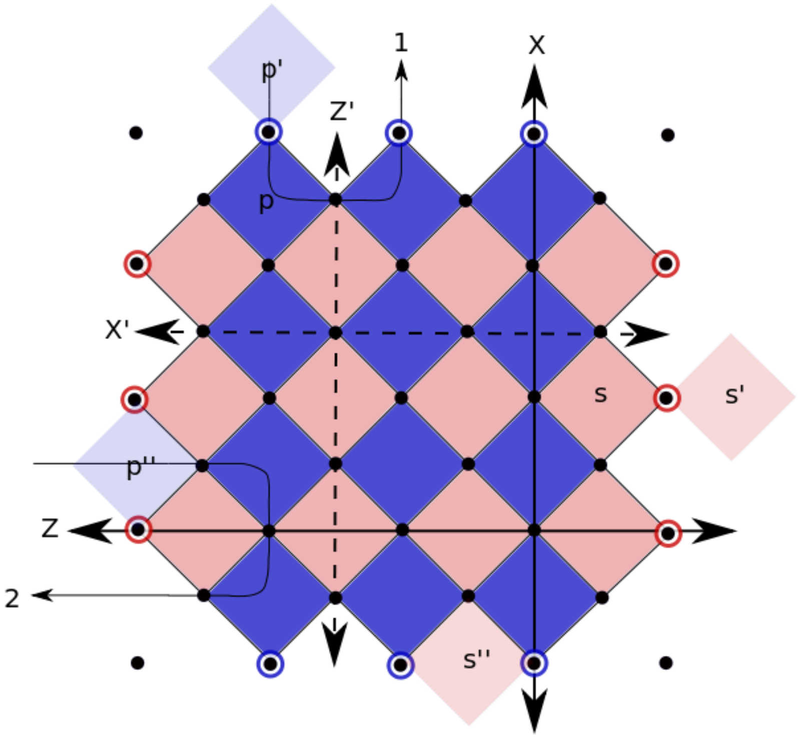

Figure 2.7: An effective planar code obtained from a honeycomb lattice with a boundary. The black dots represent effective qubits emerging from the underlying honeycomb model. The four isolated effective qubits in the corners are depicted for completeness but not needed for information storage. Blue (dark) squares (like p) are plaquette operators, red (light) squares (like s) are star operators. There are two non-equivalent ways of defining a pair of macroscopic Pauli-like observables, the "big" logical operators X and Z and the "small" logical operators X' and Z'. However, an undetectable logical error consisting of only three single-qubit errors can be performed on all of these operators. For instance, a sequence of σ_x errors on the three qubits along path 1 (2) causes an error on the logical Z' (Z) operator.

eycomb model, involving only four- but no three-qubit operators. The ground space of the Hamiltonian obtained this way, i.e. the space stabilized by all four-qubit operators $(\sigma_z)^{\otimes 4}$, $(\sigma_x)^{\otimes 4}$, has then a large degeneracy growing with the size of the memory, even if we forget about the four isolated qubits in the corners that do not interact with anything.

Let $\mathcal{G}$ denote the group generated by all four-qubit stabilizers. In an abstract language, elements of the Pauli group on all effective qubits (except the four isolated ones in the corners) that are in the centralizer $C(\mathcal{G})$ of the stabilizer group $\mathcal{G}$, but not in $\mathcal{G}$ itself, perform logical operations on the stabilized subspace that cannot be detected through violation of a stabilizer. The goal is then to find Pauli-like observables $X, Z \in C(\mathcal{G}) \setminus \mathcal{G}$ which allow us to store a qubit that is topologically protected. Elements of $C(\mathcal{G}) \setminus \mathcal{G}$ that commute with X and Z will not do any harm to the stored qubit, but those that do not commute with X or Z can. For topological protection we therefore want

- X and Z to have a macroscopic distance (i.e. to necessitate $O(L)$ single-qubit operations), and
- all elements of $C(\mathcal{G}) \setminus C(\langle X, Z \rangle)$ to have macroscopic distance.

Unfortunately, in the planar code obtained from the honeycomb model there is no choice of logical operators X and Z that fulfill these requirements. As illustrated in Figure 2.7, the pairs X, Z and X', Z' fulfill the first requirement but not the second one.

We will therefore expand $\mathcal{G}$ in such a way that all elements of $C(\mathcal{G}) \setminus \mathcal{G}$ have a macroscopic distance. For the space stabilized by $\mathcal{G}$ being nontrivial we need $\mathcal{G}$ to be Abelian and to not contain $-I$. All of these requirements are met if we add to $\mathcal{G}$ the single-qubit operators σ_x acting on all qubits surrounded by a red circle in Figure 2.7 and the operators σ_z acting on all qubits surrounded by a blue circle. Error paths 1 and 2 in Figure 2.7 now no longer are elements of $C(\mathcal{G}) \setminus \mathcal{G}$: 1 is no longer an element of $C(\mathcal{G})$ since it anti-commutes with two blue single-qubit operators in $\mathcal{G}$ while 2 becomes an element of $\mathcal{G}$ (it is the product of the two red operators enclosed by it). Therefore, the "small" operators X' and Z' now satisfy our requirements for topological protection while the "big" operators X and Z still violate the second requirement.

Our new stabilized subspace topologically protects exactly one qubit. In fact, our new code is exactly equivalent to the planar code with three-qubit operators on the boundary, since the single-qubit stabilizer operators effectively eliminate the two degrees of freedom of the qubits on the boundary. However, the Hamiltonian dynamics are different since there is no energy penalty associated with the violation of the single-qubit stabilizers on the boundary. We therefore assume that we are able to perform the measurements corresponding to the single-qubit stabilizers at the read-out step. Note that these operators act on *effective* qubits, but σ_x and σ_z measurements performed on them indeed correspond to measurements of a single *physical* qubit of the underlying honeycomb lattice. We refer to [39] for details about the mapping between physical and effective qubits.

If one of the single-qubit stabilizers on the boundary is violated, we may imagine that an anyon is present at the position adjacent to it which is outside of the actual grid. For example, a σ_x (σ_z) error can create two plaquette (star) anyons at positions p and p' (s and s') in Figure 2.7. An anyon at position p' (s') can only escape to p (s). In terms of anyon dynamics there are now for both kinds of anyons two boundaries that can create and absorb them and two boundaries that "attract" and store them. For example, a plaquette (star) anyon at position p (s) can reduce its energy by hopping to position p' (s'). Analogously, escaping from one of these boundary positions has an energy cost. An anyon that hops to position p'' or s'' has been absorbed by the corresponding boundary and can, unlike one at position p' or s', no longer be detected through a violated stabilizer operator. During error correction, an anyon stored at position p' or s' will be moved to the interior of the grid.

Repulsion between anyons and anyon holes

As discussed, the simple toric code Hamiltonian Eq. (2.1) does not provide a lifetime of the stored quantum information that can be increased by making the memory larger. Pedrocchi *et al.* [39] studied a honeycomb model as introduced above coupled to cavity modes. The cavity modes allow the read-out of the error syndrome of the effective toric code through frequency shifts. In a resonant parameter regime, the Hamiltonian

$$H_{\text{eff}} = \Delta \sum_{a,a'} n_a \bar{n}_{a'} \tag{2.27}$$

is found perturbatively [Eq. (52) in [39]]. Here, the sum $\sum_a$ runs over all stars and plaquettes (four-qubit operators only) and $\bar{n}_a = 1 - n_a$ counts anyon holes. For $\Delta > 0$ this Hamiltonian describes an effective repulsion between anyons and anyon holes. For details about how $\Delta > 0$ can be achieved, we refer to [39] and Section VII in [38].

The requirement to stay strictly in the perturbative regime puts an upper bound L^* on the linear size L of the memory [39].

With Hamiltonian Eq. (2.27) and a total of N four-qubit operators, the gap above the anyonic vacuum is $(N-1)\Delta$ and as long as $\sum_a n_a < \frac{N}{2}$ the cost to add a further anyon is at least $\frac{N}{2}\Delta$. If L denotes the number of stars from top to bottom and the number of plaquettes from left to right (so $L = 3$ in Figure 2.7) we have $N = 2L(L+1)$. With an anyon creation gap that grows quadratically in L and a natural bath like Eq. (2.15) in which the creation rate decreases exponentially with the gap, we expect the production of anyon pairs in the bulk to be negligible against the creation of anyons at the boundaries. Note that if we say that a plaquette anyon is created at a boundary where single-qubit σ_z measurements are performed, this implies that furthermore a virtual anyon is "stored" in this boundary. From the discussion of the Gambler's Ruin problem in Appendix 2.C it is clear that an anyon will do at most $\sim L^2$ hoppings before being absorbed by or stored in a boundary. We thus expect the time an anyon is present (and not stored in a boundary) to be much smaller than the time it takes to create a single anyon. To summarize, we are already for moderate values of L in the regime

$$\frac{L^2}{\gamma(0)} \ll \left[4L \cdot \gamma\left((N-1)\Delta\right)\right]^{-1} \ll \left[L^2 \cdot \gamma\left(2(N-2)\Delta\right)\right]^{-1} \tag{2.28}$$

where almost always one or no anyon is present.

In this regime, error correction works as follows.

1. Move any anyons in the interior of the grid perpendicularly to the closest of the four boundaries. (Each anyon is thereby moved to its most likely place of creation. We never assume that a pair of anyons has been created in the bulk.)

2. If an anyon is "stored" in a boundary (at position p' or s' in Figure 2.7, say), move it to the interior of the grid (to position p or s).

3. The anyons at each boundary can be matched with each other and the two-adjacent boundaries in two different not trivially suboptimal ways. Chose the one with lower weight, where the weight is given by the square of the Euclidean distance.

For this system, the perfect matching problem could be reduced to a one-dimensional one. Both possible matchings that are not trivially suboptimal can be explicitly tested, such that no approximative algorithms are needed.

Adding single-qubit measurements at the boundary spins ensures that in a planar code without three-body interactions all error paths that lead to a logical error after error correction consist of $O(L)$ single-qubit errors. Figure 2.8 illustrates schematically all error paths of a single anyon

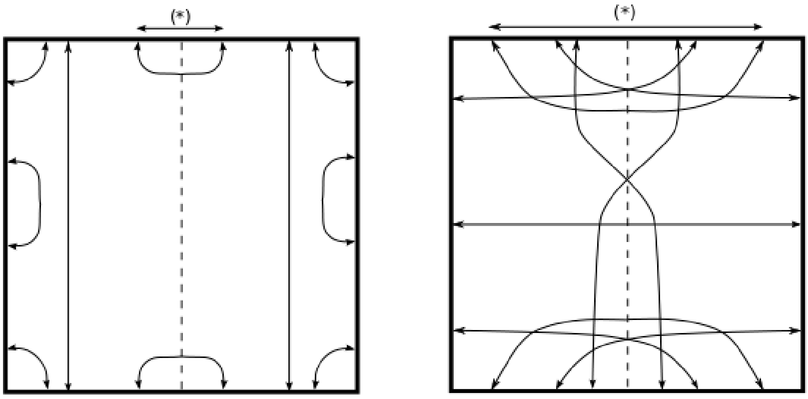

Figure 2.8: A planar code consisting only of four- and one-qubit stabilizers. We only consider σ_x-errors and the corresponding plaquette operators here. As in Figure 2.7 σ_z-measurements are performed on the top and bottom boundary. The top and bottom boundary are thus able to store and detect the presence of plaquette anyons. The logical Z operator is a path of single-qubit σ_z operators connecting the top and bottom boundary (c.f. the operator Z' in Figure 2.7). The dashed line lies midway between the left and right boundary. All error paths in the left part of the figure will not lead to a logical error after error correction, while for the error paths in the right part of the figure a logical X operator is performed. Whether an error path of type (*) is correctable depends not only on its length, but also on its position relative to the boundaries. However, any error path of type (*) and of horizontal length below $L/2$ *is* correctable.

that do lead to a logical error after error correction and all that do not. Strictly speaking, this figure is only valid for the first anyon, as a concatenation of paths that do not cause an error may lead to an error after error correction.

It is in principal possible to find an analytical expression for the probability that the first anyon causes an error in such a planar code of size L. However, we expect from the discussion of the Gambler's Ruin problem in Appendix 2.C that this probability takes the form $\frac{\gamma(0)}{\gamma(0)+\gamma((N-1)\Delta)} \cdot \frac{2}{L}$, up to some constant factor of order $O(1)$. This probability will, due to both factors, be small such that, following the discussion before Eq. (2.10), we expect the error-corrected autocorrelation function after the creation of n

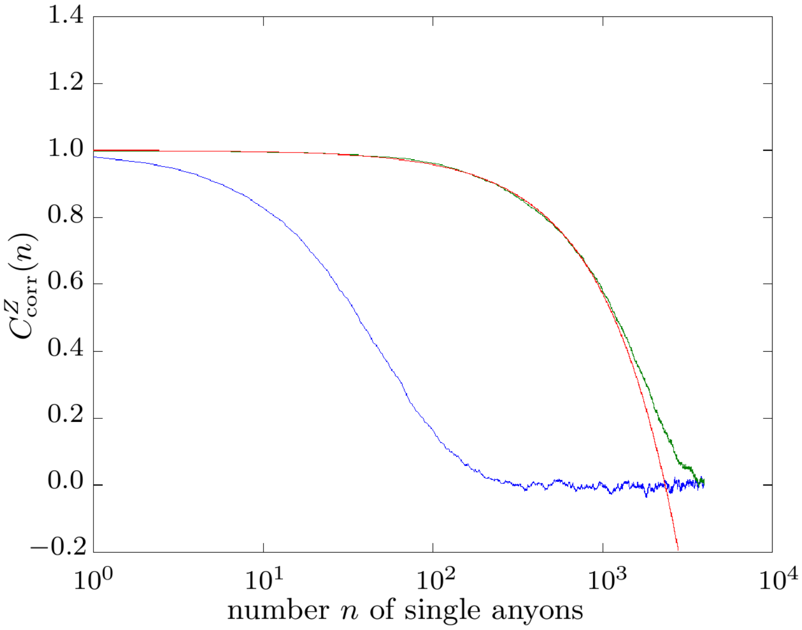

Figure 2.9: A planar code of size $L = 64$ consisting only of four- and one-qubit stabilizers in contact with a bath with $\gamma\left((N-1)\Delta\right)/\gamma(0) = 40$, where $N = 2L(L+1)$. The vertical axis shows the number n of single anyons that have been created. The green curve shows the error-corrected autocorrelation function $C^Z_{\mathrm{corr}}(n)$ and the blue curve the uncorrected autocorrelation function (Eq. (2.7) without Φ_{corr}). Both curves are sampled over $1.2 \cdot 10^4$ experiments. The red curve shows the analytical prediction Eq. (2.29) with $c' = 1.12$. We see that performing a single error correction step before the read-out of the stored quantum information allows to enhance its lifetime ($\tau(0.1)$, say) by more than an order of magnitude.

single anyons to take the form

$$C^Z_{\mathrm{corr}}(n) \simeq 1 - \frac{c'}{L} \cdot \frac{\gamma(0)}{\gamma(0) + \gamma\left((N-1)\Delta\right)} \cdot n\,, \tag{2.29}$$

where c' is a constant. Of course, this approximation can only be valid as long as $C^Z_{\mathrm{corr}}(n)$ is still relatively close to 1. The numerics in Figure 2.9 are in excellent agreement with this prediction as long as $C^Z_{\mathrm{corr}}(n) \gtrsim 0.5$.

Correspondingly, the number of single anyons that are created during

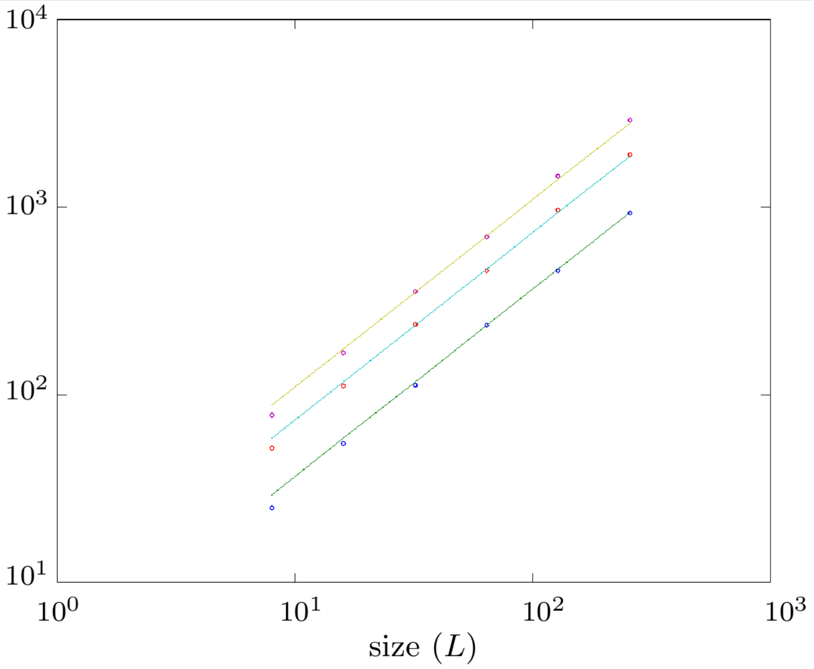

Figure 2.10: The number of single anyons created during the lifetime $\tau(\varepsilon)$ of the memory as a function of the lattice size L. The points show numerical results obtained for a bath with $\gamma\left((N-1)\Delta\right)/\gamma(0) = 40$, where $N = 2L(L+1)$, the lines show the analytical prediction Eq. (2.30) with $c' = 1.12$. From bottom to top we have $\varepsilon = 0.1, 0.2, 0.3$.

the lifetime $\tau(\varepsilon)$ of the stored quantum information will be

$$\frac{\varepsilon \cdot L}{c'} \cdot \frac{\gamma(0) + \gamma\left((N-1)\Delta\right)}{\gamma(0)} \,. \tag{2.30}$$

This prediction is compared with numerical simulations in Figure 2.10. Since there are for each kind of anyon $2 \cdot (2L+1)$ qubits where a single anyon can be created (including the ones on which single-qubit measurements are performed), we obtain a lifetime

$$\begin{aligned} \tau(\varepsilon) &\simeq \frac{\varepsilon \cdot L}{c'} \cdot \frac{\gamma(0) + \gamma\left((N-1)\Delta\right)}{\gamma(0)} \cdot \left[2 \cdot (2L+1) \cdot \gamma\left(-(N-1)\Delta\right)\right]^{-1} \\ &\simeq \frac{\varepsilon}{4c'} \cdot \frac{\exp\left((N-1)\beta\Delta\right)}{\gamma(0)} \,. \end{aligned} \tag{2.31}$$

In the last step, we applied detailed balance and $\gamma(0) \ll \gamma\left((N-1)\Delta\right)$. Since $N = 2L(L+1)$, the lifetime of the memory grows exponentially in L^2. This provides, to the best of our knowledge, the best scaling of a quantum memory lifetime with the linear size found so far in at most three dimensions. However, we have noted that strictly speaking L is bounded through the breakdown of the perturbative treatment of the underlying honeycomb Hamiltonian. So similarly as in [62] the found scaling of the lifetime is only valid up to some optimal L^*. Still, our optimal L^* is generic in the sense that changing it by a small integer will not have a drastic effect on the lifetime.

We note that the only time-scale that entered Eq. (2.31) was the time needed to create a single anyon, while $\gamma(0)$ only entered through a probability. The former canceled by detailed balance such that the only remaining time-scale was the hopping time $1/\gamma(0)$. In the toric case, anyons can only be created pairwise, such that the gap above the anyonic vacuum is increased from $(N-1)\Delta$ (as in the planar case) to $2(N-2)\Delta$, leading to a lifetime increasing as $\sim \exp(2(N-2)\beta\Delta)$, in contrast to Eq. (2.31). Besides complicating error correction, the realistic case of open boundaries thus also reduces the exponentially increasing factor in the lifetime of the memory to (almost) its square root.

Topological order at finite temperature

The above results apply to the code during its thermalization. However, it is also interesting to study its properties once it reaches thermal equilibrium. Clearly the memory will have completely decohered by this point, since the probability of the system being in any of its ground states will be equal. However, we can assess whether topological order is present. It is known that, for the non-interacting case of Eq. (2.1), the thermal state is not topologically ordered for any finite temperature. However, here we show that the interactions of Eq. (2.27) allow the topological order to remain stable for all finite temperatures at which the perturbative derivation of the Hamiltonian Eq. (2.27) is valid.

To determine whether topological order is present we can use one of the topological order parameters designed for mixed states, such as the anyonic topological entropy [76]. This requires the plaquettes and vertices of the code to be split into three regions, A, B, and C. These can be defined arbitrarily, except that A and B must be bounded, B must enclose A, C must enclose B and the number of plaquettes and vertices in each region must be $O(L^2)$. The value of the entropy depends on how well the anyon configuration within B can be used to deduce the net anyonic occupation of A. If this can be done perfectly, the entropy takes its maximum possible value (for the planar code) of $2 \ln 2$, signaling that the state is topologically ordered.

Let us consider the thermal state of the Hamiltonian Eq. (2.27). The Hamiltonian is symmetric under exchange of anyons and anyon holes. Since the gap above the ground states with all anyons or all holes grows as L^2, the thermal state in the thermodynamic limit will be an equally weighted mixture of the all hole or all anyon states. As such, measurement of the occupancy of any plaquette can be used to determine the occupancies of all plaquettes. The region B used in the definition of the anyonic topological entropy can then clearly deduce the net occupancy of the region A. The value for this entropy therefore takes its maximum value of $2 \ln 2$, and the state is found to be topologically ordered.

2.5 Conclusions

Stabilizer Hamiltonians with local interactions in 2D do not, and in 3D seem not to, offer the possibility to passively store quantum states for a time that can be made arbitrarily larger than the relevant microscopic time-scales. Inducing long-range interactions between the excitations of a 2D Hamiltonian whose ground states are topologically ordered seems thus the most promising approach towards a realistic proposal for a quantum memory. For such long-range interactions, the influence of the boundary of the memory (which every realistic memory will have) is not negligible even for large L. We discussed two Hamiltonians proposed in the recent literature and showed that for those the boundary becomes in fact dominant. Operationally, this fact becomes relevant during the error correction step before the read-out of the stored quantum state. We showed that the classical algorithm that determines how to best remove the anyonic defects has to depend on the error model, the memory Hamiltonian and the boundary conditions.

With long-range repulsion between the anyons, the energy to add a further anyon increases with the number of already existing anyons, leading to a vanishing anyon production rate. If the production rates approach their equilibrium values, the production of unpaired anyons on the boundaries will outweigh the production of anyon pairs in the bulk. The influence of the boundary anyons is beneficial since they lead to an effective bias of the bulk anyons to move towards the closer boundary.

We discussed how a planar code with topological protection of the stored qubit can be obtained from a honeycomb model with two-qubit

Ising coupling and the ability to perform single-qubit measurements on boundary qubits. In a resonant regime of a coupling of the honeycomb to cavity modes a very strong suppression of the anyon creation rate is obtained. Furthermore, most created anyons will immediately be reabsorbed by their creating boundary. In conclusion, we have found in this regime a lifetime that grows exponentially in L^2, allowing in principle to reach macroscopic storage times even at moderately high temperatures. The non-local anyon interactions in the obtained effective Hamiltonian are so strong, that the system is topologically ordered at any finite temperature for large enough L, as long as the perturbatively derived Hamiltonian Eq. (2.27) describes the dynamics of the memory accurately.

2.6 Acknowledgments

We acknowledge useful discussions with Fabio Pedrocchi. This work was supported by the Swiss NSF, NCCR Nanoscience, and NCCR QSIT.

2.A Determining the weight of the edges when anyons perform a random walk

Given an anyon at time t at position $\vec{a} = (a_1, a_2)$, where a_1 is the distance from the left boundary and a_2 the distance from the upper boundary, what is the probability $\mathrm{Pr}\,[\vec{a}, t', t]$ that it has been created at a time $0 < t' < t$ at the upper boundary? The answer can be obtained by summing Eq. (2.16) over all spins $0, \dots, L$ on the upper boundary, so

$$\begin{aligned} &\mathrm{Pr}\,[\vec{a}, t', t] \\ &\simeq \int_0^{L+1} \mathrm{d}x \, \frac{1}{4\pi D(t-t')} \cdot e^{-(a_2^2+(a_1-x)^2)/4D(t-t')} \\ &= \frac{1}{4} \frac{1}{\sqrt{\pi D(t-t')}} \cdot e^{-a_2^2/4D(t-t')} \cdot \left\{ \mathrm{Erf}\left[\frac{a_1}{2\sqrt{D(t-t')}}\right] + \mathrm{Erf}\left[\frac{L+1-a_1}{2\sqrt{D(t-t')}}\right] \right\} . \end{aligned} \tag{2.32}$$

The total probability that that an anyon that is at time t at position $\vec{a}$ has been created on the upper boundary is then

$$\mathrm{Pr}\,[\vec{a}, t] = \int_0^t \mathrm{d}t' \; \mathrm{Pr}\,[\vec{a}, t', t] \cdot \gamma_{\mathrm{boundary}}(t') \cdot \xi(t', t) \; , \tag{2.33}$$

where $\gamma_{\mathrm{boundary}}(t')$ is the creation rate of anyons on the boundary at time t' and $\xi(t', t)$ is the probability that an anyon that has been created at a boundary at time t' does still exist at time t. Unfortunately, the time integration cannot be performed in closed form even if we take $\gamma_{\mathrm{boundary}}$ and ξ to be constant and $\{\dots\} = 2$ in Eq. (2.32) (corresponding to the $L \to \infty$ limit).

Still, the above analytics is enough to find reasonable weights for the edges in our error correction algorithm. First, let us note that we can find a similar expression like the one above for the situation where we have anyons at postion $\vec{a}$ and $\vec{b}$ and are interested in the probability that they have been jointly created in the bulk. The exponential factor becomes in this case $\sim \exp\left[-(\vec{a} - \vec{b})^2/8D(t-t')\right]$. Intuitively, the distance vector of the two anyons performs a diffusive motion with diffusion constant $2D$. A sensible choice for the weight of an edge between two anyons is therefore the square of their Euclidean distance, while for an edge connecting an anyon to its closer boundary we take the weight to be *twice* the square of the distance. All terms depending on time, the position of the anyons relative to the boundaries and the creation rates give then additive logarithmic correction terms to these weights.

Note that in the matching which is obtained at the end of the algortihm the number of edges connecting two real anyons is always equal to the number of edges connecting two virtual ones. Furthermore, adding the same term to the weights of all edges or multiplying all weights with the same positive term does not change the result of the algorithm. We may therefore give the edges that connect two virtual anyons a weight which takes all logarithmic correction terms into account.

Formally, let d^2 denote the square of the Euclidean distance of the pair we are interested in. Then, giving edges that connect two real anyons a weight $\alpha \cdot d^2 + \beta_2$ (with $\alpha > 0$), edges that connect a real anyon with a virtual one a weight $\alpha \cdot 2d^2 + \beta_1$ and edges that connect two virtual anyons a weight 0 is equivalent to giving them weights $d^2 + (\beta_2 - \beta_1)/\alpha$, $2d^2$ and $-\beta_1/\alpha$ respectively, which is again equivalent to giving them weights d^2, $2d^2$ and $(\beta_2 - 2\beta_1)/\alpha$ respectively. Rather than calculating the term $(\beta_2 - 2\beta_1)/\alpha$ analytically (which we cannot) we may then consider the weight of the virtual edges as a single optimization parameter of our algorithm. We have found numerically that in the systems we are interested in varying the weight of the purely virtual edges offers hardly room for improvement of the memory lifetime. As before, we will thus take their weight to be zero throughout Sec. 2.3. However, there are certainly regimes where these weights become relevant. If, for example, the rate for creation of anyon pairs in the bulk is vanishing against the rate for creation on the boundaries, the edges between virtual anyons should be given a large weight.

2.B Bounds on the self-consistent anyon density

Using Eq. (2.19) to eliminate e_{eq} in Eq. (2.20) we find

$$1 = n_{\mathrm{eq}} \cdot \left[\exp\left(\beta(\Delta + A(L^2 n_{\mathrm{eq}} - 1))\right) + 1\right] := f(n_{\mathrm{eq}})\,. \tag{2.34}$$

Since $f(x)$ is monotonically increasing in x we have that

$$x < n_{\mathrm{eq}} \Leftrightarrow f(x) < 1\,. \tag{2.35}$$

We have

$$f(\frac{1}{L^2}) = \frac{1}{L^2}\left[\exp\left(\beta\Delta\right) + 1\right] \tag{2.36}$$

and

$$f(\frac{1}{L^{2-\varepsilon}}) > \frac{1}{L^{2-\varepsilon}} \cdot \exp\left(\beta A(L^{\varepsilon} - 1)\right) \ , \tag{2.37}$$

yielding the estimates Eq. (2.21) and Eq. (2.22).

2.C The Gambler's Ruin

In the usual version of the Gambler's Ruin problem, the probability of winning or losing is the same for every amount of money the gambler possesses. In the anyonic hopping problem we are interested in, the probability of moving towards the boundary is not excactly independent of the distance to the boundary. Since the rate for absorbtion of an anyon by a boundary $\gamma(\mathrm{absorb})$ is usually much higher than the hopping rate $\gamma(0)$, the anyon is biased to move towards the boundary if it is at a position next to it. This is in particular the case immediately after the anyon has been created.

We therefore study the following problem. Consider a lattice with rows $0, \ldots, L-1$ and an anyon initially in row 0 (it has just been created). We are only interested in hoppings between the rows and ignore all movements within the same row. In row 0 there is a probability $\tilde{p} = \frac{\gamma(\mathrm{absorb})}{\gamma(\mathrm{absorb})+\gamma(0)}$ that the anyon is absorbed by the adjacent boundary and a probability $1-\tilde{p}$ that it hops to row 1 (similarly in row $L-1$, but this will be irrelevant here). In all other rows, the anyon hops to both adjacent rows with equal probability. What is the probability that the anyon reaches row $L/2$ (let L be even for simplicity) at least once before it is reabsorbed?

Let p_i the denote the probability to reach row $L/2$ from row i. The boundary conditions are

$$p_0 = (1-\tilde{p}) \cdot p_1 \tag{2.38}$$

and

$$p_{L/2} = 1 \ . \tag{2.39}$$

For $1 \leq i \leq L/2-1$ we have $p_i = \frac{1}{2}(p_{i-1}+p_{i+1})$, or equivalently $p_{i+1}-p_i = p_i - p_{i-1}$. We find

$$1 = p_{L/2} = \sum_{i=1}^{L/2-1} (p_{i+1} - p_i) + p_1 = (L/2-1) \cdot (p_1 - p_0) + p_1 \tag{2.40}$$

Using Eq. (2.38) to eliminate p_1 we arrive at

$$p_0 = \frac{1-\tilde{p}}{(L/2-1)\cdot\tilde{p}+1} \,, \tag{2.41}$$

which for $1-\tilde{p} \ll 1$ (i.e. $\gamma(0) \ll \gamma(\mathrm{absorb})$) simplifies to

$$p_0 \simeq (1-\tilde{p})\cdot\frac{2}{L} \simeq \frac{\gamma(0)}{\gamma(\mathrm{absorb})}\cdot\frac{2}{L} \,. \tag{2.42}$$

Now let n_i denote the expected number of hoppings (perpendicular to the boundary under interest) necessary to reach row $L/2$, assuming that it is eventually reached. The boundary conditions are

$$n_0 = 1 + n_1 \tag{2.43}$$

and

$$n_{L/2} = 0 \,. \tag{2.44}$$

For $1 \le i \le L/2-1$ we have the recursion $n_i = 1 + \frac{1}{2}(n_{i-1}+n_{i+1})$ or equivalently $n_{i+1} - n_i = n_i - n_{i-1} - 2$. From this we expect a quadratic expression for n_i and thus make the *Ansatz*

$$n_i = a\cdot i^2 + b\cdot i + c \tag{2.45}$$

with the unique solution $a = -1$, $b = 0$ and $c = (L/2)^2$. We conclude that $n_0 = (L/2)^2$.

CHAPTER 3

Dynamic Generation of Topologically Protected Self-Correcting Quantum Memory

Adapted from:
Daniel Becker, Tetsufumi Tanamoto, Adrian Hutter, Fabio L. Pedrocchi, and Daniel Loss
"Dynamic Generation of Topologically Protected Self-Correcting Quantum Memory",
Phys. Rev. A **87**, 042340 (2013)

We propose a scheme to dynamically realize a quantum memory based on the toric code. The code is generated from qubit systems with typical two-body interactions (Ising, XY, Heisenberg) using periodic, NMR-like, pulse sequences. It allows one to encode the logical qubits without measurements and to protect them dynamically against the time evolution of the physical qubits. A weakly coupled cavity mode mediates a long-range attractive interaction between the stabilizer operators of the toric code, thereby suppressing the creation of thermal anyons. This significantly increases the lifetime of the memory compared to the code with noninteracting stabilizers. We investigate how the fidelity, with which the toric code is realized, depends on the period length T of the pulse sequence and the magnitude of possible pulse errors. We derive an optimal period T_{opt} that maximizes the fidelity.

3.1 Introduction

One of the most promising proposals for the realization of a thermally stable quantum memory is based on topologically ordered phases of matter like Kitaev's toric code [16,19,57].

While the toric code allows for topological protection against local imperfections at zero temperature, it is susceptible to thermal fluctuations [33,56,77,78]: Anyons that are created at constant energy cost and move freely across the memory without additional energy penalty destroy the stored quantum information in a time that does not increase with the linear size L of the memory. In fact, all two-dimensional (2D) and broad classes of three-dimensional (3D) stabilizer Hamiltonians with local interactions are subject to no-go theorems forbidding stability at finite temperature [32,35,59]. 3D stabilizer models with local interactions that do not satisfy the criteria of applicability of the no-go theorems have been proposed and studied. None of them, however, is so far expected to be stable at any nonzero temperature [60,61,79,80].

Despite the intrinsic thermal fragility of the toric code, it is possible to considerably improve the memory lifetime by allowing for long-range repulsive interactions between anyons as proposed in Ref. [38] and later studied in several systems in Refs. [39,40,81]. In fact, this leads to a suppression of the anyon density in the thermodynamic limit and thus to a memory lifetime increasing polynomially with L. Such memories are called *self-correcting*, as their stability against errors caused by the thermal environment is "built in" in the sense that no active (measurement-based) error correction is required. In similar approaches, long-range attractive interaction between anyons as a way to suppress their motion across the memory has been proposed in Ref. [57] and later studied in Ref. [65] by coupling the toric code to a bosonic bath. In this case the diffusion of anyons is reduced by the attractive interaction and the memory lifetime increases polynomially with L, but the model requires unbounded-strength interactions between anyon operators and the bosonic bath [65]. Recently, a three-dimensional model where toric code *stabilizers* are locally coupled to the spins of a ferromagnet has been proposed in Ref. [82]. The attractive interaction between stabilizers is then mediated by Goldstone modes and leads to a memory lifetime increasing exponentially with L.

In this work, we study a similar model, for which the attractive interaction between stabilizers of the toric code is mediated by cavity modes. This model was first proposed in Ref. [38] and studied in detail in Ref. [39]

as a low-energy effective Hamiltonian of an anisotropic honeycomb model coupled to a cavity mode. In the same sense as for these cavity-based setups, the model proposed here implements a passive error correction which renders it self-correcting against thermal fluctuations. This self-correcting property, however, is limited by pulse imperfections as well as the validity of the perturbation theory used to derive the effective stabilizer interaction.

The toric code Hamiltonian contains many-body interactions that are not directly realized in nature. Nevertheless, several ways have been proposed as to how the toric code (and similar stabilizer codes) can be implemented in practice. Besides the low-energy limit of the honeycomb lattice [64, 75], it can emerge dynamically as a coarse-grained description of a quantum simulation with discrete time steps using Rydberg atoms [83], ions [84, 85], or polar molecules [86, 87] in optical traps. This work is based on another kind of dynamical implementation that employs NMR-like, periodic sequences of short external pulses to induce the dynamics of the code Hamiltonian in solid-state systems, similar to a recent proposal in Ref. [88]. By its use of periodic pulses, this scheme of dynamically generating a desired Hamiltonian dynamics is related to the so-called *dynamical decoupling* methods [89–91] that mainly aim to suppress the effect of a given or even unknown system-bath interaction on (time-)average. From an abstract, mathematical point of view, both kinds of pulsing schemes are rather similar insofar as their effect can be captured by taking the time average of Hamiltonian terms or error generators that are transformed by appropriate unitary operations (the pulses). Compared to the dynamical decoupling schemes, the method used here is particularly suited to generate the Hamiltonian dynamics of the planar code with as few linewise applied rotations as possible. Also, in addition to the suppression of decoherence that is caused by a decouplinglike effect of the pulses, our proposal achieves an even stronger stabilization against the thermal environment by a coupling to a nonlocal field (the cavity mode).

Starting from a system of $1/2$ spins coupled to a cavity mode, we show how to generate a toric code with long-range attractive interactions between stabilizers. For perfect pulses, the fidelity F with which the dynamics of the code Hamiltonian is generated only depends on the structure and time period T of the generating sequence reaching the theoretical limit of $F = 1$ for $T \to 0$. In reality, however, unavoidable pulse imperfections require to minimize the number of pulses per time and the fidelity reaches its maximum for a finite period T_{opt}. We derive an explicit formula for T_{opt} and show that for pulse errors of a relative magnitude around 10^{-4} a fidelity of more than 0.99 can be realized over a long time $t \gtrsim 100\Delta^{-1}$, where Δ is the energy scale to create a bare anyon. Finally, we show how to encode a logical qubit by a sequence of magnetic pulses and thus without the need of stabilizer measurements.

The paper is organized as follows. After the model system is introduced in Sec. 3.2, we show how to generate the dynamics of the toric code Hamiltonian with a periodic pulse sequence in Sec. 3.3. We study both numerically and analytically how the gate fidelity F of the induced time evolution depends (i) on the structure of the pulse sequence and (ii) on the magnitude of random pulse errors in Sec. 3.4. Furthermore, based on both these limiting factors for F, an analytic expression for the optimal sequence period length $T_{\text{opt}} > 0$ is derived that maximizes the fidelity. In Sec. 3.5, we derive an effective low-energy Hamiltonian for a pulsed system of qubits that are weakly coupled to a cavity mode. The cavity induces an attractive stabilizer interaction that protects the system against errors caused by a thermal environment. We explain that, with respect to these errors, the resulting memory can be considered as self-correcting. Finally, the measurement-free encoding of logical qubit states into the ground state manifold is explained in Sec. 3.6. Appendices 3.A–3.C contain details about the pulse operations for arbitrarily large qubit arrays and technical derivations regarding the fidelity dependence on the sequence structure and on the magnitude of pulse errors.

3.2 The model system

We consider a quadratic lattice of noninteracting qubits with site-independent level splitting, which are weakly coupled ($0 < \delta \ll \Delta$) to a single cavity mode

$$H_0(\delta) = -4[\Delta + \delta(b + b^\dagger)] \sum_j \sigma_z^{(j)} + \hbar\omega_0 b^\dagger b, \tag{3.1}$$

where $\sigma_\varkappa^{(j)}$ with $\varkappa \in \{x, y, z\}$ denotes a Pauli matrix acting on the qubit on lattice site j. Operator b annihilates a photon of energy $\hbar\omega_0$ in the cavity. We assume that two-qubit gates can be applied by an external switching on and off of a "natural" (system-dependent) two-qubit interaction. For example, in the case of spin qubits realized in single-electron quantum dots an effective nearest-neighbor Heisenberg interaction can be switched electrically by changing the transparency of the tunneling barrier between two dots using gate electrodes [8]. The goal of this work is to show that with the choice of a proper periodic sequence of single-qubit rotations and two-qubit gates, a self-correcting topological quantum memory can be generated dynamically. We show this for the case of the planar code (toric code with boundaries), which is described by Hamiltonian

$$H_{\mathrm{PC}} = -\Delta\left(\sum_p A_p + \sum_s A_s\right) =: -\Delta \sum_a W_a. \tag{3.2}$$

For a given quadratic lattice of qubits sitting on the edges of a unit cell, indices p and s run over all *plaquettes* and *stars*, respectively. A plaquette is the set $\{p_1, \ldots, p_4\}$ of qubits sitting on the edge of a single unit cell and the corresponding operator is given by $A_p = \prod_i \sigma_z^{(p_i)}$. Associated to every star is the set $\{s_1, \ldots, s_4\}$ of qubits around a vertex connecting four neighboring cells, where $A_s = \prod_i \sigma_x^{(s_i)}$. At the edges of the code, the A_p and A_s consist of only three Pauli operators. Figure 3.1 illustrates the structure of H_{PC} schematically. The stabilizer operators W_a are identical to the plaquettes and stars and introduced to obtain a simpler notation. Hence, index a runs through all unit cells and vertices of the quadratic lattice.

We want to stress, however, that the method described here is not restricted to the planar code or the particular free Hamiltonian H_0. In fact, it can in principle be used to generate a quite large class of code Hamiltonians. Restrictions of this method rather concern the practical implementation of a particular scheme in real experiments. Details such as the required fidelities on certain time scales, addressability issues, the accuracy of external operations, etc., have to be examined with respect to a particular physical system. Below we present an example of how to implement the dynamically generated topologically protected quantum memory based on H_{PC} in realistic systems.

3.3 Dynamic generation of planar code

In this section, we explain in detail how external pulses and two-qubit operations can be used to dynamically "generate" the planar code Hamiltonian from the qubit part of $H_0(\delta = 0)$. Here and in the following "generating a Hamiltonian H_{av}" is used to mean that, due to external pulses applied between certain discrete (stroboscopic) times, a system with Hamiltonian H evolves as if its dynamics was governed by H_{av}—the

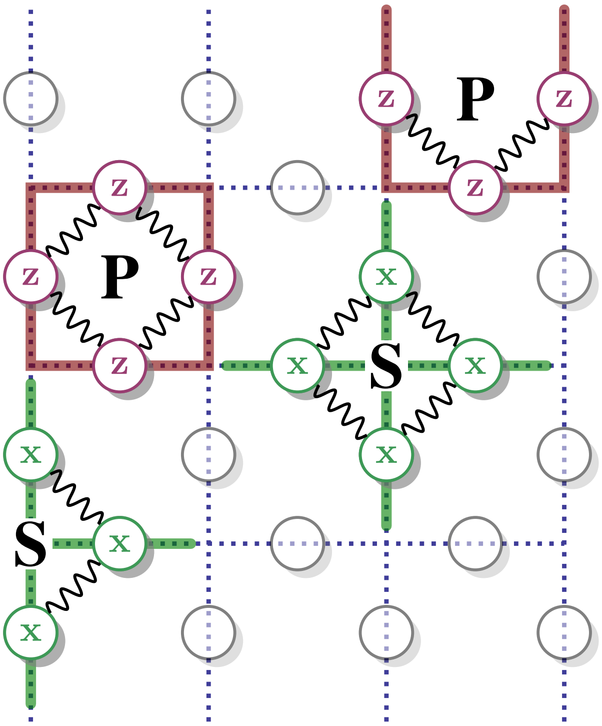

Figure 3.1: Schematic of the planar code Hamiltonian equation (3.2) on the square lattice (dotted lines). Plaquettes (P) are associated with the edges of a unit cell and stars (S) with the edges of the cells around a vertex. A circle indicates a Pauli operator acting on a qubit and the wiggly lines connect operators that have to be multiplied to obtain the corresponding stabilizer operator.

"*average Hamiltonian.*" After a short introduction to average Hamiltonian theory [92], we proceed by showing one possible sequence of pulses that generates H_{PC} from $H_0(\delta = 0)$. Finally, a nonzero coupling of the qubits to a cavity mode [as in Eq. (3.1)] can be utilized to induce a strongly nonlocal interaction between the anyon operators of H_{PC}.

Average Hamiltonian theory

Average Hamiltonian theory describes how time-periodic (externally controlled) unitary transformations can be used to let the evolution of one system mimic that of anotherm system of the experimenter's choosing. For the purpose of our paper, it is sufficient to consider the case of $n + 1$

periods $t_0, \ldots, t_n$ of free propagation with H_0, which are separated in time by n unitary transformations R_i with $i = 1, \ldots, n$ and $\prod_{i=1}^{n} R_i = \mathbb{1}$. It is assumed, that all the R_i can be performed within a typical time τ_i, where the τ_i define the smallest time scale of the system. This is illustrated in Fig. 3.2(a). The physical time of the entire sequence is then given by $T = t_0 + \sum_{i=1}^{n}(t_i + \tau_i)$, after which the model will have evolved according to the time evolution operator $U_T = U_0(t_n) R_n \cdots R_2 U_0(t_1) R_1 U_0(t_0) \equiv \exp\{-i\tilde{T} H_{\text{av}}\}$ with $\tilde{T} = \sum_{i=0}^{n} t_i \lesssim T$. Here and in the following, $\hbar$ is set to 1 and we defined $U_0(t) = \exp\{-itH_0\}$. With the Magnus expansion [92,93], such a product of unitary operators can always be written as a single exponential of the average Hamiltonian H_{av}. Hence, if the pulse sequence is applied periodically, at *integer multiples of* T (stroboscopic times) the model system will have evolved as if governed by Hamiltonian $\tilde{T} H_{\text{av}}/T$. In general, the exact H_{av} can only be given as an infinite expansion in orders of $T\Delta$, where Δ^{-1} is (of the order of) the characteristic time scale of the unpulsed system H_0:

$$H_{\text{av}} = H_{\text{av}}^{(0)} + H_{\text{av}}^{(1)} + H_{\text{av}}^{(2)} \ldots \tag{3.3}$$

For small enough $T\Delta$, however, it is often sufficient to only consider the lowest-order term

$$H_{\text{av}} \approx H_{\text{av}}^{(0)} = \frac{1}{T} \sum_{j=0}^{n} H_j t_j, \tag{3.4}$$

with $H_j = \mathcal{R}_j^\dagger H_0 \mathcal{R}_j$ for $j \neq 0$ and $\mathcal{R}_j = \prod_{k \leq j} R_k$.

Generating sequence for planar code

In order for a sequence as shown in Fig. 3.2(a) to be usable in real experiments and applications it has to be as short as possible and the operations R_i have to be decomposable into simple elementary operations. We will show how H_{PC} can be generated from $H_0(\delta = 0)$ using only (i) $\pi/2$ single-qubit rotations about the x and y axes and (ii) the two-qubit controlled phase gate $U_{\text{PG}} = \exp\{i\pi\sigma_z^{(1)}\sigma_z^{(2)}/4\} = (\mathbb{1} + i\,\sigma_z^{(1)}\sigma_z^{(2)})/\sqrt{2}$ between qubits on neighboring sites (denoted by 1 and 2). Each of these operations only have to be applicable on rows (columns, diagonals) of qubits simultaneously. In particular, we will not require that physical qubits can be addressed individually, which might be advantageous for certain qubit architectures.

In general, besides single-qubit rotations the generation of H_{PC} only requires an operation that allows one to transform Pauli terms $h = \sigma_{\varkappa}^{(p)}$

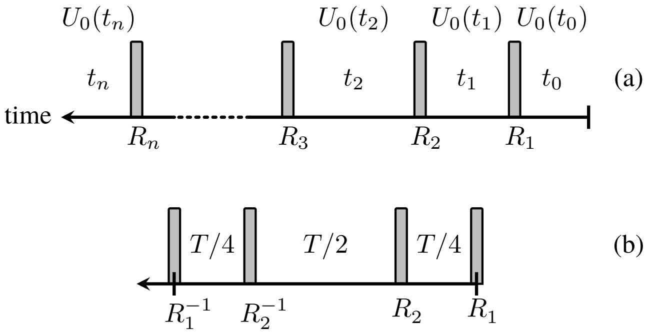

Figure 3.2: (a) Generic pulse (operation) sequence. The unitary operations R_i (gray columns) with $\prod_{i=1}^{n} R_i = \mathbb{1}$ interrupt periods of (free) propagation with H_0. (b) Structure of a sequence of duration T to generate a plaquette or star operator. A sequence of the same structure is employed to generate (each) one of the quarters of the planar code.

in the average Hamiltonian according to $\sigma_{\varkappa}^{(p)} \to \sigma_{\varkappa'}^{(p)}\sigma_{\varkappa''}^{(\bar{p})}$ for at least one axis $\varkappa$. Here, $p = 1, 2$ and $\bar{p} \neq p$ are the site indices of neighboring qubits. The spin axes $\varkappa$, $\varkappa'$, and $\varkappa''$ do not need to be different.

Gate U_{PG} is an example of such an operation, which can be seen by considering a sequence of two pulses with $\mathcal{R}_1 = R_1 = U_{\text{PG}}$, and $t_0 = t_2 = 0$ so that $t_1 \equiv T$. According to Eq. (3.4), we obtain the average Hamiltonian to be $h_{\text{av}} = U_{\text{PG}}^{\dagger} h U_{\text{PG}}$. A straightforward calculation shows that this transformation has nontrivial effects only on terms that contain *exactly one* of either σ_x or σ_y. Concretely, the transformation converts $\sigma_x^{(p)} \to \sigma_y^{(p)}\sigma_z^{(\bar{p})}$ and $\sigma_y^{(p)} \to -\sigma_x^{(p)}\sigma_z^{(\bar{p})}$.

In a system, in which the qubit interaction is Ising-like with $H_{\text{Ising}} = -J\sum_{\langle jk\rangle}\sigma_z^{(j)}\sigma_z^{(k)}$ and $J > 0$, where the sum includes all next neighbors $\langle jk\rangle$, the operation U_{PG} can be performed by switching the interaction on for a time $\tau = \pi/(4J)$. Note that similar operations can also be realized based on other nearest-neighbor interactions such as XY or Heisenberg. In the XY case, for example, this role can be played by $\exp\{\pm iJ\tau(\sigma_x^{(1)}\sigma_x^{(2)} + \sigma_y^{(1)}\sigma_y^{(2)})\}$ for $\tau = \pi/(4J)$, while using a (sightly modified) pulse sequence of similar complexity to the one we present for the Ising case. Analogous operations can be found in the Heisenberg case. Thus, our scheme is not restricted to qubit systems with a particular kind of two-particle interaction.

We proceed by showing how to generate a plaquette or star operator for a 2×2 quadratic lattice of free qubits. For simplicity, we consider the case $\Delta = 1/4$ and $\delta = 0$, given by $H_0 = \sum_{j=1}^{4} \sigma_z^{(j)}$, with j denoting the qubits as in Fig. 3.3(a), and $H_{\mathrm{av}} = A_s = \prod_j \sigma_x^{(j)}$. The pulse sequence consists of four (complex) operations with $t_0 = t_4 = 0$ and $2t_1 = 2t_3 = t_2 = T/2$. Its structure is illustrated in Fig. 3.2 (b), where we have to specify operations R_1 and R_2 so that the sequence yields the desired (lowest-order) average Hamiltonian.

A possible sequence of operations to generate a fourth-order spin Hamiltonian starting from H_0 is illustrated in Fig. 3.3, while Table 3.1 shows the terms of the transformed Hamiltonian for each step. After rotating the qubits along one diagonal [upward in Fig. 3.3(b)] about the y axis by $\pi/2$, second-order terms (indicated by wiggly lines) are generated by applying U_{PG} (hatched areas) to two parallel edges of the lattice [vertical in Fig. 3.3(c)]. Since applying the entangling gate to the remaining (horizontal) edges in the resulting configuration would yield third- instead of fourth-order terms, the qubits along one of these edges [the lower in Fig. 3.3(d)] have to be rotated, so that the z and y terms are interchanged. Subsequent application of U_{PG} to the remaining edges [horizontal in Fig. 3.3(e)] now generates [amongst others, see Eq. (3.6)] a fourth-order term.

The last step shown in Fig. 3.3(f) is not actually necessary in case of the simple 2×2 lattice. Depending on whether a plaquette or staright-hand-sideto be generated, one could either y rotate the rightmost or leftmost edge after step (e). In view of the application to a larger planar code like in Fig. 3.1, however, we interchange the lower edge qubits a second time [Fig. 3.3(f)]. A final rotation of the qubits along a properly chosen diagonal then yields the desired fourth-order operator (not shown in the figure). In the case of the planar code on a larger lattice, the additional step is required due to the presence of (third-order) boundary operators in H_{PC}. It arranges their components in straight lines with those of the interior operators, so that a final rotation along properly chosen diagonals generates a Hamiltonian with only z and x terms, respectively (cf. Appendix 3.A).

The candidate for R_1 to generate a star operator from H_0 is therefore the product of all the operations of steps (b)–(f) plus a y rotation of qubits 1 and 4 with

$$R_1 = U_{x\leftrightarrow z}^{(2,3)}\, U_{\mathrm{PG}}^{(1,3)} U_{\mathrm{PG}}^{(2,4)}\, U_{y\leftrightarrow z}^{(3,4)}\, U_{\mathrm{PG}}^{(1,2)} U_{\mathrm{PG}}^{(3,4)}\, U_{x\leftrightarrow z}^{(3,4)}\, U_{x\leftrightarrow z}^{(1,4)}, \tag{3.5}$$

where $U_{\mathrm{PG}}^{(jk)}$ entangles qubits j and k and $U_{x\leftrightarrow z}$ denotes a $\pi/2$ rotation

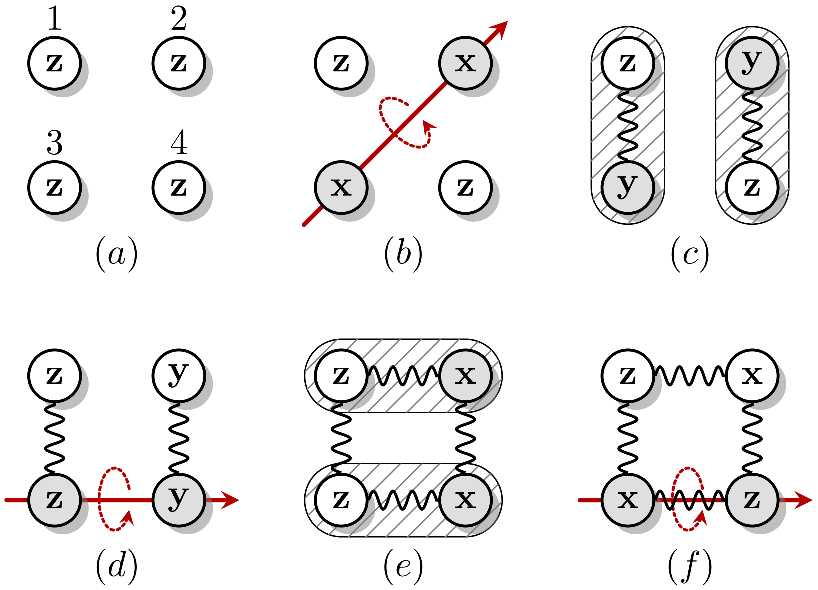

Figure 3.3: First 6 of 7 elementary steps to generate fourth-order terms in an average Hamiltonian starting from a single-particle Hamiltonian for qubits on a quadratic lattice.

Table 3.1: Hamiltonian terms for each step in Fig. 3.3 (up to a sign). Pauli operators that changed compared to the previous step are shown against a gray background. A final y rotation (not shown) of qubits 1 and 4 yields Eq. (3.6).

(a)	$\sigma_z^{(1)}$	$\sigma_z^{(2)}$		$\sigma_z^{(3)}$		$\sigma_z^{(4)}$
(b)	$\sigma_z^{(1)}$	$\sigma_x^{(2)}$		$\sigma_x^{(3)}$		$\sigma_z^{(4)}$
(c)	$\sigma_z^{(1)}$	$\sigma_y^{(2)}$	$\sigma_z^{(4)}$	$\sigma_z^{(1)}$	$\sigma_y^{(3)}$	$\sigma_z^{(4)}$
(d)	$\sigma_z^{(1)}$	$\sigma_y^{(2)}$	$\sigma_y^{(4)}$	$\sigma_z^{(1)}$	$\sigma_z^{(3)}$	$\sigma_y^{(4)}$
(e)	$\sigma_z^{(1)}$	$\sigma_z^{(1)}\sigma_x^{(2)}$	$\sigma_z^{(3)}\sigma_x^{(4)}$	$\sigma_z^{(1)}\sigma_z^{(3)}$		$\sigma_z^{(3)}\sigma_x^{(4)}$
(f)	$\sigma_z^{(1)}$	$\sigma_z^{(1)}\sigma_x^{(2)}$	$\sigma_x^{(3)}\sigma_z^{(4)}$	$\sigma_z^{(1)}$	$\sigma_x^{(3)}$	$\sigma_x^{(3)}\sigma_z^{(4)}$

about the axis perpendicular to x and z. Note that R_1 acts *on the system* by performing the elementary steps *in reverse order*. If we have only R_1 or, equivalently, set $R_2 = \mathbb{1}$, we obtain average Hamiltonian

$$H_1 = \sigma_x^{(1)}\sigma_x^{(2)}\sigma_x^{(3)}\sigma_x^{(4)} + \sigma_x^{(1)}\sigma_x^{(3)} + \sigma_x^{(3)}\sigma_x^{(4)} - \sigma_x^{(1)}. \tag{3.6}$$

Apart from the desired star operator, it contains unwanted single- and two-particle by-products (see columns 1,3, and 4 in Table 3.1). These can be removed from the average Hamiltonian with an R_2 that yields a Hamiltonian $H_2 = R_1^{-1}R_2^{-1}H_0R_2R_1$ [see Eq. (3.4)], whose first- and second-order terms have the opposite sign compared to H_1. Note that if such an operation R_2 were considered as just another step of the sequence in Fig. 3.3, it would have to be performed *prior to (b)*: With $H_0' := R_2^{-1}H_0R_2$, we can write $H_2 = R_1^{-1}H_0'R_1$. Hence, we need to find an operation R_2 that changes H_0 to H_0' in such a way that the *subsequent* application of R_1 results in the desired sign flips.

It turns out that the simple ansatz to just rotate qubits 1 and 3 by an angle of π about either the y or z axis (in an attempt to add one sign to each first- and second-order term, while adding two signs to the fourth-order operator) will not do the trick. A straightforward calculation shows that qubit 3 has to be rotated as well to give the correct result. Thus, with $R_2 = U_y^{(1,3,4)}(\pi)$ and using $H_3 = H_1$ we obtain the average Hamiltonian $H_{\text{av}} = (H_1 + H_2)/2 = \sigma_x^{(1)}\sigma_x^{(2)}\sigma_x^{(3)}\sigma_x^{(4)}$. Here, operator $U_\varkappa^{(i_1,\dots,i_n)}(\phi)$ rotates qubits $i_1, \dots, i_n$ about axis $\varkappa = x, y, z$ by angle ϕ. Finally, R_2 has to be decomposed into operations that are applied linewise. One possible way to do this is

$$R_2 = U_y^{(1,4)}(\pi/2)\, U_x^{(3,4)}(\pi)\, U_y^{(1,4)}(\pi/2). \tag{3.7}$$

With a pulse sequence of the exact same structure and similar (generalized) R_1 and R_2, we can also generate either multiple plaquette or star operators on an arbitrary large quadratic lattice. Details about both operations are given in Appendix 3.A. We point out that only one-quarter (even or odd subsets of plaquettes or stars) of H_{PC} can be generated with one such sequence. This is due to the fact that only disjoint, i.e., half of the pairs of qubits, can be coupled in an entangling step per lattice dimension, to generate fourth- and third-order terms of the correct structure. Since each quarter of the code is generated for one-quarter of the time only, the single-particle energy of Hamiltonian $H_0(\delta = 0)$ from Eq. (3.1) was set to be -4Δ to yield a H_{PC} with energy gap $-\Delta$.

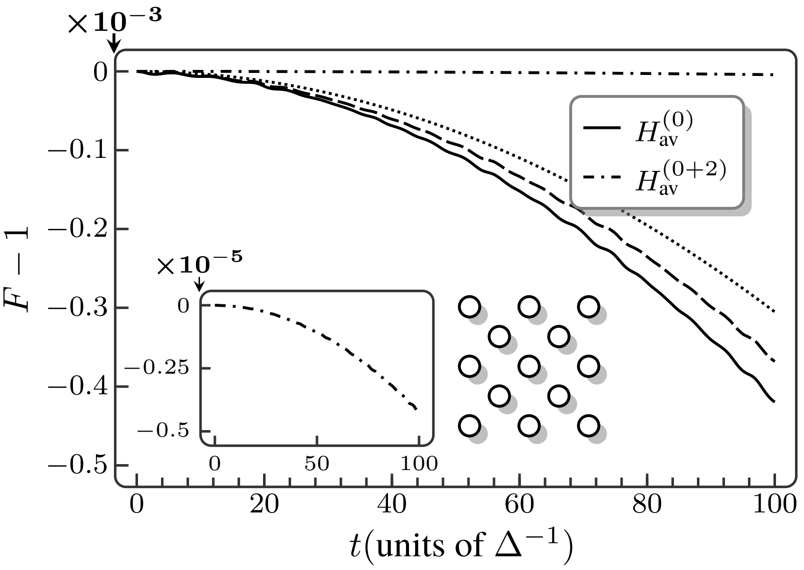

Figure 3.4: Numerical gate fidelity versus time of a dynamically generated planar code of $N = 13$ qubits (inset) coupled to a cavity mode with three dimensional Fock space. For $\Delta = \omega_0$, $\delta/\Delta = 0.1$, and $T = \Delta^{-1}/8$, already the lowest-order average Hamiltonian yields $F > 99.9\%$ for times $t \leq 100\Delta^{-1}$ (solid line). Adding the second-order contribution decreases the deviation from perfect fidelity by another two orders of magnitude (dashed and dotted line, plot in inset). Based on the two leading orders of the average Hamiltonian, the exact fidelity can be approximated reasonably well, both numerically (dashed line) and analytically (dotted line).

3.4 Fidelity limits due to sequence structure and pulse errors

A suitable measure for the similarity of the dynamically generated dynamics with that of the toric code Hamiltonian is given by the gate fidelity

$$F(t) = \left|\mathrm{Tr}[\exp(itH_{\mathrm{av}})U_{\mathrm{P}}(t)]\right|/2^N, \tag{3.8}$$

where $U_{\mathrm{P}}(t)$ denotes the evolution operator of the pulsed system. The gate fidelity indicates how well an arbitrary basis of the whole Hilbert space evolves according to H_{av}. By contrast, a state-specific fidelity only quantifies how well the dynamics is described by a particular H_{av} for that same specific set of states. For example, a high value for a fidelity that measures how much of an encoded state remains in the ground state manifold over time, is consistent with the dynamics of any Hamiltonian that coincides with that of H_{av} on the ground state manifold. For the generation of the stabilizer interaction by means of a cavity, however, it is important that besides the ground states all excited states propagate according to H_{av}, as well. Hence, in contrast to state fidelities, only a gate fidelity $F(t) \approx 1$ for $H_{\text{av}} = H_{\text{PC}}$ can be used as an indicator that the cavity indeed induces the stabilizer interaction.

For decreasing sequence duration of the order of or shorter than Δ^{-1}, by simply generating each four quarters alternatingly with a period of $T/4$, the lowest-order average Hamiltonian

$$H_{\text{av}}^{(0)} = [1 + \delta/\Delta(b + b^{\dagger})]H_{\text{PC}} + \omega_0 b^{\dagger} b \tag{3.9}$$

describes the system dynamics with increasing fidelity over longer times even between the end points of the sequence. With a suitably symmetrized version (cf. Fig. 3.8 in Appendix 3.B), all odd-order contributions to H_{av} [see Eq. (3.3)] can be completely suppressed, so that the leading-order deviation is given by

$$\begin{gathered}
H_{\text{av}}^{(2)} = \frac{\omega_0 T^2 \delta}{8\Delta}\mathbf{Q}[\mathcal{M}\mathbf{Q}^{\dagger} + \mathbf{V}(b + b^{\dagger})] \quad \text{with} \\
\mathcal{M} = \frac{\delta}{3\Delta}\begin{pmatrix} -6 & -5 & -5 & -5 \\ -5 & 0 & 1 & 1 \\ -5 & 1 & 6 & 7 \\ -5 & 1 & 7 & 12 \end{pmatrix} \qquad \mathbf{V} = \frac{\omega_0}{4}\begin{pmatrix} 7 \\ 1 \\ -3 \\ -5 \end{pmatrix},
\end{gathered} \tag{3.10}$$

where $\mathbf{Q} = (Q_1, \ldots, Q_4)$ is a vector consisting of the four quarters $Q_i = -\Delta \sum_{\{a_i\}} W_{a_i}$ of the planar code defined by appropriate, disjoint sets of anyon indices $\{a_i\}$.

Figure 3.4 shows the time-dependent gate fidelity for perfect pulses and a lattice of $N = 13$ qubits (inset) coupled to a cavity with three-dimensional Fock space $\{|n \pm 1\rangle, |n\rangle\}$, which is evaluated with a numerically exact Chebyshev expansion of the time evolution operator [94]. The system parameters are $T = \Delta^{-1}/8$, $\delta = 0.1\Delta$, and $\omega_0 = \Delta$. Already for $H_{\text{av}} = H_{\text{av}}^{(0)}$ (solid line), the fidelity does not drop below 99.9% before $t = 100\Delta^{-1}$, while adding the second-order contribution from Eq. (3.10) decreases the deviation from the perfect fidelity by another two orders of magnitude (dashed and dotted line, plot in inset). In reality, however, the fidelity will be lower than this theoretical maximum due to errors in the pulsing scheme, decoherence by the noisy environment, and fluctuations of the microwave beam that is used to induce anyon interactions. Compared to systems that directly realize the toric code Hamiltonian (rather than just its dynamics), e.g., in some low-energy limit of some suitable local lattice Hamiltonian, these effects will decrease the lifetime of codewords. Nevertheless, the numerical results indicate that $H_{\mathrm{av}}^{(0)} + H_{\mathrm{av}}^{(2)}$ describes the perfect-pulse dynamics of the system very well and therefore allows one to estimate the size of deviations from the intended Hamiltonian (3.9) that arise solely by the structure of the pulse sequence. This is illustrated by the dashed line in Fig. 3.4, which gives

$$F^{(2)} := \left|\mathrm{Tr}[\exp(iH_{\mathrm{av}}^{(0)}t)\exp(-i\{H_{\mathrm{av}}^{(0)} + H_{\mathrm{av}}^{(2)}\}t)]\right| / 2^N \tag{3.11}$$

as result of a numerically exact calculation for the 13-qubit system. Its quadratic behavior is very similar to that of the pulsed system, while the quantitative deviations are due to terms of order 4 and higher. In Appendix 3.B it is shown that $F^{(2)}$ can be approximated by $F^{(2)} \approx 1 - c_{\mathrm{av}}t^2$ with

$$c_{\mathrm{av}} = \frac{1}{3}\Big(\frac{5\omega_0 L(L-1)\delta\,\Delta}{16}\Big)^2 T^4 \tag{3.12}$$

for planar codes of arbitrary linear size L, which we define as the length of the larger quadratic sublattice for codes arranged as in Figs. 3.1, 3.4, and 3.7. For example, the code with $13 = 3^2 + 2^2$ qubits has length $L = 3$, while the code with $25 = 4^2 + 3^2$ qubits has length $L = 4$. For $L = 3$, the approximate $F^{(2)}$ is given by the dotted line in Fig. 3.4. Although Eq. (3.12) systematically overestimates the fidelity of the pulsed system F, it is sufficiently accurate to provide the bounds $1 < (1-F)/(c_{\mathrm{av}}t^2) < 2$ for deviations due to higher-order corrections to $H_{\mathrm{av}}^{(0)}$, as long as $c_{\mathrm{av}}t^2 \ll 1$.

While the deviations that are due to the structure of the pulse sequence decrease rapidly for smaller periods T, errors caused by imperfect pulses will generally increase with the pulsing rate. As a consequence, a finite magnitude of pulse errors entails an optimal, finite value of T, for which the total deviations due to both error sources are minimal. We estimate the effect of pulse imperfections using a simple model with errors manifesting in small random deviations $\delta\theta \ll 1$ from the intended angle θ_0 in $\tilde{R}(\delta\theta) = \exp(i[\theta_0 + \delta\theta]S/2)$, where $S = \sigma_{\varkappa}^{(j)}$ for rotations about axis $\varkappa$ and $S = \sigma_z^{(j)}\sigma_z^{(j+1)}$ for the phase gate, respectively. The error distribution with width $\sigma_\theta = \sqrt{\langle\delta\theta^2\rangle} > 0$ is assumed to be Gaussian, equal for all considered kinds of pulses, and unbiased ($\langle\delta\theta\rangle = 0$). In Appendix 3.C, we show that this error model leads to an average gate

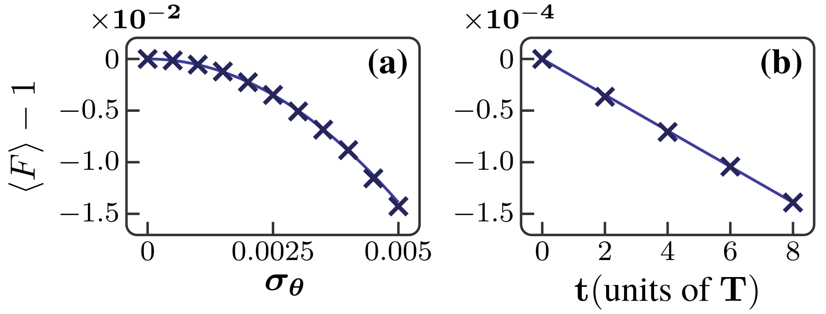

Figure 3.5: Average of numerical gate fidelity $\langle F\rangle$ with imperfect pulses and $T = \Delta^{-1}/8$. (a) shows $\langle F\rangle - 1$ versus the width σ_θ of the Gaussian distributed pulse errors for $t = \Delta^{-1}$, while (b) shows the fidelity versus time for $\sigma_\theta = 5 \times 10^{-4}$. The solid lines are evaluated using Eq. (3.13) and agree well with the numerical data (crosses).

fidelity $\langle F\rangle \approx 1 - c_{\mathrm{err}} t - \alpha c_{\mathrm{av}} t^2$ with $1 < \alpha < 2$ and

$$c_{\mathrm{err}} = (18L^2 - 10L + 7)\frac{\sigma_\theta^2}{2T} \tag{3.13}$$

for $c_{\mathrm{err}} t \ll 1$. As shown in Fig. 3.5, this simple approximation (solid lines) agrees well with the numerical results (crosses) of the $L = 3$ code for $T = \Delta^{-1}/8$ and pulse errors $\lesssim 10^{-2}$. The fidelity exhibits a linear and quadratic behavior in dependence on the time and on the magnitude of pulse errors, respectively. Thus, by minimizing the total deviations $c_{\mathrm{err}} t + \alpha c_{\mathrm{av}} t^2$ with respect to T, we can estimate the optimal period length to be

$$T_{\mathrm{opt}} = \left(\frac{96[2L(9L-5)+7]\sigma_\theta^2}{[5L(L-1)\delta\omega_0\Delta]^2 \alpha t}\right)^{1/5}. \tag{3.14}$$

For example, to maximize $\langle F\rangle$ for the $L = 3$ code with $\omega_0 = \Delta$, $\delta = 0.1\Delta$, and an error magnitude of $\sigma_\theta = 0.001$ after a propagation time of $t = 100\Delta^{-1}$, we have to set $T_{\mathrm{opt}} \approx 0.1\Delta^{-1}$, which results in a fidelity of about 91%. For $\sigma_\theta = 10^{-4}$, we obtain $T_{\mathrm{opt}} \approx 0.04\Delta^{-1}$ and $\langle F\rangle(100\Delta^{-1}) \gtrsim 99\%$. When realizing the optimal sequence period, the total deviation from perfect fidelity scales with the linear size of the memory like $O(L^{12/5})$. This limits the gain in stability that is achievable by the induced stabilizer interaction (see Sec. 3.5). In an experimental realization this leads to an optimal L that maximizes the lifetime of the memory.

3.5 Suppression of thermal anyons due to cavity-induced stabilizer interactions

In this section, we derive the effective long-range attractive interaction between stabilizers that is induced by the coupling of a cavity mode to the entire lattice of physical qubits. As long as the coupling is weak ($\delta \ll \omega_0, \Delta$), a Schrieffer-Wolff transformation [95] yields the effective low-energy Hamiltonian for a cavity that is kept in a Fock state $|n\rangle$ with a constant number n of photons. Aside from small deviations due to $H_{\text{av}}^{(2)}$ and pulse imperfections, the total average Hamiltonian is then given by

$$H = -\Delta \sum_{a} W_a - \frac{\delta^2}{\omega_0} \sum_{a \neq a'} W_a W_{a'}. \tag{3.15}$$

The interaction term, which describes an effective long-range interaction between the stabilizer operators, couples every pair of stabilizers of the code via absorption and emission of a single photon. Note that this term in the effective Hamiltonian (3.15) is at least two orders of magnitude stronger than the one that appears in the second-order average Hamiltonian in Eq. (3.10) for typical values of T_{opt} and $\delta \ll \omega_0 \approx \Delta$.

It was shown in Ref. [39] that the energy penalty for the creation of anyons grows with L^2 for a code Hamiltonian (3.15) that features an attractive constant long-range interaction between stabilizers. As a consequence, the lifetime of logical qubit states (or codewords) due to *independent single-qubit errors* that are created by the *thermal environment* increases exponentially with L^2 or, equivalently, with the number of stabilizer operators W_a. In a system that is a direct realization of Hamiltonian (3.15), the density of anyons therefore goes to zero in the thermodynamic limit and without the need for any measurements-based, active error-correction procedure, the memory retains its information indefinitely. In other words, the coupling to the cavity mode allows one to passively protect the quantum information against thermal fluctuations. In this sense the memory is called self-correcting.

Note that, while being an element of repeated external manipulation, the pulsing of the system does not in itself constitute an active error-correction procedure: Neither does it require one to extract information about the system state at any point in time (by measuring some system properties) in order to detect an error, nor to manipulate the system in a way that is conditional on the result of (such) an error syndrome measurement. Rather, any error-correcting effect is purely passive and achieved by employing a time invariant sequence of pulses to create an environment that hinders anyon creation. Consequently, we can regard the time invariant pulsing as an integral part of the system—a system that is passively protected against thermal fluctuations and therefore self-correcting in the sense explained above. In contrast to a direct realization of Hamiltonian (3.15), however, the dynamical quantum memory has a finite lifetime in the thermodynamic limit. Besides the factors discussed in Sect. 3.4, it is limited by (i) fluctuations in the cavity mode, (ii) a breakdown of the perturbation theory used to derive the effective interaction in Eq. (3.15) for large L, and (iii) system-bath interaction processes with coherence times that are of the order of or shorter than T.

In summary, the following constraints between energies and time scales have to be fulfilled by every implementation of the dynamically generated quantum memory:

$$\delta \ll \Delta, \omega_0, \quad T \ll T_1, T_2, \quad \beta^{-1} \ll \Delta, \tag{3.16}$$

where β^{-1} is the thermal energy and T_1 and T_2 are the relaxation and dephasing times of the physical qubits, respectively. The latter provide time scales both for the rates of errors created in the code as well as for the process of error creation itself. Further restrictions may appear depending on the details of the physical realization.

3.6 Preparation of Codeword States

In addition to generating the dynamics of the planar code Hamiltonian, the pulsing method can also be used to prepare codewords $\{|\bar{0}\rangle, |\bar{1}\rangle\}$ without the need to perform measurements on the system [88]. Typically, a codeword of the planar code is prepared by consecutive projective measurements of all (commuting) star operators performed on initial state $|0, 0, \dots, 0\rangle$ that is obtained by preparing all physical qubits in the spin-up state and which is already a simultaneous eigenstate of all the plaquette operators with eigenvalue(s) $+1$.

Specifically, a codeword in the ground state multiplet of H_{PC}—one that is free of anyons—is obtained by

$$|\bar{0}\rangle = \prod_s \frac{1}{\sqrt{2}}(\mathbb{1} + A_s)|0, \dots, 0\rangle. \tag{3.17}$$

The nonunitary projection operators $\propto (\mathbb{1} + A_s)$ cannot, in general, be implemented with external pulses that are essentially unitary operations.

However, if for one of the qubits $s_k \in \{s_1, \ldots, s_4\}$ of star A_s, the state prior to the projection can be written as $|\psi_i\rangle = |0\rangle_{s_k} \otimes |\phi\rangle$, where $|\phi\rangle$ is an arbitrary state in the joint Hilbert space of all $N-1$ remaining qubits, then, by dynamically generating $-\Delta\tilde{A}_s(k)$ with $\tilde{A}_s(k) = -\sigma_y^{(s_k)} \prod_{l\neq k} \sigma_x^{(s_l)}$ for a time $t = \pi/(4\Delta)$, we get

$$\exp[i\pi\tilde{A}_s(k)/4]|\psi_i\rangle = \frac{1}{\sqrt{2}}(\mathbb{1} + A_s)|\psi_i\rangle, \tag{3.18}$$

which can be traced back to the identity $-i\sigma_y|0\rangle = \sigma_x|0\rangle$.

As per Eqs. (3.17) and (3.18), one $\tilde{A}_s(k)$ for each star operatoright-hand-sideto be generated, to prepare state $|\bar{0}\rangle$. The order of their application and the set of rotated qubit terms has to be chosen such that for each $\tilde{A}_s(k)$, none of the previously applied $\tilde{A}_{s'}(k')$ has acted on the qubit s_k. For the $L = 3$ code, this is a two-step process and schematically illustrated in Fig. 3.6. In each step, one-half of the modified star operators are generated. While there are $4 \times 3 \times 3$ equivalent possibilities to choose three spin operators to rotate from x to y in step one, the corresponding operators in step two are uniquely determined. This procedure works particularly well for the $L = 3$ code, as it mainly consists of edge operators; for $L > 3$, the preparation requires a larger number of steps. It is clear, however, that such a set of steps can always be found and generated with linewise rotations and entangling gates only: In the worst case, the procedure consists of $L(L-1)$ steps—one per star operator.

Figure 3.6(c) shows the codeword fidelity, i.e., the probability $F_C := |\langle\bar{0}|U_{\text{prep}}|0,\ldots,0\rangle|^2$ to find the system in state $|\bar{0}\rangle$ after the preparation sequence U_{prep}, as a function of the pulse errors and with $\delta = 0$ for the time of preparation.[1] Again the fidelity decreases quadratically with σ_θ and agrees well with the simple approximation from Appendix 3.C: Counting the number of mutually inverse pulses in the preparation sequence corresponding to Figs. 3.6(a) and 3.6(b) yields $F_C \approx 1 - 63\sigma_\theta^2$ for the $L = 3$ code.

3.7 Conclusions

We showed how to dynamically realize a quantum memory based on noninteracting qubits that is stabilized against thermal fluctuations by

---

[1] The preparation also works for nonzero coupling although with considerably lower fidelity. For example, if $\omega_0 \approx \Delta$ and $\delta = 0.1\Delta$, we obtain $F_C \approx 90\%$.

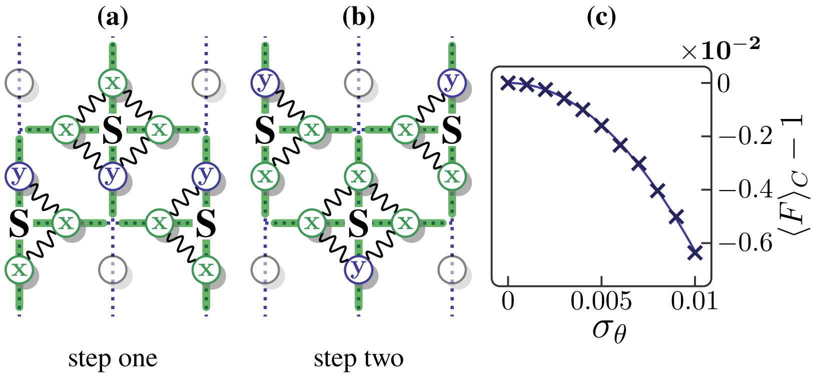

Figure 3.6: (a) and (b): Two steps for preparing $|\bar{0}\rangle$ from initial state $|0,\ldots,0\rangle$ for the $L = 3$ code. The modified star operators are obtained by rotating one σ_x to $-\sigma_y$. In each of the steps, the indicated modified stabilizers are generated for a (effective) time $t = \pi/(4\Delta)$ and the σ_y are chosen such that none of the stabilizers from step one acted on y-qubits from step two. (c) Average codeword fidelity $\langle F\rangle_C$ as a function of pulse errors. Numerics (crosses) agree well with the analytical result (solid line).

a weakly coupled microwave cavity. Properly designed, periodic sequences of pulses, implementing single-qubit rotations and controlled phase gates, can be used to induce the time evolution of Kitaev's toric code Hamiltonian. This allows one to prepare logical qubit states without stabilizer measurements and to protect them both against local sources of decoherence and thermal fluctuations for times much longer than the longest time scale of the free qubit system, even when pulse imperfections are taken into account. Furthermore this method is fairly versatile, as it can be generalized to qubit systems with Ising, XY, and Heisenberg interactions as well as to arbitrary (2D stabilizer) codes based on local stabilizers in a straightforward manner. We provided simple, accurate analytical estimates for the gate and codeword fidelities of our method as a function of the system parameters, the period length T of the pulse sequence, and the magnitude of randomly distributed pulse errors. This allows us to estimate the maximum tolerable size of pulse errors and to optimize tunable system parameters, such as T or the coupling of the qubits to the cavity δ, in order to maximize the lifetime of codeword states.

3.8 Acknowledgments

We would like to thank Andreas Nunnenkamp for discussions. This work was financially supported by the Swiss SNF, the NCCR Nanoscale Science, the NCCR Quantum Science and Technology, and IARPA.

3.A Operations to generate the planar code

We present a particular choice of operations R_1 and R_2 that can be used to dynamically generate (one-quarter of) the planar code when applied to H_0 as part of the sequence shown in Fig. 3.2(b). They are a generalization of the operations given in Sec. 3.3 to a quadratic qubit lattice of arbitrary size, i.e., their restriction to an interior unit cell equals Eqs. (3.6) and (3.7). The additional operations compared to the 2×2 lattice are needed to generate proper (third-order) boundary terms, while using strictly linewise rotations and entangling operations. Schematic illustrations of these operations are provided in Fig. 3.7 for a finite lattice of 25 qubits.

The generalized R_1 consists of nine steps, eight of which are shown in Figs. 3.7(a)–(h). Note that compared to Fig. 3.3, the lattice is rotated by $45°$. After even rows of qubit terms are transformed from z to x by a $\pi/2$ rotation about the y axis, disjoint pairs of qubits are entangled along one of the two sets of parallel diagonals [downward in Fig. 3.7(b)] so that pairs on different diagonals are aligned along the perpendicular direction. The following three steps [Fig. 3.7(b)–3.7(e)] interchange one of the z and y terms along the perpendicular direction for every interior cell, while leaving the qubits that belong to boundary *terms* unchanged. In that context, it is important to notice, that one of the three qubits contributing to a boundary term does not actually lie on that boundary. The rotations that interchange y and z terms [Fig. 3.7(d)] are performed about the x axis. Thus, by rotating the terms on the upper and lower boundaries to σ_x [Fig. 3.7(c)] *prior* to the interchange operation, their relative orientation is protected. After the interchange, the boundary qubits are rotated back [Fig. 3.7(e)]. The diagonals, along which qubits are interchanged in step 4 are chosen in the following way: (i) they are perpendicular to the entangling bonds between the second-order terms, (ii) only one pair of qubits is interchanged per unit cell, and (iii) no y qubit belonging to a boundary term is affected. This choice is always possible. The remaining pairs of qubits are entangled in step 6 [Fig. 3.7(f)] to form

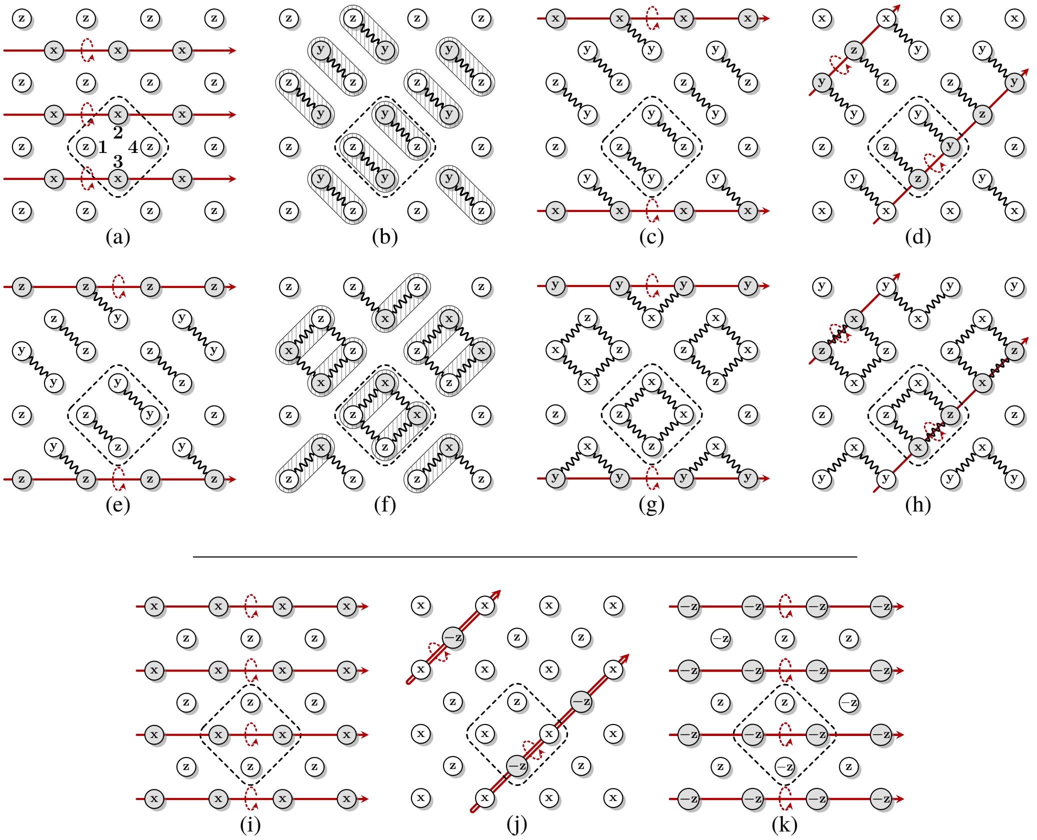

Figure 3.7: (a)–(h) Schematic illustration of the first eight of nine steps of R_1 to generate a quarter of the planar code Hamiltonian for a lattice of 25 qubits. When restricted to an interior unit cell (one is marked by a dashed rectangle) these steps reduce to those shown in Fig. 3.3. (i)–(k) Decomposition of R_2 into a sequence of linewise rotations. Single and double arrows represent rotations by $\pi/2$ and π, respectively.

third- and fourth-order terms. Finally, the qubits of those interior cells that were interchanged in step 4, have to be changed back [subfigure (h)] in step 8, again after protecting the relative orientation of the boundaries by a proper rotation [Fig. 3.7(g)]. The last step 9 (not shown) depends on whether plaquette or star operators are about to be generated. All qubits on the same *row* have the same orientation after step 8. The axis, about which each row has to be rotated in step 9, is therefore uniquely determined.

Operation R_2 eliminates unwanted single- and two-particle terms in the average Hamiltonian. For the R_1 given above, it has to flip the signs of all qubits (i) on odd rows and (ii) on the intersections of even rows with those diagonals, whose z and y orientations were interchanged in step 4 of R_1. This operation can be decomposed into three steps, as illustrated in Figs. 3.7(i)–(k). First, odd rows are rotated from z to x [Fig. 3.7(i)]. A subsequent π rotation [double arrows in Fig. 3.7(j)] about the x axis of all qubits along the diagonals of step 4 of R_1 then flips the sign of qubits (ii). Finally, the same operation as in step 1 is performed once more on the qubits on odd rows [Fig. 3.7(k)].

The remaining three-quarters of the code Hamiltonian are readily given by $\pi/2$ rotations of all those steps about the center of the code. Although the choice of R_1 and R_2 is not unique and might by modified depending on a particular experimental realization, the complexity of the operations cannot be decreased by more than one or two steps. A simplification can be achieved, e.g., by choosing entangling operations and rotations that conform to the fourfold symmetry of the quadratic lattice. Since the resulting R_1 and R_2 are not as easily generalized to lattices of arbitrary size and not as easily applicable in a linewise fashion, we do not consider them here.

3.B Second-order corrections to average Hamiltonian

The exact average Hamiltonian $H_{\mathrm{av}} = \sum_{n=0}^{\infty} H_{\mathrm{av}}^{(n)}$ is given by an infinite expansion in orders of $T\Delta$ and can, in principle, be evaluated to arbitrary orders using the Magnus expansion. For $T \ll \Delta^{-1}$ this expansion converges quickly and only the lowest orders are relevant to describe the dynamics of the pulsed system. Furthermore, all odd-order contributions can be suppressed by symmetrizing the generating pulse sequence in time with respect to its center [92]. A symmetric sequence for the planar code is obtained by reversing the order in which the different quarters are generated after every period T, as illustrated in Fig. 3.8. The corresponding Hamiltonians $\mathcal{Q}_i$ with $i = 1, \ldots, 4$ are given by

$$\mathcal{Q}_i = [1 + \delta/\Delta(b + b^\dagger)]Q_i + \omega_0 b^\dagger b. \tag{3.19}$$

Taken as a whole, the resulting sequence consists of 32 operations, which give rise to 24 toggling frame Hamiltonians. With respect to time T, these Hamiltonians are mirror symmetric ($H_i = H_{25-i}$ for $13 \leq i \leq 24$), while the sequence of 32 operations R_j is antisymmetric ($R_j = R^\dagger_{33-j}$ for $17 \leq j \leq 32$). With this, the leading-order deviation from Eq. (3.9) is essentially given by $H^{(2)}_{\text{av}} \propto (T\Delta)^2$. However, as the sub-sequences to generate the (average Hamiltonians) $\mathcal{Q}_i$ are symmetric as well, the corresponding second-order deviations scale as $(T\Delta/4)^2$ and can be neglected for the calculation of $H^{(2)}_{\text{av}}$. Hence, based on a sequence with effective toggling frame Hamiltonians $\mathcal{Q}_i$, we obtain

$$H^{(2)}_{\text{av}} = \frac{T^2}{384} \sum_{1 \leq j < k \leq l \leq 8} (1 - \delta_{kl}/2)[\mathcal{Q}_l, [\mathcal{Q}_k, \mathcal{Q}_j]], \tag{3.20}$$

where δ_{kl} is the Kronecker delta and $\mathcal{Q}_{j>4} = \mathcal{Q}_{9-j}$. Note that since the corresponding spin Hamiltonians Q_j commute, all higher-order contributions to H_{av} vanish identically for $\delta = 0$ in which case Eq. (3.9) gives the exact average Hamiltonian. In the case of a finite coupling to the cavity, $H^{(2)}_{\text{av}}$ evaluates to Eq. (3.10) using

$$[\mathcal{Q}_l, [\mathcal{Q}_k, \mathcal{Q}_j]] = -\delta\omega_0[2\delta Q_l + \omega_0(b + b^\dagger)](Q_k - Q_j). \tag{3.21}$$

To derive an approximation for the decrease in the gate fidelity $F^{(2)}$ [see Eq. (3.11)] that is caused by the leading-order correction $H^{(2)}_{\text{av}}$, we transform the propagator $\exp[-it(H^{(0)}_{\text{av}} + H^{(2)}_{\text{av}})]$ into the interaction picture with $H^{(0)}_{\text{av}}$ and $H^{(2)}_{\text{av}}$ playing the role of the noninteracting system and the interaction, respectively. The transformation of the latter can be evaluated analytically yielding

$$H^{(2)}_{\text{av}}(t) = A + \cos(\omega_0 t)B + \sin(\omega_0 t)C \tag{3.22}$$

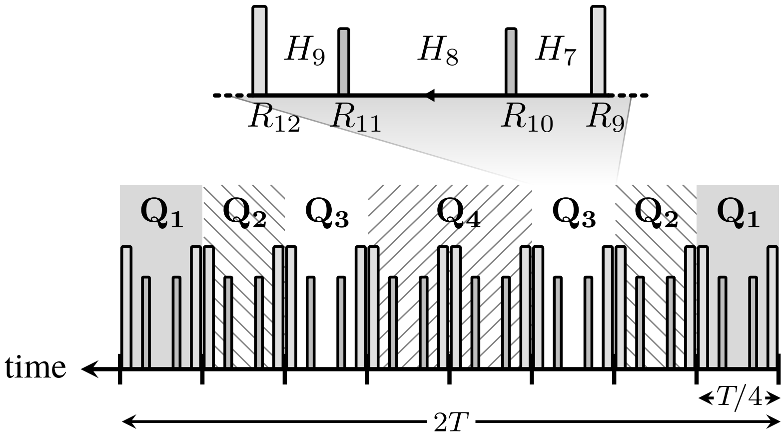

Figure 3.8: Symmetric pulse sequence for the generation of the planar code. The order in which the quarters Q_i are generated is reversed after every period T. With respect to T, the 24 toggling frame Hamiltonians $H_i = \mathcal{R}_i^\dagger H_0 \mathcal{R}_i$ are symmetric, while the 32 operations R_j are antisymmetric.

with Hermitian operators

$$\begin{aligned}
A &= \frac{\delta^2\omega_0 T^2}{48\Delta^2}\mathbf{Q}\begin{pmatrix} 9 & -7 & -19 & -25 \\ 11 & 3 & -7 & -13 \\ 11 & 5 & 3 & -1 \\ 11 & 5 & 5 & 9 \end{pmatrix}\mathbf{Q}^\dagger, \\
B &= \frac{\delta\omega_0 T^2}{8\Delta}\mathbf{QV}\Big[(b^\dagger + b) - \frac{2\delta}{\omega_0\Delta}\sum_j Q_j\Big], \\
C &= \frac{i\delta\omega_0 T^2}{8\Delta}\mathbf{QV}(b^\dagger - b).
\end{aligned} \tag{3.23}$$

To determine the approximate fidelity for times $t \gg \Delta^{-1}$, we replace the time-dependent second-order contribution by its average over the cavity's oscillation period $T_C = 2\pi/\omega_0$. It is given by $\bar{H}_{\text{av}}^{(2)} := T_C^{-1}\int_0^{T_C} H_{\text{av}}^{(2)}(t)\,dt = A$. To second-order in A, the fidelity $F^{(2)}$ can then be written as

$$F^{(2)} \approx |\mathrm{Tr}_{\mathrm{QB}}\Big(\mathbb{1} - itA - \frac{t^2}{2}A^2\Big)|\,/2^N, \tag{3.24}$$

where $\mathrm{Tr}_{\mathrm{QB}}$ denotes the trace over the qubit subsystem. Using $\mathrm{Tr}_{\mathrm{QB}}(Q_k Q_l) = \delta_{kl} L(L-1)/2$ (the number of anyon operators per code quarter for $k = l$), a straightforward calculation yields Eq. (3.12).

3.C Gate fidelity in presence of pulse errors

To second-order in $\delta\theta$, an imperfect pulse $\tilde{R}(\delta\theta) = \exp(i[\theta_0 + \delta\theta]S/2)$ can be approximated by

$$\tilde{R}(\delta\theta) \approx \Big[\Big(1 - \frac{\delta\theta^2}{8}\Big)\mathbb{1} + i\frac{\delta\theta}{2}S\Big]R, \tag{3.25}$$

where $R \equiv \tilde{R}(0)$ is the perfect pulse operator. To estimate the statistical effect of these random errors on the fidelity of the whole planar code sequence, it is sufficient to consider the case of two inverse operations with *independent* errors flanking a period of free propagation:

$$\begin{aligned} &\tilde{R}^\dagger(\delta\theta_2)U_0(t)\tilde{R}(\delta\theta_1) \\ =&\tilde{R}^\dagger(\delta\theta_2)\tilde{R}(\delta\theta_1)\tilde{R}^\dagger(\delta\theta_1)U_0(t)\tilde{R}(\delta\theta_1) \\ =&\tilde{R}^\dagger(\delta\theta_2)\tilde{R}(\delta\theta_1)\exp[-it\tilde{R}^\dagger(\delta\theta_1)H_0\tilde{R}(\delta\theta_1)] \end{aligned} \tag{3.26}$$

The third term on the right-hand-side can be interpreted as a time evolution operator with effective Hamiltonian $H_1{+}\delta H_1$, where $H_1 = \tilde{R}^\dagger(0)H_0\tilde{R}(0)$ is the perfect-pulse toggling frame Hamiltonian and

$$\delta H_1 = -\frac{\delta\theta^2}{4}(H_1 - SH_1S) + i\frac{\delta\theta}{2}[S, H_1]. \tag{3.27}$$

In the case of $H_0 = -\Delta\sigma_x^{(1)}$, $S = \sigma_y^{(1)}$, and $\theta_0 = \pi/2$, for example, application of $\tilde{R}(\delta\theta)$ leads to an average effective Hamiltonian $-\Delta[(1 - \delta\theta^2/2)\sigma_z^{(1)} + \delta\theta\sigma_x^{(1)}]$. The remaining terms from the right-hand-side of Eq. (3.27) gives

$$\begin{aligned} &\tilde{R}^\dagger(\delta\theta_2)\tilde{R}(\delta\theta_1) \\ =&\Big[\Big(1 - \frac{\delta\theta_2^2}{8}\Big)\mathbb{1} - i\frac{\delta\theta_2}{2}S\Big]\Big[\Big(1 - \frac{\delta\theta_1^2}{8}\Big)\mathbb{1} + i\frac{\delta\theta_1}{2}S\Big] \\ =&\Big(1 - \frac{\delta\theta_1^2 + 2\delta\theta_1\delta\theta_2 + \delta\theta_2^2}{8}\Big)\mathbb{1} + i\frac{\delta\theta_1 - \delta\theta_2}{2}S. \end{aligned} \tag{3.28}$$

For the estimate of how much the statistical expectation value of the gate fidelity as a function of $\delta\theta$ deviates from the perfect-pulse value, we only need to consider terms that are proportional to the identity operator (as the trace of all Pauli operators vanishes) and $\delta\theta_i^2$ (as for independent, unbiased errors $\langle\delta\theta_1\delta\theta_2\rangle = 0$). The only such terms are contained in the first summand on the right-hand-side of Eq. (3.28) and yield $\langle F\rangle \approx 1 - \sigma_\theta^2/4$ for a single pair of mutually inverse imperfect operations. Consequently, for a nested sequence of n such operations, the deviation amounts to n times that value. Hence, by counting the number $n(L)$ of mutually inverse operations in the generating sequence for a planar code of length L, we obtain $\langle F \rangle \approx 1 - t\, n(L)\sigma_\theta^2/(4T)$ for stroboscopic times $t = mT$ with integer m. Based on the operations shown in Appendix 3.A, the number $n(L)$ for the whole generating sequence evaluates to $n(L) = 36L^2 - 20L + 14$ and we obtain $\langle F \rangle \approx 1 - c_{\text{err}}t - c_{\text{av}}t^2$ with c_{err} given by Eq. (3.13).

CHAPTER 4

Enhanced Thermal Stability of the Toric Code through Coupling to a Bosonic Bath

Adapted from:
Fabio L. Pedrocchi, Adrian Hutter, James R. Wootton, and Daniel Loss
"Enhanced thermal stability of the toric code through coupling to a bosonic bath",
Phys. Rev. A **88**, 062313 (2013)

We propose and study a model of a quantum memory that features self-correcting properties and a lifetime growing arbitrarily with system size at non-zero temperature. This is achieved by locally coupling a 2D $L \times L$ toric code to a 3D bath of bosons hopping on a cubic lattice. When the stabilizer operators of the toric code are coupled to the displacement operator of the bosons, we solve the model exactly via a polaron transformation and show that the energy penalty to create anyons grows linearly with L. When the stabilizer operators of the toric code are coupled to the bosonic density operator, we use perturbation theory to show that the energy penalty for anyons scales with $\ln(L)$. For a given error model, these energy penalties lead to a lifetime of the stored quantum information growing respectively exponentially and polynomially with L. Furthermore, we show how to choose an appropriate coupling scheme in order to hinder the hopping of anyons (and not only their creation) with energy barriers that are of the same order as the anyon creation gaps. We argue that a toric code coupled to a 3D Heisenberg ferromagnet realizes our model in its low-energy sector. Finally, we discuss the delicate issue of the stability of topological order in the presence of perturbations. While we do not derive a rigorous proof of topological order, we present heuristic arguments suggesting that topological order remains intact when perturbative operators acting on the toric code spins are coupled to the bosonic environment.

4.1 Introduction

Topologically ordered phases of matter like Kitaev's toric code promise the possibility to store and process quantum information in a manner which is resilient to local imperfections [16, 19, 57, 96]. However, a finite gap for the creation of topological defects (called *anyons* in the case of the toric code) is not enough to ensure stability against thermal fluctuations [33, 56, 77, 78]. If anyons can be created at a constant energy cost and propagate without any further energy penalty, they will at any non-zero temperature T destroy the stored quantum information in a time which does not increase with the size of the memory. Indeed, it was shown that not only the toric code but a large class of 1-, 2-, and 3-dimensional Hamiltonians suffer from the aforementioned thermal instability of quantum information [32, 35, 59, 97]. This is in contrast to the classical case, where magnetic devices allow the construction of self-correcting hard drives that are stable against both local perturbations and thermal excitations. Proposals for three-dimensional spin Hamiltonians with local few-spin interactions that do not fall victim to the aforementioned no-go results exist [60,61,79,80]. None of these models is expected to allow for a storage time increasing arbitrarily with system size, while the scaling of the lifetime with temperature may be more favorable than in the bare toric code [16]. A 2D system with a similar behavior has recently been proposed in Ref. [98].

Following a different approach, it has been shown that repulsive long-range interactions between anyons lead to storage times that grow polynomially in L [38–40, 81]. When the stabilizer operators of the toric code (stabilizers) are resonantly coupled to cavity modes, even a lifetime growing exponentially with L can be achieved [39, 81]. Furthermore, the suppression of anyon diffusion by means of attractive interactions between them has been proposed in Ref. [57] and studied in Ref. [65]. Refs. [99, 100] studied disorder as a means to hinder quantum propagation of anyons.

In this work, we propose a three-dimensional (3D) model with purely local interactions of bounded strength that presents self-correcting properties. In contrast to the spin-lattice Hamiltonians discussed in Refs. [16, 19, 32, 35, 60, 61, 79, 80] and similar to Ref. [65], our Hamiltonian involves unbounded bosonic operators. However, in contrast to Ref. [65] the interaction strengths in our Hamiltonian are bounded while the obtained life-time scalings are more favorable. We consider a toric code embedded in a 3D reservoir of hopping bosons on a cubic lattice. When the stabilizers are coupled to the bosonic displacement operator, the model is exactly solvable via a polaron transformation. The coupling to the bosons leads to an energy penalty for the anyons that grows linearly with L. This is very favorbale since it can lead to a lifetime of the memory that increases exponentially with L. This scaling of the lifetime coincides with the four-dimensional toric code [34, 57], which constitutes so far the only known example of a truly self-correcting quantum memory. We also consider the case when the stabilizers are coupled to the density operator of the bosons, in which case the model is solved with a perturbative second-order Schrieffer-Wolff transformation. We show that the energy penalty for the creation of anyons scales as $\ln(L)$. This scaling of the anyons' gap is in principle sufficient to stabilize the memory and leads to a lifetime increasing polynomially with L.

We present a coupling scheme between stabilizers and bosons that allows to hinder the hopping of anyons, and not only their creation, by energy barriers that are of the same order as the anyon creation gaps, i.e., $O(L)$ or $O(\ln L)$. This is useful since imperfections in the initialization process might lead to a finite initial density of anyons.

Furthermore, we argue that a toric code coupled to a 3D Heisenberg ferromagnet in a broken-symmetry state provides a way to realize the proposed Hamiltonian as an effective low-energy theory of a spin-lattice model with bounded operators only.

Finally, we discuss the delicate issue of the stability of topological order in our model. While we do not derive a rigorous proof of topological order, we present heuristic arguments suggesting that topological order remains intact when perturbative operators acting on the toric code spins are coupled to the bosonic environment.

The paper is organized as follows. In Sec. 4.2 we introduce our model for a toric code embedded in a three-dimensional cubic lattice of hopping bosons. The stabilizer operators are locally coupled to the displacement operator of the bosonic field. In Sec. 4.2 we state that the energetics of the anyon system is accurately described by a Hamiltonian H_W with long-range attractive interactions between the stabilizers. This is valid as long as the bosons are in thermal equilibrium with the state of the anyons. We then derive the main result of our work: the energy penalty to slowly create an anyon grows linearly with L. We rigorously prove in Sec. 4.2 that the energetics of the anyons is indeed described by H_W. In Sec. 4.2 we consider the fast creation of anyons. We show that the enegy to create an anyon fast is higher than the energy to create it slowly; the energy penalty to create a defect grows in any case linearly with L. In Sec. 4.3 we consider a slightly different model where the stabilizers are locally coupled to the bosonic density operator. This model cannot be treated exactly and we solve it with a perturbative Schrieffer-Wolff transformation. We show that the energy penalty to create an anyon scales as $\ln L$ in this case. In Secs. 4.4 and 4.4 we show that an energy penalty for the anyons scaling with L and $\ln L$ leads to a lifetime of the toric growing respectively exponentially with L and polynomially with L. In Section 4.6 we mention a possible implementation of our model in a Heisenberg ferromagnet. Section 4.7 contains our final remarks and in particular a discussion of the stability of topological order. Appendix 4.A contains a short review of the Schrieffer-Wolff transformation. In Appendix 4.B we calculate all the higher moments ($n \geq 2$) of the distribution of energy costs to create an anyon and show that they are all independent of L. In Appendix 4.C we show that the the continuum approximation used in the main text is just a calculational tool that has no influence on the validity of our results.

4.2 Coupling to the bosonic displacement operator

We present here a model that involves only local interactions of bounded strength in three dimensions. We consider a toric code embedded in a 3D cubic lattice of hopping bosons, see Fig. 4.1. The stabilizer operators of the toric code are locally coupled to the creation and annihilation operators of the bosons and the total Hamiltonian reads

$$H = H_{\mathrm{b}} + A \sum_{p} W_p (a_p + a_p^\dagger)\,, \tag{4.1}$$

where the sum runs over the toric code. We denote the linear size of the cubic lattice by Λ. Here, the plaquette (stabilizer) operator $W_p = I^z_{p,1} I^y_{p,2} I^z_{p,3} I^y_{p,4}$ is the poduct of spins around the square plaquette centered at $\mathbf{R}_p$, which are defined on a square lattice of linear size L with periodic boundary conditions (we set the lattice constant to unity). To avoid boundary effects we assume $\Lambda > L$. The 3D vector $\mathbf{R}_p$ points towards the center of a plaquette, see Fig. 4.1. Note that this definition of W_p ensures that the blue and white plaquettes are equivalent to the usual toric code star and plaquette operators [16]. The anyon operator n_p is defined through $W_p = 1 - 2n_p$. In other words, when $W_p = +1$, the plaquette p carries no anyon and when $W_p = -1$, the plaquette p carries an anyon.

The Hamiltonian for the bosons

$$H_{\mathrm{b}} = \epsilon_{\mathbf{0}} \sum_{i} a_i^\dagger a_i - t \sum_{\langle i,j \rangle} a_i^\dagger a_j\,, \tag{4.2}$$

describes bosons hopping on a cubic lattice with hopping amplitude t and on-site chemical potential $\epsilon_{\mathbf{0}} = 6t$. Here, $a_i^\dagger$ creates a boson at site i, while a_i destroys a boson at site i of the cubic lattice.

Although Hamiltonian (4.1) is three-dimensional, we point out, for the sake of clarity, that quantum information is stored in the two-dimensional toric code only. As we show below, the presence of the 3D system is necessary to mediate long-range interactions between the stabilizers.

Energy of anyon configurations with bosons in thermal equilibrium

Here we are interested in the energy penalty to create an anyon. We consider a state with some fixed anyon configuration $|\alpha\rangle$ (i.e., an eigenstate

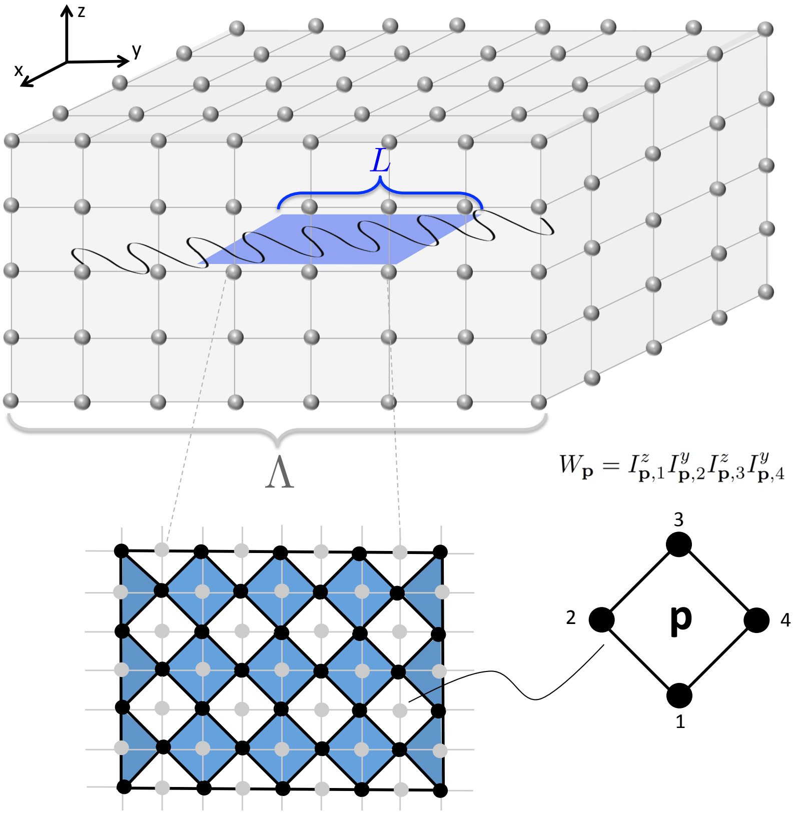

Figure 4.1: A 2D toric code (blue (dark) area in xy-plane) of size $L \times L$ is centered inside a cubic lattice of size Λ^3 with $\Lambda > L$. The stabilizers W_p of the toric code locally couple to a system of hopping bosons on a cubic lattice. A long-range attraction between the stabilizers is mediated by the low-energy collective excitations of the bosons.

of all operators W_p) and with the bosons in thermal equilibrium with respect to that anyon state. In other words, the bosons are in the Gibbs state $\rho_\alpha = e^{-\beta H_\alpha}/Z_\alpha$ with $Z_\alpha = \mathrm{tr}(e^{-\beta H_\alpha})$, $\beta = 1/T$, and the bosonic Hamiltonian $H_\alpha = \langle\alpha|H|\alpha\rangle$ with H defined in Eq. (4.1).

In Section 4.2, we prove that the energetics of the anyon system is fully described by the diagonal Hamiltonian H_W, *if the bosons are at each moment in thermal equilibrium ρ_α with respect to the current state $|\alpha\rangle$ of the anyons*. We have

$$H_W = \sum_{p \neq p'} J_{p,p'} W_p W_{p'} \, , \tag{4.3}$$

where $J_{p,p'}$ is a gravitation-like potential between stabilizers, i.e.,

$$J_{p,p'} = -\frac{A^2}{4\pi t|\mathbf{R}_p - \mathbf{R}_{p'}|} \,. \tag{4.4}$$

More precisely, in the next subsection we derive the relation (see Eq. (4.22) below)

$$\mathrm{tr}\left(|\alpha\rangle\langle\alpha| \otimes \rho_\alpha\, H\right) = \langle\alpha|H_W|\alpha\rangle + U_\mathrm{b}(\beta)\,, \tag{4.5}$$

where $U_\mathrm{b}(\beta)$ depends on the temperature T of the bosonic bath but not on the anyon configuration $|\alpha\rangle$. Since only the first summand depends on $|\alpha\rangle$ and is independent of the temperature of the bosons, the dynamics of the anyon system is described by H_W, if the boson system remains in thermal equilibrium with respect to the state of the anyons. The energy difference between an anyon state $|\alpha\rangle$ and another anyon state $|\gamma\rangle$ is defined by

$$\Delta E = \mathrm{Tr}(H|\alpha\rangle\langle\alpha| \otimes \rho_\alpha) - \mathrm{Tr}(H|\gamma\rangle\langle\gamma| \otimes \rho_\gamma)\,. \tag{4.6}$$

From Eq. (4.5) it directly follows that

$$\Delta E = \langle\alpha|H_W|\alpha\rangle - \langle\gamma|H_W|\gamma\rangle\,. \tag{4.7}$$

In particular, the energy cost $\Delta E_{0\to1}$ to create a single anyon above the anyon-free state $|0\rangle$ is

$$\Delta E_{0\to1} = \langle 1|H_W|1\rangle - \langle 0|H_W|0\rangle\,. \tag{4.8}$$

Note that in the case of periodic boundary conditions, anyons can only be created in pairs. Therefore $\Delta E_{0\to1}$ represents a lower bound for the energy gap above the anyonic vacuum, irrespective of the boundary conditions. In the remaining part of this subsection, we thus study H_W and derive how the energy cost $\Delta E_{0\to1}$ scales with L. This is justified since, as we will show in Sec. 4.2, the energy cost to create an anyon fast enough, such that the thermalization process of the bosons cannot keep pace with the anyon creation, is in fact *higher* than the energy cost $\Delta E_{0\to1}$. The Hamiltonian H_W provides thus lower bounds on the energy costs for the creation of an anyon.

Writing H_W in terms of anyon operators, $W_p = 1 - 2n_p$, we obtain

$$H_W = \mu(L)\sum_p n_p + 4\sum_{p\neq p'} J_{p,p'}n_p n_{p'} + \mathrm{const.} \tag{4.9}$$

The first summand describes a chemical potential for creating an anyon at plaquette p, i.e.

$$\Delta E_{0\to 1} = \mu(L)\,, \tag{4.10}$$

defined by

$$\mu(L) = 4\sum_{p'}(1-\delta_{p,p'})|J_{p,p'}|\,. \tag{4.11}$$

This chemical potential can be evaluated explicitly as

$$\mu(L) = \frac{A^2}{\pi\, t}\sum_{p'}\frac{1-\delta_{p,p'}}{|\mathbf{R}_{p'}|} \approx \frac{A^2}{\pi\, t}\int_{D_{L/2}} d\mathbf{R}\,\frac{1}{|\mathbf{R}|} = \frac{2A^2}{t}\,L\,, \tag{4.12}$$

where we have approximated the square lattice of the toric code by a disk of radius $L/2$ and put the plaquette p and the origin of the coordinate system at the center of the toric code. Note that the continuum approximation used to derive Eq. (4.12) is a calculational tool to estimate the corresponding sum. Furthermore, in this limit we also let the lattice constant of the surface code go to zero such that a single stabilizer remains coupled to bosonic creation and annihilation operators only at the corresponding site. This approximation is not necessary to obtain the desired behavior since a direct numerical evaluation of the sum shows that it indeed grows linearly with L, see Fig. 4.3 in Appendix 4.C. Equation (4.12) is a central result of this work; *the chemical potential to create an anyon scales linearly with* L. In Appendix 4.B we also calculate the standard deviation and all higher moments of the distribution of energy costs $\Delta E_{0\to 1}$.[1] We show that they are independent of L but increase with temperature T, as expected. This implies that for any fixed temperature T we can find a size L of the memory such that the distribution of the energy costs is negligible compared to the expected energy cost $\mu(L)$.

We point out that bosonic operators are not bounded and therefore it is not surprising that the energy cost to create an anyon can increase with the size of the system. Qualitatively, our results can be understood as follows. The long-wavelength, low-energy excitations of the bosons mediate a long-range attractive interaction between the stabilizer operators, as as can be seen explicitly in H_W. Therefore a plaquette feels the presence of all the other plaquettes. In the anyonic vacuum state ($W_p = +1$, $\forall\, p$) one needs to overcome the attraction from $L^2 - 1$ plaquettes in order to create an anyon. Since the interaction between stabilizers decreases

---

[1] D. Poulin, private communication.

with distance, the energy penalty associated to the creation of the anyon scales with L and not with L^2.

The second summand in Eq. (4.9) describes a gravitation-like interaction between anyons. Since this term helps to keep newly created anyon pairs attached to each other (for temperatures below the interaction strength $\propto A^2/t$), it will have a further beneficial effect on the memory lifetime. On the other hand, this anyon-anyon attraction effectively reduces the anyon chemical potential. However, this reduction is negligible since the anyon density is exponentially suppressed by the first term, see Section 4.4.

Proof of Eq. (4.5)

The aim of this subsection is to derive Eq. (4.5). Let us rewrite Hamiltonian (4.1) in Fourier space,

$$H = \sum_{\mathbf{q}} \epsilon_{\mathbf{q}} a_{\mathbf{q}}^\dagger a_{\mathbf{q}} + \frac{A}{\sqrt{N}} \sum_{p,\mathbf{q}} W_p (e^{i\mathbf{q}\cdot\mathbf{R}_p} a_{\mathbf{q}} + \text{h.c.}) \,, \tag{4.13}$$

where $a_{\mathbf{q}} = \frac{1}{\sqrt{N}} \sum_i e^{-i\mathbf{q}\cdot\mathbf{R}_i} a_i$ with $N = \Lambda^3$ the number of lattice sites and $\epsilon_{\mathbf{q}} = \epsilon_{\mathbf{0}} - t_{\mathbf{q}}$ with $t_{\mathbf{q}} = \frac{1}{N}\sum_{\langle ij\rangle} t e^{i\mathbf{q}\cdot(\mathbf{R}_i - \mathbf{R}_j)}$. Choosing the on-site potential such that $\epsilon_{\mathbf{0}} = t_{\mathbf{0}} = 6t$, we obtain the dispersion

$$\epsilon_{\mathbf{q}} = 2t\left(3 - (\cos(q_x) + \cos(q_y) + \cos(q_z)\right)\right) \,. \tag{4.14}$$

This Hamiltonian is similar to the independent boson model [103] and thus exactly diagonalizable via the unitary polaron transformation

$$\mathcal{S} = -\frac{A}{\sqrt{N}} \sum_p W_p \sum_{\mathbf{k}} \frac{1}{\epsilon_{\mathbf{k}}} (a_{\mathbf{k}} e^{i\mathbf{k}\cdot\mathbf{R}_p} - \text{h.c.}) \,. \tag{4.15}$$

We have

$$\begin{aligned} \widetilde{a}_i &= e^{\mathcal{S}} a_i e^{-\mathcal{S}} = a_i - \frac{A}{N} \sum_{p,\mathbf{q}} W_p \frac{1}{\epsilon_{\mathbf{q}}} e^{i\mathbf{q}\cdot(\mathbf{R}_i - \mathbf{R}_p)} \,, && (4.16) \\ \widetilde{a}_{\mathbf{k}} &= a_{\mathbf{k}} - \frac{A}{\sqrt{N}} \frac{1}{\epsilon_{\mathbf{k}}} \sum_p W_p e^{-i\mathbf{k}\cdot\mathbf{R}_p} \,. && (4.17) \end{aligned}$$

We thus obtain

$$\begin{aligned}\widetilde{H} &= e^{\mathcal{S}}He^{-\mathcal{S}} \\ &= \sum_{\mathbf{q}} \epsilon_{\mathbf{q}} a^\dagger_{\mathbf{q}} a_{\mathbf{q}} - \frac{A^2}{N}\sum_{p,p'} W_p W_{p'} \sum_{\mathbf{q}} \frac{e^{-i\mathbf{q}\cdot(\mathbf{R}_p-\mathbf{R}_{p'})}}{\epsilon_{\mathbf{q}}} \\ &= \sum_{\mathbf{q}} \epsilon_{\mathbf{q}} a^\dagger_{\mathbf{q}} a_{\mathbf{q}} + \sum_{p,p'} J_{p,p'} W_p W_{p'}\,. \end{aligned} \tag{4.18}$$

In order to calculate $J_{p,p'}$, we note that the dominant contributions to $J_{p,p'}$ come from small values of $|\mathbf{q}|$ (see the integral below) and thus employ a low-$\mathbf{q}$ approximation $\epsilon_{\mathbf{q}} \approx t\mathbf{q}^2$. We find

$$\begin{aligned} J_{p,p'} &= -\frac{A^2}{N}\sum_{\mathbf{k}} \frac{1}{\epsilon_{\mathbf{k}}} e^{i\mathbf{k}\cdot(\mathbf{R}_p-\mathbf{R}_{p'})} \\ &= -\frac{A^2}{(2\pi)^3}\int d\mathbf{k}\frac{1}{\epsilon_{\mathbf{k}}} e^{i\mathbf{k}\cdot(\mathbf{R}_p-\mathbf{R}_{p'})} \\ &\approx -\frac{A^2}{4\pi t|\mathbf{R}_p-\mathbf{R}_{p'}|}\,. \end{aligned} \tag{4.19}$$

Note that formally $J_{p,p'}$ appears to be divergent for short distances. This, however, is an artefact of the low-$\mathbf{q}$ approximation, which is accurate only for distances $|\mathbf{R}_p-\mathbf{R}_{p'}|$ sufficiently larger than one lattice constant. We have calculated the integral above for $p = p'$ numerically and obtained $J_{p,p} \approx -0.253A^2/t$. Since the $p = p'$-terms in $\widetilde{H}$ are irrelevant, we can simply write

$$\begin{aligned} \widetilde{H} &= H_{\mathrm{b}} + \sum_{p\neq p'} J_{p,p'} W_p W_{p'} + \sum_{p=p'} J_{p,p'} W_p W_{p'} \\ &= H_{\mathrm{b}} + H_W + C\,, \end{aligned} \tag{4.20}$$

where we used the fact that $W_p^2 = +1$, leading to the irrelevant constant C.

Let us define the operator $\mathcal{S}_\alpha = \langle\alpha|\mathcal{S}|\alpha\rangle$. We now calculate the energy of the state $|\alpha\rangle\langle\alpha| \otimes \rho_\alpha$, where $|\alpha\rangle$ is an eigenstate of all W_i operators. Using Eq. (4.20) and

$$e^{\mathcal{S}_\alpha} e^{-\beta H_\alpha} e^{-\mathcal{S}_\alpha} \propto e^{-\beta H_{\mathrm{b}}} \tag{4.21}$$

we find

$$\begin{aligned}\mathrm{Tr}(H|\alpha\rangle\langle\alpha|\otimes\rho_\alpha) &= \mathrm{Tr}(\widetilde{H}e^{\mathcal{S}}|\alpha\rangle\langle\alpha|\otimes\rho_\alpha e^{-\mathcal{S}})\\ &= \mathrm{Tr}(H_\mathrm{b}e^{\mathcal{S}_\alpha}\rho_\alpha e^{-\mathcal{S}_\alpha}) + \mathrm{Tr}(H_W\,|\alpha\rangle\langle\alpha|) + C\\ &= \mathrm{Tr}(H_\mathrm{b}e^{-\beta H_\mathrm{b}})/\,\mathrm{tr}(e^{-\beta H_\mathrm{b}}) + \langle\alpha|H_W|\alpha\rangle + C\\ &= U_\mathrm{b}(\beta) + \langle\alpha|H_W|\alpha\rangle + C\,, \end{aligned} \tag{4.22}$$

where $U_\mathrm{b}(\beta)$ depends only on the temperature of the bosonic bath but is independent of α. The constant C can be included in $U_\mathrm{b}(\beta)$. This completes the proof of Eq. (4.5).

Fast creation of an anyon

In this section, we are interested in the fast creation of an anyon starting from the anyonic vacuum $|0\rangle$, i.e., the state of the toric code with $W_p = +1$ for all p. We assume that the bosons do not have time to adapt to the creation of an anyon and they remain in their initial equilibrium state $\rho_0 = e^{-\beta H_{0,\mathrm{b}}}/Z_0$ with $Z_0 = \mathrm{Tr}(e^{-\beta H_{0,\mathrm{b}}})$ and

$$H_{0,\mathrm{b}} = \langle 0|H|0\rangle = H_\mathrm{b} + A\sum_p (a_p + a_p^\dagger)\,. \tag{4.23}$$

In this case, the chemical potential for an anyon is

$$\Delta E_{0\to 1,\mathrm{fast}} = -2A\langle a_p + a_p^\dagger\rangle_0\,, \tag{4.24}$$

where $\langle O\rangle_0 = \mathrm{Tr}(O\,e^{-\beta H_{0,\mathrm{b}}})/Z_0$. Defining the operator $\mathcal{S}_0 = \langle 0|\mathcal{S}|0\rangle$, we have

$$\begin{aligned}\widetilde{a}_p &= e^{\mathcal{S}_0}a_p e^{-\mathcal{S}_0}\\ &= a_p + \frac{1}{A}\sum_{p'} J_{p,p'}\\ &= a_p - \frac{\mu(L)}{4A} - \frac{|J_{p,p}|}{A}\,. \end{aligned} \tag{4.25}$$

We point out again that $|J_{p,p}|$ is finite, see remarks after Eq. (4.19). We thus have

$$\begin{aligned}\Delta E_{0\to 1,\text{fast}} &= -2A\langle a_p + a_p^\dagger\rangle_0 \\ &= -\frac{2A}{Z_0}\mathrm{Tr}(e^{\mathcal{S}_0}e^{-\beta H_{0,\mathrm{b}}}e^{-\mathcal{S}_0}e^{\mathcal{S}_0}(a_p + a_p^\dagger)e^{-\mathcal{S}_0}) \\ &= -\frac{2A}{Z_0}\mathrm{Tr}(e^{-\beta \widetilde{H}_{0,\mathrm{b}}}(\widetilde{a}_p + \widetilde{a}_p^\dagger)) \\ &= -\frac{2A}{Z_0}\mathrm{Tr}(e^{-\beta \widetilde{H}_{0,\mathrm{b}}}(a_p + a_p^\dagger)) + \mu(L) + 4|J_{p,p}| \\ &= \mu(L) + 4|J_{p,p}| > \mu(L)\,, \end{aligned} \tag{4.26}$$

where we used the fact that $\mathrm{Tr}(e^{-\beta \widetilde{H}_{0,\mathrm{b}}}(a_p + a_p^\dagger)) = 0$ since

$$\widetilde{H}_{0,\mathrm{b}} = e^{\mathcal{S}_0}H_{0,\mathrm{b}}e^{-\mathcal{S}_0} = H_\mathrm{b} + \text{const.} \tag{4.27}$$

From this calculation we conclude that the energy for the fast creation of an anyon also grows linearly with L. In fact, it costs more energy to create an anyon fast rather than slowly; this is expected since the bosons do not have time to relax to the new equilibrium configuration.

As noted in Sec. 4.2, the origin of the favorable behavior (4.26) resides in the long-range interactions mediated by the low-energy, long-wave length excitations of the bosonic bath. Let us assume that all $W_p = +1$. Due to the coupling $A \neq 0$ in Eq. (4.1), the hopping bosons feel the presence of the plaquettes and the bosonic equilibrium state is populated with bosons such that $\langle a_p + a_p^\dagger\rangle_0 \neq 0$. When the size of the toric code increases, more plaquettes are introduced in the system and the population of bosons in the equilibrium state increases, too, i.e., $\langle a_p + a_p^\dagger\rangle_0 \sim L$.

4.3 Coupling to the bosonic density

In this section we want to investigate a slightly different model where the stabilizers are locally coupled to the bosonic density $a_i^\dagger a_i$,

$$H = H_0 + V = H_0 + A\sum_p W_p\, a_p^\dagger a_p\,. \tag{4.28}$$

The main part H_0 is the Hamiltonian of the hopping bosons, i.e., $H_0 = H_\mathrm{b}$ and the perturbation $V = A\sum_p W_p a_p^\dagger a_p$. In Fourier space the perturbative part in Eq. (4.28) reads

$$V = \frac{A}{N} \sum_{p} W_p \sum_{\mathbf{q},\mathbf{q}'} e^{i\mathbf{R}_p \cdot (\mathbf{q}-\mathbf{q}')} a^{\dagger}_{\mathbf{q}} a_{\mathbf{q}'} . \tag{4.29}$$

It is now straightforward to distinguish between the diagonal part V_{d} and the off-diagonal part V_{od} of the perturbation, namely

$$\begin{aligned} V_{\mathrm{d}} &= \frac{A}{N} \sum_{p} W_p \sum_{\mathbf{q}} a^{\dagger}_{\mathbf{q}} a_{\mathbf{q}} \,, && (4.30) \\ V_{\mathrm{od}} &= \frac{A}{N} \sum_{p} W_p \sum_{\mathbf{q}\neq\mathbf{q}'} e^{i\mathbf{R}_p \cdot (\mathbf{q}-\mathbf{q}')} a^{\dagger}_{\mathbf{q}} a_{\mathbf{q}'} \,. && (4.31) \end{aligned}$$

Absorbing V_{d} into the main part of the Hamiltonian, we rewrite

$$H = H_0' + V_{\mathrm{od}} \,, \tag{4.32}$$

with

$$H_0' = \sum_{\mathbf{q}} \epsilon_{\mathbf{q}} n_{\mathbf{q}} + \frac{A}{\Lambda^3} L^2 \sum_{\mathbf{q}} n_{\mathbf{q}} \,, \tag{4.33}$$

where we assumed that the toric code is free of anyons, i.e., $W_p = +1$ for all p, and we used $N = \Lambda^3$.

Performing a second-order Schrieffer-Wolff transformation (see App. 4.A) we obtain the following effective Hamiltonian

$$\begin{aligned} H_{\mathrm{eff}} &= -\frac{i}{2} \lim_{\eta\to 0^+} \int_0^{+\infty} dt\, e^{-\eta t} [V_{\mathrm{od}}(t), V_{\mathrm{od}}] \\ &= \frac{A^2}{2N^2} \sum_{p,p'} W_p W_{p'} \sum_{\mathbf{q}\neq\mathbf{q}',\mathbf{k}\neq\mathbf{k}'} \frac{e^{i\mathbf{R}_p\cdot(\mathbf{q}-\mathbf{q}')+\mathbf{R}_{p'}\cdot(\mathbf{k}-\mathbf{k}')}}{\epsilon_{\mathbf{q}} - \epsilon_{\mathbf{q}'}} \left[a^{\dagger}_{\mathbf{q}} a_{\mathbf{q}'}, a^{\dagger}_{\mathbf{k}} a_{\mathbf{k}'} \right] \\ &= \frac{A^2}{2N^2} \sum_{p,p'} W_p W_{p'} \sum_{\mathbf{q}\neq\mathbf{q}'} \frac{n_{\mathbf{q}} - n_{\mathbf{q}'}}{\epsilon_{\mathbf{q}} - \epsilon_{\mathbf{q}'}} e^{i(\mathbf{q}-\mathbf{q}')\cdot(\mathbf{R}_p - \mathbf{R}_{p'})} \\ &= \frac{A^2}{2N^2} \sum_{p,p'} W_p W_{p'} \sum_{\mathbf{q}',\mathbf{k}} \frac{n_{\mathbf{k}+\mathbf{q}'} - n_{\mathbf{q}'}}{\epsilon_{\mathbf{k}+\mathbf{q}'} - \epsilon_{\mathbf{q}'}} e^{i\mathbf{k}\cdot(\mathbf{R}_p - \mathbf{R}_{p'})} \\ &= -\frac{A^2}{2N^2} \sum_{p,p'} W_p W_{p'} \sum_{\mathbf{q},\mathbf{k}} \frac{e^{\beta(\epsilon_{\mathbf{k}+\mathbf{q}} - \epsilon_{\mathbf{k}})}}{\epsilon_{\mathbf{k}+\mathbf{q}} - \epsilon_{\mathbf{k}}} n_{\mathbf{k}+\mathbf{q}} (n_{\mathbf{k}} + 1) e^{i\mathbf{q}\cdot(\mathbf{R}_p - \mathbf{R}_{p'})} \\ &= -\frac{A^2}{2N} \sum_{p,p'} W_p W_{p'} \sum_{\mathbf{q}} \chi(\mathbf{q}) e^{i\mathbf{q}\cdot(\mathbf{R}_p - \mathbf{R}_{p'})} , \end{aligned} \tag{4.34}$$

where we introduced the static 'susceptibility' of the bosons

$$\chi(\mathbf{q}) = \frac{1}{N}\sum_{\mathbf{k}} \frac{e^{\beta(\epsilon_{\mathbf{k}+\mathbf{q}}-\epsilon_{\mathbf{k}})}}{\epsilon_{\mathbf{k}+\mathbf{q}}-\epsilon_{\mathbf{k}}} n_{\mathbf{k}+\mathbf{q}}(n_{\mathbf{k}}+1). \tag{4.35}$$

Following the approach of Ref. [105] assuming that

$$\beta\epsilon_{\mathbf{q}+\mathbf{k}}, \beta\epsilon_{\mathbf{q}}, \beta(\epsilon_{\mathbf{k}+\mathbf{q}}-\epsilon_{\mathbf{k}}) \ll 1\,, \tag{4.36}$$

we have that

$$\chi(\mathbf{q}) = \frac{T}{8t^2}\frac{1}{|\mathbf{q}|} \quad \text{for} \quad |\mathbf{q}| \to 0\,. \tag{4.37}$$

The effective Hamiltonian then becomes

$$\begin{aligned} H_{\text{eff}} &= -\frac{A^2T}{16t^2}\sum_{p,p'} W_p W_{p'} \frac{1}{N}\sum_{\mathbf{q}} \frac{1}{|\mathbf{q}|} e^{i\mathbf{q}\cdot(\mathbf{R}_p-\mathbf{R}_{p'})} \\ &= -\frac{A^2T}{16t^2}\sum_{p,p'} W_p W_{p'} \frac{1}{(2\pi)^3}\int d\mathbf{q}\frac{1}{|\mathbf{q}|} e^{i\mathbf{q}\cdot(\mathbf{R}_p-\mathbf{R}_{p'})} \\ &= -\frac{A^2T}{32\pi^2t^2}\sum_{p,p'} W_p W_{p'} \frac{1}{|\mathbf{R}_p-\mathbf{R}_{p'}|^2}\,. \end{aligned} \tag{4.38}$$

The interaction strength between the stabilizers mediated by the bosons decays now with the square of the inverse distance ($1/R^2$) rather than with the inverse distance ($1/R$), as in the previous section. Furthermore, the coupling strength is proportional to temperature.

The Schrieffer-Wolff transformation we performed is nothing but a unitary transformation $e^{-\mathcal{S}}$ (similar to the polaron transformation) up to second order in the small parameter A/t. Therefore, the same line of reasoning as in Sec. 4.2 applies and the energetics of the anyons is fully described by H_{eff}. In other words, the energy difference ΔE between two states $|\alpha\rangle\langle\alpha| \otimes \rho_\alpha$ and $|\gamma\rangle\langle\gamma| \otimes \rho_\gamma$ is

$$\Delta E \approx \text{Tr}(H_{\text{eff}}|\alpha\rangle\langle\alpha|) - \text{Tr}(H_{\text{eff}}|\gamma\rangle\langle\gamma|)\,, \tag{4.39}$$

where the sign $\approx$ means that the effective Hamiltonian is calculated up to second order only.

From Eq. (4.38), we finally find a chemical potential for the anyons that grows now logarithmically with L,

$$\mu(L) \sim \frac{A^2T}{t^2}\ln(L/2)\,, \tag{4.40}$$

where we used

$$\int_{D_{L/2}} d^2R\,\frac{1}{R^2} \sim \ln(L/2)\,. \tag{4.41}$$

4.4 Thermally Stable Quantum Memory

As we have demonstrated in the previous sections, coupling the toric code stabilizers to a 3D bath of hopping bosons has a very beneficial effect: the energy penalty to create an anyon grows with L if we couple to the bosonic displacement operator and with $\ln(L)$ if we couple to the bosonic density. Here we show that a toric code with an anyon chemical potential growing linearly or logarithmically with L has respectively a lifetime growing exponentially or polynomially with L. The physical picture behind this is that it takes longer and longer for the anyons to reach their thermodynamic equilibrium state with increasing values of L [38,40,81,104].

Anyon chemical potential linear in L

A chemical potential for anyons in the toric code that grows linearly with L leads to a quantum information storage time that grows exponentially with L and β, where $\beta = 1/T$ is the inverse temperature of a bath weakly coupled to the memory. This follows from Sec. 8 in Ref. [104]. Assuming that the interaction with the thermal bath can be described by the Davies equation and that the thermal state is a fixed point of the Lindblad operators, the authors of [104] proved that the lifetime of the memory τ scales as $\tau = O(e^{\beta\mu}/L^2)$, where μ is the anyons' chemical potential. Here, we present alternative arguments leading to the same conclusion: when the anyons' chemical potential is $\mu(L)$, the lifetime of the toric code is at least $\tau = O(e^{\beta\mu(L)}/L^2)$. In Sec. 4.4 we will show that if $\mu(L)$ grows slow enough, this lower bound is no longer tight and the actual lifetime-scaling is more favorable.

Let us try to understand in more detail the decoherence process of the memory in contact with a simple model of a bath. We assume that the bath supports single-spin processes in which an energy ω is transfered from the anyon system to the bath with rate $\gamma(\omega)$ and that $\gamma(0) \neq 0$.[2] Let

---

[2] If we had $\gamma(0) = 0$, as is the case for super-Ohmic baths, this would of course have a greatly beneficial influence on the memory lifetime as it forbids direct hopping processes of anyons. See [38] for more details about the decoherence of quantum memories

$\delta(N)$ denote the average cost to create an anyon pair if there are already N pairs present. The gravitational interaction will lead to $\delta(N \geq 1) < \delta(0) = 2\mu(L) - A^2/(4\pi t)$. However, below we show that this reduction will not lead to a finite self-consistent number of anyon pairs and that in fact we will have $\delta(N \geq 1) \approx \delta(0)$ in the relevant regime.

Since the presence of only two anyons diffusing across the memory leads to an uncorrectable logical error in times of order $L^2/\gamma(0)$ [38], we need to show that the time for the creation of two nearby anyons that are not directly annihilated increases exponentially with system size. Whenever a new pair of anyons is created, their total hopping rate is given by $6\gamma(0)$ [3] such that the probability that one of the two anyons ever moves before the pair gets annihilated is $6\gamma(0)/[\gamma(\delta(0)) + 6\gamma(0)]$. Since $\gamma(\delta(0)) = \exp(\beta\delta(0))\gamma(-\delta(0))$ (which follows from the detailed balance condition) and the code consists of L^2 physical spins, we conclude that the total rate for creation of anyon pairs that do not directly get annihilated is given by

$$L^2\gamma(-\delta(0))\frac{6\gamma(0)}{\gamma(\delta(0)) + 6\gamma(0)} \leq 6L^2 e^{-\beta\delta(0)}\gamma(0) \,. \tag{4.42}$$

The time needed to create such a pair is thus of order $\exp(\beta\delta(0))/L^2\gamma(0)$. In conclusion, we found a lower bound for the quantum memory storage time that increases exponentially with $\delta(0)$. Since $\delta(0)$ is linear in L, the lifetime increases exponentially with L.

Assume that there are already N anyon *pairs* present. We want to determine the average (averaged over all possible positions of the existing anyons) energy cost $\delta(N)$ to create a new pair. From the point of view of one of the two newly created anyons, we assume that the existing $2N$ anyons are uniformly distributed over all L^2-2 remaining positions. The averaged interaction between one of the newly created anyons and each existing one is thus

$$\frac{1}{L^2-2}\left(4\sum_{p\neq 0}|J_{p,0}| + A^2/(4\pi t)\right) = -\frac{1}{L^2-2}\left(2\mu(L) - A^2/(4\pi t)\right) \,, \tag{4.43}$$

where we have subtracted the energy $-A^2/(4\pi t)$ due to attraction with the other anyon of the same pair. Indeed, we are only interested in the

---

under the influence of super-Ohmic baths.

[3] Strictly speaking, the energy cost for hopping is greater than zero since it increases the potential energy in the gravitational potential. However, we approximate this energy cost by zero for simplicity, neglecting the beneficial effect of the anyon attraction and obtaining a lower bound on the actual lifetime.

attraction energy due to anyons which are already present before the creation of the pair. The total energy $\delta(N)$ to create the new pair is thus given by

$$\begin{aligned} \delta(N) &= \delta(0) - \frac{4N}{L^2-2}\left(2\mu(L) - A^2/(4\pi t)\right) \\ &= \delta(0)\left(1 - \frac{4N}{L^2-2}\right) , \end{aligned} \tag{4.44}$$

where $\delta(0) = 2\mu(L) - A^2/(4\pi t)$.

The mean-field energy of N anyon pairs is thus

$$E_{\mathrm{mf}}(N) = \sum_{i=0}^{N-1} \delta(i) = \delta(0) N \frac{L^2 - 2N}{L^2-2} . \tag{4.45}$$

The symmetry $N \leftrightarrow L^2/2 - N$ is reminiscent of the fact that the energy of H_W in Eq. (4.3) can be minimized by either all stabilizers having a $+1$ eigenvalue (no anyons present) or a -1 eigenvalue (memory full of anyons). The energetic gap between the sector in which there are almost no anyons and the sector in which the memory is full of anyons is of order $\delta(0)L^2 = O(L^3)$, so transitions between these two sectors happen on time-scales much longer than the time before the stored quantum information is lost. Consequently, each sector may serve as a thermally stable quantum memory, but at each moment in time we can only use one of the two. Without loss of generality, we consider the case where the sector with (almost) no anyons present is used for quantum information storage.

From Eq. (4.44) we have that $\delta(N) = \delta(0)(1 - 2n)$, where n denotes the density of anyons. As there can only be zero or one anyon at each position, we obtain the self-consistent equation for the mean-field anyon density *in equilibrium*

$$n_{\mathrm{mf}} = \left[\exp\left(\beta\delta(0)(1 - 2n_{\mathrm{mf}})\right) + 1\right]^{-1} . \tag{4.46}$$

If the left-hand side of this equation is smaller/larger than the right-hand side, the anyon density will tend to increase/decrease. If n_{mf} solves this equation, so does $1 - n_{\mathrm{mf}}$. One self-consistent density is $n_{\mathrm{mf}} = \frac{1}{2}$. The stability of this density depends on the temperature of the bath. For $\beta\delta(0) < 2$ we have a unique self-consistent density $n_{\mathrm{mf}} = \frac{1}{2}$ and this density is also stable. For $\beta\delta(0) > 2$ the density $\frac{1}{2}$ becomes unstable and two new stable self-consistent densities n^* and $1 - n^*$ emerge (let n^* denote the smaller of the two). The system of gravitationally interacting anyons therefore shows a phase transition and spontaneous breaking of the anyon anyon-hole symmetry at a critical temperature $\delta(0)/2$, which is of order $\frac{A^2}{t}L$. For the purpose of quantum information storage, we are clearly interested in temperatures below this critical temperature.

Adding the usual toric code Hamiltonian [16] $H_{\text{toric}} = -\frac{\Delta}{2}\sum_p W_p$ to Eq. (4.1) explicitly breaks the symmetry between anyons and anyon holes and will lead to an additional summand $2N\Delta$ in Eq. (4.45). However, the modification of the self-consistent densities n^*, $1 - n^*$, and $\frac{1}{2}$ through this new term becomes vanishing for large L, as Δ does unlike $\delta(0)$ not grow with L.

Let us consider the self-consistent solution n^*. We want to show that n^* is exponentially suppressed with L and consequently that the number of anyons itself goes to zero in the thermodynamic limit. After straightforward algebra, one can show that $n = 2e^{-\beta\delta(0)} < 1/2$ with $\beta\delta(0)e^{-\beta\delta(0)} < \frac{\log(2)}{4}$ (note that this condition is readily satisfied since $\delta(0)$ grows linearly with L) satisfies

$$[\exp(\beta\delta(0)(1-2n)) + 1]^{-1} < n \, , \tag{4.47}$$

and therefore $n > n^*$. Since n is by definition exponentially suppressed with L and $n^* < n$ we finally conclude that the self-consistent solution n^* of Eq. (4.46) goes exponentially to zero with L. A direct consequence of this is that the equilibrium number of anyons n^*L^2 also vanishes exponentially with L and will generally be much smaller than the minimal positive value 2. Hence the anyon number will fluctuate between 0 and small even integers, such that $\delta(N) \approx \delta(0)$ from Eq. (4.44).

Anyon chemical potential logarithmic in L

Here we show that a chemical potential growing logarithmically with L leads to a lifetime of the memory growing polynomially with L.

By the same line of reasoning as in Sec. 4.4, modifications to the anyon chemical potential due to inter-anyonic interactions are negligible. Let us thus study a simple model in which anyons have a constant energy cost μ independent of the number of anyons which are already present. Ref. [104] predicts in this scenario a lifetime that scales at least with

$\exp(2\beta\mu)/L^2$.[4] Employing the same simple bath model as in the previous paragraph, let us probe the tightness of this bound. As remarked in Sec. 4.4, it takes a time of order $t_1 = \exp(2\beta\mu)/(L^2\gamma(0))$ to create an anyon pair that does not immediately annihilate but performs at least one hopping. One such separating pair creates an uncorrectable logical error in times of order $\sim L^2/\gamma(0)$. We ignore here dimensionless $O(1)$ factors which depend on the precise definition of the memory lifetime and on the classical algorithm employed to perform error correction. Thus if we are in the regime $\mu > 2T \ln L$, the quantum information will get destroyed by the first separating pair, which takes a time of order t_1 such that the bound in Ref. [104] is tight.

However, consider now the opposite regime $\mu < 2T \ln L$. In this regime, further anyons will be created before the two anyons of the first separating pair have time to diffuse across a distance of order L. The lifetime of the memory is then given by the time it takes the anyons to diffuse across the average inter-pair distance, which is when error correction will inevitably break down. After a time t, the density of anyons will be of order $t/(t_1L^2) = \gamma(0)t \times \exp(-2\beta\mu)$, taking the possibility for immediate annihilation into account, and existing anyons will have diffused across a distance $\sim \sqrt{\gamma(0)t}$, as the diffusion constant for anyons is essentially given by $\gamma(0)$ [38]. Consequently, after a time $\sim \exp(\beta\mu)/\gamma(0)$ existing anyons will have diffused across the current inter-pair distance, which thus constitutes the lifetime of the memory. Notably, in this case the bound from Ref. [104] is no longer tight, as $\exp(\beta\mu) > \exp(2\beta\mu)/L^2$ in the assumed regime.

To summarize, if anyons can be created at a constant energy cost μ and the quantum memory is in contact with a bath that supports processes which have an energy cost ω with a rate $\gamma(-\omega)$ and fulfills the detailed balance condition, error correction will break down after a time of order

$$\begin{aligned} &\left.\begin{array}{cc} \exp(2\beta\mu)/L^2\gamma(0), & \text{if } \mu \geq 2T\ln L \\ \exp(\beta\mu)/\gamma(0), & \text{if } \mu \leq 2T\ln L \end{array}\right\} \\ = \quad &\max\left\{\exp(2\beta\mu)/L^2, \exp(\beta\mu)\right\}/\gamma(0). \qquad (4.48) \end{aligned}$$

Now let us assume that $\mu = \mu(L) = cT \ln L$, which is what we have obtained in Sec. 4.3 when coupling the stabilizers to the boson density.

---

[4] The factor 2 in the exponent is due to the fact that anyons can only be created in pairs in a toric code whose boundary conditions are (as its name suggests) periodic. With open boundaries [81], unpaired anyons can be created such that the factor 2 drops out.

Then we obtain a lifetime scaling as $\max\left\{L^{2c-2}, L^{c}\right\}/\gamma(0)$, i.e., polynomially growing for any $c > 0$ with a change in the scaling behavior, depending on whether c is greater or smaller than 2. However, recall that in our case $c \sim A^2/t^2 \ll 1$, such that the lifetime grows only modestly with L.

We note that for bath models as employed in Refs. [38,40,81], we have $\gamma(0) \propto T$, so our estimate for the lifetime contains an implicit temperature-dependence, even though the explicit temperature dependence stemming from the Boltzmann factor drops out.

4.5 Hindering of anyon hopping

The lifetime of the memory that we discussed above does not apply if the initial state of the system has anyons already present. Suppose that errors occur during preparation of the initial state, creating a finite density of anyons. If these errors are sufficiently sparse, it will be possible for error correction to recover the initial state. It is the job of the Hamiltonian to preserve this error correctability until the desired time of readout. The coupling of the quantum memory to the hopping bosons will energetically favour the annihilation of anyons on neighboring plaquettes, undoing some of the errors. However, we can expect that a finite density of pairs will have been non-neighbouring, and so will remain. These only need to diffuse a constant distance to make correction ambiguous, which leads to a constant lifetime for the memory. To prevent this we can split the plaquettes into two types. ‘Strongly coupled’ plaquettes are coupled to the hopping bosons with a strength A_s. ‘Weakly coupled’ plaquettes have a strength $A_w < A_s$. These are chosen such that any sequence of single- or local two-spin errors that move an anyon from one weakly coupled plaquette to another must move it via a strongly coupled plaquette. Example patterns are given below. The chemical potential for the plaquettes will change from the form in Eq. (4.12), giving different values $\mu_s(L)$ and $\mu_w(L)$ for the two types of plaquette. Performing the summation (as described in the following subsection) shows that the factor A^2 in Eq. (4.12) becomes $A_s\bar{A}$ for $\mu_s(L)$ and $A_w\bar{A}$ for $\mu_w(L)$ ($\bar{A}$ being a weighted average of A_s and A_w). The energy barrier required for anyon movement is therefore of order $(1 - A_w/A_s)\mu_s(L)$, which increases linearly with system size. The resulting suppression of diffusion leads to a lifetime that increases exponentially with system size, even when the initial state has a finite density of anyons.

It may come as a surprise that associating some stabilizers with a

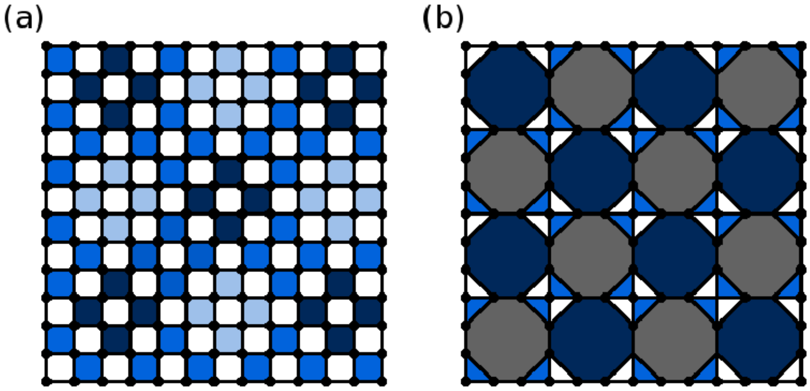

Figure 4.2: Two tilings of plaquettes are shown on which the code may be defined. Spins are located on vertices. (a) The square tiling, as usually employed for the toric code. s-plaquettes are shown in dark blue (black), blue (grey), or light blue (light grey), p-plaquettes are shown in white. (b) An alternative tiling, with alternating triangular and octagonal plaquettes. s-plaquettes are shown in dark blue (black) and blue (grey), p-plaquettes are shown in white and grey (light grey).

lower energy penalty has a beneficial effect on the memory. However, note that the weakly coupled plaquettes allow energy to be dissipated from the anyons to the bath by hopping of an anyon from a strongly to a weakly coupled plaquette. On the other hand, if the chemical potential is independent of the anyon position, as in Eq. 4.12, this is only possible through annihilation of anyons.

An example pattern for strongly and weakly coupled plaquettes

We will now look at the concepts proposed above in greater detail and find specific examples for patterns of strongly and weakly coupled plaquettes.

In the toric code model there are two types of anyon, e and m, which reside on two kinds of plaquette, s and p, respectively. Note that, when the code is defined with spins on the edges of the lattices, these correspond to the stars and plaquettes, respectively.

Consider a spin in the square tiling of Fig. 4.2 (a), shared by two s-plaquettes to the top-left and bottom-right and two p-plaquettes to the top-right and bottom-left. The application of a Pauli I^z to such a spin will affect the e anyon occupations of the two s-plaquettes. If both were initially empty, an anyon pair will be created. If both initially held an anyon, this pair will be annihilated. If only one held an anyon, it will be moved to the other plaquette. The application of a Pauli I^y has the same effect for the m anyons of the p-plaquettes. For spins where the positions of s- and p-plaquettes are exchanged, the roles of I^z and I^y are also exchanged. No operation exists that can move an anyon from an s-plaquette to a p-plaquette, or vice-versa.

Creation, movement and annilation of anyons are therefore achieved by Pauli operations. Using single spin operations, creation of a pair will always lead to the anyons occupying neighboring plaquettes (where neighoring means that they share exactly one spin). Similarly, single spin operations can only move anyons from one plaquette to a neigboring one, or annihilate anyons on neighboring plaquettes. Since we assume that the system-bath coupling supports only single spin errors, it is exactly these processes that we consider during thermalization. However, it should be remembered that two-spin perturbations may also be present in the Hamiltonian. Local two-spin errors should therefore also be considered, which can create, annihilate and transport anyons on next-to-neighboring plaquettes.

With this in mind, we wish to split both s- and p-plaquettes into two groups, one of which will be strongly to the hopping bosons with a coupling A_s and the other of which will be weakly coupled with a strength $A_w < A_s$. This will give the plaquettes of the former a higher chemical potential than those of the latter, with an energy difference that increases linearly with system size.

The pattern of strongly and weakly coupled plaquettes should be chosen such that anyons become trapped within the latter, which will occur if two conditions are satisfied. Firstly, any anyons initially on strongly coupled plaquettes should quickly move into a nearby weakly coupled plaquette. Secondly, it should not be possible for anyons to be moved from one weakly coupled plaquette (or a small cluster of weakly coupled plaquettes) to another by a sequence of either single- or two-spin operations without passing through a strongly coupled plaquette.

The first condition can be met if anyons on strongly coupled plaquettes cannot be moved over large distances by a sequence of either single or two spin operations without either moving through a weakly coupled plaquette, or through a strongly coupled plaquette that neigbors a weakly coupled one. The latter is relevant because it will ensure that the distance an anyon can move before decaying into a weakly coupled plaquette is exponentially suppressed.

Both conditions are satisfied by the pattern shown in Fig. 4.2 (a). Here, weakly coupled s-plaquettes are shown in dark blue. Strongly coupled s-plaquettes that neighbor weakly coupled s-plaquettes are shown in blue, and those that do not are shown in light blue. Regions of strongly coupled plaquettes that do not neighbor weakly coupled plaquettes are separated from each other by a width of three spins. Sequences of one- and two-spin operations therefore cannot move anyons in one such region to another without going via strongly coupled plaquettes that do neighbor weakly coupled plaquettes, which will almost certainly result in the anyon decaying into the neighboring weakly coupled plaquettes. Similarly, regions of weakly coupled plaquettes are separated by the same width, preventing movement between them without going via strongly coupled plaquettes.

The initial movement of anyons on strongly coupled plaquettes to nearby weakly coupled plaquettes may cause ambiguity for error correction if the error rate during initialization is too high. Even so, for sufficiently low error rates this movement will have no effect on correctability. Once the movement is complete, the exponential suppression of diffusion will then ensure that the correctability of the errors is preserved for a time exponential with the system size, since such an exponentially long timescale will be required for the anyons to climb out of the weakly coupled plaquettes.

We will now demonstrate that the difference in chemical potentials between strongly and weakly coupled plaquettes leads to the energy barrier required to suppress diffusion. To determine the chemical potential of an arbitrary plaquette p (which is either s- or p-type), the following sum over all plaquettes must be performed

$$\mu_p(L) = \frac{M^2}{2\pi R} A_p \sum_{p'}{}' A_{p'} \frac{1}{|p - p'|} \ , \tag{4.49}$$

where the prime in $\sum'$ means that $p' \neq p$. Here $A_{p'}$ denotes the coupling of plaquette p' which will be A_s or A_w depending on whether this plaquette is weakly or strongly coupled, respectively. By numerically performing the summation we find that, in the $L \to \infty$ limit, it takes the form

$$\sum_{p'}{}' A_{p'} \frac{1}{|\mathbf{R}_p - \mathbf{R}_{p'}|} = \frac{3A_s + A_w}{4} cL \ , \tag{4.50}$$

where $c = 4\ln(1+\sqrt{2}) \simeq 3.53$ is defined via

$$\int_{[-L/2,L/2]^2} \frac{dxdy}{\sqrt{x^2+y^2}} = cL\,. \tag{4.51}$$

The linear combination of A_s and A_w is a weighted average $\bar{A} = (3A_s + A_w)/4$, which arises from the fact that there are three times as many strongly coupled plaquettes as weakly coupled plaquettes. The chemical potentials for weakly and strongly coupled plaquettes are then

$$\mu_s(L) = \frac{cA_s\bar{A}M^2}{2\pi R}\cdot L\,, \quad \mu_w(L) = \frac{cA_w\bar{A}M^2}{2\pi R}\cdot L\,. \tag{4.52}$$

Clearly, $\mu_s(L) - \mu_w(L) = O(L)$, giving the required energy barrier.

Alternative tiling with four-body coupling

A pattern of strongly and weakly coupled plaquettes, stable against single-spin errors, is shown for an alternative tiling in Fig. 4.2 (b). Strongly (weakly) coupled s-plaquettes are shown in blue (dark blue) and strongly (weakly) coupled p-plaquettes are shown in white (grey). For this tiling it is still true that e anyons can only be created and moved between neighboring s-plaquettes, and m anyons between neighboring p-plaquettes. Note that all strongly coupled plaquettes in this tiling are triangular. The W_p for these will therefore be three-body operators, making the code-hopping boson coupling only a four-body term. On the other hand, weakly coupled plaquettes are octagons with eight-body W_p and nine-body terms required for the code-hopping boson coupling. Since these many-body terms will most likely be generated by perturbative methods, with a higher number of spins in a term generated by higher orders of perturbation theory, the difference in coupling strengths will arise naturally.

Due to the practical difficultly in generating many-body terms, we can consider not coupling the octagonal plaquettes to the hopping bosons. Only the four-body terms required to couple the triangles are then needed, which should be easier to implement than the five-body terms required for the square tiling. Despite the fact that only a fraction of the plaquettes are coupled to hopping bosons, the memory is still stable against thermal errors. This is because any single spin error must still create at least one anyon on, or move anyons through, energetically penalized triangular plaquettes. The energy barrier that increases linearly with system size is therefore still intact, and ensures that anyon creation and diffusion are exponentially suppressed.

Unfortunately, stability against local Hamiltonian perturbations does not remain strong without the coupling of octagons. Without an energy penalty, two-body perturbations are free to create and move anyons between next-to-neighboring octagonal plaquettes. This avoids the energy barrier and so leads to uncorrectable errors in a constant time. However, it is possible to avoid this by carefully considering what types of perturbation are present, and then designing the W_p such that they are unable to perform such hopping processes. For example, let us use $W_p = I^x_{p,1} I^y_{p,2} I^z_{p,3}$ for triangular s-plaquettes. Here spin 1 is that shared with the neighboring triangular s-plaquette and the numbering proceeds clockwise. Let us also use $W_p = I^z_{p,1} I^y_{p,2} I^x_{p,3}$ for triangular p-plaquettes with corresponding numbering. No nearest neighbor isotropic perturbation of the form $I^\alpha_i I^\alpha_j$, for $\alpha \in \{x, y, z\}$, commutes with all of these operators. This means such perturbations will be suppressed by the energy barrier and will not be able to move anyons between octagonal plaquettes. If only perturbations of this form are present in the system, the memory will remain stable.

4.6 Ferromagnet as bosonic bath

In this section, we would like to point out a physical system where bosonic modes (as discussed in the previous sections) naturally occur as a lowest order approximation. Indeed, the Hamiltonians (4.1) and (4.28) are closely related to the Hamiltonians describing a toric code embedded in a 3D Heisenberg ferromagnet (FM) in a broken-symmetry state at finite temperature. More explicitly, let us consider the following Hamiltonian

$$H' = H_F + A\sqrt{2/S} \sum_p W_p S^x_p \,, \tag{4.53}$$

where

$$H_{\mathrm{F}} = -J \sum_{\langle i,j \rangle} \mathbf{S}_i \cdot \mathbf{S}_j + h_z \sum_i S^z_i \tag{4.54}$$

is the Hamiltonian of a 3D Heisenberg ferromagnet (FM) of linear size $\Lambda \gg L$, where $J > 0$ is the exchange coupling constant and the sum is restricted to nearest-neighbor lattice sites. The FM is assumed to be below the Curie temperature and the spins ordered along the z-direction.

We can now perform a Holstein-Primakoff transformation [102]

$$S_i^z = -S + \hat{n}_i\,, \quad S_i^- = a_i^\dagger \sqrt{2S - \hat{n}_i}\,, \quad S_i^+ = (S_i^-)^\dagger, \tag{4.55}$$

in the formal limit $\hat{n}_i \ll 2S$, where $\hat{n}_i = a_i^\dagger a_i$ [102]. It is then straightforward to show that the low-energy sector of Hamiltonian (4.53) is equivalent to Hamiltonian (4.1). Following the same reasoning, we conclude that the Hamiltonian

$$H'' = H_F + A \sum_p W_p S_p^z \tag{4.56}$$

is in its low-energy sector equivalent to Hamiltonian (4.28).

However, since all operators in Hamiltonians H' and H'' are bounded, it is clear that the energy penalty for flipping a toric code spin very fast cannot grow without bounds as a function of L.[5] Still, it seems reasonable to expect that for adiabatic noise sources, that drag the FM along while flipping a spin, the response of the FM resembles the one of the bosonic bath studied in this work, since the stabilizers are coupled via the susceptibility of the FM. It is thus reasonable to assume that the toric code might be protected against such adiabatic noise sources when embedded in the FM. Note that the question of how to engineer five-spin interactions, as required for Hamiltonians H' and H'', remains open.

4.7 Conclusions and discussion

In this paper we have introduced a 3D-model with purely local, bounded-strength interactions in three dimensions that is self-correcting at finite temperatures. Our model is exactly solvable and consists of a toric code locally coupled to a system of hopping bosons on a cubic lattice. The stabilizer operators are locally coupled to the displacement operator of the bosons and a long-range attractive interaction between stabilizer operators is mediated by the low-energy collective excitations of the bosonic system. This leads to a chemical potential for the anyons growing linearly with L and can be used to stabilize the quantum memory against thermal fluctuations. For a given error model, a chemical potential of the anyons that grows linearly with L leads to a lifetime of the quantum memory increasing exponentially with L. When the stabilizers are coupled to the bosonic density, a chemical potential growing only with $\ln L$

---

[5] D. Poulin, private communication.

is derived. We show that such a chemical potential is enough to stabilize the memory whose lifetime increases polynomially with L.

If the degeneracy of the highly entangled states which form the code subspace is not robust against local perturbations, uncontrolled splitting of this degeneracy induced by local imperfections would lead to dephasing of the logical qubit. It was already argued in Ref. [16] and rigorously proved in Ref. [19] that for the standard toric code Hamiltonian [16], perturbations which are weak enough (compared with the anyon creation gap), time-independent, and local (or exponentially decaying) lead to a lifting of the groundstate degeneracy that is exponentially small in L. Since our Hamiltonian is not gapped and involves unbounded operators, the result of Ref. [19] do not apply. While we consider a rigorous treatment of this issue to be beyond the scope of the present work, which focuses on stability against thermal errors rather than perturbations, we briefly present arguments suggesting that robustness to local perturbations is valid in our model.

As pointed out in Ref. [106], in any real solid the degrees of freedom that do not directly constitute the "memory" (spins of the toric code) represent a gapless environment to which the memory couples. This situation is not addressed by studies of perturbations which act entirely within the Hilbert space of the memory, as is the case in Ref. [19]. The issue of accidental couplings to gapless modes is therefore by no means unique to our quantum memory proposal and will be present in any physical implementation of a quantum memory. In Ref. [106] the authors discuss topological phases coupled to a gapless environment, and find that in some cases ("strong quasi-topological phases") the topological properties, including the exponentially suppressed groundstate splitting, survive this coupling. Such strong quasi-topological phases, including the toric code coupled to a gapless environment (such as accoustic phonons or photons), thus constitute the strongest form of a quantum memory one could hope for in nature – except for the fact that they are not thermally stable. Our memory *is* thermally stable and in the following we present heuristic arguments that in our system couplings to the gapless modes may not pose a threat to the topological order either.

Recall that engineered couplings of strength A (see Hamiltonian (4.1)) between the stabilizer operators and the bosonic modes lead to an anyon creation gap of the order $O(\frac{A^2}{t}L)$. Now consider accidental couplings of the form $\varepsilon I_i^x(a_i + a_i^\dagger)$, where I_i^x is a bit-flip that acts on a physical qubit of the toric code. In second-order perturbation theory, the coupling to the bosonic field leads to terms of the form $\frac{\varepsilon A}{t}\sum_{i\neq j} I_i^x W_j/|\mathbf{R}_i - \mathbf{R}_j|$ and $\frac{\varepsilon^2}{t}\sum_{i\neq j} I_i^x I_j^x/|\mathbf{R}_i - \mathbf{R}_j|$. Summing over all plaquettes the former terms take the form $O(\frac{\varepsilon A}{t}L)I_i^x$; the condition that these perturbations are sufficiently weak compared to the anyon creation gap simply translates into the requirement that ε is sufficiently small compared to A, i.e., that the accidental couplings are sufficiently weak compared to the engineered ones. The second-order terms describing interactions between bit-flips are weaker and will have support only on two small regions, which for most pairs i and j are well-separated. This does not allow anyons to hop non-locally, as would be required to distinguish the ground states. Despite their non-local form, these perturbations are therefore still similar in effect to local perturbations. We thus believe that our Hamiltonian is robust against this type of perturbations and splitting of the ground-state degeneracy is well-suppressed with L. However, a rigorous proof remains a very interesting open question.

4.8 Acknowledgements

We would like to thank D. Poulin for helpful discussions, and L. Trifunovic for pointing out the connection to the independent boson model. This work was supported by the Swiss NSF, NCCR Nanoscience, and NCCR QSIT.

4.A Schrieffer-Wolff transformation

For the sake of completeness, we present in this appendix the derivation of the second order Schrieffer-Wolff transformation (for a general discussion see [95]). We start from

$$H = H_0 + V\,, \tag{4.57}$$

where we identify H_0 as the main part and V as a small perturbation. We decompose the spectrum $\sigma(H_0)$ of H_0 into a high-energy set of eigenvalues M_Q and a low-energy set of eigenvalues M_P such that $\sigma(H_0) = M_P \cup M_Q$, $M_P \cap M_Q = \emptyset$, and there is a gap separating the eigenvalues in M_P and M_Q. We define the operators P and $Q = 1 - P$ respectively as the projectors onto the low energy subspace $\mathcal{M}_P$ and onto the high-energy subspace $\mathcal{M}_Q$ corresponding to set of eigenvalues M_P and M_Q.

The perturbation V can then be decomposed into a diagonal part $V_{\rm d}$ and an off-diagonal part $V_{\rm od}$

$$\begin{aligned} V_{\rm d} &= PVP + QVQ\,, && (4.58)\\ V_{\rm od} &= PVQ + QVP\,. && (4.59)\end{aligned}$$

The effective Hamiltonian is given by a Schrieffer-Wolff transformation such that the transformed Hamiltonian $H_{\rm eff} = e^{S}He^{-S}$ is block-diagonal, i.e., $PH_{\rm eff}Q = QH_{\rm eff}P = 0$. Up to second order in V the effective Hamiltonian reads [95, 101]

$$H_{\rm eff}^{(2)} = H_0 + V_{\rm d} + U = H_0' + U\,, \tag{4.60}$$

where we define $H_0' = H_0 + V_{\rm d}$ and

$$U = -\frac{i}{2}\lim_{\eta\to 0^+}\int_0^\infty {\rm d}t\, e^{-\eta t}\left[V_{\rm od}(t), V_{\rm od}\right]\,, \tag{4.61}$$

where $V_{\rm od}(t) = e^{iH_0't}V_{\rm od}e^{-iH_0't}$ is given in the Heisenberg representation.

4.B Standard deviation and higher moments of the distribution of energy costs

Let us now calculate the standard deviation of the distribution of the energy costs to create an anyon. For simplicity, we consider the case of fast changes, where all relevant thermal expectation values are given by $\langle\ldots\rangle_0$, which denotes thermal averages with respect to the original thermal state of the bosons.

The standard deviation is given by

$$\sigma_{\rm fast} = \sqrt{\langle(2A(a_p + a_p^\dagger))^2\rangle_0 - \langle 2A(a_p + a_p^\dagger)\rangle_0^2}\,. \tag{4.62}$$

We first consider

$$\begin{aligned}\langle(2A(a_p + a_p^\dagger))^2\rangle_0 &= \frac{4A^2}{Z_0}{\rm Tr}(e^{-\beta H_{0,\rm b}}(a_p + a_p^\dagger)^2)\\ &= \frac{4A^2}{Z_0}{\rm Tr}(e^{-S}e^{-\beta\widetilde{H}_{0,\rm b}}(\widetilde{a}_p^2 + (\widetilde{a}_p^\dagger)^2 + 1 + 2\widetilde{a}_p^\dagger\widetilde{a}_p)e^{S})\,.\end{aligned} \tag{4.63}$$

We have

$$\begin{aligned} \widetilde{a}_p^2 &= a_p^2 - 2\frac{\mu(L)+4|J_{pp}|}{4A}a_p + ((\mu(L)+4|J_{p,p}|)/4A)^2 \\ (\widetilde{a}_p^\dagger)^2 &= (a_p^\dagger)^2 - 2\frac{\mu(L)+4|J_{p,p}|}{4A}a_p^\dagger + ((\mu(L)+4|J_{p,p}|)/4A)^2 \\ \widetilde{a}_p^\dagger\widetilde{a}_p &= a_p^\dagger a_p - \frac{\mu(L)+4|J_{p,p}|}{4A}(a_p+a_p^\dagger) + ((\mu(L)+4|J_{p,p}|)/4A)^2 \end{aligned} \tag{4.64}$$

By inserting (4.64) into (4.63), and using the fact that

$$\mathrm{Tr}(e^{-S}e^{-\beta\widetilde{H}_0}a_pe^S) = \mathrm{Tr}(e^{-S}e^{-\beta\widetilde{H}_0}a_p^\dagger e^S) = 0\,, \tag{4.65}$$

we obtain

$$\langle(2A(a_p+a_p^\dagger))^2\rangle_0 = (\mu(L)+4|J_{p,p}|)^2 + 4A^2 + 8A^2\frac{\mathrm{tr}(e^{-\beta H_{\mathrm{bos}}}a_p^\dagger a_p)}{\mathrm{tr}(e^{-\beta H_{\mathrm{b}}})}\,. \tag{4.66}$$

Furthermore, we have shown in Eq. (4.26) that

$$-2A\langle a_p + a_p^\dagger\rangle_0 = \mu(L) + 4|J_{p,p}|\,. \tag{4.67}$$

In conclusion,

$$\begin{aligned} \sigma_{\mathrm{fast}} &= 2A\sqrt{1+2\frac{1}{N}\sum_{\mathbf{k}}\frac{1}{e^{\beta\omega_{\mathbf{k}}}-1}} \\ &\simeq 2A\sqrt{1+2\frac{4\pi}{(2\pi)^3}\int_0^\infty \mathrm{d}k\frac{k^2}{e^{\beta Dk^2}-1}} \\ &= 2A\sqrt{1+\frac{\zeta(3/2)}{4(\pi\beta D)^{3/2}}}\,. \end{aligned} \tag{4.68}$$

We see that the standard deviation is of order A, slowly increases with temperature, and, crucially, is independent of L, such that $\frac{\sigma_{\mathrm{fast}}}{\mu(L)} \sim \frac{t}{AL}$ becomes negligible for large L.

Let us now calculate the higher moments of the distribution. In order to simplify our notation, we define $X_p = -2A(a_p + a_p^\dagger)$, such that the expected energy cost is $\Delta E_{0\to 1,\mathrm{fast}} = \langle X_p\rangle_0$. We define the n-th moment of the distribution to be

$$C_n = \langle(X_p - \langle X_p\rangle_0)^n\rangle_0^{1/n}\,. \tag{4.69}$$

We find

$$\begin{aligned} C_n^n &= \left\langle \sum_{k=0}^{n} \binom{n}{k} X_p^{n-k} (-1)^k \langle X_p \rangle_0^k \right\rangle_0 \\ &= \sum_{k=0}^{n} (-1)^k \binom{n}{k} \left\langle X_p^{n-k} \right\rangle_0 \langle X_p \rangle_0^k \, . \end{aligned} \tag{4.70}$$

Now in order to evaluate these averages we write

$$\left\langle X_p^m \right\rangle_0 = \left\langle e^{-S} \widetilde{X}_p^m e^S \right\rangle_0 = \left\langle \widetilde{X}_p^m \right\rangle_{\mathrm{b}} \tag{4.71}$$

where $\langle \ldots \rangle_{\mathrm{b}}$ denotes thermal averages w.r.t. H_{b} and $\widetilde{X}_p = e^S X_p e^{-S} = X_p + \mu(L) + 4|J_{p,p}|$. For the second equality in Eq. (4.71) we have used the fact that $\widetilde{H}_0 = H_{\mathrm{b}} + \mathrm{const}$. Then, using Wick's Theorem and the fact that $\langle (a_p + a_p^\dagger)^{2k+1} \rangle_{\mathrm{b}} = 0$,

$$\begin{aligned} \left\langle X_p^m \right\rangle_0 &= \sum_{k=0}^{m} \binom{m}{k} (\mu(L) + 4|J_{p,p}|)^{m-k} \langle X_p^k \rangle_{\mathrm{b}} \\ &= \sum_{k=0}^{\lfloor m/2 \rfloor} \binom{m}{2k} (\mu(L) + 4|J_{p,p}|)^{m-2k} \langle X_p^{2k} \rangle_{\mathrm{b}} \\ &= \sum_{k=0}^{\lfloor m/2 \rfloor} \binom{m}{2k} \frac{(2k)!}{2^k k!} (\mu(L) + 4|J_{p,p}|)^{m-2k} \langle X_p^2 \rangle_{\mathrm{b}}^k \, . \end{aligned} \tag{4.72}$$

For the last equality, we have used that the number of possible contractions is $(2k-1) \times (2k-3) \ldots 3 \times 1 = \frac{(2k)!}{2^k k!}$. As a simplest case, we have $\langle X_p \rangle_0 = \mu(L) + 4|J_{p,p}|$. In conclusion, we find

$$\begin{aligned} C_n^n &= \sum_{k=0}^{n} (-1)^k \binom{n}{k} \sum_{r=0}^{\lfloor (n-k)/2 \rfloor} \binom{n-k}{2r} \frac{(2r)!}{2^r r!} (\mu(L) + 4|J_{p,p}|)^{n-k-2r} \langle X_p^2 \rangle_{\mathrm{b}}^r (\mu(L) + 4|J_{p,p}|)^k \\ &= n! (\mu(L) + 4|J_{p,p}|)^n \sum_{k=0}^{n} \sum_{r=0}^{\lfloor (n-k)/2 \rfloor} \frac{(-1)^k}{k! r! (n-k-2r)!} \left(\frac{\langle X_p^2 \rangle_{\mathrm{b}}}{2(\mu(L) + 4|J_{p,p}|)^2} \right)^r \, . \end{aligned} \tag{4.73}$$

This sum can be evaluated by use of the identity

$$\sum_{k=0}^{n} \sum_{r=0}^{\lfloor (n-k)/2 \rfloor} \frac{(-1)^k}{k! r! (n-k-2r)!} \xi^r = \begin{cases} \frac{\xi^{n/2}}{(n/2)!} \, , & \text{if } n \text{ is even} \\ 0 \, , & \text{if } n \text{ is odd} \end{cases} \, . \tag{4.74}$$

We thus obtain, for n even,

$$C_n = \left(\frac{n!}{(n/2)!}\right)^{1/n} \sqrt{\langle X_p^2 \rangle_{\mathrm{b}}/2}\,. \tag{4.75}$$

Furthermore,

$$\begin{aligned}\sqrt{\langle X_p^2\rangle_{\mathrm{b}}} &= 2A\left(1 + 2\frac{1}{N}\sum_{\mathbf{k}}\langle a_{\mathbf{k}}^\dagger a_{\mathbf{k}}\rangle_{\mathrm{b}}\right)\\ &= 2A\sqrt{1+\frac{\zeta(3/2)}{4(\pi\beta t)^{3/2}}}\,,\end{aligned} \tag{4.76}$$

see Eq. (4.68).

Our final result is thus

$$C_n = \sqrt{2}A\left(\frac{n!}{(n/2)!}\right)^{1/n}\sqrt{1+\frac{\zeta(3/2)}{4(\pi\beta t)^{3/2}}} \tag{4.77}$$

for n even, and 0 otherwise. For $n = 2$ we retrieve (4.68) for the the standard deviation. For larger n, recall that $\left(\frac{n!}{(n/2)!}\right)^{1/n} \approx \sqrt{2n/e}$, such that

$$C_n \approx 2A\sqrt{n/e}\sqrt{1+\frac{\zeta(3/2)}{4(\pi\beta t)^{3/2}}}\,. \tag{4.78}$$

In conclusion, all the higher moments grow like $O((T/t)^{3/4})$ with temperature but are independent of L.

4.C Continuum approximation

Here we numerically evaluate the sum $\sum_p \frac{1}{|\mathbf{R}_p|}$ and show that the continuum approximation is just a convenient mathematical tool that allows to analytically evaluate the behavior of the sum as function of L.

In Fig. (4.3) we plot the sum $\sum_p \frac{1}{|\mathbf{R}_p|}$ as function of L. Here we choose $a = 1$ for the lattice constant. The linear behavior is in agreement with the continuum approximation calculation. The other sums appearing in this work can similarly be evaluated numerically and the results agree with the continuum approximation. As mentioned in the main text, we

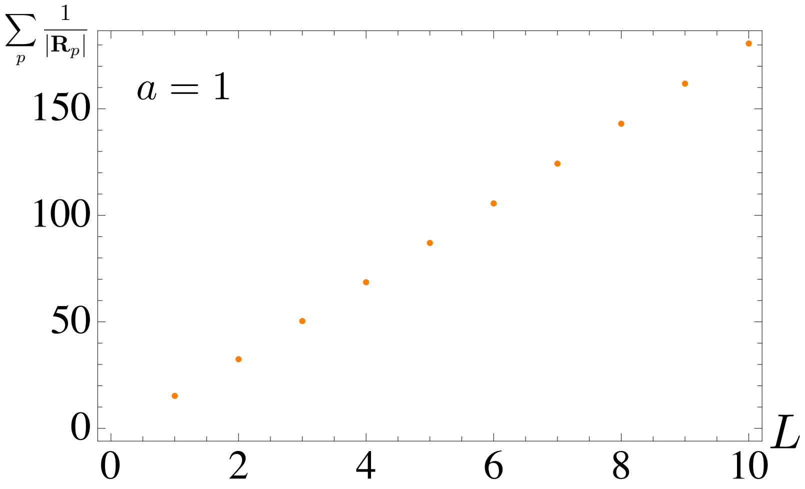

Figure 4.3: Numerical evaluation of the sum $\sum_p \frac{1}{|\mathbf{R}_p|}$ as function of L for a lattice constant $a = 1$. The sum increases linearly with L, in agreement with the continuum approximation calculation.

point out again that in the continuum approximation we let the lattice constant a of the surface code go formally to zero such that a single stabilizer remains coupled to a bosonic creation an annihilation operators at the corresponding site.

CHAPTER 5

Effective Quantum-Memory Hamiltonian From Local Two-Body Interactions

Adapted from:
Adrian Hutter, Fabio L. Pedrocchi, James R. Wootton, and Daniel Loss
"Effective quantum-memory Hamiltonian from local two-body interactions",
Phys. Rev. A **90**, 012321 (2014)

In [Phys. Rev. A 88, 062313 (2013)] we proposed and studied a model for a self-correcting quantum memory in which the energetic cost for introducing a defect in the memory grows without bounds as a function of system size. This positive behavior is due to attractive long-range interactions mediated by a bosonic field to which the memory is coupled. The crucial ingredients for the implementation of such a memory are the physical realization of the bosonic field as well as local five-body interactions between the stabilizer operators of the memory and the bosonic field. Here, we show that both of these ingredients appear in a low-energy effective theory of a Hamiltonian that involves only two-body interactions between neighboring spins. In particular, we consider the low-energy, long-wavelength excitations of an ordered Heisenberg ferromagnet (magnons) as a realization of the bosonic field. Furthermore, we present perturbative gadgets for generating the required five-spin operators. Our Hamiltonian involving only local two-body interactions is thus expected to exhibit self-correcting properties as long as the noise affecting it is in the regime where the effective low-energy description remains valid.

5.1 Introduction

Kitaev's toric code [16] serves as the simplest toy model of a quantum memory as well as being the archetypical example of a topological phase of matter. Topological protection of Josephson junction qubits [107] as well as topological error correction [108] have by now been experimentally demonstrated. Implementations of spin-lattice models with topologically ordered groundstates using polar molecules stored in optical lattices [109] or laser-excited Rydberg [83] atoms have been proposed.

A challenge to any scalable implementation of topological protection of quantum information is the issue of thermal stability. In its standard form, the toric code Hamiltonian requires a set of local, commuting four-qubit stabilizer operators $W = (\sigma^x)^{\otimes 4}, (\sigma^z)^{\otimes 4}$. Unfortunately, the "bare" toric code Hamiltonian $-A\sum W$ (with $A > 0$) does not allow for thermally stable storage of quantum information [32, 33, 35, 56, 77]. While performing a bit- or phase-flip on a single qubit (and thus creating two anyonics defects) has an energy cost $4A$, these defects can then propagate without any further energy cost and thus destroy the stored quantum information. As a consequence, the lifetime of the quantum information is *independent* of the size of the memory. Furthermore, interactions in nature are usually two-body, such that the four-body operators W cannot be generated directly but have to emerge from an underlying structure of two-body interactions. Since W will then appear in high-order perturbation theory [64, 110–112], the energy penalty A will naturally be weak.

These negative results on the bare toric code have motivated the study of long-range interactions between the stabilizer operators W as a means to suppress the creation and/or diffusion of anyons and thereby increase the lifetime of the stored quantum information [38–40, 57, 65, 81, 82]. Such long-range interactions can lead to quantum information lifetimes that grow polynomially or even exponentially with L [38, 40, 65, 81, 82].

In order to mediate these interactions in a physically plausible way, all of these proposals require five-body operators of the form $W \otimes O$, where the operator O allows to couple the stabilizer operator W to an external field which mediates the interaction. The external field can either be elementary (e.g. photons as discussed in Ref. [39]) or emerge from the energetically low-lying excitations of a many-body system (e.g. phonons as discussed in Ref. [65]). In Ref. [82] we have studied in detail the case of bosons hopping in a cubic lattice, leading to a parabolic dispersion near the center of the Brillouin zone.

Beyond the fundamental question of whether passive storage of quantum information for a long time is, in principle, possible, building a quantum memory is also a practically relevant endeavor. Many proposed applications of quantum technology, such as quantum key distribution and quantum networks, rely on the possibility of long-range quantum state transfer. Quantum memories are crucial to the implementation of quantum repeaters, which allow one to combat the heavy losses involved in such long-range quantum communication [113]. Furthermore, it has been suggested that quantum memories based on interacting anyons are compatible with a recent proposal for fault-tolerant holonomic quantum computation based on adiabatic deformation of the system Hamiltonian [114].

In the present paper, we focus on the physical implementation of the quantum memory Hamiltonian proposed in Ref. [82]. We start from a spin Hamiltonian involving only *local two-body interactions* and study its low-energy theory via a perturbative Schrieffer-Wolff transformation. The bosonic field emerges from the energetically low-lying excitations of an ordered Heisenberg ferromagnet (magnons). For small wave-numbers, magnons indeed feature a parabolic dispersion. Furthermore, we present perturbative gadgets for generating the five-body operators $W \otimes O$, describing interactions between the four-qubit stabilizer operators W of the toric code and a spin operator O of the ferromagnet. Since the quantum-memory Hamiltonian of Ref. [82] emerges as the effective low-energy/long-wavelength theory of our Hamiltonian with only local two-spin interactions, this system is expected to exhibit self-correcting properties *as long as this effective theory remains valid*.

The rest of this paper is organized as follows. We briefly review the main results of Ref. [82] in Sec. 5.2 and discuss the relation to the present work. In Sec. 5.3, we present perturbative gadgets that allow effective five-body terms $W \otimes O$ to be obtained from local two-body interactions only. In Sec. 5.4, we show that using these five-body operators to couple the stabilizer operators W to an ordered Heisenberg ferromagnet leads to a low-energy effective theory which coincides with the quantum memory Hamiltonian from Ref. [82]. We can thus obtain an effective quantum memory Hamiltonian from a system (perturbative gadgets plus Heisenberg ferromagnet) with two-spin interactions only. In Sec. 5.5 we study the regime in which this effective description is expected to be valid. In Sec. 5.6 we study the backaction of the coupling onto the ferromagnet and how to counteract it. We conclude in Sec. 5.7.

5.2 Previous work

In Ref. [82] we have studied the following model $H_{\text{int}} + H_b$ for a self-correcting quantum memory. Consider a bosonic Hamiltonian

$$H_b = \sum_{\mathbf{k}} \omega_{\mathbf{k}} a^\dagger_{\mathbf{k}} a_{\mathbf{k}} \tag{5.1}$$

with a dispersion, which in the low-$\mathbf{k}$ limit is parabolic, $\omega_{\mathbf{k}} \approx D|\mathbf{k}|^2$. The four-qubit stabilizer operators W_p are arranged on a 2D array of size $L \times L$ and locally couple to the bosonic field,

$$H_{\text{int}} = A \sum_p W_p O_p \, , \tag{5.2}$$

where either $O_p = a^\dagger_p a_p$ or $O_p = a_p + a^\dagger_p$. Here, a_p and $a^\dagger_p$ are Fourier transforms of the bosonic operators $a_{\mathbf{k}}$ and $a^\dagger_{\mathbf{k}}$, $a_p = \frac{1}{\sqrt{N}} \sum_{\mathbf{k}} e^{i\mathbf{R}_p \mathbf{k}} a_{\mathbf{k}}$, where $\mathbf{R}_p$ is the spatial location of stabilizer W_p and N is the number of bosonic modes. In other words, the operator a_p ($a^\dagger_p$) annihilates (creates) a boson at position $\mathbf{R}_p$.

The stabilizer operators (or stabilizers for short) W_p are of the form $W_p = (\sigma^x)^{\otimes 4}$ or $W_p = (\sigma^z)^{\otimes 4}$, see Fig. 5.1 for an illustration. All stabilizers commute with each other and have eigenvalues ± 1.

Under the assumption that the bosons are in thermal equilibrium, the bosonic field mediates long-ranged interactions between the stabilizer operators W_p. Technically speaking, it is possible to integrate out the bosonic field (either exactly or perturbatively) and derive an effective Hamiltonian for the stabilizers. This Hamiltonian is of the form

$$H_{\text{stab}} = \frac{1}{2} \sum_{p \neq p'} J_{pp'} W_p W_{p'} \, , \tag{5.3}$$

where $J_{pp'}$ describes a mediated attractive long-range interaction between the stabilizers.

More specifically, we have shown the following [82]. For $O_p = a^\dagger_p a_p$, we have $J_{pp'} \sim |\mathbf{R}_p - \mathbf{R}_{p'}|^{-2}$, such that the energy cost for violating a stabilizer ("creating an anyon") grows logarithmically with L and the quantum memory lifetime grows polynomially with L. If, on the other hand, $O_p = a_p + a^\dagger_p$, we have $J_{pp'} \sim |\mathbf{R}_p - \mathbf{R}_{p'}|^{-1}$, such that the energy cost for creating an anyon grows linearly with L and the lifetime does so exponentially.

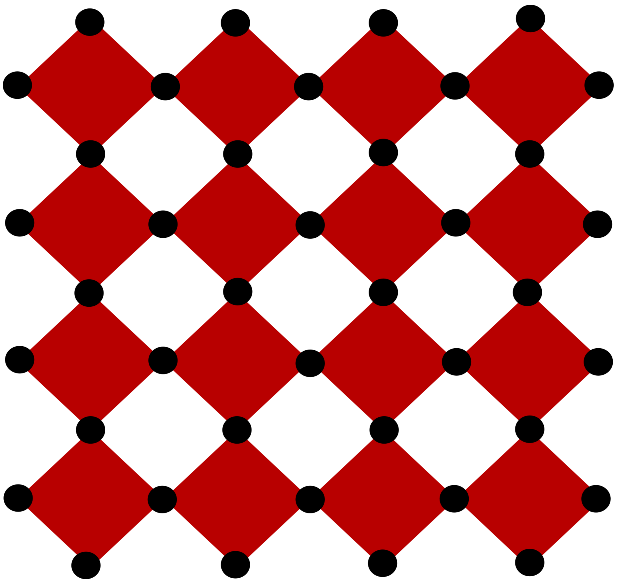

Figure 5.1: An excerpt of a toric code. Black dots are code qubits. Stabilizer operators W_p involve operators acting on the four qubits around a white or a dark plaquette. Operators acting on the four qubits around a white plaquette are of the form $W_p = (\sigma^x)^{\otimes 4}$, while operators acting on the four qubits around a dark plaquette are of the form $W_p = (\sigma^z)^{\otimes 4}$.

Relation to the present work

The goal of this work is to show that the Hamiltonian H_{stab} can be obtained as an effective low-energy Hamiltonian of a Hamiltonian that involves only nearest-neighbor two-spin interactions. This Hamiltonian is then expected to exhibit self-correcting properties, given that the noise affecting the memory is such that the effective low-energy description remains valid. We realize the bosonic field by a 3D ordered Heisenberg ferromagnet (FM) to which the stabilizers of the toric code couple locally. The long-range interactions $J_{pp'}$ in Eq. (5.3) are then mediated by massless excitations of the FM (Goldstone modes), so-called magnons.

Our model consists of a "gadgetry" and a "ferromagnet" part,

$$H = H_G + H_F \,, \tag{5.4}$$

where $H_G = \sum_p H_p$ is a sum of identical gadget terms for each of the stabilizers. The summands H_p are sums of two-qubit terms, where one of the two qubits involved is part of the toric code and the other one is

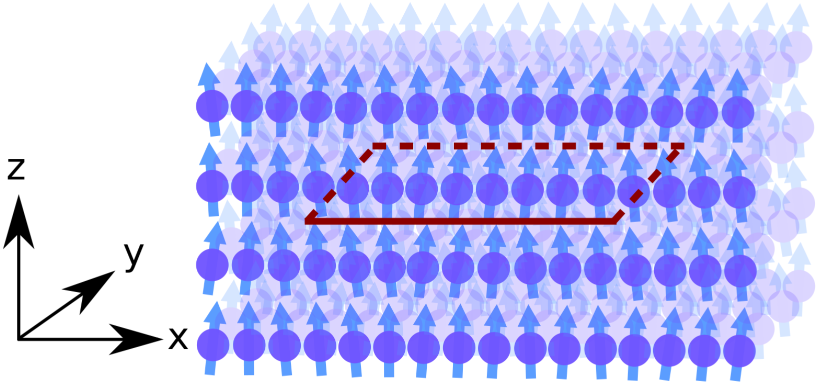

Figure 5.2: A 2D toric code (whose contoures, lying in an xy-plane, are sketched by red lines) is embedded in a 3D Heisenberg ferromagnet (blue) which is ordered in z-direction. The stabilizer operators of the toric code W_p (illustrated in Fig. 5.1) couple to the x-component of an adjacent spin $\mathbf{S}_p$ of the ferromagnet. The linear size of the planar toric code (L) is assumed to be much smaller than the one of the ferromagnet (Λ), *i.e.*, $L \ll \Lambda$.

an auxiliary or "mediator" qubit. By integrating out all mediator qubits, we obtain a first effective Hamiltonian

$$H' = (H_G)_{\text{eff}} + H_F \,, \tag{5.5}$$

describing four-qubit stabilizer operators locally coupled to the FM. Here, $(H_G)_{\text{eff}}$ is akin to H_{int} in Eq. (5.2).

The ordered Heisenberg ferromagnet described by H_F can be mapped to a bath of bosons (magnons) by means of the well-known Holstein-Primakoff transformation. Even beyond the one-magnon approximation (*i.e.*, taking magnon-magnon interaction into account), the interactions between the stabilizers mediated by the ferromagnet can be described by a final effective Hamiltonian H_{eff} akin to H_{stab} in Eq. (5.3). The effective interactions $J_{pp'}$ are thereby given by the static susceptibility of the FM.

5.3 Perturbative gadgets for five-body operators

Given some Hamiltonian with only local two-body interactions, one is often interested in an *effective* Hamiltonian that describes the low-energy

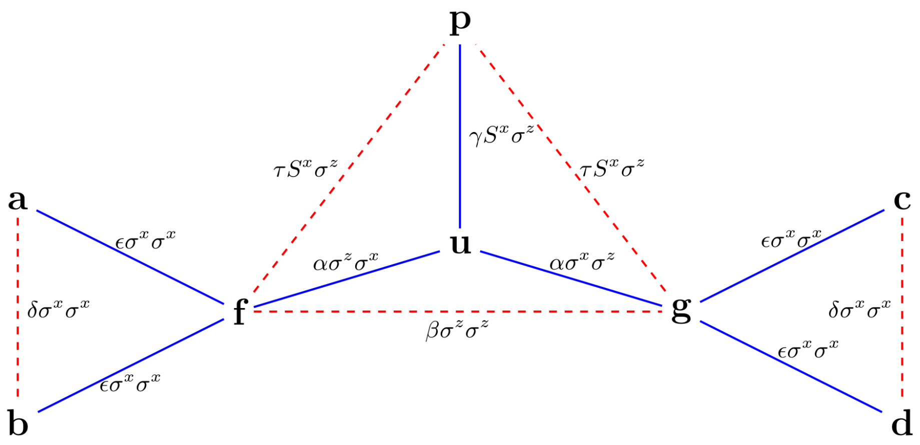

Figure 5.3: Auxiliary qubits f, g, and u mediate a five-body interaction $W_p \otimes S_p^x$ between qubits a, b, c, and d, and the operator S_p^x (spin of the FM). This interaction emerges from local two-body interactions only. The excited state of the auxiliary qubits is penalized by an energy Δ, which is the dominant energy scale in the system. The interactions which are indicated by solid lines produce the actual five-body interaction. Interactions which are indicated by dashed lines allow one to tune the strength of two-, three-, and four-body terms without changing the strength of the five-body term. Choosing δ and τ appropriately allows one to counter undesired two- and three-body terms. Finally, the parameter β allows one to tune the strength of the four-qubit interaction W_p independently of the five-body interaction $W_p \otimes O_p$.

dynamics of the system. This is achieved by "integrating out" the high-energy degrees of freedom. The effective low-energy Hamiltonian then often features a higher complexity than the original one. This lead to the idea of *perturbative gadgets* [74, 115, 116], which allows one to systematically construct Hamiltonians with local two-qubit interactions that yield some desired effective (low-energy) few-qubit Hamiltonian. In particular, Ref. [116] showed that any local Hamiltonian can be generated from some 2-local Hamiltonian.

The Schrieffer-Wolff (SW) transformation [95, 117] (see Appendix 5.A for a technical summary) provides a natural framework for obtaining such effective terms. Ref. [118] combined the gadgets of Ref. [116] with the SW method to discuss the simulation of local many-body Hamiltonians by use of 2-local interactions. The schemes we propose in order to generate the five-body terms $AW_p \otimes O_p$ shall be analyzed by means of a

SW transformation but are simpler than had they been constructed with the perturbative gadgets described in Refs. [116,118].

Note that while all of the proposals in Refs. [38–40,57,65,81,82] require five-body terms of the form $AW_p \otimes O_p$, other quantum memory proposals are not based on coupling stabilizer operators to external fields. However, these alternate proposals in fact involve interactions between more than five qubits. Specifically, the 3-dimensional toric code with "welding" [80] requires six-qubit operators, while the 4-dimensional toric code [57] and Haah's cubic code [60–62] require eight-qubit operators. These models can thus only be realized with gadgets that are even more involved than the ones discussed in the following.

We introduce two sets of spins, namely $\mathbf{S}_j$ for the spins of the 3D FM located at site j of a cubic lattice and $(\sigma_i^x, \sigma_i^y, \sigma_i^z)^T$ for the physical spins-$1/2$ (qubits) of the 2D toric code. Both spins satisfy the usual commutation relations. The code qubits are arranged on a quadratic lattice with periodic boundary conditions. The four-qubit stabilizer operators W_p are of the form $\sigma_a^x \sigma_b^x \sigma_c^x \sigma_d^x$ or $\sigma_a^z \sigma_b^z \sigma_c^z \sigma_d^z$, where the operators act on the four qubits around one plaquette of the lattice, as illustrated in Fig. 5.1.

We seek to construct effective terms of the form $W_p \otimes S_p^x$, where for the moment we consider $W_p = \sigma_a^x \sigma_b^x \sigma_c^x \sigma_d^x$. Here, $\mathbf{S}_p$ is the spin of the FM adjacent to the spins of the stabilizer W_p, see Fig. 5.2. Let the summands in the gadget Hamiltonian $H_G = \sum_p H_p$ be given by

$$\begin{aligned} H_p = & -\frac{\Delta}{2}\sigma_f^z - \frac{\Delta}{2}\sigma_g^z - \frac{\Delta}{2}\sigma_u^z \\ & + \gamma S_p^x \otimes \sigma_u^z + \tau S_p^x \otimes (\sigma_f^z + \sigma_g^z) \\ & + \varepsilon \sigma_f^x \otimes (\sigma_a^x + \sigma_b^x) + \varepsilon \sigma_g^x \otimes (\sigma_c^x + \sigma_d^x) \\ & + \alpha \sigma_u^x \otimes (\sigma_f^z + \sigma_g^z) + \beta \sigma_f^z \otimes \sigma_g^z \\ & + \delta \sigma_a^x \otimes \sigma_b^x + \delta \sigma_c^x \otimes \sigma_d^x \end{aligned} \tag{5.6}$$

with Δ being larger than (the absolute value of) all other energies (see Fig. (5.3) for an illustration).

We now apply the SW method to successively integrate out the mediator qubits f, g, and u and calculate for each mediator qubit the resulting terms up to third order. Consider a mediator qubit r with energy splitting Δ, $H_0 = -\frac{\Delta}{2}\sigma_r^z$, and a perturbation $V = V_\mathrm{d} + V_\mathrm{od}$. With $V_\mathrm{d} = \sigma_r^z \otimes \tilde{V}_\mathrm{d}$, $V_\mathrm{od} = \sigma_r^x \otimes \tilde{V}_\mathrm{od}$, and $[\tilde{V}_\mathrm{d}, \tilde{V}_\mathrm{od}] = 0$, we obtain after integrating out the auxiliary qubit r as described in Appendix 5.A

$$H_{\text{eff}} = -\frac{\Delta}{2} + \tilde{V}_{\text{d}} - \frac{1}{\Delta}\tilde{V}_{\text{od}}^2 - \frac{2}{\Delta^2}\tilde{V}_{\text{od}}^2\tilde{V}_{\text{d}} + \dots \tag{5.7}$$

The unitaries applied during the SW procedure to integrate out qubits f, g, and u (cf. Appendix 5.A) do not commute and higher order terms will thus depend on the order in which this three qubits are integrated out. However, up to the orders stated below, the effective terms are independent of this ordering.

For the sake of a shorter notation, let $R_p := \sigma_a^x\sigma_b^x + \sigma_c^x\sigma_d^x$ and $\xi := \frac{2\varepsilon}{\Delta}$. We neglect terms in the interaction strengths which are smaller by at least a factor ξ^2 than the mentioned terms. After straightforwardly applying Eq. (5.7) in Appendix 5.A to the mediator qubits f, g, and u, we find

$$\begin{aligned}(H_p)_{\text{eff}} = {} & \left[\gamma + 2\tau - 8\frac{\gamma\alpha^2}{\Delta}\right] S_p^x - \xi^2\left[\tau - 8\frac{\alpha^2\gamma}{\Delta^2}\right] R_p \otimes S_p^x \\ & + \left[\delta - \xi^2\left(\frac{\Delta}{2} - \beta + 4\frac{\alpha^2}{\Delta}\right)\right] R_p + \xi^4\left[\beta - 2\frac{\alpha^2}{\Delta}\right] W_p \\ & - 4\xi^4\frac{\alpha^2\gamma}{\Delta^2} W_p \otimes S_p^x + \text{const}\,. \end{aligned} \tag{5.8}$$

The parameter β allows one to tune the strength of the plaquette term W_p without affecting the strength of the five-body operator $W_p \otimes S_p^x$. The interaction strength of the undesired operators R_p and $R_p \otimes S_p^x$ can be tuned to zero through appropriate choice of the parameters $\delta \simeq \frac{2\varepsilon^2}{\Delta}$ and $\tau \simeq 8\frac{\alpha^2\gamma}{\Delta^2}$, respectively. We obtain an undesired one-body term $\simeq (\gamma + 2\tau)S_p^x$ which can be countered by an appropriate local field. Finally, the strength of our desired five-body term $W_p \otimes S_p^x$ is to leading order given by $A := -64\frac{\varepsilon^4\alpha^2\gamma}{\Delta^6}$. If we use the operator $W_p \otimes S_p^x$ to couple the plaquette W_p to external fields, effective two-plaquette interactions mediated by the field will be of even order in A. The sign of α, γ, and ε is thus irrelevant.

Relabeling $x \to z \to y \to x$ on all qubits, such that the commutation relations of the spin operators are preserved, we can obtain operators of the form $(\sigma^z)^{\otimes 4} \otimes S_p^x$ rather than $(\sigma^x)^{\otimes 4} \otimes S_p^x$. In conclusion, integrating out the mediator qubits in each gadget leads to an effective coupling Hamiltonian

$$(H_G)_{\text{eff}} = \sum_p A W_p \otimes S_p^x\,, \tag{5.9}$$

which is of the same form as Eq. (5.2).

Note that if we let $\alpha, \gamma, \tau \to 0$ in Eq. (5.6), we find the simpler effective Hamiltonian

$$(H_p)_{\text{eff}} = \left[\delta - 2\frac{\varepsilon^2}{\Delta} - 4\frac{\beta\varepsilon^2}{\Delta^2}\right] R_p + 16\frac{\beta\varepsilon^4}{\Delta^4} W_p \,. \tag{5.10}$$

We can thus obtain stabilizer operators W_p as they appear in Kitaev's toric code [16] as effective terms using only two auxiliary qubits, nearest neighbor Ising interactions and single-qubit energy splittings. This adds a particularly simple gadget to the list of proposals for perturbatively generating Kitaev's toric code [64, 110–112].

We have discussed how the strength of the undesired terms R_p and $R_p \otimes S_p^x$ can be tuned to zero by appropriate choice of the interaction strengths δ and τ. Of course, assuming that the strength of these interactions vanishes exactly is unphysical. Weak terms acting as R_p are no threat to the toric code, as it is inherently stable against such local perturbations [16, 19]. However, as the terms $R_p \otimes S_p^x$ themselves couple to the gapless magnon field, one might fear that their combined non-local interaction may destabilize the toric code groundstate. We have qualitatively discussed the effect of such non-locally coupled perturbations on the stability of the toric code in Ref. [82] and argued that they pose no threat to toric code stabilized by the FM as long as the strength of the accidental terms $R_p \otimes S_p^x$ is sufficiently smaller than the engineered coupling strength A.

5.4 Effective long-range interactions mediated by the ferromagnet

After integrating out all mediator qubits in the perturbative gadgets, we arrived at a first effective Hamiltonian

$$H' = (H_G)_{\text{eff}} + H_F = A \sum_p W_p S_p^x + H_F \tag{5.11}$$

describing four-qubit stabilizer operators of the toric code coupled to the FM. Let us now study the interactions between the effective stabilizer operators W_p which are mediated by the ordered Heisenberg FM H_F, to which they are coupled over the operators S_p^x.

The Hamiltonian of the 3D Heisenberg FM is given by $H_{\mathrm{F}} = -J\sum_{\langle i,j\rangle}\mathbf{S}_i\cdot\mathbf{S}_j + h_z\sum_i S_i^z$, where $J > 0$ is the exchange constant and the sum is restricted to nearest-neighbor lattice sites. The FM is of linear size Λ, which is much larger than the linear size of the toric code, $\Lambda \gg L$. The FM is assumed to be below the Curie temperature and the spins ordered along the z-direction. To break the symmetry of the FM, a small magnetic field h_z in z-direction is applied. This field also stabilizes the FM against the effective longitudinal magnetic field produced by coupling the stabilizer operators of the toric code to the x-component of adjacent FM spins (see below). Although H_F is three-dimensional, we point out for the sake of clarity, that the actual quantum memory is the two-dimensional toric code. The presence of the 3D system is necessary to mediate long-range interactions between the stabilizers. However, the place where the logical qubits are stored is the two-dimensional toric code.

For $A \ll J$, we make use of a perturbative second-order Schrieffer-Wolff transformation [95,101,117] to derive the effective plaquette-plaquette interaction (see Appendix 5.B) given by

$$H_{\mathrm{eff}} = \frac{1}{2}\sum_{p\neq p'} J_{pp'} W_p W_{p'} \ , \tag{5.12}$$

where the coupling is $J_{pp'} = -A^2\chi_{xx}(\mathbf{R}_p - \mathbf{R}_{p'})$ and $\chi_{\alpha\beta}(\mathbf{r})$ is the static spin susceptibility of the FM. This effective Hamiltonian is of the same form as in Eq. (5.3) and, as we will discuss now, the mediated interaction strength $J_{pp'}$, too, is of the same form.

The real space static susceptibility $\chi_{\alpha\beta}(\mathbf{r})$ is defined as the Fourier transform of

$$\chi_{\alpha\beta}(\mathbf{q},\omega) = i\lim_{\eta\to 0^+}\int_0^\infty \mathrm{d}t\, e^{(i\omega-\eta)t}\left\langle\left[S_{\mathbf{q}}^\alpha(t), S_{-\mathbf{q}}^\beta\right]\right\rangle \ , \tag{5.13}$$

for $\omega = 0$, where $\langle\ldots\rangle$ denotes thermal equilibrium expectation values of the $\mathbf{S}$-spins at temperature T. The Fourier components are defined as $S_{\mathbf{q}}^\alpha = \frac{1}{\sqrt{N_s}}\sum_i e^{-i\mathbf{q}\cdot\mathbf{R}_i}S_i^\alpha$, where $N_s = \Lambda^3$ is the number of spins in the FM, and $\mathbf{R}_i$ is a 3D vector pointing to the site of spin $\mathbf{S}_i$ of the FM.

It is not necessary to explicitly calculate the spin susceptibility in the ferromagnetically ordered state to understand its general behavior at large distances (or small $\mathbf{q}$) [119]. Indeed, for $h_z = 0$, the spontaneous $SO(3)$ symmetry breaking of the state with finite magnetization pointing along the z-axis, implies the presence of low-frequency Goldstone modes (called magnons in this context) and long-range correlations, *i.e.*, the xx-

(and yy-) susceptibility has to diverge for $\mathbf{q} \to \mathbf{0}$ and takes the following generic form in the hydrodynamic regime (low-energy and long wavelength regime) [119]

$$\chi_{xx}(\mathbf{q}, \omega = 0) = \frac{M^2}{\rho |\mathbf{q}|^2} \quad \text{for } \mathbf{q} \to \mathbf{0}\,. \tag{5.14}$$

Here, $\rho > 0$ is the stiffness constant of the FM and $M = \langle s^z \rangle$ is the magnetization density with $s^z = \frac{1}{N_s} \sum_i S_i^z$. The divergence at $\mathbf{q} \to \mathbf{0}$ in Eq. (5.14) is directly connected with the broken symmetry of the ground state: starting from a ferromagnetic state aligned along the z-direction, the slightest x-magnetic field is able to rotate and align all spins in x-direction and thus the response to an external magnetic field indeed diverges at $\mathbf{q} \to \mathbf{0}$.

Eq. (5.14) is the expression for the spin susceptibility in the continuum approximation (lattice constant a going formally to zero). To be valid this approximation does not require that the number of spins goes to infinity, but rather that the distance between neighboring spins is much smaller than the distances we are interested in. Since we are concerned with the long-distance physics of our model on the scale of L, this approximation is justified and simply requires $a/L \ll 1$. In this limit, both the lattice constants of the ferromagnet and of the toric code are taken to zero such that a single plaquette remains coupled to a single FM spin.

Below we give an explicit expression for the stiffness ρ in the one-magnon approximation. The presence of the symmetry-breaking magnetic field h_z introduces a gap in the magnon spectrum and thus a mass term in the susceptibility, *i.e.*, $\chi_{xx}(\mathbf{q}, \omega = 0) = \frac{M^2}{\rho|\mathbf{q}|^2 + S h_z}$ for $\mathbf{q} \to \mathbf{0}$. The real space static susceptibility now follows by Fourier transformation which leads to $\chi_{xx}(\mathbf{r}) = \frac{M^2}{\rho} \frac{1}{4\pi|\mathbf{r}|} e^{-|\mathbf{r}|/L_h}$, with magnetic length $L_h = \sqrt{R/S h_z}$. Consequently, Eq. (5.12) describes a stabilizer Hamiltonian with plaquette-plaquette interactions given by a Yukawa-like potential,

$$J_{pp'} = -\frac{A^2 M^2}{4\pi\rho} \frac{e^{-|\mathbf{R}_p - \mathbf{R}_{p'}|/L_h}}{|\mathbf{R}_p - \mathbf{R}_{p'}|}\,. \tag{5.15}$$

Since, again, $\rho > 0$ (see also below), the interaction between stabilizer operators $W_\mathbf{p}$ is *attractive*.

For the sake of illustration we calculate ρ in the one-magnon (harmonic) approximation by making use of the Holstein-Primakoff transformation

$$S_i^z = -S + \hat{n}_i\,, \quad S_i^- = a_i \sqrt{2S - \hat{n}_i}\,, \quad S_i^+ = (S_i^-)^\dagger, \tag{5.16}$$

in the formal limit, where the occupation $\hat{n}_i = a_i^\dagger a_i$ is much smaller than $2S$ [102]. Only in this regime do a_i and $a_i^\dagger$ satisfy bosonic commutation relations and the associated quasi-particles are the well-known magnons (or spin wave excitations). Indeed, replacing $\hat{n}_i$ by its thermal expectation value $\langle \hat{n}_i \rangle$, one finds

$$[a_i, a_i^\dagger] = 1 - \frac{\langle \hat{n}_i \rangle}{2S} + O\left((\frac{\langle \hat{n}_i \rangle}{2S})^2 \right) . \tag{5.17}$$

Since J is typically a large energy-scale ($J \approx 10^3 K$), temperatures which are low enough such that $\langle \hat{n}_i \rangle \ll 2S$ is well-satisfied are readily achieved.

In Fourier space, we get $H_F \approx \sum_{\mathbf{q}} (\omega_{\mathbf{q}} + h_z) a_{\mathbf{q}}^\dagger a_{\mathbf{q}}$, up to some irrelevant constant, with magnon dispersion $\omega_{\mathbf{q}} = 4JS[3 - (\cos(q_x) + \cos(q_y) + \cos(q_z))]$, where $a_{\mathbf{q}} = \frac{1}{\sqrt{N_s}} \sum_i e^{-i\mathbf{q}\cdot\mathbf{R_i}} a_i$, with N_s the number of FM spins. Inserting Eq. (5.16) into Eq. (5.14) and using a small $\mathbf{q}$ expansion leads to $\chi_{xx}^{(0)}(\mathbf{q}, \omega = 0) = \frac{S}{2JS|\mathbf{q}|^2 + h_z}$, which allows us to identify the stiffness in lowest order $\rho^{(0)} = 2JS^2$ since here $M^{(0)} = -S$. We thus obtain $\chi_{xx}^{(0)}(\mathbf{r}) = \frac{1}{8\pi J|\mathbf{r}|} e^{-|\mathbf{r}|/L_h}$ and from this the approximate plaquette coupling

$$J_{pp'}^{(0)} = -\frac{A^2}{8\pi J} \frac{e^{-|\mathbf{R}_p - \mathbf{R}_{p'}|/L_h}}{|\mathbf{R}_p - \mathbf{R}_{p'}|}, \tag{5.18}$$

which is explicitly attractive since $J > 0$. We emphasize that Eq. (5.18) is the one-magnon approximation of Eq. (5.15). The sole effect of both temperature and magnon-magnon interactions is to renormalize the coefficients of the interaction (5.18), *i.e.*, $(M^{(0)})^2/R^{(0)} \to M^2/R$ [119], while the form of the potential is not affected. Note that the dimensionality of the 3D FM is critical since Heisenberg FMs in lower dimensions do not order at $T > 0$ [120].

If h_z is small enough such that $L_h \gg L$, the transverse susceptibility of the FM and hence the mediated interaction $J_{pp'}$ in Eq. (5.15) decay like $|\mathbf{R}_p - \mathbf{R}_{p'}|^{-1}$ on the length-scale L of the toric code. The same decay of $J_{pp'}$ was reported in Sec. 5.2 for the case of coupling to the bosonic operator $O_p = a_p + a_p^\dagger$. This is of course no surprise, since the spin operator S_p^x takes in the Holstein-Primakoff picture and in the limit $|\langle \hat{n}_i \rangle| \ll 2S$ indeed the form $\sqrt{2S}(a_p + a_p^\dagger)$.

The external magnetic field h_z is necessary for stabilizing the magnetization of the FM, keeping it along the z-direction. Indeed, the only condition which needs to be satisfied for the stability of the global magnetization of the FM is that the Zeeman energy $E_z = h_z S \Lambda^3$ due to the

h_z field remains much larger than the Zeeman energy $E_x = ASL^2$ due to the toric code. As a specific example, one can make the following scaling choice satisfying all constraints: $h_z \propto 1/L^4$ and $\Lambda \propto L^3$, which satisfy $L_h \propto L^2 \gg L$ and $E_z/E_x \propto L^3 \gg 1$. Under these conditions, it is clear that the total magnetization will not be affected by the presence of the memory and the FM spins will not rotate into the x-direction*on average*. This is in agreement with a Metropolis simulation of the classical Heisenberg FM, see Fig. 5.4. However, we show below that backaction effects become eventually important for the FM spins *close* to the memory.

5.5 Validity of the effective theory

Here we analyze in detail the conditions of validity of our effective theory.

As we discussed in Ref. [82], the thermal stability of the toric code protected by the effective Hamiltonian H_{eff} in Eq. (5.12) is due to the fact that the cost for inverting a stabilizer W_p (creating an anyon) grows without bounds as a function of L. Indeed, assume that initially all stabilizers have a $+1$ eigenvalue ($W_p \equiv +1$). Then, the energy cost for inverting one of them is given by

$$\mu(L) = \sum_p 2|J_{pp'}| \sim \frac{A^2M^2}{\rho} L \,, \tag{5.19}$$

where we used Eq. (5.15) and the assumption $L_h \gg L$. This seems to be in contradiction to the fact that our original Hamiltonian $H = H_G + H_F$ is a sum of bounded local terms, such that the energy cost for a local change certainly is bounded and does not grow with system size. However, in the case where the effective Hamiltonian (5.12) emerges from a system with two-body interactions, it describes the system correctly in the *long-wavelength* and *low-energy limit* only.

We first note that the Schrieffer-Wolff transformation employed in the derivation of H_{eff}, followed by tracing out the degrees of freedom of the mediator qubits and the ferromagnet is not a unitary operation. Hence, the spectra of H and H_{eff} are, in general, not identical. They match only in the low-energy sector where H_{eff} leads to bounded results. Indeed, when the quantum memory is in contact with a thermal heat bath at inverse temperature β, the expected anyon density (fraction of stabilizer operators W_p with a -1 value) is approximately $1/(e^{\beta\mu(L)} + 1)$ (cf. Sec. IV in

Ref. [82] for a more careful discussion, taking inter-anyonic interactions into account). The thermal energy of the code system is thus

$$\langle H_{\text{eff}} \rangle \approx L^2 \frac{\mu(L)}{e^{\beta\mu(L)} + 1} , \tag{5.20}$$

which vanishes exponentially as $L \to \infty$. The thermal density of anyons is self-consistently suppressed by the effective anyon chemical potential $\mu(L)$. The total thermal energy $\langle H_{\text{eff}} \rangle$ remains thus finite and small even for large L. The fact that $\mu(L)$ diverges as a function of L therefore does not invalidate our effective theory when its full effects are taken into account.

The effective description breaks down in the high-temperature limit, $\beta\mu(L) \ll 1$, which corresponds to populating high-energetic states with finite probability, *i.e.*, the anyon density becomes of order unity. Indeed, in this limit, we get $\langle H_{\text{eff}} \rangle \sim \mu(L)L^2$, which is clearly in contradiction with a finite upper bound on the energy density $\langle H_{\text{eff}} \rangle / L^2$. This breakdown of the low-energy effective theory is of course not surprising, since in this regime the perturbative gadgets no longer work and the magnon expansion for the FM becomes invalid. (For $T > \Delta, J$, the fraction of excited mediator qubits and the magnon occupation numbers become of order unity.)

Thus, our effective long-wave length and low-energy description is self-consistent for sufficiently low temperatures T and sufficiently large code sizes L. This is similar to e.g. the harmonic approximation of crystal vibrations described by phonons. The Hamiltonian $H_{\text{phonon}} = \sum_{\mathbf{q}} D|\mathbf{q}|n_{\mathbf{q}}$ is only valid in the low-energy regime, and high-energy (large $\mathbf{q}$) excitations are self-consistently suppressed by the Bose-Einstein factor $\langle n_{\mathbf{q}} \rangle = 1/(e^{\beta D|\mathbf{q}|} - 1)$.

The effective Hamiltonian (5.12) is not suited to describe the high-energy part of the spectrum, where the anyon density is of order unity. High-energy excitations are produced when anyons are created non-adiabatically, forcing the mediator qubits and the FM to leave their local equilibrium. In such a scenario the gadgets and the FM have no time to react and do not penalize the creation of anyons. In fact, the energy cost to create an anyon "instantaneously" is bounded by a finite constant as argued above. The fast creation of an anyon produces a bunch of high-energy and short-wavelength excitations in the gadgets/FM and these kinds of processes are not described by our effective theory.

In the following, we provide analytical expressions for the regime of validity of our effective theory. In the derivation of Hamiltonian (5.12) we explicitly assumed that mediator qubits reside in their groundstate and the FM is locally aligned along z-direction. This has to remain valid when thermal anyons are produced. So besides the requirement that the coupling B to the external bath is small, *i.e.*, $|B| \ll A$, we work in the *adiabatic regime* where the external bath creates errors in the code on a timescale much longer than $1/A$, or in other words, when the error rate is much smaller than A. For instance, modeling the coupling between code and bath by a generic spin-boson model [73], the error rate $\gamma(\omega)$ describing processes in which an energy ω is transferred from a code qubit to the bath takes the following form [38]

$$\gamma(\omega) = \kappa_n \left| \frac{\omega^n}{1 - e^{-\beta\omega}} \right| e^{-\omega/\omega_c} , \tag{5.21}$$

where ω_c is an arbitrary cut-off and κ_n contains the coupling B to the external bath (in Born approximation, $\kappa_n \propto B^2$). For $n = 1$ the bath is called Ohmic, while it is called super-Ohmic for $n \geq 2$. The adiabaticity condition then simply reads $\gamma(-A) \ll A$. In this case, the mediator qubits and the FM have enough time to adapt to the perturbation generated by an error and stay respectively in an unexcited state or locally aligned along z-direction. In this regime, trying to flip a single qubit of the code will "drag along" a large number of other spins, leading to a large effective energy penalty. To conclude, in such a scenario the low-energy description H_{eff} of the two-spin Hamiltonian H, involving long-range interactions between four-qubit operators, remains valid.

5.6 Backaction effects onto the ferromagnet

Strictly speaking, our analysis of the toric code coupled to a FM (by means of a perturbative Schrieffer-Wolff transformation) is valid when the FM spins are aligned close to the z-direction. This is the reason why we introduced the external field h_z; it stabilizes the FM against the transverse effective magnetic field induced by the toric code and forbids energetically the turning of the total magnetization. However, backaction effects are substantial for the FM spins close to the code and it is interesting to study the dynamics of the FM spins in contact to the toric code. Our study of backaction effects involve both analytical and numerical results and give a good picture of the dynamics of a Heisenberg ferromagnet subject to transverse magnetic field that is localized in a given plane of the lattice.

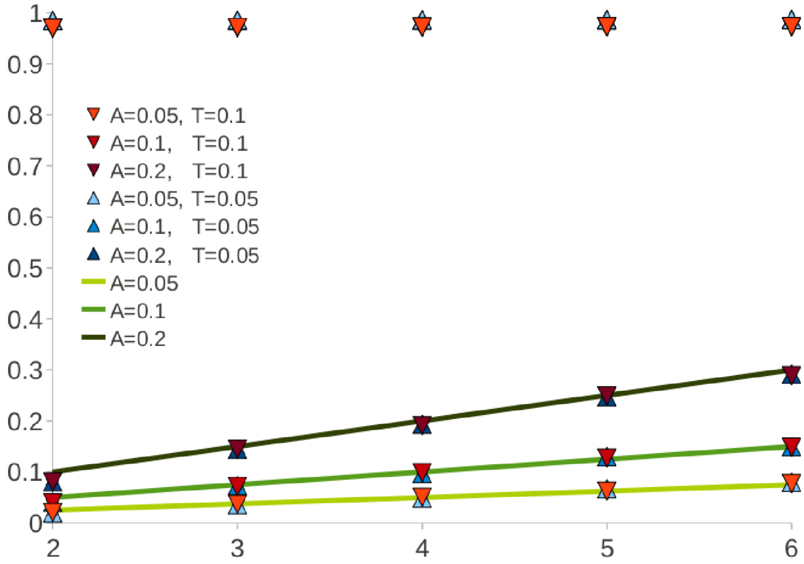

Figure 5.4: A graph of $\langle S_i^x \rangle$ (in the middle of the code) against L for the classical Heisenberg FM with $J = 1$. The data was obtained numerically by using the Metropolis algorithm. The magnetic length is $L_h = L^2$ and the FM size is $\Lambda = 2L_h$. The data shows agreement to the relation $S_i^x(t \to \infty) \propto LA/J$, obtained from Eq. (5.22). On the same graph we plot the total z-magnetization $\frac{1}{N_s}\sum_i \langle S_i^z \rangle$ against L demonstrating that the backaction is only a localized effect. The scaling chosen here is different than the one in the main text. This different choice is only motivated by the difficulty to simulate the classical Heisenberg ferromagnet with a large number of spins. This does not alter the analysis since the chosen scaling satisfies the necessary requirements $E_z \gg E_x$ and $L_h \gg L$.

Let us consider the situation where the coupling of the surface code to the FM is turned on at $t = 0$ and let us calculate the dynamics of the x-component of a FM spin $\mathbf{S}_i$ assuming that $W_j = +1 \, \forall j$. At time $t > 0$ we have, $\langle S_i^x(t) \rangle = \mathrm{Tr} \rho_F S_i^x(t)$, where $\rho_F = e^{-\beta H_F}/\mathrm{Tr} e^{-\beta H_F}$ and $S_i^x(t) = e^{iH't} S_i^x e^{-iH't}$, with H' as in Eq. (5.11). Here, i in $S_i^x(t)$ labels an arbitrary site $\mathbf{R}_i$ of the FM. The dynamics of $\langle S_i^x(t) \rangle$ can be calculated exactly as H' is exactly diagonalizable, see Appendix 5.C. We find that

$$\langle S_i^x(t) \rangle = \frac{A}{\pi J} \sum_p \frac{C\left(\frac{|\mathbf{R}_i - \mathbf{R}_p|}{\sqrt{4\pi J S t}}\right) + S\left(\frac{|\mathbf{R}_i - \mathbf{R}_p|}{\sqrt{4\pi J S t}}\right) - 1}{|\mathbf{R}_i - \mathbf{R}_p|} \tag{5.22}$$

where $C(x)$ and $S(x)$ are the Fresnel integrals. This expression can be evaluated analytically in several limits (see Appendix 5.C for details).

Let us first consider a spin at a FM site $\mathbf{R}_i$ which is directly adjacent to the toric code. For a small code ($L < JS/A$) we find the long-time limit $\langle S_i^x(t \to \infty)\rangle = -AL/J$. We compare this result with a Metropolis simulation of the classical Heisenberg FM and obtain good agreement, see Fig. 5.4. On the other hand, consider a code which is assumed to be large enough such that it can be formally extended to infinity. For this case, we find the finite-time behavior

$$\langle S_i^x(t)\rangle = -4A\sqrt{\frac{St}{\pi J}} \tag{5.23}$$

for spins adjacent to the toric code. The FM spins next to the code adapt to the effective magnetic field in x-direction in a diffusive way with diffusion constant $\sim A^2S/J$. Note that this expression diverges in the long-time limit, which is of course unphysical since $|\langle S_i^x(t)\rangle|$ is bounded by S. This divergence is an artefact of the harmonic (one-magnon) approximation. We thus trust this approximation at most only for times which are such that $|\langle S_i^x(t)\rangle| \leq S$.

The deviations $\langle S_i^x(t)\rangle$ in x-direction become comparable with S after a time of order $t_r \sim JS/A^2$. We refer to t_r as the refreshing time: at this time, the backaction of the surface code on the FM has become substantial with the FM spins close to the code being tilted away from the magnetization direction of the FM (along the z-axis) and pointing now along the x-axis. To restore the full effect of the FM, we refresh the ferromagnetic state with, e.g., a magnetic pulse, so that all spins point again along the z-axis. This procedure has to be repeated periodically on a time scale t_r, which, importantly, is independent of the code size L. This refreshing can be considered as part of a cooling cycle to get the heat generated by the surface code out of the system (note that no measurements of stabilizers or entangling operations are involved). This refreshing prevents the total system, FM plus surface code, to reach a new common equilibrium state, and instead ensures that the FM stays in its own equilibrium state.

Finally, let us consider a spin at a FM site $\mathbf{R}_i$ with a distance d away from the toric code, which is again assumed to be very large. For this case, Eq. (5.22) evaluates to

$$\langle S_i^x(t)\rangle = \frac{16A}{d^2}\sqrt{\frac{JS^3t^3}{\pi}}\left(\cos\left(\frac{d^2}{8JSt}\right) + \sin\left(\frac{d^2}{8JSt}\right)\right) + O(d^{-3})\,. \tag{5.24}$$

The deviation of the FM spins from the ordering along z-direction decays quadratically with the distance from the code.

Longitudinal coupling to the ferromagnet

We note that the refreshing process represents a sufficent condition for maintaining an effective quantum memory Hamiltonian. However, it is not necessary. Indeed, let us consider the extreme case where all the spins of the FM tilt into x-direction (possible if we allow E_x to exceed E_z by assuming e.g. $h_z = 0$). In this worst case scenario, the interaction between plaquettes is not given by the transverse susceptibility of the FM anymore but by the longitudinal one. This fact is derived perturbatively in more detail in Appendix 5.B. The longitudinal susceptibility of the FM has been studied in detail both with a spin wave analysis [105] and with a decoupling method [122,122]. The small $\mathbf{q}$ result reads $\chi_{||}(\mathbf{q}, \omega = 0) = k_B T/8D^2|\mathbf{q}|$. This is valid when $h \ll Dq^2 \ll k_B T$, which is the regime of interest here since we focus on distances smaller than L_h. We note that, contrary to the transverse susceptibility, $\chi_{||}(\mathbf{q}, \omega = 0)$ vanishes at $T = 0$, since it corresponds to particle-hole excitations. Here h points in longitudinal direction and is composed of an external magnetic field (which, as above, is assumed to scale as $1/L^4$) and the magnetic field produced by the surface code. Since the latter scales as $L^2/\Lambda^3 \propto 1/L^7$, see Appendix 5.B, the longitudinal field produced by the memory can safely be ignored. The magnetic length thus scales again as $L_h \propto L^2$. In real space we have $\chi_{||}(\mathbf{r}) \propto T/r^2$.

This worst case is thus analogous to choosing $O_p = a_p^\dagger a_p$ in the Hamiltonian discussed in Sec. 5.2, for which the anyon chemical potential grows logarithmically with L and the memory lifetime grows polynomially. Again, this is what one would have expected, since in the Holstein-Primakoff picture the longitudinal spin component at $\mathbf{R}_p$ is given by $-S + a_p^\dagger a_p$.

5.7 Conclusions

Whether there is a physical Hamiltonian that allows for thermally stable storage of quantum information is a big open question in theoretical physics. The answer will depend on what properties are required for a Hamiltonian to deserve the label "physical". If one only requires bounded strength and locality of interactions, the answer is affirmative, as the 4D toric code shows [34]. The 4D toric code also constitutes the only known example of a quantum memory Hamiltonian for which it is rigorously proven that the lifetime grows without bounds (below a critical temperature) and that it is stable against arbitrary (local and weak enough) perturbations. Requiring locality in at most three dimensions excludes the 4D toric code, but boson-mediated long-range interactions still can make the energetic penalty for creating an anyon arbitrarily high [39,81,82]. If one additionally requires that all operators be bounded (and thereby excludes bosonic operators), the cubic code [60–62] still exhibits self-correcting behavior. Finally, if one takes into account that interactions in nature are in fact two-body and thus requires that all terms in the Hamiltonian involve at most two spins, one excludes all existing proposals.

In this work, we have shown that even under this most rigid understanding of what constitutes a "physical" Hamiltonian, we can still expect to observe self-correcting behavior. The quantum memory Hamiltonian of Ref. [82] emerges as the low-energy effective theory of a 3D model with bounded-strength interactions between nearest-neighbor spins only. This effective Hamiltonian describes the low-energy, long-wavelength response of the system, and self-correcting behavior can only be observed if the noise affecting the memory is such that this description remains valid.

5.8 Acknowledgements

This work was supported by the Swiss NF, NCCR QSIT, and IARPA.

5.A Schrieffer-Wolff transformation

Consider some Hamiltonian H_0 with an energetic gap Δ between a low- and a high-energy subspace. In the context of the perturbative gadgets in Sec. 5.3, H_0 will simply describe the energy splitting Δ of a *mediator qubit*, *i.e.*, an auxiliary qubit that mediates interactions between adjacent qubits. Given some perturbation V with $\|V\| < \frac{\Delta}{2}$, the modified Hamiltonian $H_0 + V$ will display a low-energy subspace of the same dimension as the one of H_0, which is separated from the high-energy spetrum by a gap of at least $\Delta - 2\|V\|$. The SW transformation is then defined as a unitary operator e^S (with S anti-Hermitian), such that $e^S(H_0 + V)e^{-S}$ is block-diagonal with respect to the high- and low-energy subspaces of H_0. Together with the requirement that S be block-off-diagonal with respect to the low- and high-energy subspaces of H_0 and that $\|S\| < \frac{\pi}{2}$, this specifies S uniquely [95].

Let P denote the projector onto the low-energy subspace of H_0. The *effective low-energy Hamiltonian*

$$H_{\text{eff}} = Pe^{S}(H_0 + V)e^{-S}P \tag{5.25}$$

can be expanded in a perturbative series $H_{\text{eff}} = H_{\text{eff}}^{(0)} + H_{\text{eff}}^{(1)} + H_{\text{eff}}^{(2)} + H_{\text{eff}}^{(3)} + \ldots$, where explicit formulae for the low-order effective terms can be derived from Ref. [95]. Let $Q = \mathbb{1} - P$, $V_{\text{d}} = PVP + QVQ$, and $V_{\text{od}} = PVQ + QVP$. We have

$$H_{\text{eff}}^{(0)} = PH_0P\,, \tag{5.26}$$

$$H_{\text{eff}}^{(1)} = PV_{\text{d}}P\,, \tag{5.27}$$

$$H_{\text{eff}}^{(2)} = \frac{1}{2}P\left[L_0^{-1}V_{\text{od}}, V_{\text{od}}\right]P\,, \tag{5.28}$$

and

$$H_{\text{eff}}^{(3)} = \frac{1}{2}P\left[L_0^{-1}\left[L_0^{-1}V_{\text{od}}, V_{\text{d}}\right], V_{\text{od}}\right]P\,. \tag{5.29}$$

In the last two expressions, L_0 is the Liouvillian superoperator $L_0O = [H_0, O]$, whose inverse is given by

$$L_0^{-1}O = -i\lim_{\mu\to 0^+}\int_0^\infty \mathrm{d}t\, e^{-\mu t}e^{iH_0t}Oe^{-iH_0t}\,. \tag{5.30}$$

For the second order effective Hamiltonian, one finds the concise formula

$$H_{\text{eff}}^{(2)} = -\frac{i}{2}\lim_{\mu\to 0^+}\int_0^\infty \mathrm{d}t\, e^{-\mu t}P\left[V_{\text{od}}(t), V_{\text{od}}\right]P\,. \tag{5.31}$$

We note that with $H_0 = -\frac{\Delta}{2}\sigma_r^z$ we have

$$L_0^{-1}\sigma_r^x = -\frac{i}{\Delta}\sigma_r^y\,, \tag{5.32}$$

which leads to Eq. (5.7).

5.B Interactions mediated by a translationally invariant system

Coupling to the transverse component of the FM spins

We show here a detailed derivation of Eq. (5.12) of the main text with the use of a perturbative Schrieffer-Wolff transformation similar to Ref. [101].

We assume here that the FM is in broken-symmetry state with magnetization along z-direction and we couple the surface code to the transverse x component of the FM spins:

$$H = H_0 + V = H_0 + \sum_{\mathbf{q}} S^x_{\mathbf{q}} A_{-\mathbf{q}}\,, \tag{5.33}$$

where H_0 is a general S-spin Hamiltonian and A_i arbitrary operators which commute with H_0 and with each other. The Fourier components are defined through $S_{\mathbf{q}} = \frac{1}{\sqrt{N_s}}\sum_i e^{-i\mathbf{q}\cdot\mathbf{R}_i}\mathbf{S}_i$ and $A_{\mathbf{q}} = \frac{1}{\sqrt{N_s}}\sum_i e^{-\mathbf{q}\cdot\mathbf{R}_i}A_i$, where N_s denotes the number of spins $\mathbf{S}_i$ and $\mathbf{R}_i$ their site. Here we identify the projector P as the operator projecting onto the subspace with a fixed number of magnons $n_{\mathbf{q}}$. Since S^x does not conserve the number of magnons, it is clear that $V_{\mathrm{d}} = 0$ and $V_{\mathrm{od}} = V$. Note that we have absorbed the symmetry-breaking term $h_z\sum_i S^z_i$ into H_0. Up to second order, we obtain from Eq. (5.31)

$$\begin{aligned}
H^{(2)}_{\mathrm{eff}} &= -\frac{i}{2}\lim_{\eta\to0^+}\sum_{\mathbf{q},\mathbf{q}'}\int_0^\infty \mathrm{d}t\, e^{-\eta t}\left[S^x_{\mathbf{q}}(t)A_{-\mathbf{q}}, S^x_{\mathbf{q}'}A_{-\mathbf{q}'}\right]\\
&= -\frac{i}{2}\lim_{\eta\to0^+}\sum_{\mathbf{q},\mathbf{q}'}\int_0^\infty \mathrm{d}t\, e^{-\eta t}\times\\
&\left([S^x_{\mathbf{q}}(t), S^x_{\mathbf{q}'}]A_{-\mathbf{q}'}A_{-\mathbf{q}} + S^x_{\mathbf{q}}(t)S^x_{\mathbf{q}'}\underbrace{[A_{-\mathbf{q}}, A_{-\mathbf{q}'}]}_{=0}\right).
\end{aligned} \tag{5.34}$$

We assume that the S-spins are in thermal equilibrium, described by the canonical density matrix $\rho = e^{-\beta H_F}/\mathrm{Tr}\, e^{-\beta H_F}$, where H_F is the S-spin Hamiltonian without the coupling to the plaquettes and corresponds to the main part of the Hamiltonian in Eq. (5.33), *i.e.*, $H_F = H_0$. In doing so, we neglect the backaction of the toric code on the ferromagnet. This backaction will be addressed in Appendix 5.C below where we show that it leads to a localized effect on the ferromagnet which becomes relevant when the size of the toric code increases (see also Sec. 5.6 in the main text). Here, we rely on a formal perturbation expansion in powers of $\|A_i\|/J$. Convergence of this formal expansion is an interesting question by itself and can be approached along the lines discussed in Ref. [95]. However, such rigorous treatment is beyond the present scope. Still, in the one-magnon (or harmonic) approximation, the effective Hamiltonian Eq. (5.12) in the main text is exact in all orders of $\|A_i\|$, thus showing that all higher order contributions of the Schrieffer-Wolff expansion vanish exactly in the one-magnon regime.

The equilibrium expectation values are denoted by $\langle\ldots\rangle$. Since H_0 is translationally invariant, such that $\langle S^\alpha_{\mathbf{r}_i} S^\beta_{\mathbf{r}_j}\rangle = \langle S^\alpha_{\mathbf{0}} S^\alpha_{\mathbf{r}_j-\mathbf{r}_i}\rangle$, we have $\langle S^\alpha_{\mathbf{q}} S^\alpha_{\mathbf{q}'}\rangle = \langle S^\alpha_{\mathbf{q}} S^\alpha_{-\mathbf{q}}\rangle \delta_{\mathbf{q}+\mathbf{q}',\mathbf{0}}$, and thus

$$\begin{aligned} H^{(2)}_{\text{eff}} &= -\frac{i}{2} \lim_{\eta\to 0^+} \sum_{\mathbf{q}} \int_0^\infty \mathrm{d}t\, e^{-\eta t} \left\langle [S^x_{\mathbf{q}}(t), S^x_{-\mathbf{q}}] \right\rangle A_{\mathbf{q}} A_{-\mathbf{q}} \\ &= -\frac{1}{2} \sum_{\mathbf{q}} A_{-\mathbf{q}} \chi_{xx}(\mathbf{q}) A_{\mathbf{q}}\,, \end{aligned} \tag{5.35}$$

where $\chi_{xx}(\mathbf{q})$ is the static spin susceptibility.

Coupling to the longitudinal component of the FM spins

We are now interested in the case where the surface code is coupled to the longitudinal component of the FM spins:

$$H = H_0 + V = H_0 + A \sum_i W_i S^z_i\,, \tag{5.36}$$

where the sum runs over the L^2 lattice sites lying in the plane of the surface code. The main part H_0 is the Hamiltonian of the FM, *i.e.*, $H_0 = H_F$, which contains the symmetry-braking term $h_z \sum_i S^z_i$. As above, we identify P as the operator projecting onto the subspace with a fixed number of magnons $n_{\mathbf{q}}$. In order to distinguish between the diagonal and off-diagonal parts of the perturbation, it is useful to apply the Holstein-Primakoff transformation in the harmonic approximation (see Eq. (6) in the main text). Doing so we obtain

$$V = -SA \sum_i W_i + A \sum_i W_i a^\dagger_i a_i\,. \tag{5.37}$$

In Fourier space Eq. (5.37) reads

$$V = -SA\sum_i W_i + \frac{A}{N_s}\sum_i W_i \sum_{\mathbf{q},\mathbf{q}'} e^{i\mathbf{R}_i\cdot(\mathbf{q}-\mathbf{q}')} a^\dagger_{\mathbf{q}} a_{\mathbf{q}'}. \tag{5.38}$$

It is now straightforward to distinguish between the diagonal and the off-diagonal part of the perturbation, namely

$$\begin{aligned} V_{\mathrm{d}} &= -SA\sum_i W_i + \frac{A}{N_s}\sum_i W_i \sum_{\mathbf{q}} a^\dagger_{\mathbf{q}} a_{\mathbf{q}}\,, &(5.39)\\ V_{\mathrm{od}} &= \frac{A}{N_s}\sum_i W_i \sum_{\mathbf{q}\neq\mathbf{q}'} e^{i\mathbf{R}_i\cdot(\mathbf{q}-\mathbf{q}')} a^\dagger_{\mathbf{q}} a_{\mathbf{q}'}\,. &(5.40)\end{aligned}$$

Absorbing V_{d} into the main part of the Hamiltonian, we rewrite

$$H = H_0' + V_{\mathrm{od}}\,, \tag{5.41}$$

with (in the harmonic approximation)

$$H_0' = -SA\sum_i W_i + \sum_{\mathbf{q}} \epsilon_{\mathbf{q}} n_{\mathbf{q}} + \frac{A}{\Lambda^3}L^2\sum_{\mathbf{q}} n_{\mathbf{q}}, \tag{5.42}$$

where, as in the main text $\epsilon_{\mathbf{q}} = \omega_{\mathbf{q}} + h_z$, we assumed that the surface code is free of anyons, *i.e.*, $W_i = +1$, and we used $N_s = \Lambda^3$. We see from Eq. (5.42) that the backaction effect of the surface code increases the gap of the magnons from h_z to $h_z' = h_z + AL^2/\Lambda^3$. However this additional term has no weight in the thermodynamic limit since it scales with Λ^{-3}. Using the specific choice of scaling from the main text, we have $h_z \propto 1/L^4$ while $L^2/\Lambda^3 \propto 1/L^7$. In the thermodynamic limit the magnetic length is thus just given by the external magnetic field h_z

$$L_{h_z'} \to L_{h_z} \propto L^2 \quad \text{for} \quad L \to \infty\,. \tag{5.43}$$

This allows us to safely conclude that the backaction of the surface code is negligible in this case.

Using Eq. (5.31), we find

$$
\begin{aligned}
H_{\mathrm{eff}}^{(2)} &= \frac{A^2}{2N_s^2}\sum_{i,j} W_i W_j \sum_{\mathbf{q}\neq\mathbf{q}',\mathbf{k}\neq\mathbf{k}'} \frac{e^{i\mathbf{R}_i\cdot(\mathbf{q}-\mathbf{q}')+\mathbf{R}_j\cdot(\mathbf{k}-\mathbf{k}')}}{\epsilon_{\mathbf{q}}-\epsilon_{\mathbf{q}'}} \left[a_{\mathbf{q}}^{\dagger}a_{\mathbf{q}'}, a_{\mathbf{k}}^{\dagger}a_{\mathbf{k}'}\right] \\
&= \frac{A^2}{2N_s^2}\sum_{i,j} W_i W_j \sum_{\mathbf{q}\neq\mathbf{q}'} \frac{n_{\mathbf{q}}-n_{\mathbf{q}'}}{\epsilon_{\mathbf{q}}-\epsilon_{\mathbf{q}'}} e^{i(\mathbf{q}-\mathbf{q}')\cdot(\mathbf{R}_i-\mathbf{R}_j)} \\
&= \frac{A^2}{2N_s^2}\sum_{i,j} W_i W_j \sum_{\mathbf{q}',\mathbf{k}} \frac{n_{\mathbf{k}+\mathbf{q}'}-n_{\mathbf{q}'}}{\epsilon_{\mathbf{k}+\mathbf{q}'}-\epsilon_{\mathbf{q}'}} e^{i\mathbf{k}\cdot(\mathbf{R}_i-\mathbf{R}_j)} \\
&= -\frac{A^2}{2N_s^2}\sum_{i,j} W_i W_j \sum_{\mathbf{q},\mathbf{k}} \frac{e^{\beta(\epsilon_{\mathbf{k}+\mathbf{q}}-\epsilon_{\mathbf{k}})}}{\epsilon_{\mathbf{k}+\mathbf{q}}-\epsilon_{\mathbf{k}}} n_{\mathbf{k}+\mathbf{q}}(n_{\mathbf{k}}+1) e^{i\mathbf{q}\cdot(\mathbf{R}_i-\mathbf{R}_j)} \\
&= -\frac{A^2}{2N_s}\sum_{i,j} W_i W_j \sum_{\mathbf{k}} \chi_{zz}(\mathbf{q},\omega=0) e^{i\mathbf{q}(\mathbf{R}_i-\mathbf{R}_j)} \qquad (5.44)
\end{aligned}
$$

where the last equality comes from the definition of the susceptibility in Eq. (5.14) evaluated in the one-magnon approximation. Following the approach of Ref. [105] assuming that $\beta\epsilon_{\mathbf{q}+\mathbf{k}}, \beta\epsilon_{\mathbf{q}}, \beta(\epsilon_{\mathbf{k}+\mathbf{q}}-\epsilon_{\mathbf{k}}) \ll 1$, we have that

$$
\chi_{zz}(\mathbf{q},\omega=0) = \frac{k_B T}{8D^2}\frac{1}{|\mathbf{q}|} \quad \text{for} \quad |\mathbf{q}| \to 0, \qquad (5.45)
$$

where $D = 2JS$. From Eqs. (5.44) and (5.45), we finally find a chemical potential for the anyons $\mu \propto k_B T \ln(L/2)$ as shown in the main text. We note that the term $-SA\sum_i W_i$ in H_0' leads to an increase of the chemical potential by $2SA$. However, this term does not scale with L and can be neglected for large L.

5.C Detailed study of the ferromagnetic spin dynamics under the effective longitudinal magnetic field produced by the toric code

For simplicity, we write in this Appendix H instead of H', where H' is as given in Eq. (5.11). Furthermore, we are interested in the stable regime of the quantum memory, where topological defects are created on timescales larger than the time on which FM-spins close to the toric code adjust. We thus assume $W_i \equiv +1$ for all stabilizers W_i. In the one-magnon approximation, we then have

$$H = \sqrt{2S}A \sum_p (a_p + a_p^\dagger) + \sum_{\mathbf{k}} \epsilon_{\mathbf{k}} a_{\mathbf{k}}^\dagger a_{\mathbf{k}} \,, \tag{5.46}$$

with $\epsilon_{\mathbf{k}} = \omega_{\mathbf{k}} + h_z$ and $\omega_{\mathbf{k}} = 4JS[3 - (\cos(k_x) + \cos(k_y) + \cos(k_z))] \approx 2JS\mathbf{k}^2$.

Non-equilibrium response for S^x

We now calculate the time-dependent expectation value of the local x-magnetization, defined as

$$\langle S_i^x(t) \rangle = \mathrm{tr}\{\rho_F S_i^x(t)\} \tag{5.47}$$

where

$$S_i^x(t) = e^{iHt} S_i^x e^{-iHt} \tag{5.48}$$

with

$$\rho_F = e^{-H_F/k_B T}/Z_F, \;\; Z_F = \mathrm{Tr} e^{-H_F/k_B T} \tag{5.49}$$

and $H_F = \sum_{\mathbf{k}} \epsilon_{\mathbf{k}} a_{\mathbf{k}}^\dagger a_{\mathbf{k}}$ in one-magnon approximation.

We define the polaron transformation [82, 103]

$$\mathcal{S} = \frac{\sqrt{2S}A}{\sqrt{N_s}} \sum_p \sum_{\mathbf{k}} \frac{1}{\epsilon_{\mathbf{k}}} (e^{i\mathbf{k}\mathbf{R}_p} a_{\mathbf{k}} - \text{h.c.}) \tag{5.50}$$

which exactly diagonalizes H. We have

$$e^{\mathcal{S}} a_i e^{-\mathcal{S}} = a_i + [\mathcal{S}, a_i] = a_i - \frac{\sqrt{2S}A}{N_s} \sum_p \sum_{\mathbf{k}} \frac{1}{\varepsilon_{\mathbf{k}}} e^{i\mathbf{k}(\mathbf{R}_i - \mathbf{R}_p)} \tag{5.51}$$

and

$$e^{\mathcal{S}} a_{\mathbf{k}} e^{-\mathcal{S}} = a_{\mathbf{k}} + [\mathcal{S}, a_{\mathbf{k}}] = a_{\mathbf{k}} - \frac{\sqrt{2S}A}{\sqrt{N_s}} \sum_p \frac{1}{\varepsilon_{\mathbf{k}}} e^{-i\mathbf{k}\mathbf{R}_p} \tag{5.52}$$

Using these two relations, one easily shows that

$$e^{\mathcal{S}} H e^{-\mathcal{S}} = H_F + \mathrm{const}\,. \tag{5.53}$$

We can thus calculate

$$\begin{aligned}\langle S_i^x(t)\rangle &= \mathrm{tr}\left\{\rho_F e^{iHt} S_i^x e^{-iHt}\right\} \\ &= \mathrm{tr}\left\{\rho_F e^{-\mathcal{S}} e^{iH_F t} e^{\mathcal{S}} S_i^x e^{-\mathcal{S}} e^{-iH_F t} e^{\mathcal{S}}\right\}\ .\end{aligned} \tag{5.54}$$

In the Holstein-Primakoff picture, $S_i^x = \sqrt{2S}(a_i + a_i^\dagger)$, such that

$$\begin{aligned}\langle S_i^x(t)\rangle &= \sqrt{2S}\,\mathrm{tr}\left\{\rho_F e^{-\mathcal{S}} e^{iH_F t}(a_i + a_i^\dagger) e^{-iH_F t} e^{\mathcal{S}}\right\} \\ &\quad - \frac{4SA}{N_s}\sum_p\sum_{\mathbf{k}}\frac{1}{\varepsilon_{\mathbf{k}}}\cos(\mathbf{k}(\mathbf{R}_i - \mathbf{R}_p)) \\ &= \sqrt{2S}\frac{1}{\sqrt{N_s}}\sum_{\mathbf{k}}\mathrm{tr}\left\{\rho_F e^{-\mathcal{S}}\left(e^{i\mathbf{k}\mathbf{R}_i} e^{-\varepsilon_{\mathbf{k}} t} a_{\mathbf{k}} + \mathrm{h.c.}\right) e^{\mathcal{S}}\right\} \\ &\quad - \frac{4SA}{N_s}\sum_p\sum_{\mathbf{k}}\frac{1}{\varepsilon_{\mathbf{k}}}\cos(\mathbf{k}(\mathbf{R}_i - \mathbf{R}_p)) \\ &= \frac{2SA}{N_s}\sum_p\sum_{\mathbf{k}}\frac{1}{\varepsilon_{\mathbf{k}}} e^{i\mathbf{k}(\mathbf{R}_i - \mathbf{R}_p)} e^{-\varepsilon_{\mathbf{k}} t} + \mathrm{c.c.} \\ &\quad - \frac{4SA}{N_s}\sum_p\sum_{\mathbf{k}}\frac{1}{\varepsilon_{\mathbf{k}}}\cos(\mathbf{k}(\mathbf{R}_i - \mathbf{R}_p)) \\ &= \frac{4SA}{N_s}\sum_p\sum_{\mathbf{k}}\frac{1}{\varepsilon_{\mathbf{k}}}\left(\cos[\mathbf{k}(\mathbf{R}_i - \mathbf{R}_p] - \varepsilon_{\mathbf{k}} t) - \cos[\mathbf{k}(\mathbf{R}_i - \mathbf{R}_p)]\right)\end{aligned} \tag{5.55}$$

In order to further evaluate the sum $\sum_{\mathbf{k}}$, we go to the continuum limit and replace it by the integral $\frac{N_s}{(2\pi)^3}\int \mathrm{d}\mathbf{k}$. We also use the small-$\mathbf{k}$/small-$h_z$ expansion of the magnon dispersion, $\varepsilon_{\mathbf{k}} \approx 2JS\mathbf{k}^2$. We obtain

$$\begin{aligned}\langle S_i^x(t)\rangle &\approx \frac{2}{(2\pi)^3}\frac{A}{J}\sum_p\int \mathrm{d}\mathbf{k}\frac{1}{\mathbf{k}^2}\left(\cos[\mathbf{k}(\mathbf{R}_i - \mathbf{R}_p] - 2JS\mathbf{k}^2 t) - \cos[\mathbf{k}(\mathbf{R}_i - \mathbf{R}_p)]\right) \\ &\approx \frac{A}{\pi J}\sum_p\frac{1}{|\mathbf{R}_i - \mathbf{R}_p|}\left(C(\frac{|\mathbf{R}_i - \mathbf{R}_p|}{\sqrt{4\pi JSt}}) + S(\frac{|\mathbf{R}_i - \mathbf{R}_p|}{\sqrt{4\pi JSt}}) - 1\right)\ ,\end{aligned} \tag{5.56}$$

where $C(x) = \int_0^x \cos(\frac{\pi}{2}t^2)\mathrm{d}t$ and $S(x) = \int_0^x \sin(\frac{\pi}{2}t^2)\mathrm{d}t$ are the Fresnel integrals.

Let us first study a FM spin adjacent to the code plane. In the long-time limit $t \to \infty$, we have, approximating the code by a disk of radius

$L/2$ around our spin of interested at $\mathbf{R}_i$,

$$\begin{aligned}\langle S_i^x(t)\rangle &= -\frac{A}{\pi J}\sum_p \frac{1}{|\mathbf{R}_i-\mathbf{R}_p|}\\ &\approx -\frac{A}{\pi J}\int_0^{L/2} \mathrm{d}R(2\pi R)\frac{1}{R}\\ &= -\frac{AL}{J}\,. \end{aligned} \tag{5.57}$$

As $|\langle S_i^x(t)\rangle|$ is bounded by S, this can of course only be valid for code sizes $L \leq \frac{JS}{A}$. Let us thus consider the opposite limit of a code which is large enough such that the integral in the integration over all code plaquettes can formally be extended to infinity. Then,

$$\begin{aligned}\langle S_i^x(t)\rangle &= \frac{A}{\pi J}\int_0^{\infty} \mathrm{d}R(2\pi R)\frac{1}{R}\left(C(\frac{R}{\sqrt{4\pi JSt}})+S(\frac{R}{\sqrt{4\pi JSt}})-1\right)\\ &= -4A\sqrt{\frac{St}{\pi J}}\,. \end{aligned} \tag{5.58}$$

The FM spins next to the code align with the local field in a diffusive way, with diffusion constant $\sim A^2S/J$. For a large enough code, the evolution of a local FM spin is independent of the code size, as expected. For a spin with distance d to the code, the integration is more involved and one finds

$$\begin{aligned}\langle S_i^x(t)\rangle &= \frac{A}{\pi J}\int_0^{\infty} \mathrm{d}R(2\pi R)\frac{1}{\sqrt{d^2+R}}\left(C(\frac{\sqrt{d^2+R}}{\sqrt{4\pi JSt}})+S(\frac{\sqrt{d^2+R}}{\sqrt{4\pi JSt}})-1\right)\\ &= \frac{16A}{d^2}\sqrt{\frac{JS^3t^3}{\pi}}\left(\cos(\frac{d^2}{8JSt})+\sin(\frac{d^2}{8JSt})\right)+O(d^{-3})\,. \end{aligned} \tag{5.59}$$

The deviation decays quadratically with the distance from the code. The results in Eqs. (5.58) and (5.59) both diverge as $t\to\infty$. This is an artefact of the harmonic (one-magnon) expansion. We thus trust these results only for times t such that $|\langle S_i^x(t)\rangle| \leq S$.

Part II

Quantum Error Correction and Non-Abelian Anyons

CHAPTER 6

An Efficient Markov Chain Monte Carlo Algorithm for the Surface Code

Adapted from:
Adrian Hutter, James R. Wootton, and Daniel Loss
"An efficient Markov chain Monte Carlo algorithm for the surface code",
Phys. Rev. A **89**, 022326 (2014)

Minimum-weight perfect matching (MWPM) has been the primary classical algorithm for error correction in the surface code, since it is of low runtime complexity and achieves relatively low logical error rates [Phys. Rev. Lett. **108**, 180501 (2012)]. A Markov chain Monte Carlo (MCMC) algorithm [Phys. Rev. Lett. **109**, 160503 (2012)] is able to achieve lower logical error rates and higher thresholds than MWPM, but requires a classical runtime complexity which is super-polynomial in L, the linear size of the code. In this work we present an MCMC algorithm that achieves significantly lower logical error rates than MWPM at the cost of a runtime complexity increased by a factor $O(L^2)$. This advantage is due to taking correlations between bit- and phase-flip errors (as they appear, for example, in depolarizing noise) as well as entropic factors (i.e., the numbers of likely error paths in different equivalence classes) into account. For depolarizing noise with error rate p, we present the first efficient algorithm for which the logical error rate is suppressed as $O((p/3)^{L/2})$ for $p \to 0$ – an exponential improvement over all previously existing efficient algorithms. Our algorithm allows for trade-offs between runtime and achieved logical error rates as well as for parallelization, and can be also used to correct in the case of imperfect stabilizer measurements.

6.1 Introduction

An important primitive for the *processing* of quantum information is the ability to *store* it despite constant corruptive influence of the external environment on the applied hardware and imperfections of the latter. While one approach seeks to achieve this by constructing a *self-correcting quantum memory* (see Ref. [113] for a recent review), an alternative possibility is to dynamically protect the stored quantum information by constantly pumping entropy out of the system. Topological quantum error correction codes [16, 17] store one logical qubit in a large number of physical qubits, in a way which guarantees that a sufficiently low density of errors on the physical qubits can be detected and undone, without affecting the stored logical qubit. Most promising is the surface code [44,47,57,66], which requires only local four-qubit parity operators to be measured. While proposals for direct measurement of such operators exist [39,123,124], most of the literature focuses on time-dependent interactions between the four qubits and an auxiliary qubit, allowing to perform sequential CNOT gates and to finally read the measurement result off the auxiliary qubit. See Ref. [48] for a recent review.

In order to decode the syndrome information, i.e., use the outcomes of all four-qubit measurements to find out how to optimally perform error correction, a classical computation is necessary. This classical computation is not trivial and brute force approaches are infeasible. Decoding algorithms based on renormalization techniques [125] or minimum-weight perfect matching (MWPM) [126] have a runtime complexity $O(L^2)$ and can be parallelized to $O(L^0)$ (neglecting logarithms), where L is the linear size of the code. As these algorithms are approximative, the logical error rates achievable with them fall short of those theoretically achievable by brute force decoding. A Markov chain Monte Carlo (MCMC) algorithm [127] can cope with higher physical error rates than the two mentioned algorithms, but has super-polynomial (yet sub-exponential) runtime complexity. In this work, we present an efficient MCMC decoding algorithm that allows to achieve logical error rates lower than those achievable by means of MWPM.[1] Equivalently, a smaller code size is required to achieve a certain target logical error rate. Our algorithm allows for trade-offs between runtime and achieved logical error rate. If we define the runtime of our algorithm to be the minimal computation time such that the achieved logical error rate is lower than the one achievable by means of MWPM, we find it to be $O(L^4)$.

Furthermore, we describe a method for achieving logical error rates which, in the limit of a vanishing error rate $p \to 0$, are exponentially smaller than those of previous methods. After completion of this work, a method for achieving the same asymptotic error suppression with optimal run-time complexity has been described in Ref. [128].

In summary, in comparison to alternative algorithms [125,126] our algorithm allows for lower quantum information error rates and smaller code sizes at the cost of a (polynomially) higher classical runtime complexity. Given the current state of the art of quantum and classical information processing, shifting requirements from quantum to classical seems desirable. Our algorithm is generalizable to the (realistic) case of imperfect stabilizer measurements, though we restrict numerical simulations in this work to the case of perfect measurements for simplicity.

6.2 Error correction in surface codes

Stabilizer operators are, in the context of the surface code, tensor products of σ^x or σ^z operators (see Fig. 6.1) which are required to yield a

---

[1] As the error correction algorithm of Ref. [125] itself allows for trade-offs between runtime and error rates, and MWPM based algorithms have attained most interest in the literature, we do not directly compare our algorithm to the former.

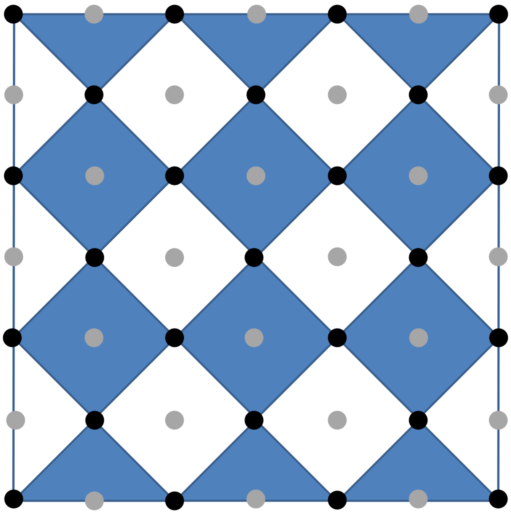

Figure 6.1: An $L = 4$ surface code. Black dots are data qubits, grey dots are syndrome qubits that allow to read off the results of the stabilizer measurements when sequential CNOT gates have been performed between them and the adjacent data qubits. Stabilizer operators are either tensor products of σ^x operators (acting on the data qubits around a white square/triangle) or tensor products of σ^z operators (acting on the data qubits around a blue (dark) square/triangle).

$+1$ eigenvalue when applied to the quantum state stored in the code. Eigenvalues -1 are treated as errors and interpreted as the presence of an *anyon*. A surface code of size L has $n_{\text{stab}} = 2L(L-1)$ (3- and 4-qubit) stabilizers. Since all stabilizers commute, they can be measured simultaneously and hence the presence of anyons can be detected. Any Pauli operator σ^x, σ^y, or σ^z applied to a data qubit creates at least one anyon as it anti-commutes with at least one stabilizer. We call violated σ^x-stabilizers s-anyons and violated σ^z-stabilizers p-anyons.

Given some anyon configuration A, the goal is to apply a series of single-qubit σ^x and σ^z operators, such that all anyons are removed and a trivial operation has been performed on the code subspace. Two such hypotheses about what errors the physical qubits have suffered are equivalent if they can be deformed into each other through the application of stabilizers. Equivalent error chains will lead to the same operation performed on the code subspace (consisting of the states which are $+1$ eigenstates of each stabilizer). For the surface code, there are four such equivalence classes. The goal is therefore to find the most probable equivalence class of error chains and not to find the most likely error chain. The most likely error chain need not be an element of the most likely equivalence class, though trying to correct by undoing the most likely error path is a reasonable approximation and is the idea behind minimum-weight perfect matching correction algorithms. More precisely, MWPM matches both kinds of anyons independently of each other and thus ignores potential correlations between σ^x- and σ^z-errors.

Decoherence models in which each qubit independently is subject to the channel

$$\rho \mapsto p_I \rho + p_x \sigma^x \rho \sigma^x + p_y \sigma^y \rho \sigma^y + p_z \sigma^z \rho \sigma^z \tag{6.1}$$

(with $p_I + p_x + p_y + p_z = 1$) allow for efficient simulation on a classical computer. While physical decoherence models may not exactly have the form of Eq. (6.1), they may be approximated by such a channel through a *Pauli twirl approximation* [129, 130]. The two most frequently studied noise models of the form of Eq. (6.1) are *independent bit- and phase-flip errors* ($p_x = p_b(1 - p_p)$, $p_z = p_p(1 - p_b)$ and $p_y = p_b p_p$ for independent bit- and phase-flip probabilities p_b and p_p) and *depolarizing noise* ($p_x = p_z = p_y = \frac{p}{3}$). The theoretical maximal error rates up to which error correction is possible by exact error correction are known to be $p_b, p_p < 10.9\%$ for independent bit- and phase-flip errors [57] and $p < 18.9\%$ for depolarizing noise [131]. Any approximate error correction algorithm will yield threshold error rates below these theoretical maxima.

Minimum weight matching considers bit-flip errors (which create p-anyons) and phase-flip errors (which create s-anyons) independently. As such it is only well designed for noise models with no correlations between σ^x- and σ^z-errors. Errors models that do have these correlations, such as depolarizing noise, can only be treated approximately. Typically this means that the correction will be done as if the bit and phase-flip errors occurred with independent probabilities $p_b = p_x + p_y$ and $p_p = p_x + p_y$, calculated according to the true (correlated) noise model.

This suboptimal treatment of correlated noise leads to suboptimal behaviour. Thresholds are significantly lower than the theoretical maxmima and the effectiveness below threshold is also significantly affected. For example, let us consider the behaviour for depolarizing noise with very low p. In this case the probability of a logical error is dominated by the probability of the most likely fatal error pattern (one which causes the decoder to guess the wrong equivalence class). This means the fatal error pattern with the minimum number of single qubit errors.

Perfect matching treats this noise model as one in which bit and phase-flip errors occur independently with probabilities $p_b = p_p = 2p/3$. A fatal error pattern that causes a logical bit-flip error requires, for odd L, at least $\frac{L+1}{2}$ single qubit bit-flips to occur in a line, such that they create a pair of p-anyons separated by just over half the size of the code (or a single p-anyon which is closer to the boundary to which it is not connected by the error chain). This is because the matching will incorrectly think that they were created by the $\frac{L-1}{2}$ bit-flips required to create them within the opposite equivalence class, since this matching has a smaller weight.

If p is low enough ($p \ll 1/L^2$), the probability of a logical error is dominated by the most probable error chains that are capable of leading to a logical error after error correction. For perfect matching, this means that in this regime the probability of a logical error is suppressed as $O(p_b^{\frac{L+1}{2}}) = O((2p/3)^{\frac{L+1}{2}})$. Note that this describes the scaling as a function of p only – we have omitted combinatorial prefactors that depend upon L but not upon p.

An optimal decoder that takes the possibility of p_y-errors into account, on the other hand, will only fail for a small fraction of these most likely errors. If there are s-anyons along the error path, it will conclude that p_y-errors have happened and thus infer the correct equivalence class. Such an optimal decoder can only fail if 0 or 1 of the $\frac{L+1}{2}$ bit-flips are due to p_y-errors. The probability of a logical error is thus suppressed as $O((p/3)^{\frac{L+1}{2}})$ – an exponential improvement over MWPM. Recall that this scaling is only valid in the regime $p \ll 1/L^2$.

In Sec. 6.3, we introduce an enhanced version of MWPM. It is the first efficent algorithm that achieves an $O((p/3)^{\frac{L+1}{2}})$ scaling although it is not an optimal decoder in the above sense. The second algorithm, discussed in Sec. 6.4, uses enhanced MWPM as a starting point and then performs Markov chain Monte Carlo sampling in order to further reduce the logical error rate. It *is* an efficient optimal decoder for $p \to 0$ and – more importantly in practice – achieves for non-vanishing values of p significantly lower error rates than both standard and enhanced MWPM due to taking entropic factors, i.e., the *numbers* of likely error paths in the different equivalence classes into account.

6.3 Enhanced MWPM

Our first method consists of only a small change to the standard MWPM decoding, but it nevertheless has a large effect. To explain this fully, we must first explain standard MWPM decoding for the surface code (see, e.g., Ref. [132]) in more detail.

For a graph with weighted edges between an even number of vertices, Edmond's MWPM algorithm [70] finds the pairing of minimal weight efficiently. To use this for decoding of the surface code, the problem of determining the most likely equivalence class with which to correct the errors must therefore be mapped to a matching problem. In fact, the decoding of the surface code becomes two separate matching problems, one for the s-anyons and one for the p-anyons. In each case the anyons are used as the vertices of the graph, and the weight assigned to the edge between any two anyons is taken to be the minimal number of single qubit errors necessary to link them (their Manhattan distance).

To take into account the effects of the boundaries of the code, for each anyon a virtual partner is placed on the closer boundary of the type which is able to absorb it (top and bottom for s-anyons and left and right for p-anyons). An edge is added between each anyon and its virtual partner, whose weight is given by the minimal number of single qubit errors necessary to link the anyon to the boundary. Including these virtual anyons ensures that the number of vertices in the graph is even and that each anyon can be matched to the closest absorbing boundary.

All virtual anyons are connected to each other with zero weight, allowing for virtual anyons on opposite sides of the code to be matched. Without loss of generality, we can assume that there is either no such code-spanning matching or there is only one. Any other case can be mapped to either one of these without increasing the weight of the matching. Note that, for any given anyon configuration, whether there is zero or one code-spanning matching of virtual anyons is in one-to-one correspondence with the equivalence class of the matching.

For the s-anyons, the result of the matching can be interpreted as a pattern of σ^z-errors that are consistent with the syndrome. The minimal weight matching therefore gives the pattern with the smallest number of σ^z errors. The minimal weight matching for the p-anyons gives the corresponding result for σ^x errors. When superimposed, any spin that has suffered both a σ^x- and a σ^z-error can be interpreted as having suffered a σ^y. The total error configuration therefore contains the minimum number of errors when a σ^y is counted as two errors: a σ^x and a σ^z. For error models in which bit- and phase-flips occur independently, the matching corresponds to the most likely error configuration. It can therefore be assumed that the most likely equivalence class is the same as that of this matching, and so the errors can be corrected accordingly. The four equivalence classes of errors in the surface code may be identified by determining the parity of the number of errors that lie on a given line that links the top and bottom or left and right boundary.

The total error configuration output by the matching does not, however, necessarily contain the minimum number of errors when a σ^y is counted as a single error. This would be the relevant measure of the error number for depolarizing noise, since this has all error types occur with equal probability. It is clear that the equivalence class of the matching will still most likely correspond to the most likely class in many cases, and so this decoding will yield good suppression of errors [132]. However, its performance will be suboptimal.

To enhance the results of MWPM, consider the case that an additional virtual anyon is added to each edge. These will be connected to each other and to all the virtual anyons on their edge with zero weight. They are not connected to any real anyons. We consider also that the virtual anyons on each edge are no longer connected to the virtual anyons of the other edge. Despite these differences, the results of the matching will be the same as those above, since the additional anyons can provide the same effect as the single code-spanning matching. If such a matching is required, the two virtual anyons on each edge that would have matched to each other will match to their respective additional anyon. If it is not required, the additional anyons match to each other.

Using the above set-up, we can now determine how to force MWPM to output the minimum weight matching for each equivalence class, rather than simply the overall minimum. If the two additional virtual anyons are removed, the corresponding result cannot have a code-spanning matching. If they are added but not connected to each other, they are forced to each match with a virtual anyon on their edge. This therefore forces a result for which there is a code spanning matching. These two results will therefore contain the true overall minimum weight matching, as well as the minimum weight matching for the opposite equivalence class. See Fig. 6.2 for an illustration.

There is one case for which the above is not true. If all anyons exist only on one side of the code, the additional virtual anyon will be the only virtual anyon on the other side. With nothing to match to, the matching algorithm will not yield a result. To mitigate this, the additional anyon is connected to all real anyons on the other side of the code when its own side is empty. If there are no physical anyons, the additional virtual anyons on each edge are connected to each other.

Given the two results obtained using the above method, choosing the

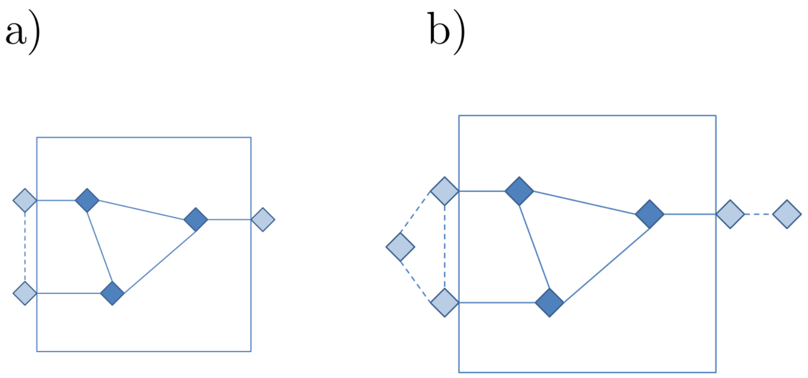

Figure 6.2: Three p-anyons (solid squares) have been detected in a surface code. In order to find hypotheses of minimum weight (maximal probability) about what errors have occurred, we first add virtual anyons (light squares) on the closest absorbing boundary of each real anyon and connect virtual anyons residing on the same boundary; see the a) part of the figure. Dashed lines represent zero-weight edges, solid lines represent non-zero-weight edges. In part b) of the figure, we place an additional virtual anyon on the left and right boundary. Note that each possible pairing in part b) is an element of a different equivalence class then the pairings which are possible in part a).

equivalence class corresponding to the matching with the lowest weight is equivalent to the decoding using the standard matching algorithm. Our enhanced matching differs in that it obtains the lowest weight matching for both equivalence classes of both anyon types. This results in 2×2 possibilities for superimposing these two matchings on top of each other. Each of these matchings is the most likely within its equivalence class for the approximate error model where the correlations between σ^x- and σ^z-errors are ignored. The probabilities of these four error configurations, when calculated using the true correlated error model, will not be in direct correspondence with the weights calculated by the matching algorithm. Hence the error configuration with the highest probability will not necessarily be the one output by the standard matching algorithm. By choosing the equivalence class that corresponds to the most likely error configuration, we can therefore get improved results.

The highly efficient version of MWPM for the surface code [126] requires that the weights in the graph correspond to the geometrical (Manhattan) distance between the corresponding anyons. The zero-weight edges between virtual anyons thus prevent us from straightforwardly employing this algorithm. We thus employ the library `Blossom V` [69], which finds a minimal-weight pairing for arbitrary graphs. For a graph with n vertices and m edges, `Blossom V` has a runtime complexity $O(mn \log n)$. If we pair all real anyons with each other ($n = O(L^2)$, $m = O(L^4)$), we obtain a runtime complexity $O(L^6 \log L)$. The number of edges can be reduced to $m = O(L^2)$ by connecting each anyon only with other anyons within some $O(1)$ distance (and increasing this distance if no anyon is found within the initial one). A more sophisticated method of achieving $m = O(L^2)$ would be to employ a Delaunay-triangulation of all real anyons, which has been used for performing error correction in the surface code for the first time in Ref. [38] . Both methods lead to a runtime complexity $O(L^4 \log L)$. Furthermore, a version of perfect matching for graphs with integer weights only (as in our case) that are upper-bouned by N has runtime complexity $O(m^{3/4} n \log N) = O(L^{3.5})$ [133]. This is less than the $O(L^4)$ runtime wich we use for the Metropolis sampling (see Sec. 6.4).

However, for our actual numerical simulations we simply use `Blossom V` and connect all real anyons with each other. This allows us to compare our MCMC algorithm with the best performance that could possibly be achieved using MWPM.

To determine the low-p scaling of the logical error rate with L, it is sufficient to consider the minimal error configurations that can cause a logical (say, X-)error. These act only on a single line, and create p-anyons on that line at the boundaries between spins that have suffered a σ^x- or σ^y-error and those that have not.

For the types of errors we consider here, the matching of the s-anyons will yield one error configuration that is much less likely than the other. We will therefore consider only the other, which is the same as would be given by standard MWPM. Only two total error configurations are therefore considered, with two possible layouts of the σ^x-errors determined by the matching of the p-anyons for both classes, superimposed with the single layout of σ^z-errors given by the standard matching of the s-anyons. Note that, since all p-anyons will be on a line, the minimum weight matching for each equivalence class will be unique.

Consider the case of even L, and that n_x σ^x-errors and n_y σ^y-errors occur on the same line with $n_x + n_y = L/2$. Both matchings of the p-anyons will have the same weight in all cases. The probabilities of the corresponding error configurations will therefore have the same probability when $n_y = 0$. Since there is no reason to choose one over the other, the

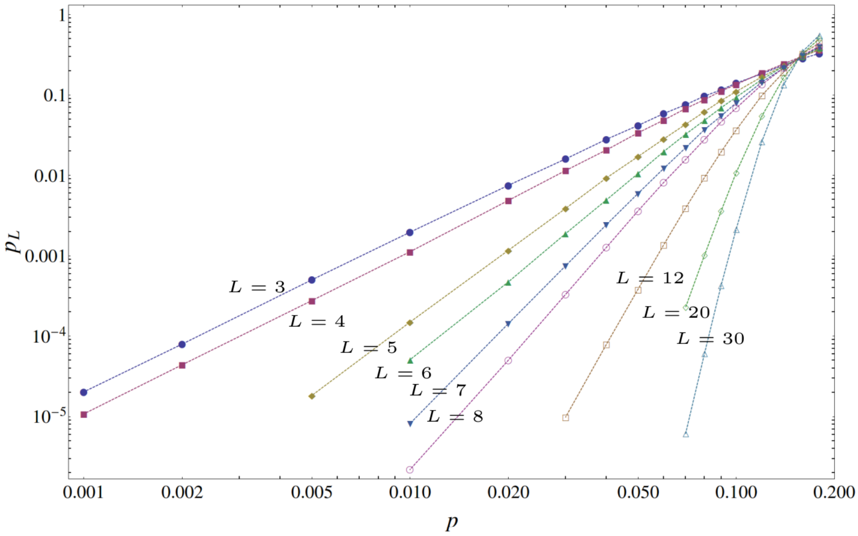

Figure 6.3: Decoherence rates p versus logical error rates p_L for standard MWPM.

wrong one will be chosen and a logical error will occur with probability $1/2$.

For $n_y > 0$ there will also be pairs of s-anyons created, with one on each side of the line in which the p-anyons live. As long as the matching of at least one of these pairs crosses the line, the probability of the error configuration for which the p- and s-anyon matchings coincide will be greater than that for which they do not. The s-anyons therefore show which of the two matchings should be chosen to correct without causing a logical error. At least one s-matching will certainly cross the line as long as there is at least one odd length chain of σ^y-errors. For large L, this will occur with a probability close to unity. The presence of any σ^y-errors therefore, most likely, allows the decoder to make the correct choice. The $p \to 0$ scaling of the logical error rate with L is therefore determined only by the probability of σ^x-errors, and so realizes the optimal $(p/3)^{\frac{L}{2}}$ scaling.

Fig. 6.3 shows the logical error rates of standard MWPM and Fig. 6.4 the ones of enhanced MWPM. The advantages of enhanced over standard MWPM in these figures are still relatively small (at most a factor of 4), showing that we are not yet in the regime of low enough p and high enough L where high exponential improvements can be seen. A numerical comparison of enhanced and standard MWPM can be found in Fig. 6.8.

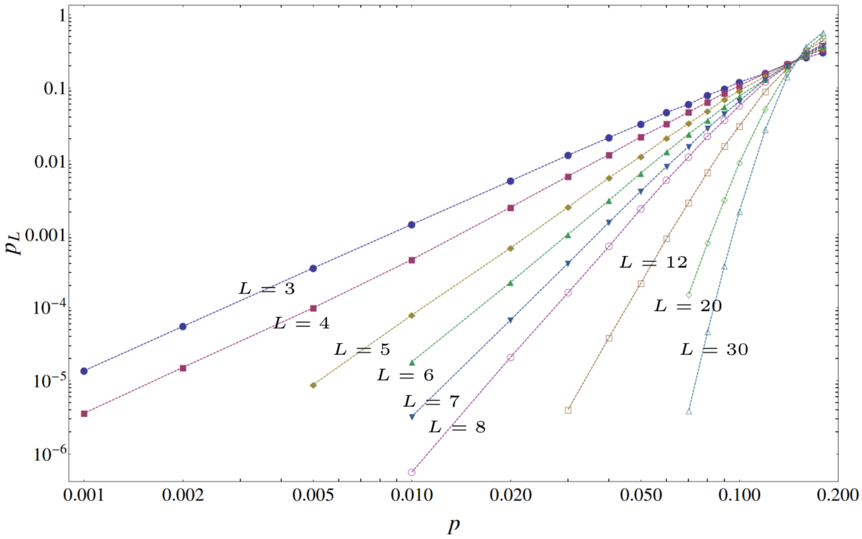

Figure 6.4: Decoherence rates p versus logical error rates p_L for enhanced MWPM.

6.4 Markov chain Monte Carlo Algorithm

We now consider an algorithm based on an analytically exact rewriting of the probability of each equivalence class which allows evaluation with the Metropolis algorithm. Let us discuss depolarizing noise here and note that our discussion generalizes straightforwardly to arbitrary error models of the form of Eq. (6.1). We have defined a depolarization rate p to mean that each spin has suffered a σ^x, σ^y, or σ^z error with probability $p/3$ each and no error with probability $1-p$. Consequently, the probability of an error chain involving n single-qubit errors is up to a normalization constant given by $\left(\frac{p/3}{1-p}\right)^n \equiv e^{-\bar{\beta}n}$, where $\bar{\beta}$ is defined through

$$\bar{\beta} = -\log\left(\frac{p/3}{1-p}\right) . \tag{6.2}$$

Given an anyon configuration A, the relative probability of equivalence class E can be written as

$$Z_E(\bar{\beta}) = \sum_E e^{-\bar{\beta}n} , \tag{6.3}$$

where the sum runs over all error chains that are compatible with the anyon configuration A and elements of equivalence class E, and n denotes the number of single-qubit errors in a particular error chain. The goal is to find the equivalence class E with maximal $Z_E(\bar{\beta})$.

The Metropolis algorithm allows us to approximate expressions of the form

$$\langle f(n)\rangle_{\beta,E} := \frac{\sum_E f(n)e^{-\beta n}}{Z_E(\beta)} \tag{6.4}$$

(we use β to denote a generic "inverse temperature" and $\bar{\beta}$ to denote the specific one defined through Eq. (6.2)). The sum is here over all error configurations in equivalence class E that are compatible with the syndrome information A. In order to approximate an expression of the form in Eq. (6.4) by use of the Metropolis algorithm, we pick one stabilizer at random and calculate the number Δn by which the total number of errors n in the code would change if that stabilizer were applied. If $\Delta n \leq 0$, we apply the stabilizer and if $\Delta n > 0$ we apply it with probability $e^{-\beta\Delta n}$. Summing up $f(n)$ over all steps and dividing by the total number of steps then yields our approximation to Eq. (6.4).

Deforming error patterns only through the application of stabilizers ensures that all error patterns in one such Markov chain belong to the same class, and that all of them are compatible with the same anyon configuration A. Since we will need the average $\langle f(n)\rangle_{\beta,E}$ for each equivalence class E, we need an initial error configuration from each equivalence class which is compatible with the measured anyon syndrome A. In fact, we will start the Metropolis Markov chains with the minimum weight error configuration from each equivalence class, provided by the method described above in Section 6.3 and Fig. 6.2. The reason for starting with the minimum weight error configuration rather than a random initial configuration from the same equivalence class is based on the intuition that "heating up" from the groundstate to inverse temperatures β as needed for the equilibrium averages in Eq. (6.4) takes less time than "cooling down" from a high energy configuration.

Note that $\sum_E$ in Eq. (6.4) has $2^{n_{\text{stab}}}$ summands for each equivalence class E, so knowing an averaged sum is as good as knowing the whole sum. We have

$$Z_E(\bar{\beta}) = \left\langle e^{-\bar{\beta}n}\right\rangle_{\beta=0,E} \times 2^{n_{\text{stab}}} \,, \tag{6.5}$$

corresponding to a simple Monte Carlo sampling of the sum. However, the sum is dominated by an exponentially small fraction of summands with "energy" n close to the minimal value, so Monte Carlo sampling is computationally similarly expensive as a brute force calculation of the sum. Our goal is thus to rewrite $Z_E(\bar{\beta})$ in a way that involves only quantities which are evaluable efficiently with the Metropolis algorithm. Applying the fundamental theorem of calculus we have

$$\begin{aligned} \log Z_E(\bar{\beta}) &= \int_0^{\bar{\beta}} \mathrm{d}\beta \partial_\beta \log Z_E(\beta) + \log Z_E(\beta = 0) \\ &= -\int_0^{\bar{\beta}} \mathrm{d}\beta \, \langle n \rangle_{\beta,E} + n_{\text{stab}} \log 2 \, . \end{aligned} \tag{6.6}$$

If we know the functions $\langle n \rangle_{\beta,E}$, the most likely equivalence class is, according to Eq. (6.6), the one in which the area under the curve is smallest. In the correctable regime ($p < p_c$) the differences in "free energy"

$$\begin{aligned} F_E(\bar{\beta}) &= -\frac{1}{\bar{\beta}} \log Z_E(\bar{\beta}) \\ &= \frac{1}{\bar{\beta}} \int_0^{\bar{\beta}} \mathrm{d}\beta \, \langle n \rangle_{\beta,E} + \text{const} \end{aligned} \tag{6.7}$$

between the different equivalence classes grow proportionally in L and correspondingly the probability of all equivalence classes but the most likely one decreases exponentially with L.

For a positive β, the average number of errors $\langle n \rangle_{\beta,E}$ can be efficiently calculated to arbitrary accuracy by means of the Metropolis algorithm. The integral $\int_0^{\bar{\beta}} \mathrm{d}\beta$ can be calculated to arbitrary accuracy by first calculating the values $\langle n \rangle_{\beta,E}$ for a sufficient number of inverse temperatures β and then applying a quadrature formula like Simpson's Rule.

The single-temperature algorithm

Recall that we are not interested in the precise value of the integrals $\int_0^{\bar{\beta}} \mathrm{d}\beta \, \langle n \rangle_{\beta,E}$, but only in knowing for which equivalence class E this integral is smallest. For this reason, calculating the whole integral is quite often an overkill. In fact, most of the relevant information contained in the function $\langle n \rangle_{\beta,E}$ can be extracted by finding its value for a *single* inverse temperature β^*.

Assume that we determine the values $\langle n \rangle_{\beta^*,E}$ for some $\beta^* > 0$ for all equivalence classes E. If the functions $\langle n \rangle_{\beta,E}$ for the different equivalence classes do not cross, knowing the values $\langle n \rangle_{\beta^*,E}$ is as good as knowing the

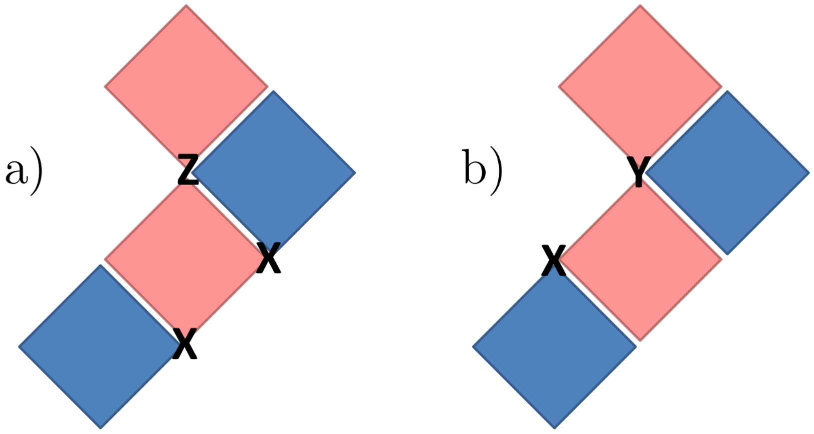

Figure 6.5: Squares represent stabilizers at which a -1 eigenvalue has been measured, i.e., anyons. Red (light) stabilizers are tensor products of σ^x and blue (dark) stabilizers are tensor products of σ^z. If the correlations between bit- and phase-flips present in depolarizing noise are ignored, both a) and b) are error patterns of minimal weight compatible with the anyon configuration. MWPM will thus result in either one of them with the same likelyhood. While enhanced MWPM will correctly assign a weight of 3 to a) and a weight of 2 to b), it considers only that of the two configurations which comes out of the matching algorithm. By contrast, if we start the single-temperature algorithm with configuration a), it will eventually apply the lower of the two red (light) stabilizer operators and thereby convert it to the true minimum-weight configuration b).

whole integrals $\int_0^{\bar{\beta}} \mathrm{d}\beta \, \langle n \rangle_{\beta,E}$ for deciding for which equivalence class E the integral is smallest.

As $\beta \to 0$, each qubit is affected by an x-, y-, or z-error or no error at all with probability $\frac{1}{4}$, so $\langle n \rangle_{\beta,E} \to \frac{3}{4} n_{\text{qubits}}$, where $n_{\text{qubits}} = n_{\text{stab}} + 1$ is the number of data qubits in the code. The low-β tail of the function $\langle n \rangle_{\beta,E}$ thus contains almost no information about the equivalence class E. So while the integral $\int_0^{\bar{\beta}} \mathrm{d}\beta \, \langle n \rangle_{\beta,E}$ is dominated by its low-β part ($\langle n \rangle_{\beta,E}$ is a monotonically decreasing function of β), the *differences* between these integrals for the different equivalence classes are mainly due to their high-β part. So even if there are crossings in the low-β tails of the functions $\langle n \rangle_{\beta,E}$, basing the decision for the most likely equivalence class on a single value $\langle n \rangle_{\beta^*,E}$ is likely to yield the same outcome as basing the decision on the whole integral $\int_0^{\bar{\beta}} \mathrm{d}\beta \, \langle n \rangle_{\beta,E}$. We thus define our *single-temperature algorithm* as sampling the values $\langle n \rangle_{\beta^*,E}$ for all equivalence classes and performing error correction in accordance with the equivalence class E for which this value is smallest.

This algorithm has only two free parameters, namely β^* and n_{sample}, the number of steps for which we perform the Metropolis algorithm in order to sample $\langle n \rangle_{\beta^*,E}$. For $\beta^* \to \infty$ (zero temperature), the single-temperature algorithm will never increase the weight of an error configuration. Still, it provides an improvement over enhanced MWPM since applying stabilizers allows to find error configurations which, taking correlations between bit- and phase-flips into account, are of lower weight than the ones found by MWPM. This does not require that the weight of the error configuration be ever increased, see Fig. 6.5 for an illustration. At finite temperature, a second improvement over (enhanced) MWPM comes into play. Namely, temperature allows to take entropic contributions to the free energy into account, i.e., consider error configurations which are not of minimal weight but give a non-negligible contribution to the free energy due to their large number. Furthermore, a finite temperature allows us to escape local minima MWPM may have led us into. However, for $\beta^* \to 0$ (infinite temperature) the single-temperature algorithm becomes useless ($\langle n \rangle_{\beta^*=0,E} = \frac{3}{4} n_{\text{qubits}}$ for all equivalence classes), such that some finite value of β^* is optimal. Indeed, we find empirically that for depolarizing noise the optimal values for β^* are close to $\bar{\beta}$. We thus set $\beta^* = \bar{\beta}$ throughout for this error model.

As for n_{sample}, we may ask how many Metropolis steps are necessary for our single-temperature algorithm to achieve logical error rates below those achievable with MWPM. In order to set the bar high, we compare our algorithm with the better of either standard or enhanced MWPM, i.e., that with the lower error rate. Fig. 6.6 shows the ratio of the logical error rate achieved by the single-temperature algorithm divided by the smaller of the two logical error rates achievable by the two variants of MWPM. If L is higher than a certain p-dependent threshold, the logical error rate will be increased if n_{sample} is too small, and only improve when it is made larger. For some fixed L, this regime of increased logical error rate vanishes if p is small enough, see the blue curve in Fig. 6.6. Then, already a handful of Metropolis steps is sufficient in order to outperform both variants of MWPM. As for the limit of a vanishing error rate p, recall that in this limit enhanced MWPM performs optimally and the single-temperature algorithm becomes redundant.

Let us discuss the scaling of the necessary values of n_{sample} as a function of L if we are in the regime where the single-temperature algorithm *can* perform worse than (at least one variant of) MWPM when n_{sample} is too low. The approximation made by MWPM is, effectively, to approximate the free energy for each equivalence class by the number of errors in its minimum weight error chain. The simplest improvement to this that can be achieved by the single temperature algorithm is to calculate $\langle n \rangle_{\beta,E}$ by sampling within the vicinity of the minimum weight chains. This will give a better approximation of the free energy by taking into account some of the effects of entropy. Since such sampling requires only $O(1)$ deformations per string in the minimum weight error chain, this approximation is equivalent to assuming that the autocorrelation time for the calculation of $\langle n \rangle_{\beta,E}$ (when starting from the minimum weight chain) is $O(1)$ for each string. The runtime complexity required to generate independent Metropolis samples for the entire code is then $O(L^2)$, which is thus the time-scale needed to estimate $\langle n \rangle_{\beta,E}$ up to some given *relative* error. The quantities $\langle n \rangle_{\beta,E}$ themselves grow like $O(L^2)$, and so does a constant relative error. However, the distinguishability, i.e., the difference in the quantity $\langle n \rangle_{\beta,E}$ between the correct and the remaining equivalence classes, only grows like $O(L)$ below threshold (see below), such that the relative difference between the equivalence classes *decreases* like $O(L^{-1})$. A constant relative error is thus not sufficient – we need a relative error of order $O(L^{-1})$. As the relative error decreases with the inverse square root of the sample size, this leads to a further factor $O(L^2)$ in the runtime complexity. The inset in Fig. 6.6 numerically verifies the $O(L^4)$ scaling anticipated from the above analysis.

Consider again the limit of $p \to 0$. We have discussed that, for even L, enhanced MWPM will successfuly correct any $L/2$ σ^x- and σ^y-errors in one line, if the number of σ^y-errors is $n_y \geq 1$ and there is at least one odd-length chain of σ^y-errors. However, if there are, say, $n_y = 2$ σ^y-errors adjacent to each other, enhanced MWPM may still fail since the four resulting s-anyons are with probability $\frac{1}{2}$ connected such that the edges connecting them do not cross the line of σ^x-errors. The single-temperature algorithm, however, will within an $O(L^2)$ time see that the number of errors can be reduced if the four s-anyons are connected such that the edges connecting them cross the line of σ^x-errors. Therefore, the single-temperature algorithm is an efficient optimal decoder for $p \to 0$.

The quantity which determines whether error correction will be successful is the difference $\min \langle n \rangle_{\beta^*,\text{false}} - \langle n \rangle_{\beta^*,\text{true}}$, where $\min \langle n \rangle_{\beta^*,\text{false}}$ de-

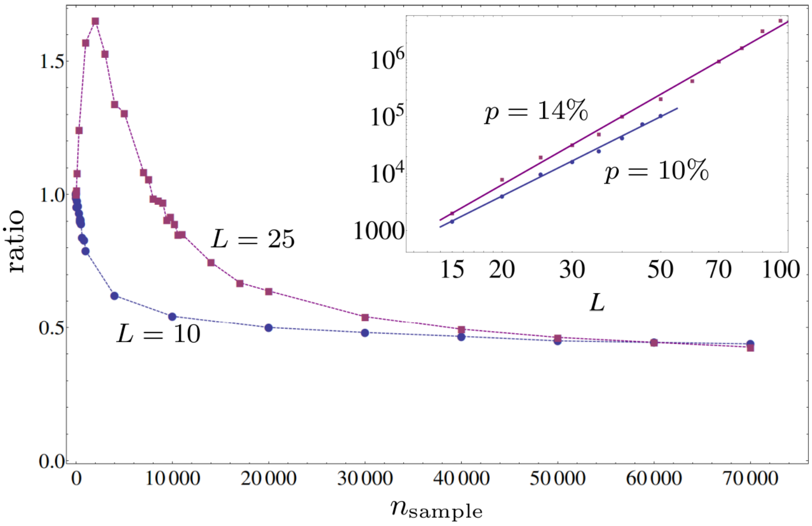

Figure 6.6: The ratio of the logical error rate achieved with the single-temperature algorithm to the lower of the two error rates achieved by the two MWPM-algorithms as a function of n_{sample}. The data were obtained for a depolarization rate of $p = 10\%$ and for code sizes $L = 10$ and $L = 25$, respectively. The inset shows the value of n_{sample} which is necessary to achieve a unit ratio against L for the case of depolarizing noise with $p = 10\%$ and $p = 14\%$. The fitting lines correspond to the functions $0.11L^{3.51}$ and $0.04L^{4.00}$. Each data point in the two figures is averaged over as many error configurations as were required for $2\,000$ logical errors to occur.

notes the minimal averaged number of errors of all three false equivalence classes. This difference is displayed for various values of p and L in Fig. 6.7. For $p < 16\%$ this difference increases linearly with L, while for $p = 17\%$ it becomes even negative for large enough L. This is to be expected: for an error rate sufficiently close to the 18.9% threshold, each of the averages $\langle n \rangle_{\beta^*,E}$ for the four equivalence classes E has the same probability for being the smallest one, such that the probability that one of the three false equivalence classes becomes minimal approaches $\frac{3}{4}$.

The inset in Fig. 6.7 shows the logical error rates achievable with our single-temperature algorithm if we set $n_{\text{sample}} = L^4$. There is a threshold for p between 15% and 16% below which the logical error rate decreases exponentially with L. This means that the threshold error rate for our algorithm is significantly below the theoretical maximum of 18.9% [131] and the value of 18.5% achieved in Ref. [127] but closer to the threshold

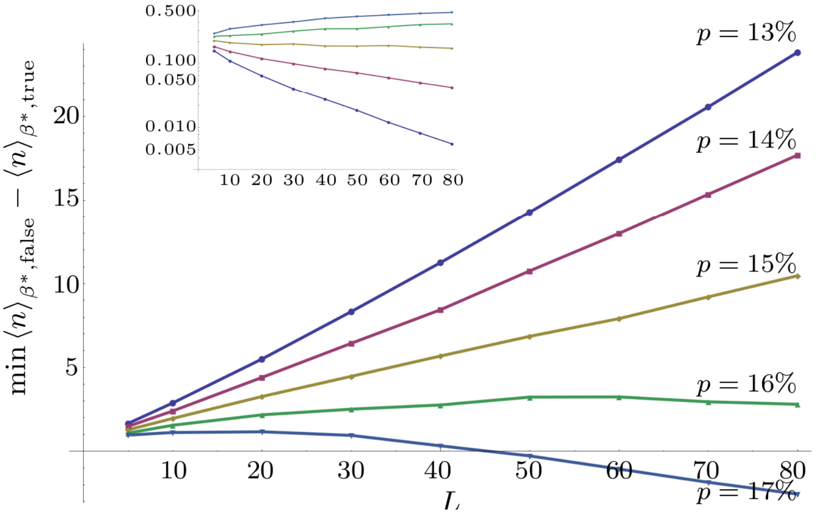

Figure 6.7: The plot shows the distinguishabilities $\min \langle n \rangle_{\beta^*,\text{false}} - \langle n \rangle_{\beta^*,\text{true}}$ (vertical axis; we use $\beta^* = \bar{\beta}$ and $n_{\text{sample}} = L^4$) for various depolarization rates p and code sizes L (horizontal axis). Different lines correspond to different depolarization rates p. Each data point is averaged over as many error configurations as are necessary to obtain $2\,000$ logical errors. The inset shows the logical error rates of our single-temperature algorithm for the same system sizes and depolarization rates, with depolarization rates increasing from bottom to top.

of MWPM [132]. This is unsurprising since we use MWPM as a starting point for our Markov chains and use only the runtime complexity for n_{sample} which is necessary to match MWPM. However, the relevant figures of merit in practice are the logical error rates achievable well below threshold (where our algorithm offers significant improvement over MWPM, see below) and the runtime complexity (where our algorithm offers significant improvement over the algorithm of Ref. [127]).

Fig. 6.8 compares the logical error rates achievable with different algorithms for $L = 15$ and different depolarization rates p. We set the logical error rates achievable with standard MWPM to unity and divide them by the logical error rates achievable with alternate algorithms. The algorithms which are displayed are:

A) Standard, unimproved MPWM, as employed in Ref. [132]. An x- and a z-error on the same qubit count as two errors.

B) Enhanced MWPM. An x- and a z-error on the same qubit count as two errors during the matching, but as one error during a final comparison of all equivalence classes. Corresponds to the single-temperature algorithm with $n_{\text{sample}} = 0$.

C) Single-temperature algorithm with $n_{\text{sample}} = L^4$ Metropolis steps and $\beta^* = \bar{\beta}$.

D) The parallel-tempering algorithm developed in Ref. [127].

The logical error rates decrease from A to D, while the runtime complexities increase. We see that the advantages achievable over algorithm A vanish as $p \to p_c = 18.9\%$ but increase the lower p gets. We believe our single-temperature algorithm C to offer the most attractive trade-off ratio between low logical error rates and low classical runtime complexity, as it increases the latter only modestly compared with algorithms A and B, while algorithm D has a super-polynomial (in L) runtime complexity.

We have verified numerically that estimating the entire integral $\int_0^{\bar{\beta}} \mathrm{d}\beta \, \langle n \rangle_{\beta,E}$ by sampling the values $\langle n \rangle_{\beta,E}$ for 21 equidistant temperatures β over L^4 Metropolis steps and then applying Simpson's quadrature formula leads only to modest improvements over algorithm C. It would be more beneficial to invest the additional computational cost into increasing n_{sample} in algorithm C.

Fig. 6.9 shows the logical error rates of algorithm A divided by those of algorithm C for various values of p and L. We see the advantage of algorithm C increasing for lower p and larger L. Note that we expect real quantum computers to be operated at error rates p below and code distances L above those displayed in Fig. 6.9.

To get an idea about what effect this reduction of the logical error rates has on the necessary code size, let us have a look at the code size which is needed for a proof of principle experiment. I.e., given some physical error rate p, which code size L is needed to bring the logical error rate below the physical one? For $p = 13\%$, we need $L \geq 6$ in order to achieve a logical error rate below p with algorithm C and need $L \geq 15$ with algorithm A. So by modestly enhancing the classical runtime complexity, we are able to reduce the number of physical data qubits required for such a proof of principle experiment from 421 to 61.

The advantage of algorithm C over algorithms A and B is due to at least two different reasons. First, MWPM is naturally suited to the error model of independent bit- and phase-flips, where each type of anyon can be treated independent of the other. It is much less suited to error models such as depolarizing noise which feature correlations between bit-

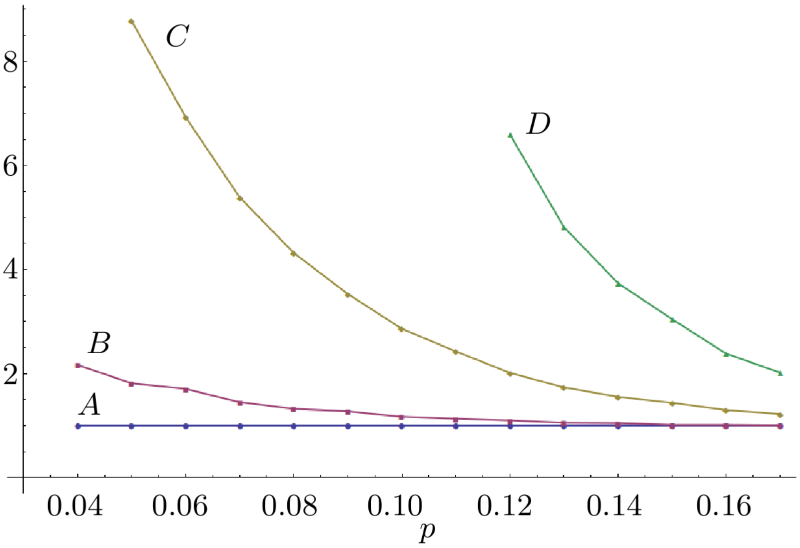

Figure 6.8: The plots show the logical error rate of MWPM (algorithm A in the main text) divided by the logical error rate of algorithms A to D described in the main text, for various depolarization rates p (horizontal axis) and a code of linear size $L = 15$. Each data point is averaged over as many error configurations as are necessary to obtain $2\,000$ logical errors. A value greater than 1 denotes an increase in effectiveness over MWPM, with greater increases for higher values.

and phase-flip errors. Algorithm B can only partially overcome these limitations. Second, while algorithms A and B are based on finding the most likely error chain and hoping that it is an element of the most likely equivalence class, algorithms C to F are based on finding the most likely equivalence class. An interesting question is thus how our single-temperature algorithm compares with MWPM for independent bit- and phase-flip errors, the error model MWPM is best suited to and where only the second advantage applies. Empirically, we find that for this error model choosing $\beta^* = 0.85\bar{\beta}$ works best and that for a bit-/phase-flip probability of 10% (close to the theoretical threshold) $O(L^4)$ Metropolis steps are again sufficient to achieve a logical error rate below the one of MWPM,[2] with $0.38L^{3.77}$ giving the best fit to the required number. For $L = 30$, a bit-/phase-flip probability of 8%, and by sampling over $10L^4$

---

[2] Note that for independent bit- and phase-flip errors, there is only one variant of the MWPM algorithm, as different error types are by assumption uncorrelated.

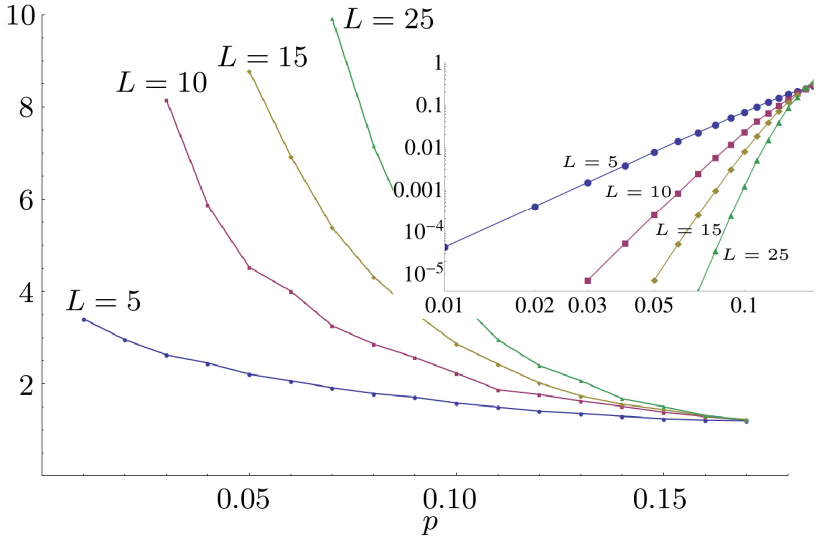

Figure 6.9: The plots show the logical error rate of algorithm A divided by the logical error rate of algorithm C for various depolarization rates p (horizontal axis) and code sizes L. Each data point is averaged over as many error configurations as are necessary to obtain $2\,000$ logical errors. The inset shows the logical error rates of algorithm C on which the ratios in the main part of the figure are based.

Metropolis steps we achieve a logical error rate which is a factor 1.3 lower than the one of MWPM. So significant improvements over MWPM can be achieved even for the error model best suited to it, though the advantage is much more drastic for an error model with correlations between bit- and phase-flip errors, with which our single-temperature algorithm can deal very naturally.

6.5 Parallelization

The runtime of the MCMC sampling can be reduced by a factor $O(L^2)$ using parallelization which exploits the fact that our algorithm needs local changes only. We partition the whole code into $O(L^2)$ rectangles of area $O(L^0)$. Adjacent rectangles overlap along lines of data qubits, while qubits in the corners belong to four rectangles, see Fig. 6.10. The rectangles are collected into four groups $0, 1, 2, 3$ such that the rectangles within one group have no overlapping qubits. At step i of the Metropo-

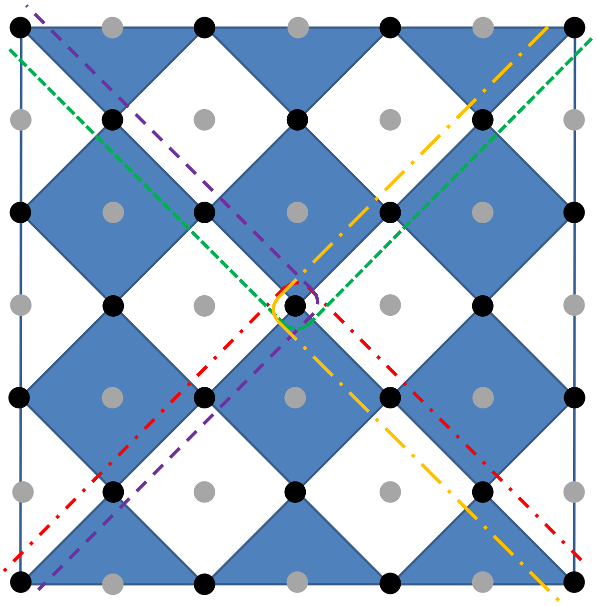

Figure 6.10: The dashed lines partition the code into rectangles of size $O(1)$. Data qubits along the boundaries belong to two rectangles and data qubits in the corners to four.

lis Markov chain, we choose one stabilizer in each rectangle belonging to group $(i \mod 4)$ at random and probe whether to apply it or not according to the Metropolis procedure. This way we can guarantee that no data qubit is affected by more than one applied stabilizer at each step. If a randomly chosen stabilizer is applied and flips a qubit which is shared with an other rectangle (other rectangles), this flip is communicated to the adjacent rectangle(-s). For each rectangle, we add up the number of local errors n over the different Metropolis steps and calculate the total average $\langle n \rangle_{\beta^*,E}$ in the end. To compensate for double-(quadruple-)counting, errors on qubits along the boundary thereby have to be discounted by a factor $\frac{1}{2}$ and errors on qubits in the corners by a factor $\frac{1}{4}$. As we probe now $O(L^2)$ stabilizers in each time step, the runtime reduces from $O(L^4)$ to $O(L^2)$.

6.6 Imperfect stabilizer measurements

Let us assume that each stabilizer measurement yields the wrong result with probability p_M. If stabilizers are measured by use of CNOT gates, this model is a simplification in that it ignores correlations between spatio-temporally nearby syndrome measurement failures induced by these gates [134]. In order to make the failure probability small despite non-negligible p_M, we now necessarily need to perform stabilizer measurements at several times $t = 1, 2, \ldots, t_{\max}$. A hypothesis about what errors have happened then not only has to state which data qubit has suffered an error in which time interval $[t, t+1]$, but also which stabilizer measurement has been erroneous at which time t. Such hypotheses can be deformed into equivalent ones by applying a bit-/phase-flip σ^x/σ^z to a particular qubit at time intervals $[t-1, t]$ and $[t, t+1]$ and inverting the hypothesis about whether the stabilizer measurements at time t that anti-commute with this error have been erroneous (see the illustration in Fig. 6.11).

In the case of depolarizing noise, a hypothesis that involves n data-qubit errors and m erroneous syndrome measurements has a relative probability

$$\left(\frac{p/3}{1-p}\right)^n \times \left(\frac{p_M}{1-p_M}\right)^m \equiv \exp\left[-\bar{\beta}(n+\xi m)\right] \ , \tag{6.8}$$

where $\bar{\beta}$ is as defined in Eq. (6.2) and

$$\xi = \frac{1}{\bar{\beta}} \log \frac{1-p_M}{p_M} \ . \tag{6.9}$$

The "energy" of a hypothesis is thus given by $n + \xi m$ where ξ determines the relative weight of erroneous syndrome measurements to data qubit errors. Our method to find the most probable equivalence class in the case of perfect stabilizer measurements can thus be generalized to the case where syndrome measurements fail with a considerable probability. Numerical results for the latter case will appear in future work.

6.7 Conclusions

We have developped two novel error correction algorithms – enhanced MWPM and the single-temperature MCMC algorithm – and compared them with each other and with standard MWPM over several regimes of the error rate p: close to threshold, intermediate values, and vanishing values. For the first two regimes, numerical simulations have provided us with insight into their respective performance, while in the third regime, analytical arguments are both unavoidable and possible.

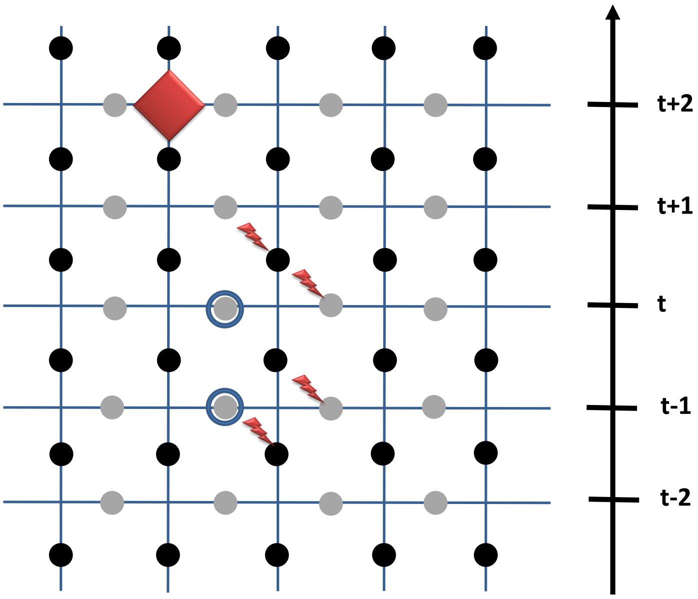

Figure 6.11: Only one type of errors and stabilizers and a single chain of data qubits (black dots) and syndrome qubits (grey dots) are depicted here for simplicity. Time runs from bottom to top. Stabilizer operators are measured at times $\ldots, t-1, t, t+1, \ldots$. The two encircled syndrome qubits have detected errors (-1 eigenvalues). A possible hypothesis is that no data qubit has suffered an error and both syndrome measurements have been erroneous. An alternate hypotheses would state that the data qubits indicated by red lightning bolts have suffered errors and that syndrome measurement by use of the syndrome qubits indicated by red lightning bolts has been erroneous. Different equivalent hypotheses can be deformed into each other through the application of operators like the red (dark) square that invert whether a hypothetical error has happened or not at two adjacent syndrome qubits and one data qubit at two subsequent times.

The relevant regime in practice will be the second one. In this regime, any $n_{\text{sample}} > 0$ leads to an improvement over the two MWPM-algorithms, so any CPU-time not needed to perform MWPM can be used to lower the logical error rate by the method described in this work. We have numerically investigated the decreases in the logical error rates which are achievable if we are willing to increase the classical runtime complexity by $O(L^2)$. Note that advantages much higher than those displayed Figs. 6.8 and Fig. 6.9 can likely be achieved, as we have probed only relatively small values of L and high values of p, quantum computers will be operated at error rates significantly below threshold, and the advantages increase for higher values of L and lower values of p.

Besides lowering the logical error rate for a given code size, our algorithm also reduces the code size necessary for a proof of principle experiment and thus reduces the experimental requirements for such an experiment.

Like the renormalization group method [135] but unlike MWPM our algorithm readily generalizes to the $\mathbb{Z}_d$ toric codes with $d > 2$ [16]. Our algorithm relies on the availability of a low energy state of each equivalence class as a starting point for the Markov chains. In the case of $d = 2$ (studied in this work), such a low energy state can be efficiently obtained by use of MWPM, while for $d > 2$ the Broom algorithm of Ref. [61] may be applied.

6.8 Acknowledgments

This work is supported by the Swiss NSF, NCCR QSIT, and IARPA. We thank Austin Fowler for encouraging us to discuss the $p \to 0$ limit and David Poulin for comments concerning the applicability of our algorithm.

CHAPTER 7

Breakdown of Surface Code Error Correction Due to Coupling to a Bosonic Bath

Adapted from:
Adrian Hutter and Daniel Loss
"Breakdown of Surface Code Error Correction Due to Coupling to a Bosonic Bath",
Phys. Rev. A **89**, 042334 (2014)

We consider a surface code suffering decoherence due to coupling to a bath of bosonic modes at finite temperature and study the time available before the unavoidable breakdown of error correction occurs as a function of coupling and bath parameters. We derive an exact expression for the error rate on each individual qubit of the code, taking spatial and temporal correlations between the errors into account. We investigate numerically how different kinds of spatial correlations between errors in the surface code affect its threshold error rate. This allows us to derive the maximal duration of each quantum error correction period by studying when the single-qubit error rate reaches the corresponding threshold. At the time when error correction breaks down, the error rate in the code can be dominated by the direct coupling of each qubit to the bath, by mediated subluminal interactions, or by mediated superluminal interactions. For a 2D Ohmic bath, the time available per quantum error correction period vanishes in the thermodynamic limit of a large code size L due to induced superluminal interactions, though it does so only like $1/\sqrt{\log L}$. For all other bath types considered, this time remains finite as $L \to \infty$.

7.1 Introduction

Due to its high error threshold and since it requires only nearest-neighbor gates to be performed, the surface code [44, 57] is the most promising platform for scalable, fault-tolerant, and universal quantum computation [48]. In order to test its resilience and benchmark the performance of classical algorithms for quantum error correction (QEC), the surface code is often studied with simplistic stochastic error models, where an error is an unphysical event that happens instantaneously at a specified point in space-time. Furthermore, it is usually assumed that these errors are not spatially correlated (see, e.g., Refs. [125–128, 134, 136, 137]). It is thus of importance to study to what degree these assumptions are satisfied for realistic models of a physical environment, and in case they are not, what the resilience of the surface code against the resulting effective error model is.

In this work, we will consider a surface code coupled to a thermal bath of freely propagating modes. A pair of recent articles [138, 139] studied the fidelity of the surface code in this setup (at zero temperature). They showed that, under the assumption of a trivial error syndrome (all stabilizer operators of the code still yield a $+1$ eigenvalue), there is a sharp transition between maximal and minimal surface code fidelity as the coupling strength to the bath is increased. This transition provides an upper bound to the resilience of the surface code, since a logical error with a trivial error syndrome certainly cannot be corrected.

By contrast, our goal here is to find the actual time when QEC in the surface code breaks down as a function of coupling and bath parameters. This is the time at which an error correction algorithm is no longer able to pair the surface code defects in a way that leads to a trivial operation performed on the code subspace.

In order to find these times, we follow a three-step strategy. First, calculate the error rate on each individual qubit as a function of time and physical parameters. There are three different physical mechanisms contributing to this error rate – the direct interaction of each qubit with the bath, subluminal interactions mediated by the bath as well as superluminal ones. Second, study numerically how spatial correlations between such errors affect the threshold error rate of the surface code. Third, solve for the times for which the single-qubit error rate reaches the modified threshold error rates.

When deriving actual threshold estimates, Refs. [138, 139] resort to the case of nearest-neighbor correlations only. However, we show that both subluminal and superluminal mediated long-range interactions can actually be the dominant error mechanism at the time for which the error rate reaches critical values.

7.2 Problem and Overview

We consider a surface code each qubit of which is coupled to a bosonic bath at thermal equilibrium. In accordance with Refs. [138, 139], we only consider bit-flip errors here (σ^x) and make the simplifying assumption that the bath is in thermal equilibrium at the beginning of each QEC cycle, i.e., that bath correlations between different QEC cycles are negligible. Physically, this can be thought of as the bath thermalizing with an even larger bath during one QEC period. However, we generalize the discussion in Refs. [138, 139] to the case of finite temperature.

Sums and products with a tilde on top run over all surface code qubit indices i, while sums without a tilde are over bath modes $\mathbf{k}$. Let $H = H_0 + V$ with

$$H_0 = H_{\text{bos}} = \sum_{\mathbf{k}} \omega_{\mathbf{k}} a_{\mathbf{k}}^\dagger a_{\mathbf{k}}, \tag{7.1}$$

and

$$V = \tilde{\sum}_i \sigma_i^x \otimes \frac{\lambda}{\sqrt{N}} \sum_{\mathbf{k}} |\mathbf{k}|^r \left(e^{i\mathbf{k}\mathbf{R}_i} a_{\mathbf{k}} + e^{-i\mathbf{k}\mathbf{R}_i} a_{\mathbf{k}}^\dagger \right), \tag{7.2}$$

where $a_{\mathbf{k}}^\dagger$ ($a_{\mathbf{k}}$) are the standard creation (annihilation) operators obeying bosonic commutation relations. Here, $\mathbf{R}_i$ is the spatial location of qubit i and $N = \sum_{\mathbf{k}} 1$ is the number of bosonic modes of the bath. Physically interesting are the cases $r = 0, \pm\frac{1}{2}$ [139]. We consider a linear dispersion of the bath modes, $\omega_{\mathbf{k}} = v|\mathbf{k}|$, as is accurate for acoustic phonons, spin-waves in an antiferromagnet, or electromagnetic waves. Here, v is the corresponding velocity of the modes.

Let the initial qubit density matrix be given by ρ_q and the thermal state of the bath by $\rho_B \propto \exp(-\beta H_{\text{bos}})$, where $T = 1/\beta$ is the bath temperature. The surface code requires a set of commuting many-qubit Pauli operators, called *stabilizer operators*, to yield a $+1$ eigenvalue. All of these operators are measured at the end of each QEC cycle. Stabilizer measurements can be performed either by applying entangling gates between code and auxiliary qubits [48, 57] or by direct measurement of the corresponding many-qubit parity operators [123, 124]. Eigenvalues -1 signal that an error has occurred and are interpreted as the presence of an *anyon*. Quantum information is stored in the subspace for which all stabilizers yield a $+1$ eigenvalue. Correspondingly, the state ρ_q is restricted to this subspace, i.e., ρ_q is an anyon-free state. QEC is successful if the anyons are paired in a way which is homologically equivalent to the way they have been created. Finding such a pairing is the task of a classical error correction algorithm [125–128, 134, 136, 137], one of which we will encounter in Sec. 7.6. For more details about the surface code, see Ref. [48].

The decoherent evolution of the qubits is given by

$$\rho_q \mapsto \Phi_d(\rho_q) = \mathrm{tr}_B \left\{ e^{-iHt}(\rho_q \otimes \rho_B) e^{+iHt} \right\} \ . \tag{7.3}$$

At the end of each QEC cycle, after some time t, we perform a measurement of all surface code stabilizer operators, which is described by the quantum channel

$$\Phi_m(\sigma) = \sum_a P_a \sigma P_a \ . \tag{7.4}$$

Here, P_a projects onto the space with anyon configuration a and the sum runs over all possible anyon configurations a.

Finally, we study the state $\rho_i(t) = \mathrm{tr}_{\bar{i}} \circ \Phi_m \circ \Phi_d(\rho_q)$ of one particular qubit. Here, $\mathrm{tr}_{\bar{i}}$ denotes a partial trace over all qubits except qubit i. Since ρ_q is an anyon-free state and the stabilizer measurement projects the density matrix of the qubits to the spaces with well-defined anyon numbers, $\rho_i(t)$ has no contributions of terms $\sigma_i^x \rho_i$ or $\rho_i \sigma_i^x$ (here, $\rho_i = \mathrm{tr}_{\bar{i}}\, \rho_q$). We can thus write $\rho_i(t) = (1 - p_x(t))\rho_i + p_x(t)\sigma_i^x \rho_i \sigma_i^x$.

$$\rho_q \xrightarrow[\Phi_d]{\text{decoherence}} \xrightarrow[\Phi_m]{\substack{\text{syndrome}\\ \text{measurement}}} \xrightarrow[\mathrm{tr}_{\bar{i}}]{\substack{\text{restrict to}\\ i\text{-th qubit}}} \begin{aligned} \rho_i(t) &= \mathrm{tr}_{\bar{i}} \circ \Phi_m \circ \Phi_d(\rho_q) \\ &= (1 - p_x(t))\rho_i + p_x(t)\sigma_i^x \rho_i \sigma_i^x \end{aligned}$$

Our first goal is to calculate $p_x(t)$ as a function of the time t, the parameters in H, and the bath temperature $T = 1/\beta$, which is what we carry out in Sec. 7.3. Using the results from Sec. 7.3, we calculate in Sec. 7.4 the exact evolution of the density matrix of two qubits coupled to the bath and discuss the use of this bath coupling as an entangling gate.

Secondly, we discuss what implications such an error rate has for surface code error correction. Error correction will inevitably break down once the error rate p_x on each qubit surpasses a certain critical value p_c. This critical value depends on the spatial correlations between errors in the code, on the classical algorithm that is employed in order to find a pairing of the anyons, and on the probability p_m with which a syndrome measurement fails. In the symmetric case of $p_x = p_m$ and for uncorrelated errors, efficient error correction algorithms are able to perform successful error correction up to a critical value of $1.9\% - 2.9\%$ [137,140]. In a more involved, circuit-based modelling of syndrome extraction, critical error rates are around 1% [44,126,134].

The higher p_m, the lower the probability of error p_x for which successful correction is possible. Following Refs. [138,139], we consider in the following the perfect measurement case $p_m = 0$ for definiteness and simplicity. Generalization to the more realistic case of $p_m > 0$ is straightforward; it merely corresponds to replacing p_c (or $\tilde{p}_c$, see below) by a lower value.

If the errors on different qubits are independent from each other and stabilizer measurements are flawless ($p_m = 0$), error correction inevitably breaks down if $p_x(t) > p_c = 10.9\%$ [57]. For $p_x(t) < p_c$ the probability of an error is exponentially small in L, the linear size of the code, if quantum error correction is performed optimally. The problem of performing error correction in the surface code with perfect syndrome measurements can be mapped to the classical Ising model with erroneous qubits corresponding to antiferromagnetic bonds. The critical value p_c corresponds to an order-disorder transition in this model [57].

For uncorrelated errors, the maximal duration τ of one QEC cycle can thus be obtained by simply inverting $p_x(\tau) = p_c$, which we exemplify for an Ohmic bath in Sec. 7.5. Alternative bath types are discussed in Appendix 7.A. When the errors on different qubits are not independent, the breakdown of error correction will in general occur at a single-qubit error probability $\tilde{p}_c$ different from p_c. If the correlations between the errors on different qubits are ignored, $\tilde{p}_c$ may be lower than p_c. On the other hand, taking knowledge about such correlations properly into account can even increase $\tilde{p}_c$ beyond p_c. We present an efficient algorithm that is capable of doing this for a specific kind of correlations in Appendix 7.B. However, we do not know the value of $\tilde{p}_c$ for the kind of correlations between errors that arise from coupling to the bosonic bath. Still, solving $p_x(\tau) = \tilde{p}_c$ for τ will provide us with the correct scaling of τ as a function of physical parameters like the bath temperature.

Furthermore, in Sec. 7.6 we numerically find values for $\tilde{p}_c$ for different kinds of spatial correlations between errors and provide heuristic evidence that the value of $\tilde{p}_c$ for the errors arising due to the bath coupling does not differ drastically from p_c. We also show that for correlated two-qubit errors the surface code can, due to being a degenerate code, be used to perform error correction in regimes where the entropy in the noise exceeds the information obtained from stabilizer measurements – which is in contrast to the uncorrelated case.

The resulting maximal QEC cycle times τ for the more general case of correlated errors are derived in Sec. 7.7. The obtained expressions for τ for a variety of different parameter regimes are summarized in Sec. 7.7. We conclude in Sec. 7.8.

7.3 The single-qubit error rate $p_x(t)$

In this section, we calculate exactly the joint unitary dynamics of the qubits in the surface code and the modes in the bosonic bath. From this, we derive the probability of an error on each qubit $p_x(t)$ as a function of time, taking into account all correlations with errors affecting other qubits.

We have

$$\begin{aligned} \Phi_d(\rho_q) &= \mathrm{tr}_B \left\{ e^{-iHt} (\rho_q \otimes \rho_B) e^{+iHt} \right\} \\ &= \mathrm{tr}_B \left\{ e^{iH_0 t} e^{-iHt} (\rho_q \otimes \rho_B) e^{+iHt} e^{-iH_0 t} \right\} \\ &= \mathrm{tr}_B \left\{ U(t) (\rho_q \otimes \rho_B) U(t)^\dagger \right\} \ , \end{aligned} \tag{7.5}$$

where $U(t) = e^{iH_0 t} e^{-iHt} = \mathcal{T} e^{-i \int_0^t \mathrm{d}t' \, V(t')}$ denotes the evolution operator in the interaction picture. It follows directly from the Magnus expansion (cf. Ref. [139, Appendix A]) and the fact that $[V(t_1), [V(t_2), V(t_3)]] = 0$ that

$$\begin{aligned} U(t) &= \exp\left\{ -i \int_0^t \mathrm{d}t_1 \, V(t_1) - \frac{1}{2} \int_0^t \mathrm{d}t_1 \int_0^{t_1} \mathrm{d}t_2 \, [V(t_1), V(t_2)] \right\} \\ &=: \exp\left\{ \tilde{\sum}_i \sigma_i^x \otimes X_i(t) \right\} \exp\left\{ -\frac{i}{2} \tilde{\sum}_{ij} J_{ij}(t) \sigma_i^x \otimes \sigma_j^x \right\} \ . \end{aligned} \tag{7.6}$$

We have defined

$$X_i(t) = \frac{\lambda}{\sqrt{N}} \sum_{\mathbf{k}} \frac{|\mathbf{k}|^r}{\omega_{\mathbf{k}}} \left(e^{i\mathbf{k}\mathbf{R}_i} (e^{-i\omega_{\mathbf{k}} t} - 1) a_{\mathbf{k}} - e^{-i\mathbf{k}\mathbf{R}_i} (e^{i\omega_{\mathbf{k}} t} - 1) a_{\mathbf{k}}^\dagger \right) \tag{7.7}$$

and

$$\begin{aligned} J_{ij}(t) &= -i \frac{\lambda^2}{N} \sum_{\mathbf{k}} |\mathbf{k}|^{2r} \int_0^t \mathrm{d}t_1 \int_0^{t_1} \mathrm{d}t_2 \left\{ e^{i\mathbf{k}(\mathbf{R}_i - \mathbf{R}_j)} e^{-i\omega_{\mathbf{k}}(t_1 - t_2)} - \mathrm{c.c.} \right\} \\ &= 2\lambda^2 \int \mathrm{d}\mathbf{k} \, \frac{|\mathbf{k}|^{2r}}{\omega_{\mathbf{k}}^2} \cos\left(\mathbf{k}(\mathbf{R}_i - \mathbf{R}_j) \right) \left(\sin(\omega_{\mathbf{k}} t) - \omega_{\mathbf{k}} t \right) \ . \end{aligned} \tag{7.8}$$

In Appendix 7.A, we provide the functions $J_{ij}(t)$ for different bath types (i.e., different combinations of spatial dimension, $D = 2, 3$, and bath coupling, $r = 0, \pm\frac{1}{2}$).

It is straightforward to show that $[X_i(t), X_j(t)] = 0$ and thus we can also write

$$\begin{aligned} U(t) &= \tilde{\prod}_i \exp\left\{\sigma_i^x \otimes X_i(t)\right\} \tilde{\prod}_{\{i,j\}} \exp\left\{-iJ_{ij}(t)\sigma_i^x \otimes \sigma_j^x\right\} \\ &= \tilde{\prod}_i \left(\cosh(X_i(t)) + \sigma_i^x \otimes \sinh(X_i(t))\right) \\ &\quad \times \tilde{\prod}_{\{i,j\}} \left(\cos(J_{ij}(t)) - i\sin(J_{ij}(t))\sigma_i^x \otimes \sigma_i^x\right) \ . \end{aligned} \tag{7.9}$$

The product $\tilde{\prod}_{\{i,j\}}$ is over all pairs $\{i, j\}$, i.e., without double-counting.

We will refer to the first factor in Eqs. (7.6) and (7.9) as the *decoherent* part of the evolution, and to the second part as the *coherent* part. Note that only the decoherent part of the evolution will lead to a dependence of the evolution of the code on the state of the bath (in particular its temperature). The coherent part is, in principle, reversible and does not lead to a transfer of quantum information from the code qubits into the bath.

Inserting Eq. (7.9) into Eq. (7.5) and expanding the products can only be done if the number of qubits coupled to the bath is small. In Sec. 7.4 we consider the case of two qubits coupled to the same bath and calculate the exact evolution of the two-qubit density matrix. However, if the number of qubits coupled to the bath is large, we need to follow a different route. Note that we are only interested in whether a net-error (i.e., an odd number of σ^x-errors) occurs on qubit i after application of Φ_d and Φ_m. This probability can be found with an inductive argument over N_q, the number of qubits in the code.

Since ρ_q is a state with no anyons, the syndrome measurement Φ_m eliminates all terms in $\Phi_d(\rho_q)$ that apply a different tensor product of Pauli errors 'to the left' and 'to the right' of ρ_q. Formally, let ℓ label the 2^{N_q} possible configurations of σ^x errors on the code and let ξ_ℓ denote the ℓ-th error configuration. Then,

$$\Phi_m\left(\xi_{\ell_1}\rho_q\xi_{\ell_2}^\dagger\right) = \delta_{\ell_1\ell_2}\xi_{\ell_1}\rho_q\xi_{\ell_1}^\dagger \ . \tag{7.10}$$

Let us call terms which have the same tensor products of Pauli operators on the left and on the right and hence survive application of Φ_m 'valid' terms.

Consider first the case $N_q = 1$. Then we simply have

$$\Phi_d(\rho_q) = \left\langle \cosh^2\left(X_i(t)\right)\right\rangle \rho_q - \left\langle \sinh^2\left(X_i(t)\right)\right\rangle \sigma^x \rho_q \sigma^x \; . \tag{7.11}$$

(Note that $X_i(t)$ is anti-Hermitian, so $(\sinh\left(X_i(t)\right))^\dagger = -\sinh\left(X_i(t)\right)$.) We have introduced the notation $\langle O\rangle = \mathrm{tr}_B\{O\rho_B\}$. Let us thus define the single-qubit decoherence rate by $p_d(t) = -\left\langle \sinh^2\left(X_i(t)\right)\right\rangle$.

Let $p_x(t)$ denote the error probability on qubit 1. In the case of the surface code, this is then up to boundary effects the error probability on all other qubits as well. The error probability $p_x(t)$ is the total probabilistic weight of all valid terms that apply an odd number of errors to qubit 1. Let $p_x(t)_{N_q}$ denote the probability of an error on qubit 1 if there is a total number of N_q qubits in the code. Clearly, we have $p_x(t)_1 = p_d(t)$. When increasing $N_q \mapsto N_q + 1$, the parity of errors on qubit 1 is only changed if a pair of errors is applied to qubit 1 and qubit $N_q + 1$. The weight of this happening is $\sin^2(J_{1,N_q+1}(t))$, while the weight of it not happening is $\cos^2(J_{1,N_q+1}(t))$. This leads to the recursive formula

$$p_x(t)_{N_q+1} = \cos^2(J_{1,N_q+1}(t))p_x(t)_{N_q} + \sin^2(J_{1,N_q+1}(t))(1-p_x(t)_{N_q}) \; . \tag{7.12}$$

Let sums and products with a prime run over all qubits except qubit 1, i.e., from 2 to N_q. The solution is then evidently given by

$$p_x(t)_{N_q} = \prod_i{}' \cos^2(J_{1i}(t)) \times \\ \left\{ p_d(t) \sum_{\substack{m_i\in\{0,1\} \\ \sum_i' m_i \equiv 0\,(\mathrm{mod}\,2)}} \prod_i{}' (\tan^2(J_{1i}(t)))^{m_i} + (1-p_d(t)) \sum_{\substack{m_i\in\{0,1\} \\ \sum_i' m_i \equiv 1\,(\mathrm{mod}\,2)}} \prod_i{}' (\tan^2(J_{1i}(t)))^{m_i} \right\} . \tag{7.13}$$

7.4 Evolution of a two-qubit density matrix coupled to the bath

Consider two qubits i and j at locations $\mathbf{R}_i$ and $\mathbf{R}_j$, respectively, that are coupled to a bosonic bath. We assume them to be uncorrelated with the bath at $t = 0$, $\rho(0) = \rho_{ij} \otimes \rho_B$. The evolution of the two-qubit density matrix can be found using Eqs. (7.5) and (7.9). We keep the technicalities in Appendix 7.C and present here the final result for the state of the two-qubit density matrix after some time t. We have

$$\begin{aligned}
\rho_{ij}(t) = &\left(\frac{1}{4}(1+e^{-4\Lambda(t)}\cosh(4C_{ij}(t))) + \frac{1}{2}e^{-2\Lambda(t)}\cos(2J_{ij}(t))\right) \times \rho_{ij} \\
&+ \left(\frac{1}{4}(1-e^{-4\Lambda(t)}\cosh(4C_{ij}(t))\right) \times (\sigma_i^x\rho_{ij}\sigma_i^x + \sigma_j^x\rho_{ij}\sigma_j^x) \\
&+ \left(\frac{1}{4}(1+e^{-4\Lambda(t)}\cosh(4C_{ij}(t))) - \frac{1}{2}e^{-2\Lambda(t)}\cos(2J_{ij}(t))\right) \times \sigma_i^x\sigma_j^x\rho_{ij}\sigma_i^x\sigma_j^x \\
&+ \left(-\frac{i}{2}e^{-2\Lambda(t)}\sin(2J_{ij}(t))\right) \times \left(\sigma_i^x\sigma_j^x\rho_{ij} - \rho_{ij}\sigma_i^x\sigma_j^x\right) \\
&+ \left(\frac{1}{4}e^{-4\Lambda(t)}\sinh(4C_{ij}(t))\right) \times \left(\sigma_i^x\sigma_j^x\rho_{ij} + \rho_{ij}\sigma_i^x\sigma_j^x - \sigma_i^x\rho_{ij}\sigma_j^x - \sigma_j^x\rho_{ij}\sigma_i^x\right) \; .
\end{aligned} \tag{7.14}$$

Here, $J_{ij}(t)$ is as defined in Eq. (7.8) and

$$C_{ij}(t) = \langle X_i(t)X_j(t)\rangle = -\frac{\lambda^2}{N}\sum_{\mathbf{k}} |\mathbf{k}|^{2r}\cos\left(\mathbf{k}(\mathbf{R}_i - \mathbf{R}_j)\right)\coth(\beta\omega_{\mathbf{k}}/2)\frac{\sin^2(\omega_{\mathbf{k}}t/2)}{(\omega_{\mathbf{k}}/2)^2} \; . \tag{7.15}$$

Furthermore, we introduced the non-negative function

$$\Lambda(t) = -C_{ii}(t) \geq 0 \; . \tag{7.16}$$

It characterizes the decoherence of each individual qubit due to its coupling to the bath and will be discussed in more detail in the next section.

Unlike the functions $J_{ij}(t)$, the functions $C_{ij}(t)$ depend on temperature. For $i \neq j$, they are in general hard to evaluate at finite temperature. At zero temperature, they have been calculated for 2D baths in Ref. [139]. In the rest of this work, we will follow Ref. [138] and focus on a bath with $r = 0$, $D = 2$, corresponding to an Ohmic bath. For this case, the correlator $C_{ij}(t)$ evaluates *at zero temperature* to

$$C_{ij}(t) = -\frac{\lambda^2}{\pi v^2}\theta(vt - R)\text{arccosh}(vt/R) \; . \tag{7.17}$$

As it turns out, however, the single-qubit error rate $p_x(t)$ depends only on the functions $\Lambda(t)$ and $J_{ij}(t)$, but not on $C_{ij}(t)$ for $i \neq j$. For example, one easily verifies that the partial trace $\rho_i(t)$ of Eq. (7.14) is independent of $C_{ij}(t)$ and, using Eq. (7.21) below, that the probability for a σ^x-error agrees with Eq. (7.13) for $N_q = 2$. This allows us in the following sections to evaluate $p_x(t)$ without knowing the functions $C_{ij}(t)$ for $i \neq j$.

Bath coupling as an entangling gate

Recently, the idea of perfoming entangling gates between two qubits by coupling them to an ordered ferromagnet (which can be seen as a "magnon bath") and exploiting the mediated interaction has been studied in Ref. [141]. The availability of entangling gates between nearest-neighbor qubits is crucial for the circuit-based implementation of the surface code [48, 57, 134]. Using the above result, it is straightforward to evaluate the fidelity of such a gate. For concreteness, let us study the fidelity of maximally entangled two-qubit states (ebits) obtained using such a gate.

Consider the initial state $\rho_{ij} = |0\rangle\langle 0|_i \otimes |0\rangle\langle 0|_j$ and the maximally entangled states $|\psi^{\pm}\rangle = \frac{1}{\sqrt{2}}(|0\rangle_i|0\rangle_j \pm i|1\rangle_i|1\rangle_j)$. Then,

$$\langle\psi^{\pm}|\rho_{ij}(t)|\psi^{\pm}\rangle = \frac{1}{4}(1 + e^{-4\Lambda(t)}\cosh(4C_{ij}(t))) \mp \frac{1}{2}e^{-2\Lambda(t)}\sin(2J_{ij}(t)) \,. \tag{7.18}$$

At times for which $J_{ij}(t)$ is an odd multiple of $\pi/4$, we obtain ebits with fidelity $\frac{1}{4}(1 + e^{-4\Lambda(t)}\cosh(4C_{ij}(t))) + \frac{1}{2}e^{-2\Lambda(t)}$. For nearby qubits, $C_{ij}(t) \simeq -\Lambda(t)$, such that the fidelity simplifies to $\frac{3}{8} + \frac{1}{8}e^{-8\Lambda(t)} + \frac{1}{2}e^{-2\Lambda(t)}$. High-fidelity ebits can thus only be obtained for times t such that $\Lambda(t) \ll 1$. The gate is only useful if $J_{ij}(t)$ reaches $\pi/4$ in such times.

Note that the magnon bath considered in Ref. [141] has a dispersion which is parabolic rather than linear, as assumed in this work. For a 2D Ohmic bath ($r = 0$, $D = 2$), the function $J_{ij}(t)$ can be calculated as described in Ref. [139, Appendix C] and evaluates to

$$J_{ij}(t) = \frac{\lambda^2}{2\pi^2 v^2}\left(\theta(R - vt)\arcsin(vt/R) + \theta(vt - R)\frac{\pi}{2}\right) \,, \tag{7.19}$$

where we have defined $R := |\mathbf{R}_i - \mathbf{R}_j|$. Note that $J_{ij}(t)$ reaches a stationary value of $\frac{\lambda^2}{4\pi v^2}$ for times t such that $vt > |\mathbf{R}_i - \mathbf{R}_j|$. Choosing $\lambda = \pi v$ thus produces ebits with fidelity $\simeq 1 - 2\Lambda(t)$ for times such that $vt > |\mathbf{R}_i - \mathbf{R}_j|$. High-fidelity ebits are obtained in the time-interval for which $vt > |\mathbf{R}_i - \mathbf{R}_j|$ and $\Lambda(t) \ll 1$, if this interval exists.

Baths in 3D behave very differently in this respect: for all values of $r = 0, \pm\frac{1}{2}$, $J_{ij}(t)$ grows linearly with t for $t > R/v$ in 3D (see Appendix 7.A). Similarly, $J_{ij}(t)$ grows linearly with t for large enough t, see Sec. 7.A. In these cases, ebits can be obtained by maintaining the bath-coupling for a certain amount of time.

7.5 Maximal QEC cycle time for uncorrelated errors

Let us now first consider the simple case where the noise on the different qubits is uncorrelated, which is relevant if the qubits are sufficiently far apart from each other such that each qubit effectively couples to its "private bath". Note that for the noise to be uncorrelated, it is not enough to require that $J_{ij}(t)$ vanish for all i and j. The decoherent part of the evolution, too, leads to correlations between the errors on different qubits, which can be quantified by correlators $\langle X_i(t) X_j(t) \ldots X_m(t) \rangle$. Uncorrelated noise requires that both $J_{ij}(t) \approx 0$ and $C_{ij}(t) = \langle X_i(t) X_j(t) \rangle \approx 0$ for all $i \neq j$. In this case, we simply have $p_x(t) = p_d(t)$ for each qubit.

Since $X_i(t)$ is linear in the creation/annihilation operators of the bath, we can apply Wick's theorem to calculate thermal expectation values of products of the operators $X_i(t)$. I.e.,

$$\left\langle X_i(t)^{2k} \right\rangle = \frac{(2k)!}{2^k k!} \left\langle X_i(t)^2 \right\rangle^k \,, \tag{7.20}$$

where $(2k-1) \times (2k-3) \times \ldots \times 3 \times 1 = \frac{(2k)!}{2^k k!}$ is the number of possible contractions. We thus find

$$\begin{aligned} p_d(t) &:= -\left\langle \sinh^2\left(X_i(t)\right) \right\rangle \\ &= -\sum_{n,m=0}^{\infty} \frac{1}{(2n+1)!} \frac{1}{(2m+1)!} \left\langle X_i(t)^{2n+2m+2} \right\rangle \\ &= -\sum_{n,m=0}^{\infty} \frac{1}{(2n+1)!} \frac{1}{(2m+1)!} \frac{(2n+2m+2)!}{2^{n+m+1}(n+m+1)!} \left\langle X_i(t)^2 \right\rangle^{n+m+1} \\ &= -\sum_{k=0}^{\infty} \left\langle X_i(t)^2 \right\rangle^{k+1} \frac{(2k+2)!}{2^{k+1}(k+1)!} \times \underbrace{\sum_{n=0}^{k} \frac{1}{(2n+1)!} \frac{1}{(2k-2n+1)!}}_{2^{2k+1}/(2k+2)!} \\ &= \frac{1}{2}\left(1 - \exp\left\{2\left\langle X_i(t)^2 \right\rangle\right\}\right) \\ &= \frac{1}{2}\left(1 - \exp\left\{-2\Lambda(t)\right\}\right) \,, \end{aligned} \tag{7.21}$$

where we have defined $k = n + m$ and $\Lambda(t) = -\left\langle X_i(t)^2 \right\rangle \geq 0$.

Different baths are characterized by their spectral density function

$$J(\omega) = \frac{\lambda^2}{N} \sum_{\mathbf{k}} |\mathbf{k}|^{2r} \delta(\omega - \omega_{\mathbf{k}}) = \alpha \omega^s \omega_0^{1-s} e^{-\omega/\omega_c} \, . \tag{7.22}$$

Here, α is a dimensionless bath strength, ω_0 is a characteristic frequency of the bath, and ω_c is a high-frequency cut-off. A bath with $s < 1$ is called sub-Ohmic, one with $s = 1$ is called Ohmic, and one with $s > 1$ is called super-Ohmic.

The function $\Lambda(t)$ depends only on the spectral density function of the bath and its temperature, namely we have

$$\Lambda(t) = \int_0^\infty \mathrm{d}\omega \, J(\omega) \coth\left(\beta\omega/2\right) \frac{\sin^2\left(\omega t/2\right)}{(\omega/2)^2} \, . \tag{7.23}$$

We see that for $s \geq 1$ a finite ω_c is necessary to ensure the convergence of Eq. (7.23). With a linear dispersion, $\omega_{\mathbf{k}} = v|\mathbf{k}|$, and a D-dimensional bath, we have $s = D + 2r - 1$.

For uncorrelated errors, surface code error correction breaks down if $p_x(t) > p_c = 10.9\%$ [57]. Inverting Eq. (7.21), we thus find the maximal time τ of one error correction cycle from

$$\Lambda(\tau) = \frac{1}{2} \log \frac{1}{1 - 2p_c} \simeq 0.123 \, . \tag{7.24}$$

This solves the problem up to evaluation of the integral in Eq. (7.23) and inversion of Eq. (7.24).

Following Ref. [138], we restrict in the main text to the case $D = 2$ and $r = 0$, corresponding to an Ohmic bath. The dimensionless bath strength parameter evaluates in this case to $\alpha = \frac{\lambda^2}{2\pi v^2}$. The functions $\Lambda(t)$ for the remaining combinations of $D = 2, 3$ and $r = 0, \pm\frac{1}{2}$ are presented in Appendix 7.A.

For the integral in Eq. (7.23), we find with $s = 1$ and $\beta\omega_c \gg 1$, using

$\coth(x) = 1 + 2\sum_{n=1}^{\infty} e^{-2nx}$,

$$\begin{aligned}
\Lambda(t) &= \int_0^\infty \mathrm{d}\omega\, \alpha\omega e^{-\omega/\omega_c} \coth\left(\beta\omega/2\right) \frac{\sin^2\left(\omega t/2\right)}{(\omega/2)^2} \\
&= \int_0^\infty \mathrm{d}\omega\, \alpha\omega e^{-\omega/\omega_c} \frac{\sin^2\left(\omega t/2\right)}{(\omega/2)^2} \\
&\quad + 2\sum_{n=1}^{\infty} \int_0^\infty \mathrm{d}\omega\, \alpha\omega e^{-\omega/\omega_c} e^{-2n\beta\omega/2} \frac{\sin^2\left(\omega t/2\right)}{(\omega/2)^2} \\
&= \alpha \log\left[1 + \omega_c^2 t^2\right] + 2\alpha \sum_{n=1}^{\infty} \log\left[1 + \frac{\omega_c^2 t^2}{(1 + n\beta\omega_c)^2}\right] \\
&\simeq \alpha \log\left[1 + \omega_c^2 t^2\right] + 2\alpha \sum_{n=1}^{\infty} \log\left[1 + \frac{t^2}{n^2\beta^2}\right] \\
&= \alpha \log\left[1 + \omega_c^2 t^2\right] + 2\alpha \log\left[\frac{\beta}{\pi t} \sinh(\frac{\pi t}{\beta})\right] .
\end{aligned} \tag{7.25}$$

Inserting this into Eq. (7.21) yields

$$p_d(t) = \frac{1}{2} - \frac{1}{2}\left[(1 + \omega_c^2 t^2)\frac{\sinh^2(\pi t/\beta)}{(\pi t/\beta)^2}\right]^{-2\alpha} , \tag{7.26}$$

which for non-vanishing times ($t \gg \frac{1}{\omega_c}$) is well-approximated by

$$p_d(t) = \frac{1}{2} - \frac{1}{2}\left[\frac{\beta\omega_c}{\pi} \sinh(\frac{\pi t}{\beta})\right]^{-4\alpha} . \tag{7.27}$$

Inverting $p_d(\tau) = p_c$ leads to our final solution

$$\tau = \frac{\beta}{\pi} \text{arcsinh}\left[\frac{\pi}{\beta\omega_c}(1 - 2p_c)^{-1/4\alpha}\right] . \tag{7.28}$$

7.6 Surface code error correction for spatially correlated errors

The form of the evolution operator derived in Eq. (7.9) reveals that the state $\Phi_m \circ \Phi_d(\rho_q)$ contains correlations between the errors on arbitrary numbers of qubits. The coherent part of the evolution affects each pair $\{i, j\}$ of qubits by a two-qubit error with probability $\sin^2(J_{ij}(t))$, while any set $\{1, 2, \ldots, m\}$ of m qubits suffers an m-qubit error with probability

$(-1)^m \left\langle \sinh^2(X_1(t)) \ldots \sinh^2(X_m(t)) \right\rangle$ due to the decoherent evolution. If the decoherent evolution were uncorrelated, this probability would be given by $(-1)^m \left\langle \sinh^2(X_1(t)) \right\rangle \ldots \left\langle \sinh^2(X_m(t)) \right\rangle$. The difference between the two terms implies the presence of correlations: if a qubit suffers an error, nearby qubits have a higher chance of also being affected by an error than one would expect from the single-qubit error rate Eq. (7.13) alone.

The threshold error rate of $p_c = 10.9\%$ derived in Ref. [57] applies in the case of uncorrelated errors. The correlations mentioned above will change this value to an unknown threshold $\tilde{p}_c$. A recent work studied the effect of clusters of errors on surface code correction when the probability of a certain cluster size is exponentially or polynomially suppressed [142]. Thresholds were not studied in terms of the single-qubit error rate p_x but in terms of an over-all probability p for single-qubit errors and clusters of errors. If the probability of a large cluster decays sufficiently slowly, any $p > 0$ will lead to $p_x \to \frac{1}{2}$ for large enough L. This makes a direct application of the results of Ref. [142] to our problem impossible.

In the following, we thus want to investigate how different kinds of spatial correlations between errors affect the threshold error rate for the single-qubit error rate p_x. The modified threshold error rate $\tilde{p}_c$ strongly depends on the type of correlations that are present between the errors.

Fig. 7.1 summarizes our results. A worst case is given by ballistically propagating anyons, leaving a linear trail of errors behind. In this case, $\tilde{p}_c$ can be smaller than p_c by an order of magnitude or more. To understand this, note that the task of error correction is to pair the anyons in a way that is homologically equivalent to the way they have been created. Error correction breaks down if choosing the right homology class becomes ambiguous. This is achieved with the smallest number of errors if the anyons in each pair propagate into opposite directions.

If anyons perform a diffusive random walk in the toric code, the modified threshold error rate $\tilde{p}_c$ can also be significantly smaller than p_c. This scenario is physically relevant if there is a non-trivial surface (or toric) code Hamiltonian that energetically penalizes the creation, but not the propagation of anyons. The error model of diffusive errors and its effect on error correction have been studied in this context in Refs. [38, 81].

For both ballistic propagation and a diffusive random walk of anyons, there is a tendency for errors to form string-like patterns. By contrast, the correlations discussed at the beginning of this section favor a clustering of errors (i.e., it is more likely than in the uncorrelated case that errors

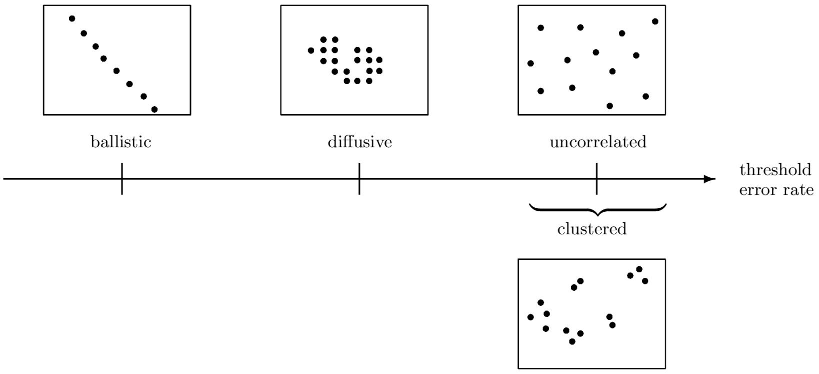

Figure 7.1: Different kinds of spatial correlations between errors in the surface code and how they affect its threshold error rate.

are spatially close to each other) but there is no mechanism that favors string-like error configurations.

We do not expect clustering of errors to strongly harm the threshold error rate p_c. Most clusters of nearby errors do not form string-like patterns and thus do not help to bring pairs of anyons apart from each other and make a homologically correct pairing ambiguous. For a fixed single-qubit error rate p_x, the presence of regions with a high density of errors implies the presence of regions with a low density of errors. The latter help to avoid ambiguities.

In the following subsections we study the modified threshold error rate $\tilde{p}_c$ for different kinds of spatial correlations between surface code errors by use of Monte Carlo simulations. In agreement with our expectations, we find that clustering of errors leads to at most a mild decrease of the threshold error rate – and can even be beneficial in the strongly correlated regime.

We conclude that even in the presence of spatial correlations between errors *without a mechanism that prefers string-like arrangements* the modified threshold error rate $\tilde{p}_c$ does not differ drastically from p_c. Heuristically, we expect correlations between errors arising from coupling the code to the bath not to be of the string-like type. We will thus in the following section invert the equation $p_x(\tau) = \tilde{p}_c$ without knowing the exact value of $\tilde{p}_c$, and simply assume that it is of the same order of magnitude as p_c.

Ballistic propagation of anyons

In the following subsections, we study the impact of correlated errors on the correctability of the surface code by use of Monte Carlo simulations. That is, we produce a large number of error configurations using a certain error model, and see whether we are able to find a pairing of the resulting anyon configuration that is homologically equivalent to the actual one. Finding such a paring is the task of a classical decoding algorithm. Only if unrealistic computing power is available can we hope to actually perform correction up to the theoretical threshold of $p_c = 10.9\%$ (in the uncorrelated case). Therefore, an efficient approximate error correction algorithm is needed in practice. We will employ minimum-weight perfect matching (MWPM) [70], which, for a graph with weighted edges and an even number of vertices provides the matching of minimal weight. Here, the vertices correspond to the anyons found as a result of the stabilizer measurements, and the weight of an edge connecting two anyons is simply given by the minimal number of qubits that have to suffer an error in order to create that pair from the anyonic vacuum (i.e., their Manhattan distance). We employ the library `Blossom V` [69] to perform MWPM. Using MWPM for performing error correction in the surface code reduces the threshold error rate to 10.2% [38, 126].

For our first "worst case" error model, we envision anyons that after creation start to ballistically propagate into a certain direction. More precisely, we specify the error model by two parameters f and l. First, we draw a number n at random from a Poisson distribution with mean $2fL^2$. Then, we perform n times the following. Choose one of the L^2 anyon locations and an angle $\phi \in [0, 2\pi)$ at random. (Recall that we consider one type of error only, so for a surface code of linear size L with periodic boundary conditions, there are L^2 anyon locations of the relevant type.) Draw random numbers l_h and l_v from Poisson distributions with mean $l|\cos(\phi)|$ and $l|\sin(\phi)|$, respectively (the expectation value for $l_h + l_v$ is thus $\frac{4}{\pi}l$). Starting from the initial anyon location, apply l_h errors horizontally and l_v errors vertically, with the directions given by the sign of the trigonometric functions. After doing this n times, perform error correction by means of MWPM.

For each value of l, there is a threshold value f_c such that for $f < f_c$ the logical error rate decreases exponentially with L and for $f > f_c$ the logical error rate approaches $\frac{1}{2}$. For each triple of l, f, and L, we generate a number N of error configurations which is such that error correction fails 10^4 times. The logical error rate can then be estimated as $10^4/N$. The threshold values f_c are then determined for each value of l by comparing the logical error rates for code sizes up to $L = 60$. Finally, once we know the threshold value f_c we can determine the threshold $\tilde{p}_c$ for the single-qubit error rate p_x by determining the fraction of qubits that suffer an error for the given pair of l and f_c. An even number of errors on the same qubit count as no error, and on odd number as one. If the errors are sufficiently sparse such that the probability of several errors happening on the same qubit is negligible, we have $p_x = \frac{4}{\pi}l \times 2fL^2/(2L^2) = \frac{4}{\pi}lf$, while otherwise it will be smaller.

The single-qubit threshold error rates $\tilde{p}_c$ as a function of l are illustrated by the purple squares in Fig. 7.2. While for $l = \frac{1}{2}$ the threshold is still comparable with the value of 10.2% for the uncorrelated case, it decreases strongly as l is increased.

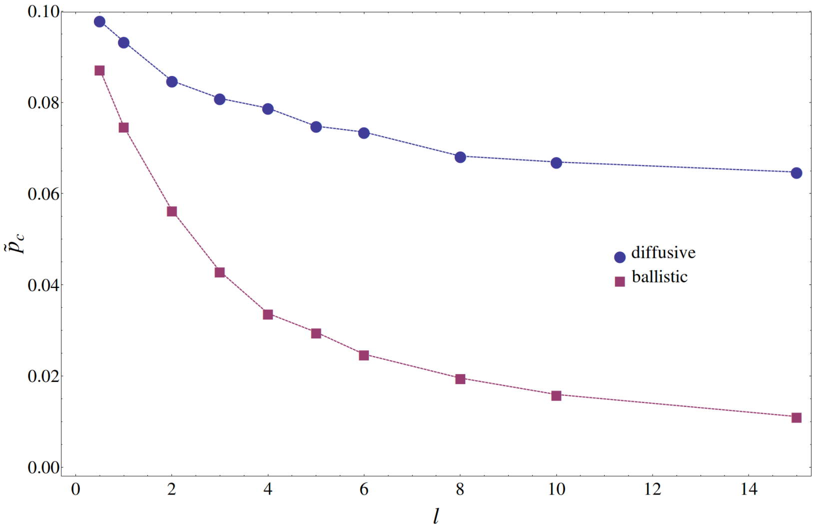

Figure 7.2: Single-qubit error rate $\tilde{p}_c$ for which error correction breaks down for two error models that lead to string-like error patterns: ballistic and diffusive propagation of anyons.

Diffusive propagation of anyons

In the case where anyons perform a random walk, the simulation works in much the same way as described in the previous subsection. For each initial anyon location, we draw a random number from a Poisson distribution with mean l, and then perform a random walk whose length is given by this number. The resulting thresholds are displayed by the blue circles in Fig. 7.2. Threshold error values are, for a given value of l, significantly higher than in the ballistic case though significantly lower than in the uncorrelated case.

Clustered errors

Here, we study a family of error models that describe clustering of errors in the surface code. For $l \leq m^2$, we define the error model m-l-cluster as follows: from each square of $m \times m$ qubits in the surface code, pick l qubits at random and apply an error to all of them with probability f. The resulting single-qubit error rate is $p_x \lesssim fl$. (Note that the same qubit can suffer several errors and an even number corresponds to no error at all, leading to $p_x < fl$.) The modified critical error rates $\tilde{p}_c$ are again determined as described in Sec. 7.6.

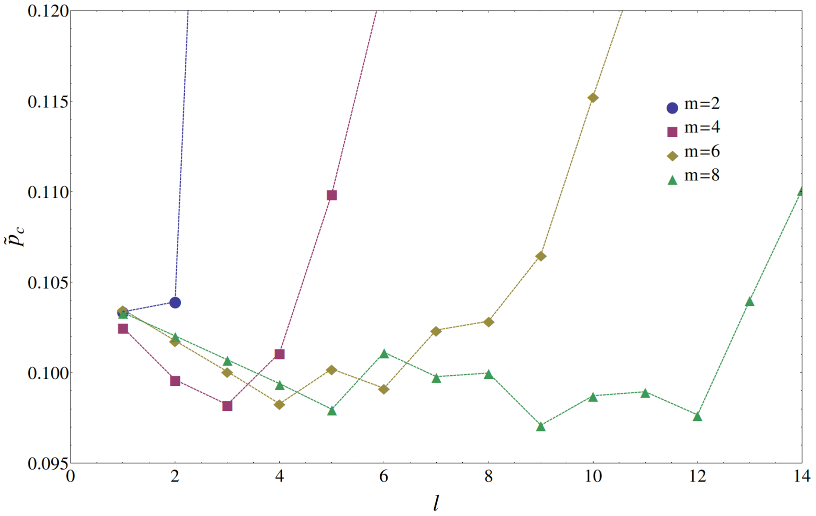

Figure 7.3: Single-qubit error rate $\tilde{p}_c$ for which error correction breaks down in the m-l-cluster error models.

Fig. 7.3 shows our results. If $l \ll m$, errors are essentially uncorrelated and the threshold values for $\tilde{p}_c$ are close to 10.2%, the threshold for MWPM-based error correction in the uncorrelated case. For $l \lesssim m$, $\tilde{p}_c$ falls slightly below 10%, though the decrease is not dramatic. This decrease is due to the possibility of forming string-like patterns of length l, which leads to a smaller number of errors being necessary for correction to become ambiguous. Finally, for $l > m$ the threshold increases significantly beyond p_c. Additional errors now make it easier to recognize the cluster and increase the probability that several errors together form a (partial) stabilizer operator and therefore do no harm to the code. For instance, in the 2-4-cluster case the threshold error rate is as high as $\tilde{p}_c = 29.0\%$, since half of all errors combine to a stabilizer operator. In reality, we do of course not expect the environment to apply exclusively 2×2 squares of errors, but to find ourselves in the regime where the clustering of errors leads to a slight reduction of the single-qubit threshold error rate.

Correlated two-qubit errors

Let us now study the case where there are correlations between errors on pairs of qubits only. Note that the coherent part of the evolution is able to produce such correlations only. The regime considered here is thus relevant if correlations between error events on more than two qubits due to the decoherent evolution are weak.

The study of correlated two-qubit errors is simplified by the fact that there is a clear worst-case, namely a two-qubit error on a pair of nearest-neighbor qubits. We assume that each qubit in the code suffers an error with probability p_1 and that, furthermore, each pair of nearest neighbors in the code suffers a pair of errors with probability p_2. We expect and have verified in numerical simulations (see below) that correlated errors on pairs of qubits which are not nearest neighbors have, for a fixed single-qubit error rate p_x, less of an effect on error correction than correlated errors on nearest neighbor qubits. Studying this particular case thus allows us to find the maximal impact of correlated two-qubit error events.

With the above parameters, and since each qubit in the code has four nearest neighbors, the single-qubit error rate p_x can be calculated in analogy to Eq. (7.13) as

$$\begin{aligned} p_x &= p_1 \sum_{k\text{ even}} \binom{4}{k} p_2^k (1-p_2)^{4-k} + (1-p_1) \sum_{k\text{ odd}} \binom{4}{k} p_2^k (1-p_2)^{4-k} \\ &= \frac{1}{2} - \frac{1}{2}(1-2p_1)(1-2p_2)^4 \, . \end{aligned} \tag{7.29}$$

We can make two estimates for where error correction will break down in the above model. First, we can simply assume that the correlations do neither help nor derogate the correctability of the code. In this case, the breakdown occurs for $p_x = p_c$ (or, with MWPM correction, for $p_x =$

10.2%), independently of p_2. A second estimate is of entropic nature. It is obtained by studying whether it is at all possible that the stabilizer measurements provide us with enough information to infer what errors have happened. Assume that there are n qubits in the code. There are $2n$ pairs of nearest neighbors and $n/2$ plaquette stabilizers that can give us information about bit-flip errors. For large n, the total information contained in the noise can be compressed to $nh(p_1) + 2nh(p_2)$ bits, where $h(p) = -p\log_2(p) - (1-p)\log_2(1-p)$ is the binary entropy function. On the other hand, the plaquette stabilizers give us at most $n/2$ bits of information. Error correction will thus break down if

$$2h(p_1) + 4h(p_2) = 1\ . \tag{7.30}$$

If we needed to know exactly which qubits have suffered a bit-flip, Eq. (7.30) would put a rigorous upper bound on the correctability of the surface code. However, we only need to know the error pattern *modulo application of stabilizer operators*. For this reason, Eq. (7.30) should rather be seen as an estimate of an upper bound. Such an entropic estimate predicts the unavoidable breakdown of surface code error correction to high accuracy for both uncorrelated bit-flip errors [57] (i.e., $2h(p_c) \simeq 1$) and depolarizing noise [131]. Ref. [40] shows that variations of the surface code tailored for stability against biased noise ($p_x \neq p_z$) give thresholds that fall only a few percents short of the ones suggested by such entropic arguments – even with error correction performed by an efficient approximate algorithm.

We will use two different algorithms for performing error correction for the above error model. Both of them are based on MWPM, but they differ in the weights they assign to the edges. The first one is the algorithm used in the previous subsections. It ignores correlations and assigns the Manhattan distance between two anyons to the edge connecting them. The second algorithm, described in more detail in Appendix 7.B, uses a more sophisticated assignment of edge weights that allows it to take spatial correlations between the errors into account.

Fig. 7.4 compares the above estimates with the resulting combinations (p_1, p_2) for which error correction breaks down in actual numerical simulations, when the two algorithms described above are used for performing error correction. If the Manhattan distance between two anyons is used as the edge weight and correlations between the errors are ignored, error correction breaks down for $p_x = 10.2\%$ for $p_2 \to 0$, slightly below the value of p_c for perfect error correction. In the maximally correlated regime, $p_1 \to 0$, error correction already breaks down for $p_x = 9.6\%$ – a

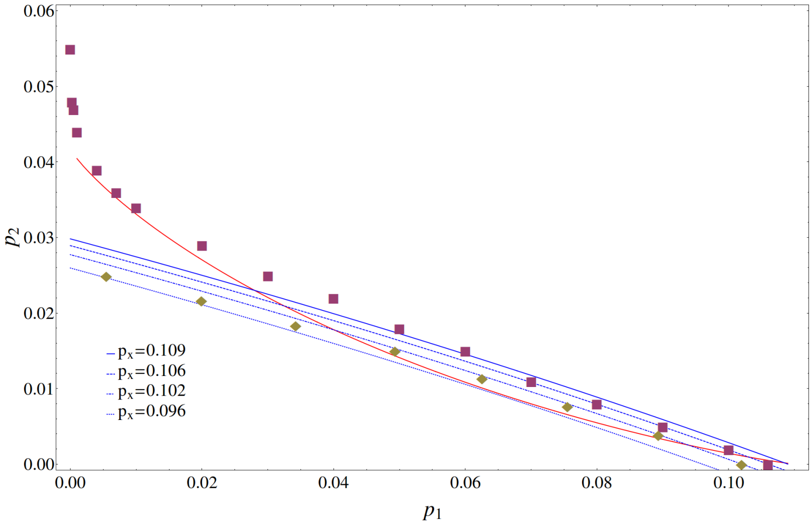

Figure 7.4: Each qubit is independently subjected to an error with probability p_1. Furthermore, each pair of nearest-neighbor qubits is subjected to a a pair of errors with probability p_2. The blue lines correspond to a constant value of p_x, calculated according to Eq. (7.29), while the red line shows the entropic bound Eq. (7.30). Diamonds represent threshold error rates (p_1, p_2) when error correction is performed with MWPM and correlations are ignored. Squares represent threshold error rates for an algorithm that takes correlations into account. Threshold error rates have been determined to accuracy 10^{-3}, by comparing logical error rates for code sizes between 10 and 50 (periodic boundary conditions). For each combination of error rates and code sizes, the logical error rates were obtained from as many error configurations as were necessary to obtain 10^4 logical errors.

pretty insignificant decrease. We have obtained similar data to the one displayed in Fig. 7.4 for correlated errors that happen on pairs of qubits which are further away from each other than nearest neighbors. In this case, the deviations from the line $p_x = 10.2\%$ are smaller. Already for pairs of qubits that are three lattice constants away from each other, the obtained threshold error rates are indistinguishable (to accuracy 10^{-3}) from this line.

For the second, improved algorithm, error correction breaks down for $p_x = 10.6\%$ in the uncorrelated case ($p_2 \to 0$), close to the theoretical value of p_c, and for $p_x = 18.6\%$ in the maximally correlated case

($p_1 \to 0$). The threshold error rates (p_1, p_2) approximately follow that of the two above estimates wich predicts the higher threshold value and significantly beat both estimates in some regimes. Beyond the red line in Fig. 7.4, it is information-theoretically impossible that we learn from the stabilizer measurements what errors have happened. That it is possible to error correct beyond that line shows that due to its degenerate nature (i.e., different error configurations can lead to the same syndrome) the surface code is able to take care of some of the entropy in the noise itself.

In conclusion, ignoring during error correction that pairs of qubits can be affected by correlated errors hardly affects the single-qubit threshold error rate of the surface code. If an algorithm takes these correlations into account, the single-qubit threshold error rate can be significantly boosted in the strongly correlated regime. Due to its degenerate nature, the surface code is able to correct in regimes where it is information-theoretically impossible that we learn what errors the code has suffered.

7.7 Maximal QEC cycle time for correlated errors

Assuming that the form of spatial correlations between errors that will be present in $\Phi_m \circ \Phi_d(\rho_q)$ does not lead to a threshold error rate $\tilde{p}_c$ that differs drastically from p_c, the single-qubit error rate $p_x(t)$ in Eq. (7.13) contains already all the information we need in order to predict the maximal QEC period τ. A great advantage of Eq. (7.13) is that it depends only on $p_d(t)$ and the coherent interaction strengths $J_{ij}(t)$, but not on the temperature-dependent correlators $C_{ij}(t)$ for $i \neq j$.

Our goal is thus to solve the equation $p_x(\tau) = \tilde{p}_c$ for τ, where $p_x(t)$ is given by Eq. (7.13). Since $\tilde{p}_c$ is an order of magnitude smaller than 1, we can approximate $p_x(t)$ by its leading-oder contributions,

$$p_x(t) \simeq p_d(t) + \sum_i{}' \sin^2(J_{1i}(t)) \,. \tag{7.31}$$

We follow again Ref. [138] and study an Ohmic bath ($r = 0$, $D = 2$). The function $J_{ij}(t)$ for this bath type has been provided in Eq. (7.19). Note that $J_{ij}(t)$ decays inversely with distance outside of the light-cone. Therefore, the second summand in Eq. (7.31) diverges logarithmically with the code size L at any non-zero time (up to constant prefactors of order 1, we have $\sum_i{}' \frac{1}{|\mathbf{R}_1 - \mathbf{R}_i|^2} \sim \int_1^{L/2} \frac{1}{r^2} r \mathrm{d}r \sim \log(L)$). Correspondingly, the maximal QEC period vanishes in the thermodynamic limit (though it does so very slowly, see below). For all other combinations of $D = 2, 3$ and $r = 0, \pm\frac{1}{2}$, $J_{ij}(t)$ decays stronger than $|\mathbf{R}_i - \mathbf{R}_j|^{-1}$ outside of the light-cone (see Appendix 7.A). The maximal QEC period remains thus finite in the thermodynamic limit for all other bath types.

Setting the lattice constant of the surface code to unity and assuming a linear code size L, we can estimate

$$\sum_i{}' \sin^2(J_{1i}(t)) \simeq \\ 2\pi \int_0^{L/2} \mathrm{d}R\, R \sin^2 \left[\frac{\lambda^2}{2\pi^2 v^2} \left(\theta(R - vt) \arcsin(vt/R) + \theta(vt - R) \frac{\pi}{2} \right) \right] . \tag{7.32}$$

Since we are interested in times where this sum is (still) sufficiently smaller than 1, in particular each summand has to be much smaller than 1. Defining $m(t) = \min\{L/2, vt\}$, we find

$$\begin{aligned} \sum_i{}' \sin^2(J_{1i}(t)) &\simeq 2\pi \int_{m(t)}^{L/2} \mathrm{d}R\, \frac{1}{R} \left(\frac{\lambda^2 t}{2\pi^2 v} \right)^2 + 2\pi \int_0^{m(t)} \mathrm{d}R\, R \left(\frac{\lambda^2}{4\pi v^2} \right)^2 \\ &= \frac{\lambda^4 t^2}{2\pi^3 v^2} \log(\frac{L/2}{m(t)}) + \frac{\lambda^4}{16\pi v^4} m^2(t) . \end{aligned} \tag{7.33}$$

Combining Eqs. (7.27), (7.31), and (7.33) we conclude that for times t which are small enough such that $p_x(t) \ll 1$ we have

$$p_x(t) \simeq \underbrace{\frac{1}{2} - \frac{1}{2} \left[\frac{\beta\omega_c}{\pi} \sinh(\frac{\pi t}{\beta}) \right]^{-2\lambda^2/\pi v^2}}_{A(t)} + \underbrace{\frac{\lambda^4 t^2}{2\pi^3 v^2} \log(\frac{L/2}{m(t)})}_{B(t)} + \underbrace{\frac{\lambda^4}{16\pi v^4} m^2(t)}_{C(t)} . \tag{7.34}$$

We can recognize three different mechanisms contributing to the single-qubit error rate $p_x(t)$. Summand $A(t)$ describes errors due to each qubit coupling individually to the bath. Correspondingly, this term is independent of L. It is the only term that depends on temperature and the only term that contributes if the qubits do not interact via the bath. Summand $B(t)$ describes errors due to superluminal interactions between the qubits mediated by the bath. It diverges logarithmically with L for short enough times but vanishes once all qubits are within their mutual light-cones. Finally, summand $C(t)$ describes errors due to subluminal interactions between the qubits. Once all qubits are within their mutual light-cones,

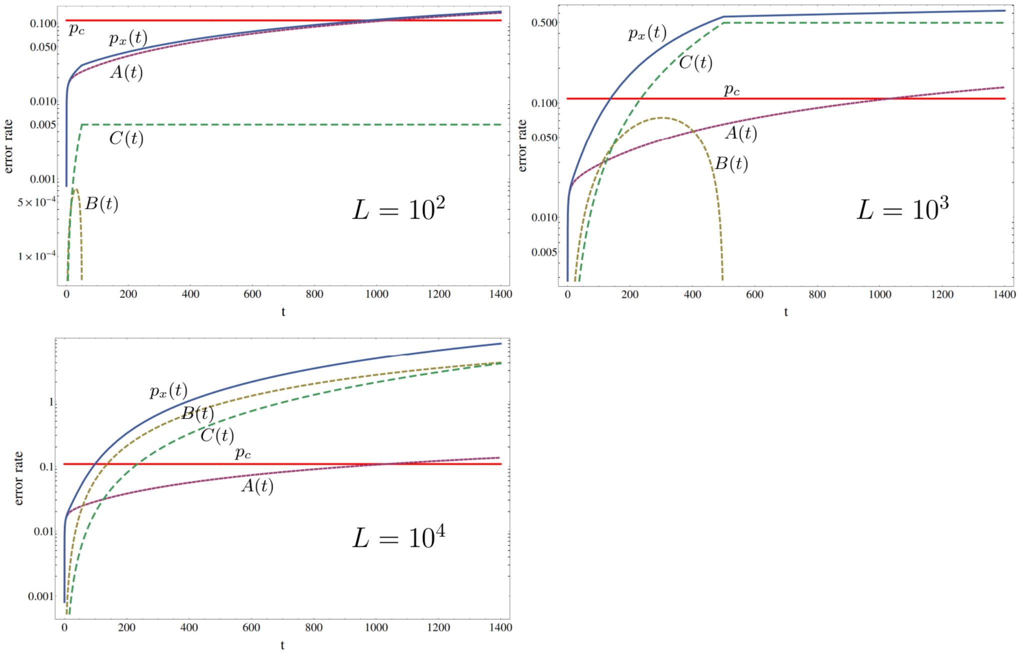

Figure 7.5: The three summands $A(t)$, $B(t)$, and $C(t)$ and their sum $p_x(t)$ compared with p_c for code sizes $L = 10^2$, $L = 10^3$, and $L = 10^4$. We have used paramters $v = 1$, $\lambda = 0.1$, $T = 0.01$, and $\omega_c = 30$. Note that the assumptions $\beta\omega_c \gg 1$ and $\tau_d \gg 1/\omega_c$ made during the derivation of $A(t)$ are well-satisfied.

this term reaches a time-independent constant which is proportional to the number of qubits in the code.

We have already studied the times τ_d which are necessary for summand $A(t)$ to reach critical levels ($A(\tau_d) \simeq p_c$) in Sec. 7.5. The only question that remains is whether $B(t)$ or $C(t)$ reach critical levels before $A(t)$ and if so, on what time-scales. As shown in Fig. 7.5, each of the three summands can be the dominant force leading to the breakdown of error correction. A higher temperature increases the weight of summand $A(t)$, while a larger code size increases the weight of summands $B(t)$ and $C(t)$.

In order to find the maximal QEC period τ, we make the simplifying assumption that the breakdown is due to the dominant mechanism alone, i.e., we approximate $p_x(t) \simeq \max\{A(t), B(t), C(t)\}$. Note that for times much smaller than L/v, we have $B(t) > C(t)$, while for times of order L/v or larger, we have $B(t) < C(t)$. For times larger than $L/2v$, $C(t)$ reaches its maximal value $\frac{\lambda^4 L^2}{64\pi v^4}$. Therefore, for $L > 8\sqrt{\pi\tilde{p}_c}\frac{v^2}{\lambda^2}$ the term $C(t)$

Code size	Breakdown in a time	Dominant mechanism
$L < 4.7\frac{v^2}{\lambda^2}$	τ_d	direct bath coupling
$4.7\frac{v^2}{\lambda^2} < L < 16.1\frac{v^2}{\lambda^2}$	$\min\{\tau_d, \tau_{\text{sub}}\}$	... or subluminal interactions
$L > 16.1\frac{v^2}{\lambda^2}$	$\min\{\tau_d, \tau_{\text{super}}\}$	... or superluminal interactions

Table 7.1: Maximal time before error correction in the surface code breaks down for a 2D Ohmic bath in different parameter regimes. The times τ_d, τ_{sub}, and τ_{super} are summarized in Sec. 7.7.

will reach critical values ($\tilde{p}_c$) in a time

$$\tau_{\text{sub}} = \frac{4\sqrt{\pi\tilde{p}_c}v}{\lambda^2} , \tag{7.35}$$

while otherwise it will never do so. Elementary calculus shows that the maximal value, which $B(t)$ can achieve while still being larger than $C(t)$, is $\frac{e^{-\pi^2/4}}{64\pi}\frac{\lambda^4}{v^4}L^2$, and that $B(t)$ is monotonically increasing until it reaches this value. Therefore, $B(t)$ reaches $\tilde{p}_c$ before $C(t)$ if and only if $L > 8e^{\pi^2/8}\sqrt{\pi\tilde{p}_c}\frac{v^2}{\lambda^2}$. The (relevant) solution to $B(\tau_{\text{super}}) = \tilde{p}_c$ is given by

$$\tau_{\text{super}} = 2\pi\sqrt{\pi\tilde{p}_c}\frac{v}{\lambda^2}\left|W_{-1}(-16\pi^3\tilde{p}_c v^4/\lambda^4 L^2)\right|^{-1/2} , \tag{7.36}$$

where W_{-1} is the lower branch of the Lambert W function.[1] For $z \to 0^-$, we have $W_{-1}(z) \simeq \log|z|$, showing that the available QEC time vanishes in the thermodynamic limit $L \to \infty$ like $\tau \sim 1/\sqrt{\log(L)}$, that is, very slowly.

Summary of results

Let us summarize our results for a 2D Ohmic bath. There are three different mechanisms that contribute to the error rate on each qubit and hence put limits on the maximal QEC period τ: the individual coupling of each qubit to the bath, superluminal interactions between the qubits mediated by the bath as well as subluminal ones.

---

[1] The Lambert W function by definition satisfies $z = W(z)e^{W(z)}$. For $-e^{-1} < z < 0$, there are two solutions, giving rise to two branches $W_{-1}(z)$ and $W_0(z)$ with $W_{-1}(z) < W_0(z) < 0$. The equation $a = x^2\log(\xi/x)$ with $a > 0$ and $\xi > \sqrt{2ae}$ has the two solutions $x = \sqrt{2a}\left|W_k(-2a/\xi^2)\right|^{-1/2}$, with $k = -1, 0$. Since we are interested in the smaller of the two solutions, we choose the $k = -1$ branch and obtain Eq. (7.36).

The direct interaction of each qubit with the bath puts an upper bound τ_d on the maximal time for which error correction can suceed. This time is given by Eq. (7.28), for which we find a high- and a low-temperature value

$$\begin{aligned}\tau_d &= \frac{1}{\pi T}\text{arcsinh}\left[\frac{\pi T}{\omega_c}(1-2\tilde{p}_c)^{-\pi v^2/2\lambda^2}\right]\\ &\simeq \begin{cases}\frac{1}{\omega_c}\exp(cv^2/\lambda^2) & \text{if} \quad T < \frac{\omega_c}{\pi}\exp(-cv^2/\lambda^2)\\ \\ \frac{1}{\pi T}\left(cv^2/\lambda^2 - \log\left[\frac{\omega_c}{2\pi T}\right]\right) & \text{if} \quad T > \frac{\omega_c}{\pi}\exp(-cv^2/\lambda^2)\,.\end{cases}\end{aligned} \tag{7.37}$$

Here, $c = \frac{\pi}{2}\log\frac{1}{1-2\tilde{p}_c}$. Assuming $\tilde{p}_c \simeq p_c$, we find $c \simeq 0.4$.

The interaction between the qubits mediated by the bath is a further source of errors, both due to subluminal and superluminal interactions. Errors due to mediated interactions can only reach critical values if the linear code size L is large enough; if $L < 8\sqrt{\pi\tilde{p}_c}\frac{v^2}{\lambda^2}$, neither the error strength due to sub- nor due to super-luminal interactions will ever reach $\tilde{p}_c$. For $8\sqrt{\pi\tilde{p}_c}\frac{v^2}{\lambda^2} < L < 8e^{\pi^2/8}\sqrt{\pi\tilde{p}_c}\frac{v^2}{\lambda^2}$, errors due to sub-luminal interaction reach a critical strength in a time $\tau_{\text{sub}} \sim v/\lambda^2$. If errors due to superluminal interactions also reach criticality, they will do so on times larger than τ_{sub} for these values of L. Finally, if $L > 8e^{\pi^2/8}\sqrt{\pi\tilde{p}_c}\frac{v^2}{\lambda^2}$, superluminally meadiated errors reach criticality before subluminal ones, and they do so in a time $\tau_{\text{super}} \sim v/\lambda^2\sqrt{\log L}$. This time vanishes very slowly in the thermodynamic limit. These results are summarized in Tab. 7.1 (assuming $\tilde{p}_c \simeq p_c$).

7.8 Conclusions

Quantum information is fragile and can only be maintained if the accumulation of entropy in the information-bearing degrees of freedom of a storage device can be suppressed – either by preventing entropy from entering or by removing it at a sufficient pace. Any possible measure to achive this can only succeed for certain classes of system-environment couplings. Correspondingly, a proposal that promises stability of quantum information is only as valuable as the error source against which it protects is realistic.

In this work, we have investigated how long the surface code is able to protect a quantum state against noise emerging from a physically relevant type of environment – a bath of freely propagating bosonic modes.

We have seen that there are two very distince kinds of error mechanisms: the individual decoherence of each qubit, and induced interactions between the code qubits. Both mechanisms lead to spatial and temporal correlations between the errors happening in the code. However, we have shown that a tendency of errors to cluster without a tendency to form string-like configurations does not strongly derogate the correctability of the surface code – even when these correlations are ignored during error correction.

We have managed to express the time before the error rates in the code reach critical values in terms of code size (L), accidental coupling strength (λ), mode velocity (v), and bath temperature (T) across a wide range of different parameter regimes. Two further parameters that determine the physical character of the qubits' decoherence mechanism are the spatial dimension of the medium in which the modes propagate (D) and the nature of the coupling to the bath (r). We have focused our discussion on the specific combination ($D = 2$, $r = 0$) investigated in Ref. [138], which corresponds to an Ohmic bath. This combination is of particular interest since it is the only one for which the maximal QEC time vanishes (very slowly) in the thermodynamic limit. For all other combinations of $D = 2, 3$ and $r = 0, \pm\frac{1}{2}$, this time remains finite.

Following Refs. [138,139], we have made several simplifying assumptions to make the actual problem analytically tractable. These are: a trivial Hamiltonian for the qubits; undamped and non-interacting bath modes; no residual bath correlations between different QEC periods; one type of errors only (bit-flips); immediate and flawless syndrome measurement and error correction (including no time cost for efficient classical computations). Relaxing these assumptions opens a wide field of additional challenges. For instance, fully fault-tolerant syndrome extraction and error correction are discussed in Ref. [134,137]. A finite probability of syndrome measurement failure will lead to a lower value of $\tilde{p}_c$ and hence necessitate shorter QEC periods. Moreover, we have in this work been concerned exclusively with spatial and temporal correlations between errors in the surface code. If there are non-commuting error types on the same qubit (bit- and phase-flips), a further type of correlation in the noise emerges, namely correlations between different error types on the same qubit. Such correlations are present in the often-used error model of depolarizing noise. How they can be taken into account during error correction is studied in Refs. [125, 127, 128, 136]. Finally, adding an energy splitting $-\frac{\Delta}{2}\tilde{\sum}_i \sigma_i^z$ for the code qubits would transform the problem into a many-spin generalization of the well-studied spin-boson problem. For a single spin-qubit coupled to an Ohmic bath, the spin-boson problem has been solved within the Born approximation in Ref. [73]. However, the generalization of this problem to the many-qubit case may well be analytically intractable [143].

7.9 Acknowledgements

We would like to thank J. R. Wootton, P. Jouzdani, B. M. Terhal, and A. G. Fowler for helpful discussions. This work was supported by the Swiss NF, NCCR QSIT, and IARPA.

7.A Different bath types

Induced interactions

Linear dispersion

The bath-induced pairwise interaction between code qubits is described by the function

$$J_{ij}(t) = 2\lambda^2 \int \mathrm{d}\mathbf{k}\, e^{-v|\mathbf{k}|/\omega_c} \frac{|\mathbf{k}|^{2r}}{\omega_{\mathbf{k}}^2} \cos\left(\mathbf{k}(\mathbf{R}_i - \mathbf{R}_j)\right) \left(\sin(\omega_{\mathbf{k}} t) - \omega_{\mathbf{k}} t\right) \ , \quad (7.38)$$

where we have introduced a cut-off factor $e^{-v|\mathbf{k}|/\omega_c}$ into the expression given in Eq. (7.8). The cut-off factor is only necessary in the case (3D, $r = \frac{1}{2}$), while in all other cases we can let $\omega_c \to \infty$. In 2D, the functions $J_{ij}(t)$ can be calculated as described in Ref. [139, Appendix C]. With $\omega_{\mathbf{k}} = v|\mathbf{k}|$ and $R := |\mathbf{R}_i - \mathbf{R}_j|$, the results are

$$J_{ij}(t) = \begin{cases} \frac{\lambda^2}{2\pi^2 v^2}\theta(vt-R)\left(\sqrt{v^2t^2-R^2} - vt\log(\frac{vt+\sqrt{v^2t^2-R^2}}{R})\right) & \text{for } r = -\frac{1}{2} \\ \frac{\lambda^2}{2\pi^2 v^2}\left(\theta(R-vt)\arcsin(vt/R) + \theta(vt-R)\frac{\pi}{2}\right) & \text{for } r = 0 \\ \frac{\lambda^2}{2\pi^2 v^2}\frac{\theta(vt-R)}{\sqrt{v^2t^2-R^2}} & \text{for } r = \frac{1}{2}\,, \end{cases} \quad (7.39)$$

while in 3D, we find

$$J_{ij}(t) = \begin{cases} -\frac{\lambda^2}{2\pi R v^2}(vt-R)\theta(vt-R) & \text{for } r = -\frac{1}{2} \\ \frac{\lambda^2}{2\pi^2 R v^2}\left(\log\left|\frac{R+vt}{R-vt}\right| - \frac{2vt}{R}\right) & \text{for } r = 0 \\ \frac{2\lambda^2}{\pi^2 R^4 v\omega_c}\frac{2R^2-v^2t^2}{(R^2-v^2t^2)^2}v^3t^3 & \text{for } r = \frac{1}{2}\,. \end{cases} \quad (7.40)$$

Note that in three cases the interaction vanishes exactly outside of the light-cone. The combination (2D, $r = 0$) considered in the main text shows the longest-range superluminal interactions. It is the only one for which the sum $\sum_i{}' \sin^2(J_{1i}(t))$ in Eq. (7.31) diverges for any non-zero time in the thermodynamic limit. Correspondingly, it is the only one for which the maxmial QEC period (theoretically) vanishes in this limit.

Ordered ferromagnet: parabolic dispersion

Recently, the idea of performing entangling gates between qubits by coupling them to an ordered Heisenberg ferromagnet has attracted interest [141]. An ordered Heisenberg ferromagnet can be seen as a 3D magnon bath ($\omega_{\mathbf{k}} = D\mathbf{k}^2$). If we couple to a spin component which is orthogonal to the ordering, we obtain a coupling of type $r = 0$. The ferrogmanet thus acts as a sub-Ohmic bath ($s = \frac{1}{2}$). Then,

$$\begin{aligned} J_{ij}(t) = \frac{\lambda^2}{4\pi^2 D^2 R} \Bigg[& -2\pi Dt - \pi(R^2 - 2Dt) C\left(\frac{R}{\sqrt{2\pi Dt}}\right) \\ & + \pi(R^2 + 2Dt) S\left(\frac{R}{\sqrt{2\pi Dt}}\right) + \sqrt{2\pi Dt} R(\cos(\frac{R^2}{4Dt}) + \sin(\frac{R^2}{4Dt})) \Bigg] , \end{aligned} \tag{7.41}$$

where $C(x) = \int_0^x \cos(t^2)\mathrm{d}t$ and $S(x) = \int_0^x \sin(t^2)\mathrm{d}t$ are the Fresnel-integrals. For times such that $R \ll \sqrt{Dt}$, the first summand in the bracket dominates and we find

$$J_{ij}(t) = -\frac{\lambda^2 t}{2\pi DR} . \tag{7.42}$$

Decoherence

We have shown in Sec. 7.5 that the probability of an error due to the coupling of a qubit to the bath is given by

$$p_d(t) = \frac{1}{2}\left(1 - \exp\left\{-2\Lambda(t)\right\}\right) , \tag{7.43}$$

where the function $\Lambda(t)$ is given in Eq. (7.23). It depends only on the spectral function $J(\omega) = \alpha\omega^s\omega_0^{1-s}e^{-\omega/\omega_c}$ of the bath and its temperature. The cases $s = 0, 1, 2, 3$ are relevant for the kinds of couplings to a bath with linear dispersion in 2D or 3D considered in the main part of this

Condition	Type	Contribution to p_{ij}
	$m_2 = 0$	$\binom{a+b}{a}\left(\frac{p_1}{1-p_1}\right)^{a+b}$
$a + b \equiv 0 \pmod 2$	$m_1 = 0$	$\binom{b}{(b-a)/2}\left(\frac{p_2}{1-p_2}\right)^{b}$
$a + b \equiv 1 \pmod 2 \wedge a + b \geq 3$	$m_1 = 1 \wedge m_2 \geq 1$	$\frac{a+b+1}{2}\binom{b}{(b-a-1)/2}\frac{p_1}{1-p_1}\left(\frac{p_2}{1-p_2}\right)^{b-1}$
$a \geq 1 \wedge a + b \geq 4$	$m_1 \geq 2 \wedge m_2 = 1$	$(a+b-1)\binom{a+b-2}{a-1}\left(\frac{p_1}{1-p_1}\right)^{a+b-2}\frac{p_2}{1-p_2}$

Table 7.2: Contributions to p_{ij} we consider if anyons i and j have horizontal distance a and vertical distance b, or *vice versa*, with $a \leq b$.

work. The case $s = \frac{1}{2}$ is relevant for an ordered Heisenberg ferromagnet (see previous subsection).

For those values of s, we find

$$\Lambda(t) = \begin{cases} \alpha\pi\omega_0 t & \text{if} \quad s = 0 \quad \text{and} \quad \beta \to \infty \\ 2\alpha\sqrt{2\pi\omega_0 t} + 2\alpha\sqrt{\frac{\beta\omega_0}{\pi}}\left(4\pi \mathrm{Re}\,\zeta(-\frac{1}{2}, 1 + \frac{it}{\beta}) + \zeta(\frac{3}{2})\right) & \text{if} \quad s = \frac{1}{2} \quad \text{and} \quad \beta\omega_c \gg 1 \\ \alpha\log(1 + \omega_c^2 t^2) + 2\alpha\log\left(\frac{\beta}{\pi t}\sinh(\frac{\pi t}{\beta})\right) & \text{if} \quad s = 1 \quad \text{and} \quad \beta\omega_c \gg 1 \\ \frac{\alpha}{\omega_0}\left(-\frac{2\omega_c^2 t^2}{1+\omega_c^2 t^2} - \frac{4}{\beta}\psi(\frac{1}{\beta\omega_c}) + \frac{4}{\beta}\mathrm{Re}\,\psi(\frac{1+i\omega_c t}{\beta\omega_c})\right) & \text{if} \quad s = 2 \\ \frac{\alpha}{\omega_0^2}\left(-\frac{2\omega_c^4 t^2(3+\omega_c^2 t^2)}{(1+\omega_c^2 t^2)^2} + \frac{4}{\beta^2}\psi'(\frac{1}{\beta\omega_c}) - \frac{4}{\beta^2}\mathrm{Re}\,\psi'(\frac{1+i\omega_c t}{\beta\omega_c})\right) & \text{if} \quad s = 3\,. \end{cases} \tag{7.44}$$

Here, $\zeta(-\frac{1}{2}, z)$ denotes a Hurwitz zeta function and $\psi(z)$ is the digamma function. The case $s = 0$ requires at finite temperature an infrared cutoff for convergence. The result for $s = 1$ has been derived in Eq. (7.25), the result for $s = \frac{1}{2}$ can be derived in a very analogous way. Note that a well-defined $\omega_c \to \infty$ limit exists only for sub-Ohmic baths.

The expressions in Eq. (7.44) (for $s > 0$) are displayed for a specific set of parameters α, ω_0, ω_c, and β in Fig. 7.6 and compared to the critical value of $\Lambda(t)$ in the case of uncorrelated errors given in Eq. (7.24). We see that for super-Ohmic baths this critical value is reached distinctively earlier than for Ohmic and sub-Ohmic baths.

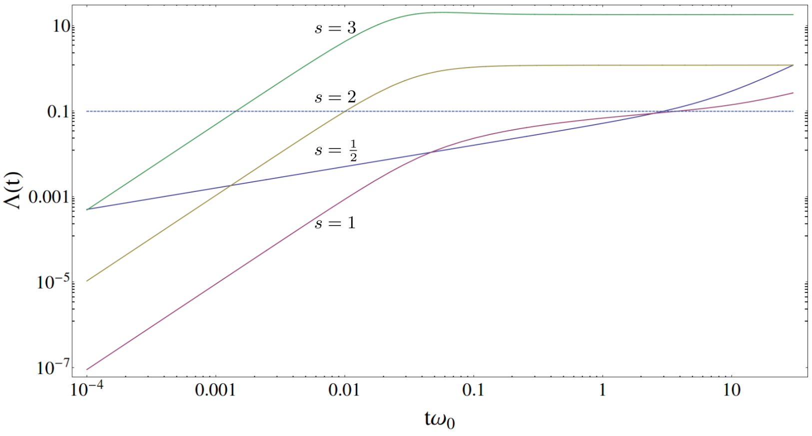

Figure 7.6: (The bold lines show the functions $\Lambda(t)$ given in Eq. (7.44). We have used parameters $\alpha = 0.01$, $\omega_c/\omega_0 = 30$, and $\beta\omega_0 = 10$. The dashed line shows the critical value $\frac{1}{2}\log\frac{1}{1-2p_c} \simeq 0.123$, when error correction breaks down in the uncorrelated case.

7.B An algorithm that is able to take correlations between errors on nearest neighbors into account

We assume again a single-qubit error rate p_1 and a rate of two-qubit errors on nearest neighbors p_2. To an edge connecting anyons i and j, we want to assign a weight $-\log(p_{ij})$, where p_{ij} is the sum of the probabilities of all error chains connecting anyons i and j. The minimal-weight error chain is then the most likely one. Taking the negative logarithm ensures that the weights are additive for independent error chains. More precisely, we will not consider the absolute probabilities but the probabilities relative to no errors happening. This leads to a constant shift of all weights, which is irrelevant since the number of edges involved in each matching is identical.

Using the Manhattan distance of the anyons as the weight, as we did for the algorithm that ignores correlations between errors, corresponds to approximating p_{ij} by the probability of the most likely single-qubit error path connecting anyons i and j, without taking the degeneracy of this probability into account. While calculating p_{ij} exactly is unfeasible, the algorithm presented here is based on a better approximation of p_{ij}, which, in particular, takes the possibility of two-qubit errors into account.

We will restrict to those error chains which probabilistically dominate for either $p_1 \gg p_2$ or $p_1 \ll p_2$.

Assume that anyons i and j have horizontal distance a and vertical distance b, or *vice versa*, with $a \leq b$. In Tab. 7.2, we list all contributions to p_{ij} which we consider. The probability-independent prefactors are the number of possible paths of the respective type. We denote with m_1 the number of one-qubit events and with m_2 the number of two-qubit events in an error path. We consider all error paths contributing to p_{ij} for which $m_1 \leq 1$ or $m_2 \leq 1$, and which are such that there is no error path with error numbers m_1' and m_2' connecting anyons i and j such that $m_1' \leq m_1$, $m_2' \leq m_2$, and $m_1' + m_2' < m_1 + m_2$.

7.C Exact evolution of two-qubit density matrix

Let us assume that only two qubits, i and j, couple to the bath and let us study their joint evolution, which according to Eqs. (7.5) and (7.9), is given by

$$\rho_{ij}(t) = \exp\left\{-iJ_{ij}(t)\sigma_i^x \otimes \sigma_j^x\right\} \mathcal{E}_t(\rho_{ij}) \exp\left\{+iJ_{ij}(t)\sigma_i^x \otimes \sigma_j^x\right\} \ . \tag{7.45}$$

where

$$\begin{aligned}
\mathcal{E}_t(\rho_q) = \mathrm{tr}_B &\left\{ e^{\sigma_i^x \otimes X_i(t)} e^{\sigma_j^x \otimes X_j(t)} (\rho_{ij} \otimes \rho_B) e^{-\sigma_i^x \otimes X_i(t)} e^{-\sigma_j^x \otimes X_j(t)} \right\} \\
= &\ \rho_{ij} \times \left\langle \cosh^2(X_i(t)) \cosh^2(X_j(t)) \right\rangle \\
&- \sigma_i^x \rho_{ij} \sigma_i^x \times \left\langle \sinh^2(X_i(t)) \cosh^2(X_j(t)) \right\rangle \\
&- \sigma_j^x \rho_{ij} \sigma_j^x \times \left\langle \cosh^2(X_i(t)) \sinh^2(X_j(t)) \right\rangle \\
&+ \sigma_i^x \sigma_j^x \rho_{ij} \sigma_i^x \sigma_j^x \times \left\langle \sinh^2(X_i(t)) \sinh^2(X_j(t)) \right\rangle \\
&+ \left(\sigma_i^x \sigma_j^x \rho_{ij} + \rho_{ij} \sigma_i^x \sigma_j^x - \sigma_i^x \rho_{ij} \sigma_j^x - \sigma_j^x \rho_{ij} \sigma_i^x \right) \\
&\quad \times \left\langle \cosh(X_i(t)) \sinh(X_i(t)) \cosh(X_j(t)) \sinh(X_j(t)) \right\rangle \ .
\end{aligned} \tag{7.46}$$

Our goal is to express all appearing expectation values in terms of the correlators

$$C_{ij}(t) = \langle X_i(t) X_j(t) \rangle = -\frac{\lambda^2}{N} \sum_{\mathbf{k}} |\mathbf{k}|^{2r} \cos\left(\mathbf{k}(\mathbf{R}_i - \mathbf{R}_j)\right) \coth(\beta\omega_{\mathbf{k}}/2) \frac{\sin^2(\omega_{\mathbf{k}} t/2)}{(\omega_{\mathbf{k}}/2)^2} \ . \tag{7.47}$$

The fuctions $\Lambda(t) = -C_{ii}(t)$ are discussed in detail in Sec. 7.5.

Recall that $\sinh^2(x) = \frac{1}{2}(\cosh(2x) - 1)$ and $\cosh^2(x) = \frac{1}{2}(\cosh(2x) + 1)$. The first four expectation values (those corresponding to diagonal terms) can thus be reduced to $\langle \cosh(2X_i(t)) \rangle$ and $\langle \cosh(2X_i(t)) \cosh(2X_j(t)) \rangle$. We already know that

$$\langle \cosh(2X_i(t)) \rangle = 2\langle \sinh^2(X_i(t)) \rangle + 1 = \exp\{-2\Lambda(t)\} \tag{7.48}$$

(see Eq. (7.21)). Let us thus calculate

$$\begin{aligned}
&\langle \cosh(2X_i(t)) \cosh(2X_j(t)) \rangle \\
&= \sum_{m,n=0}^{\infty} \frac{2^{2m+2n}}{(2m)!(2n)!} \langle X_i(t)^{2m} X_j(t)^{2n} \rangle \\
&= \sum_{m,n=0}^{\infty} \sum_{k}^{\min(m,n)} \frac{2^{2m+2n}}{(2m)!(2n)!} \binom{2m}{2k} (2k)! \binom{2n}{2k} \langle X_i(t)^{2m-2k} \rangle \langle X_i(t) X_j(t) \rangle^{2k} \langle X_j(t)^{2n-2k} \rangle \\
&= \sum_{m,n=0}^{\infty} \sum_{k}^{\min(m,n)} (-1)^{m+n} \frac{2^{2m+2n}}{(2m)!(2n)!} \binom{2m}{2k} (2k)! \binom{2n}{2k} \frac{(2m-2k)!}{2^{m-k}(m-k)!} \frac{(2n-2k)!}{2^{n-k}(n-k)!} \\
&\quad \times \Lambda(t)^{m+n-2k} C_{ij}(t)^{2k} \\
&= \sum_{m,n=0}^{\infty} \sum_{k}^{\min(m,n)} \frac{(-2)^{m+n+2k} \Lambda(t)^{m+n-2k} C_{ij}(t)^{2k}}{(m-k)!(n-k)!(2k)!} \; .
\end{aligned} \tag{7.49}$$

To simplify this expression, we define $u := m - k$ and $v := n - k$. Then,

$$\begin{aligned}
\langle \cosh(2X_i(t)) \cosh(2X_j(t)) \rangle &= \sum_{u,v,k=0}^{\infty} \frac{(-2)^{u+v+4k} \Lambda(t)^{u+v} C_{ij}(t)^{2k}}{u!v!(2k)!} \\
&= e^{-4\Lambda(t)} \cosh(4C_{ij}(t)) \; .
\end{aligned} \tag{7.50}$$

We conclude that

$$\begin{aligned}
\left\langle \cosh^2(X_i(t)) \cosh^2(X_j(t)) \right\rangle &= \frac{1}{4} + \frac{1}{2} e^{-2\Lambda(t)} + \frac{1}{4} e^{-4\Lambda(t)} \cosh(4C_{ij}(t)) \; , \\
\left\langle \sinh^2(X_i(t)) \cosh^2(X_j(t)) \right\rangle &= \left\langle \cosh^2(X_i(t)) \sinh^2(X_j(t)) \right\rangle \\
&= \frac{1}{4} e^{-4\Lambda(t)} \cosh(4C_{ij}(t)) - \frac{1}{4} \; , \text{ and} \\
\left\langle \cosh^2(X_i(t)) \sinh^2(X_j(t)) \right\rangle &= \frac{1}{4} - \frac{1}{2} e^{-2\Lambda(t)} + \frac{1}{4} e^{-4\Lambda(t)} \cosh(4C_{ij}(t)) \; .
\end{aligned} \tag{7.51}$$

Let us now also calculate the remaining expectation value in Eq. (7.46). We find

$$\begin{aligned}
&\langle \cosh(X_i(t)) \sinh(X_i(t)) \cosh(X_j(t)) \sinh(X_j(t)) \rangle \\
&\quad = \frac{1}{4} \langle \sinh(2X_i(t)) \sinh(2X_j(t)) \rangle \\
&\quad = \frac{1}{4} \sum_{m,n=0}^{\infty} \frac{2^{2m+1}}{(2m+1)!} \frac{2^{2n+1}}{(2n+1)!} \left\langle X_i(t)^{2m+1} X_j(t)^{2n+1} \right\rangle \\
&\quad = \frac{1}{4} \sum_{m,n=0}^{\infty} \sum_{k=0}^{\min(m,n)} \frac{2^{2m+1}}{(2m+1)!} \frac{2^{2n+1}}{(2n+1)!} \\
&\quad \times \binom{2m+1}{2k+1} (2k+1)! \binom{2n+1}{2k+1} \left\langle X_i(t)^{2m-2k} \right\rangle \langle X_i(t) X_l(t) \rangle^{2k+1} \left\langle X_j(t)^{2n-2k} \right\rangle \\
&\quad = \frac{1}{4} \sum_{m,n=0}^{\infty} \sum_{k=0}^{\min(m,n)} (-1)^{m+n} \frac{2^{2m+1}}{(2m+1)!} \frac{2^{2n+1}}{(2n+1)!} \\
&\quad \times \binom{2m+1}{2k+1} (2k+1)! \binom{2n+1}{2k+1} \frac{(2m-2k)!}{2^{m-k}(m-k)!} \frac{(2n-2k)!}{2^{n-k}(n-k)!} \Lambda(t)^{m+n-2k} C_{ij}(t)^{2k+1} \\
&\quad = \sum_{m,n=0}^{\infty} \sum_{k=0}^{\min(m,n)} \frac{(-2)^{m+n+2k}}{(m-k)!(n-k)!(2k+1)!} \Lambda(t)^{m+n-2k} C_{ij}(t)^{2k+1} \\
&\quad = \sum_{u,v,k=0}^{\infty} \frac{(-2)^{u+v+4k}}{u!v!(2k+1)!} \Lambda(t)^{u+v} C_{ij}(t)^{2k+1} \\
&\quad = \frac{1}{4} e^{-4\Lambda(t)} \sinh(4C_{ij}(t)) \,. \qquad (7.52)
\end{aligned}$$

Therefore,

$$\begin{aligned}
\rho_{ij}(t) = \exp\left\{ -iJ_{ij}(t) \sigma_i^x \otimes \sigma_j^x \right\} &\left[\left(\frac{1}{4} + \frac{1}{2} e^{-2\Lambda(t)} + \frac{1}{4} e^{-4\Lambda(t)} \cosh(4C_{ij}(t)) \right) \times \rho_{ij} \right. \\
&+ \left(\frac{1}{4} - \frac{1}{4} e^{-4\Lambda(t)} \cosh(4C_{ij}(t)) \right) \times \left(\sigma_i^x \rho_{ij} \sigma_i^x + \sigma_j^x \rho_{ij} \sigma_j^x \right) \\
&+ \left(\frac{1}{4} - \frac{1}{2} e^{-2\Lambda(t)} + \frac{1}{4} e^{-4\Lambda(t)} \cosh(4C_{ij}(t)) \right) \times \sigma_i^x \sigma_j^x \rho_{ij} \sigma_i^x \sigma_j^x \\
&\left. + \frac{1}{4} e^{-4\Lambda(t)} \sinh(4C_{ij}(t)) \times \left(\sigma_i^x \sigma_j^x \rho_{ij} + \rho_{ij} \sigma_i^x \sigma_j^x - \sigma_i^x \rho_{ij} \sigma_j^x - \sigma_j^x \rho_{ij} \sigma_i^x \right) \right] \\
&\quad \times \exp\left\{ +iJ_{ij}(t) \sigma_i^x \otimes \sigma_j^x \right\} \,. \qquad (7.53)
\end{aligned}$$

Using now $\exp\left\{\pm iJ_{ij}(t)\sigma_i^x \otimes \sigma_j^x\right\} = \cos(J_{ij}(t)) \pm i\sin(J_{ij}(t))\sigma_i^x \otimes \sigma_j^x$, we arrive at Eq. (7.14).

CHAPTER 8

Improved HDRG Decoders for Qudit and Non-Abelian Quantum Error Correction

Adapted from:
Adrian Hutter, Daniel Loss, and James R. Wootton
"Improved HDRG decoders for qudit and non-Abelian quantum error correction",
New J. Phys. **17**, 035017 (2015)

Hard-decision renormalization group (HDRG) decoders are an important class of decoding algorithms for topological quantum error correction. Due to their versatility, they have been used to decode systems with fractal logical operators, color codes, qudit topological codes, and non-Abelian systems. In this work, we develop a method of performing HDRG decoding which combines strenghts of existing decoders and further improves upon them. In particular, we increase the minimal number of errors necessary for a logical error in a system of linear size L from $\Theta(L^{2/3})$ to $\Omega(L^{1-\epsilon})$ for any $\epsilon > 0$. We apply our algorithm to decoding $D(\mathbb{Z}_d)$ quantum double models and a non-Abelian anyon model with Fibonacci-like fusion rules, and show that it indeed significantly outperforms previous HDRG decoders. Furthermore, we provide the first study of continuous error correction with imperfect syndrome measurements for the $D(\mathbb{Z}_d)$ quantum double models. The parallelized runtime of our algorithm is poly$(\log L)$ for the perfect measurement case. In the continuous case with imperfect syndrome measurements, the averaged runtime is $O(1)$ for Abelian systems, while continuous error correction for non-Abelian anyons stays an open problem.

8.1 Introduction

Over the last decade, topological error correcting codes have emerged as the primary candidate for quantum error correction [16, 57]. Errors in these codes can be interpreted in terms of the creation, transport and annihilation of quasiparticles, allowing the design of intuitive decoding algorithms [126, 135, 136, 144, 145]. The anyonic nature of the quasiparticles also makes them well suited to implement quantum computation on the stored information [48, 113].

Recently a novel class of decoding algorithms was introduced for topological quantum error correcting codes [62, 146]. They were prominently used for correcting codes with fractal logical operators [60], for which no alternative decoding procedure was available. These decoders have since been referred to as 'hard-decision renormalization group' or 'HDRG' decoders [147].

The main advantage of HDRG decoders arises when they are applied to codes for which syndrome measurements do not have a simple binary output, but instead give more detailed information. Properly taking this information into account will greatly improve the success rate of a decoding algorithm, but will also greatly increase the run-time. The design of HDRG decoders allows them to make a compromise, providing decoding that is fast but successful.

These decoders are also hugely important to the emerging field of non-Abelian decoding [148, 149]. For these much of the additional syndrome information is not initially accessible. The method by which it can be extracted (fusing anyons and observing the fusion outcome) exactly mirrors the way in which it is used within HDRG decoders. Their development is therefore vitally important for topological quantum computation.

Finally, HDRG decoders are also relevant for correcting finite-temperature quantum memories [31], a purpose for which they have been employed in Refs. [62, 98]. A quantum memory model of particular recent interest, for which decoding is an open problem and for which HDRG methods might prove useful, is developed in Ref. [30].

HDRG decoding was first introduced in Ref. [140]. Based on ideas from Ref. [140], Ref. [62] developed an HDRG decoder that was designed to be generally applicable to topological codes, and also to allow an analytic proof that it realizes a finite threshold error rate for local noise. However, it was later shown that developments to the method can allow better decoding [146]. Here we expand upon this work. We consider strengths and weaknesses of the existing methods, and determine how the strenghts of the different decoders can be combined and how they can be improved further. In particular, we increase the minimal number of errors necessary for a logical error in a code of linear size L from $\Theta(L^{2/3})$ to $\Omega(L^{1-\epsilon})$ for any $\epsilon > 0$.

For concreteness we consider a particular choice of topological codes to act as a sandbox, namely the $D(\mathbb{Z}_d)$ quantum double models [16], the qudit generalization of the more familiar qubit toric code. However, our results will apply more generally to other types of anyonic systems. Systems with qudits of internal dimension higher than 2 are of interest for quantum computing due to the possibility of magic state distillation with improved error thresholds and reduced overhead [150, 151] and of transverse non-Clifford gates [151]. The possibility of implementing quantum computation with these codes was explored in Ref. [153].

We consider the case of perfect syndrome measurements, which has been studied previously using both HDRG and non-HDRG decoders [135, 146]. We also do the first study of these codes for imperfect syndrome measurements, which we model using measurement outcome errors. Finally, we employ the developed methods for decoding the non-Abelian Φ-Λ model. We find for this model a threshold error rate of 15%, while previous HDRG methods achieved 7%.

The rest of this paper is organized as follows. Sec. 8.2 briefly introduces the $D(\mathbb{Z}_d)$ quantum double models, which serve as a testbed in the following sections. Sec. 8.3 defines HDRG decoders and introduces decoders used in the previous literature. Sec. 8.4 discusses strengths and weaknesses of different decoders and how they can be improved upon. In Sec. 8.5 we present a minimum-weight perfect matching based HDRG decoder, which incorporates the lessons learned in Sec. 8.4. We apply our decoder to the $D(\mathbb{Z}_d)$ model in Sec. 8.6 and to a non-Abelian anyon model in Sec. 8.7. We discuss the run-time of our algorithm in Sec. 8.8 and conclude in Sec. 8.9.

8.2 $D(\mathbb{Z}_d)$ quantum double models

First we introduce the topological error correcting codes on which the methods we develop will be tested: the $D(\mathbb{Z}_d)$ quantum double models [16]. In particular we consider their planar variant, defined on the spin lattice shown in Fig. 8.1.

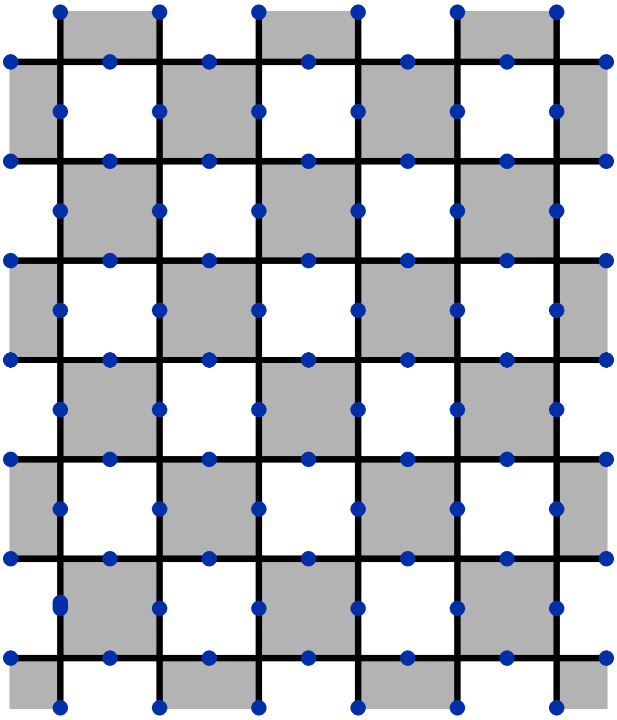

Figure 8.1: Spin lattice on which the codes are defined, with spins placed on edges.

Stabilizer operators for these codes are defined on the qudits around the plaquettes and vertices of the lattice. The plaquette and vertex operators are independent of each other, and also dual to each other. We can thus consider only the plaquette operators for simplicity, since all results will apply to the vertex operators also. For a more detailed introduction, the reader is referred to Ref. [154], which provides the first study of $\mathbb{Z}_d$ gauge theories as error correcting codes.

To define the plaquette operators we bicolour the plaquettes black and white in chessboard fashion. On white plaquettes these stabilizers are defined as

$$B_p = \prod_{j \in p} \sigma_j^z. \tag{8.1}$$

Here the product is over each qudit j around the plaquette p. The σ^z operator is a qudit generalization of the standard Pauli operator. This is defined as

$$\sigma^z = \sum_{j=0}^{d-1} e^{i\omega j} |j\rangle\langle j|, \quad \omega = \frac{2\pi}{d}, \tag{8.2}$$

for a d-level qudit. The plaquette operators for black plaquettes are simply defined as $B_p^\dagger$.

The plaquette operators have d possible eigenvalues. These correspond to the dth roots of unity ω^g for $g = 0, \dots, d-1$. Syndrome measurements determine the value of g for each plaquette. The case of $g = 0$ is the trivial syndrome, and is associated with anyonic vacuum, 1 on the corresponding plaquette. All other values of g correspond to unique anyon types m_g. The value g is referred to as the magnetic charge, or simply the charge, of the anyon.

The syndrome is affected by single spin operators of the form

$$(\sigma^x)^g = \sum_{j=0}^{d-1} |j + g \mod d\rangle\langle j|. \tag{8.3}$$

The effects of these on a spin will be to create an anyon of type m_g in the white plaquette adjacent to the qudit on which it was applied, and one of type m_{d-g} in the black plaquette. If anyons are already present on these plaquettes they will fuse with the newly created ones according to the fusion rules

$$m_g \times m_h = m_{g+h \mod d}. \tag{8.4}$$

Here $m_0 = 1$. Note that the antiparticle of any m_g is m_{d-g}. Henceforth we will refer to the latter simply as m_{-g}.

Given these operations it is possible to move anyons. An anyon of type m_g on a white black can be moved onto a neighbouring black plaquette by applying $(\sigma^x)^{-g}$ to the qudit between them. This creates an m_{-g} anyon in the white plaquette and an m_g on the black. The former annihilates the original anyon, and so results in its effective movement to the black plaquette. Corresponding operators can be applied for other cases.

Given this means of transport, the minimum number of qudits on which these operations must be applied in order to move an anyon from one plaquette to another is the Manhattan distance (L_1 metric) between them. It is therefore this metric that we use to evaluate distances between anyons.

The stabilizer space of the code is defined as that for which all plaquettes and vertices hold vacuum. This space is d^2 dimensional, and so capable of storing two logical qudits. The effect of errors acting on a state initially in the stabilizer space is to create anyons, and then to move, split and fuse them. The pattern of errors applied in any given case is called the error chain, E. The resulting pattern of anyons is the syndrome, S.

The job of a decoding algorithm is to remove the effects of the errors. It must therefore remove the anyons by annihilating them with each other. In principle this would be done by applying operators of the form $(\sigma^x)^h$ to the spins. However, this is unnecessary in practice. Instead the operations can be performed effectively by accounting for them in all future measurements and operations on the effected spins. The total operation applied (either actually or virtually) is known as the recovery operator, R. The error correction is successful if the total effect of errors and correction, RE, is a product of the stabilizer operators. This is satisfied as long as RE contains no loops of errors that wrap around the non-trivial cycles of the torus.

We consider a simple error model that has previously been used to benchmark decoders for this code. This is that of $(\sigma^x)^g$ type errors applied independently to each physical qubit. The strength of the noise is parameterized p, which denotes the probability for each qudit that an error of this form with $g \neq 0$ is applied. We consider the case that all non-zero g are applied with equal probability $p/(d-1)$.

8.3 HDRG decoders

Until now only the decoder of Ref. [62] and its derivatives have been referred to as HDRG in the context of topological codes. However, in this work we use the term to refer to a more general class of decoders.

In order to define this class, we must first introduce some terminology. Subsets of the syndrome, S, are referred to as clusters. A cluster is said to be neutral if it is possible for it to be removed without otherwise affecting the syndrome. Otherwise the cluster is non-neutral. For the $D(\mathbb{Z}_d)$ codes a cluster, which is a set of anyons, is neutral if the sum of their charges is zero modulo d. A set of errors that creates a single neutral set of anyons is called an error net. Those that create only two anyons at their endpoints are known as an error string.

The class of decoders we consider are those that use the repeated application of the following process. Initially, each non-trivial element of the syndrome is considered to be a separate cluster.

1. Form at least one new cluster by combining existing clusters.

2. Check for each new cluster whether it is neutral, and find a neutralization operator R_j for each neutral cluster C_j.
3. Update S by removing all neutral clusters.

This continues until the syndrome is empty. The decoder then outputs $R = \prod_j R_j$ as a proposed correction operator.

Note that once elements of the syndrome are included in the same cluster, they will remain within the same cluster for the rest of the process. It is this feature that allows the procedure to be applicable to non-Abelian anyons, since in that case neutrality tests are performed by the irreversible act of fusion.

Only the first step of this process is not uniquely defined. The exact means by which the clustering is performed is what distinguishes the different HDRG decoders. Below we present the HDRG decoders that have been applied to topological codes so far.

BH and ABCB decoders

The HDRG decoders of Refs. [62] (BH) and [146] (ABCB) work as follows. Firstly they define a physical distance $d_{j,k}$ between all pairs of non-trivial syndrome elements j and k. For BH the Chebyshev distance (L_∞ metric) is used, whereas for ABCB this is a combination of the Chebyshev distance and Manhattan distance (L_1 metric). A search distance $D(n)$ is also defined for the nth iteration of the algorithm. For BH $D(n) = 2^n$, whereas for ABCB it is simply $D(n) = n + 1$. The algorithm then runs through the following steps.

1. Form a graph with a vertex corresponding to each non-trivial syndrome element and no edges. Set $n = 0$.
2. Add an edge between all pairs of vertices for which $d_{jk} \leq D(n)$.
3. Clusters are connected components of this graph. Check all clusters for neutrality. Remove all vertices corresponding to each neutral cluster C_j.
4. If vertices remain, increment n by 1 and repeat from step 2. Otherwise proceed to step 5.
5. For each neutral cluster C_j find an operator R_j that acts only on the spins in its neighbourhood, the action of which would remove the syndrome.

6. Output the total recovery operator $R = \prod_j R_j$.

An 'enhanced' version of the ABCB decoder has also been considered Ref. [146]. This has an initialization step in which neutral clusters are searched for over a small area. The search is performed such that elements of the syndrome included within the same cluster at one point included within different clusters later. This enhancement is therefore no longer an HDRG decoder according to our definition.

Expanding diamonds decoder

We consider the variant of the expanding diamonds algorithm [144, 145] presented in [145]. This also requires distances d_{jk} and $D(n)$, with the Manhattan distance used for the former and $D(n) = n + 1$ for the latter. The clustering at the $(n+1)$th iteration is done by finding pairs of mutually nearest neighbouring clusters in the nth iteration. It does this as follows.

1. Assign each non-trivial syndrome element its own cluster, and label these from 1 to N_0 (the number of non-trivial syndrome elements). Set $n = 0$.

2. Number the clusters left to right and top to bottom. Loop through them in this order. For each cluster, j, check whether there exists a cluster $k > j$ for which $d_{jk} < D(n)$. If so, merge the clusters. If any such cluster is neutral, remove it from the syndrome.

3. Label the N_{n+1} clusters that remain from 1 to N_{n+1}. Set the distance d_{jk} between clusters j and k to be the minimum distance from an anyon of one to an anyon of the other.

4. For $N_{n+1} > 0$, increment n by 1 and repeat from step 2. Otherwise proceed to step 6.

5. For each neutral cluster C_j find an operator R_j that acts only on the spins in its neighbourhood, the action of which would remove the syndrome.

6. Output the total recovery operator $R = \prod_j R_j$.

8.4 Improving HDRG decoders

One major difference between the algorithms described above is the speed at which they increase cluster size. Expanding diamonds does this very slowly, with each new cluster formed out of only two previous ones. The BH and ABCB decoders do it more quickly, with the exponentially increasing search distance of BH making it the fastest of all.

It is natural to ask which speed of cluster increase leads to the best results. Both extremes have their advantages. Slow increase of cluster size means that the clusters checked for neutrality will typically contain less anyons. This therefore reveals more information about their relative charges. When clusters are typically large, this information is far more coarse grained.

Smaller cluster size also means that there will be more clusters, and hence more neutrality checks. Although this may seem like an advantage, recall that any cluster found to be neutral will be removed from the syndrome in all of the HDRG decoders above.

If the resulting annihilation operator for the anyons within the cluster is topologically equivalent to the error that created them, this removal poses no problems. However, this may not be the case. Consider a cluster composed of two anyons, one of type m_a and one m_{-a}. Since these are antiparticles, they could have been created by a single error string. However, it is also possible that they were created by different error strings, whose other endpoints lie outside the cluster. The fact the cluster is neutral is then due only to random chance, and does not correspond to successful correction from the decoder. Discarding information about these neutral clusters makes it impossible for the decoder to realize and correct its mistakes. This therefore can give an advantage to algorithms with quickly growing cluster size, since they are more careful about declaring clusters neutral.

In summary, slowly increasing clusters lead to more syndrome information being extracted and used by the decoder. However, it also leads to more being lost as neutral clusters are found. Quickly increasing clusters extract less of the syndrome, but also lose less. It is not clear which speed of cluster increase leads to maximal syndrome usage, and so which should lead to best decoding.

Rather than searching for the optimal speed, we will consider how the advantages might be combined and the disadvantages negated. This can be achieved using an algorithm with slowly increasing cluster size, but which does not completely forget about the neutral clusters. The challenge then is to determine how information about neutral clusters might be used in a way that does not affect the efficiency of HDRG decoders.

The simplest way to carry forward information about neutral clusters is by using a simple modification of the physical distance. To motivate this, consider two strings of errors along a line. Each are length l_0, and create an anyon of type m_a on their left and m_{-a} on their right. The distance between the two strings is $l_0 - 1$. Both expanding diamonds and ABCB would see that the shortest distance between two anyons is that between the $-a$ of the left string and the a of the right. They would then form a cluster out of these, see it is neutral and remove it from the syndrome. The same is true of BH if l_0 is a power of two. However, we will restrict our attention to the other decoders for simplicity.

This action taken by the decoders is a mistake. However, this mistake will not lead to any ill effects as long as the remaining m_a from the left and m_{-a} from the right end up in the same cluster (without looping around the torus). This will certainly happen if no anyon is closer to either than the other. However, note that the distance between them is $3l_0 - 1$. This does not just include the $2l_0$ errors that occurred between them, but also the $l_0 - 1$ gap. The distance between the anyons should really only reflect the number of errors required to connect them. This increased distance makes them less likely to find each other than they should be.

This issue can be solved by recalling the existence of the neutral cluster. The number of errors required to connect the two anyons is only that needed to connect them both to the neutral cluster, and so the distance should be defined accordingly. This would then give the correct distance $2l_0$ between them. Whenever a neutral cluster $C = \{c_1, c_2, \ldots\}$ is found, the physical distance between the remaining clusters should thus be updated according to

$$d_{jk} \to \min\left(d_{jk}, \min_{c_m, c_n \in C} (d_{jc_m} + d_{c_m k})\right). \tag{8.5}$$

By allowing the distance to take shortcuts between neutral clusters, information about their positions is retained by the decoder. Also note that this principle is not restricted to neutral clusters, and so shortcuts via non-neutral clusters can also be used.

Example: Cantor-like error chains

The effectiveness of the redefined physical distance can be seen by considering Cantor-like error chains [144, 145]. These can cause all of the decoders considered above to fail with only $\Theta(L^\beta)$ errors, where $\beta < 1$, when the shortcuts are not used. The use of the shortcuts, however, means that the required number of errors is asymptotically greater than $\Theta(L^\beta)$ for any $\beta < 1$ (though not as high as $\Theta(L)$). The minimal number of errors that make a decoder fail is of practical relevance since the failure rate of the decoder is exponentially suppressed with the corresponding exponent in the low-p limit.

Consider again the two error strings discussed above, which both have an anyon of type a on their left and $-a$ on their right. They are both of length l_0 and lie along a line. We will use g_0 to denote the distance between them, and we will refer to any such pair of strings as a level-1 bundle. Note that the total length of a level-1 bundle, including the gap, is $l_1 = 2l_0 + g_0$.

We similarly define a level-$(n + 1)$ bundle to be a pair of level-n bundles along the same line and with a gap g_n between them. The size of a level-$(n + 1)$ bundle is then $l_{n+1} = 2l_n + g_n$.

Let us consider the case of a level-m bundle such that $l_m \geq \lfloor (L+1)/2 \rfloor$. If g_0 is significantly smaller than l_0, the decoders will incorrectly annihilate the inner two anyons of each level-1 bundle. Each level-2 bundle will then be composed of two strings of length l_1 with a gap of g_1 between them. Again, g_1 being significantly smaller than l_1 will lead to incorrect annihilation. If all g_n are significantly smaller than the corresponding l_n, this chain of mistakes will lead to a pair of anyons separated by $l_m \geq \lfloor (L+1)/2 \rfloor$. This will then lead to a logical error (with probability $\frac{1}{2}$ if L is even and $l_m = L/2$, and with certainty in all other cases).

The exact requirements for g_n and l_n required to cause a logical error depend on the decoders. We wish to consider fatal error chains with the smallest number of errors, and so the largest possible gaps. For the expanding diamonds and ABCB decoders, a logical error will occur when $g_n < l_n \; \forall n$. We will therefore consider the minimal case of $g_n = l_n - 1$. For simplicity we will also use $l_0 = 2$.

In this case, the length of a level-n bundle will follow

$$l_{n+1} = 2l_n + g_n = 3l_n - 1 = \frac{3^{n+1} + 1}{2} \, . \tag{8.6}$$

A level-m bundle with $l_m \geq \lfloor (L + 1)/2 \rfloor$ then requires $m \geq \lceil \log_3(L - 1) \rceil$. The number of errors within any level-n bundle is clearly 2^{n+1}. The total number of errors required to cause a logical error is then $\Omega(L^{\beta})$, where $\beta = \log_3 2 \approx 0.63$.

For BH, the corresponding minimal condition for a logical error is

$$g_n = 2^{\lceil \log_2 l_n \rceil - 1}, \ \forall n \,. \tag{8.7}$$

This reflects the fact that the search distance $D(k)$ treats all distances from $2^{k-1} + 1$ to 2^k the same for any k. The length of a level-n bundle is then

$$l_{n+1} = 2l_n + 2^{\lceil \log_2 l_n \rceil - 1} \,. \tag{8.8}$$

Assume that $l_n = 2^k + c$ with $0 < c \leq 2^{k-1}$. For any l_0, either l_0 or l_1 is of this form. Then, $l_{n+1} = 3 \times 2^k + 2c$ and $l_{n+2} = 2^{k+3} + 4c$. Note that the first summand grows by a factor of 8 while the second summand grows by a factor of 4, such that the latter becomes vanishing relative to the former. So asymptotically, the ratio l_{n+1}/l_n oscillates between 3 and $\frac{8}{3}$, and hence $l_n = (2\sqrt{2})^{n+O(1)}$. A level-$n$ bundle with $l_n \geq \lfloor (L+1)/2 \rfloor$ then requires $n \geq \log(L)/\log(2\sqrt{2}) + O(1)$ and thus involves at least $2^{n+1} = \Theta(L^{\beta})$ errors with $\beta = \frac{2}{3}$. The exponent $\beta = \frac{2}{3} \approx 0.67$ is a slight improvement over expanding diamonds and ABCB, but not greatly so.

When the redefined distances are used, the error chains considered above will no longer lead to logical errors. Instead let us define the width of a bundle to be the distance between its extremal anyons when all others have been annihilated incorrectly. Taking the shortcuts into account, this obeys $w_n = 2^n l_0$. Note that w_n is then equal to the number of errors in a level-n bundle.

For expanding diamonds and ABCB the requirement for a logical error is now $g_n < w_n$. The total length of a minimal bundle leading to a logical error (i.e., $g_n = w_n - 1$) then obeys

$$\begin{aligned} l_{n+1} &= 2l_n + g_n \\ &= 2l_n + 2^n l_0 - 1 \\ &= (n+1)2^n + 1 \\ &= \Theta(n2^n) \,. \end{aligned} \tag{8.9}$$

For BH the corresponding condition for a logical error is

$$g_n = 2^{\lceil \log_2 w_n \rceil - 1}, \ \forall n \,. \tag{8.10}$$

Considering again the case of $l_0 = 2$ gives $g_n = 2^n$, leading to $l_{n+1} = \Theta(n2^n)$.

All of the decoders considered therefore result in the same scaling $l_{n+1} = \Theta(n2^n)$ for minimal uncorrectable error chains when the shortcuts are used. We thus have $l_n = O((2+\epsilon)^n)$ for any $\epsilon > 0$. In order to create a logical error, we need $l_m \geq \lfloor (L+1)/2 \rfloor$ and therefore a bundle of level $n = \Omega(\log_{2+\epsilon} L)$, which involves $w_n = 2^n l_0 = \Omega(L^{\log_{2+\epsilon} 2})$ errors. This is higher than any $\Theta(L^\beta)$ for $\beta < 1$, but does not reach the value of $\beta = 1$ that non-HDRG decoders may realize. Nevertheless it is a marked improvement over $\beta = \log_3 2 \approx 0.63$ and $\beta = 2/3 \approx 0.67$.

Note that using the shortcuts, the smallest code which can lead to a logical error with less than $\lfloor (L+1)/2 \rfloor$ errors is of size $L = 9$. For such a code, a level-1 bundle leads to a logical error with probability $\frac{1}{2}$.

8.5 Minimum Weight Matching HDRG decoder

We now introduce a novel decoder, based on the lessons learned above. Like expanding diamonds, this will have a slow increase of cluster size for which each new cluster will be composed of two previous ones. However, the means by which the clustering is performed will not be based on a search distance. Instead it will use a generalization of the minimum weight perfect matching algorithm that gives high quality decoding in the $D(\mathbb{Z}_2)$ case [126]. Shortcuts will also be used.

Minimum Weight Matching Algorithm

The backbone of the decoder is an algorithm for finding the minimum weight matching (MWM) of a graph. This is in turn based upon an algorithm for minimum weight perfect matching (MWPM).

A perfect matching is a decomposition of the vertices of a graph into pairs. This must be such that the two vertices, j and k, of each pair are connected by an edge jk of the graph. For a weighted graph, each edge jk will have a weight W_{jk}. We can then associate a total weight to a perfect matching by summing the weights of the edge corresponding to each pair. A minimum weight perfect matching is such a pairing that achieves minimal weight. Clearly, a MWPM can only exist for graphs with an even number of vertices.

A non-perfect matching does not cover all vertices. It corresponds to a partial pairing of the vertices, with some vertices left unpaired. In order to define a total weight for a such a matching, let us assign a weight W_j

to each vertex j. All paired vertices then contribute their corresponding edge weight to the total, and all unpaired vertices contribute their vertex weight.

Any algorithm that is able to find minimum weight perfect matchings of graphs will also be able to find minimum weight matchings according to this definition. To do to this for a weighted graph G we create a graph G'. This includes two vertices j and j', for each vertex j of G. Every edge jk in G corresponds to edges jk and $j'k'$ in G' with weights

$$W'_{jk} = W_{jk}, \;\; W'_{j'k'} = 0\,. \tag{8.11}$$

The graph G' also includes edges jj' for each j of G. The weight of these is set to the vertex weight: $W_{jj'} = W_j$.

For the graph G' constructed in this way, a pair can only take three forms: jk, $j'k'$ and jj'. The jk type pairs correspond to a pairing in the graph G and has corresponding weight W_{jk}. For each of these a corresponding $j'k'$ pair can occur in order to ensure that the matching is perfect with zero weight. The pairs of the form jj' correspond to a vertex of G that does not pair with anything, and have the corresponding weight W_j. Any MWPM of G' therefore corresponds directly to a MWM of G.

Algorithms to efficiently find the MWPM of a graph are well known [69,126]. These can therefore be used to implement the following decoding method.

Decoding algorithm

Each anyon of the syndrome is associated with the vertices of a graph, G. In general we will consider this to be a complete graph, with an edge between each pair of vertices. However, not all edges will need to be considered in practice.

Each edge is assigned a weight whose value depends on the distance between the corresponding anyons. Each vertex is assigned a weight that depends on the distance from the anyon to its nearest neighbours. These weights are defined in more detail in the following sections.

Given the weighted graph G, the MWM algorithm is run in order to find a set of non-overlapping anyon pairs. These pairs are treated as clusters, and are therefore checked for neutrality.

For each non-neutral pair, the corresponding vertices j and k are combined into a single vertex (jk). The edge between j and k is removed. The edge weights and vertex weights are refined for the new cluster as explained in the following sections.

For each neutral pair the corresponding vertices are removed from the graph, as are all edges incident upon them. Since all weights are based on the distances between anyons, the weights for remaining edges and vertices should be updated in order to take advantage of shortcuts via the neutral cluster. Shorcuts via non-neutral clusters are also considered.

This process is repeated on the resulting graph until all vertices have been removed. The final recovery operation is the product of annihilation operators for each neutral cluster.

Pairing Weight

Consider a specific error chain, E, which contains $|E|$ errors. The probability of this, up to normalization, is

$$P(E) = \left(\frac{p/(d-1)}{1-p} \right)^{|E|} = e^{-\beta |E|} \, . \tag{8.12}$$

Here β is defined as

$$\beta = -\log \left(\frac{p/(d-1)}{1-p} \right) \, . \tag{8.13}$$

In order to motivate the definition of the pairing weights W_{jk}, let us consider a modified error model. This acts according to the standard error model defined above, except that no splittings or fusions are allowed. All error nets are therefore strings: they simply create two anyons that are the antiparticles of each other. Since there are $d-1$ types of different non-trivial particle, there are $d-1$ types of string.

For this case, one possible tactic for an HDRG decoder is to consider all possible error chains E that are consistent with the syndrome and determine which is most likely. The resulting pairs of anyons are then used as the clusters.

The most likely error strings are those that have the smallest number of errors. For each pair of anyons, j and k, created by the same error string, the minimum number of errors is d_{jk}. The probability of the corresponding error chain can then be expressed as

$$P(E) = \prod_{(j,k)} e^{-\beta d_{jk}} \, . \tag{8.14}$$

Note that this probability assumes that the path and type of error string between each pair is specified. However, the decoder does not care about this information. It wants to find the most probable pairing, without regard to the path that the errors took between the anyons. Also, since the decoder is HDRG, it does not use the anyon charge information when performing the clustering. It therefore does not care which of the $d-1$ possible types of error string occurred in each case.

Let us use $\{E\}$ to denote the set of all error chains with the same pairing as E, that differ only in path and type of the error string. Let us also use $\mu_{j,k}$ to denote the number of minimum distance error strings between j and k, including the multiplicities in both path and error type,

$$\mu_{jk} = (d-1)\binom{d_{jk}}{d^x_{jk}} . \tag{8.15}$$

Here d^x_{jk} denotes the distance between j and k in the x direction, such that the Manhattan distance can be expressed $d_{jk} = d^x_{jk} + d^y_{jk}$. The probability for the set $\{E\}$ is then

$$P(\{E\}) = \prod_{(j,k)} \mu_{jk} \; e^{-\beta d_{jk}} . \tag{8.16}$$

The task of finding a pairing that maximizes $P(\{E\})$ is clearly equivalent to one that minimizes $-\log P(\{E\})$. It can thus be achieved using MWPM using the following weight for each pair

$$W_{jk} = d_{j,k} - (\log \mu_{j,k})/\beta . \tag{8.17}$$

Even though these weights are defined for an alternative error model, and we will need to use MWM rather than MWPM for the true error model, we will continue to use these weights. The vertex weights will then be defined such that the whole minimization problem is consistent with the true error model.

When two anyons (or non-neutral clusters), j and k, are combined to form a non-neutral cluster (jk), the weight for this cluster to be paired with another anyon or non-neutral cluster l must be defined. This is done by defining the distance between (jk) and l to be

$$d_{(jk)l} = \min(d_{jl}, d_{kl}) . \tag{8.18}$$

The multiplicity $\mu_{(jk)l}$ is taken to be μ_{jl} if $d_{jl} < d_{kl}$, μ_{kl} if $d_{kl} < d_{jl}$, and $\mu_{jl} + \mu_{kl}$ if the distances are equal.

The distances and multiplicities must also be modified to take shortcuts into account, via both neutral and non-neutral clusters. For clusters

j and k connected via a cluster l the distance becomes

$$d_{jk} \to \min(d_{jk}, d_{j,l} + d_{l,k})\,. \tag{8.19}$$

If the latter distance via the cluster k is indeed minimal, the multiplicity is updated according to

$$\mu_{jk} = \mu_{jl}\ \mu_{lk}\,, \tag{8.20}$$

while this expression is added to μ_{jk} if the two distances are equal. Note that this introduces an extra factor of $d-1$ for every cluster that the shortcut goes via. This would be expected for non-neutral clusters, since the anyon deposited by the error string from j does not need to have any relation to that deposited by the string from k. However these should be antiparticles for neutral clusters, and this restriction should mean that this extra factor is not included. However, for simplicity we use Eq. (8.20) irrespective of the anyonic charge of the cluster.

These methods of updating the distances and multiplicities for the edge weights also apply to their use within the vertex weights, as defined below.

Tag-along weight

The true error model does include splittings and fusions. Therefore, the most likely error chain will not typically be composed only of strings, but more general error nets. However in order to motivate our choice of the vertex weights W_j in the graph G', we will again consider a restricted error model, allowing only error nets composed of strings that meet at anyons. Like the pairing, this also allows us to associate error chains with edge covers.

It is clear that the edge cover corresponding to the most likely error chain will not contain simple cycles. This is because edges can be removed from these (and hence the probability will increase) while maintaining the edge cover. All disconnected subgraphs will therefore be trees. This same argument can be applied to any tree that is not a star graph. A star that contains n vertices has $n-1$ external vertices which are incident upon only one edge and one internal vertex incident upon $n-1$ edges. A pair, for $n=2$, is the simplest example of this.

A moment's thought shows that the most likely error chain contains only stars which are either of size 2 or for which the internal vertex is each externel vertex' nearest neighbor. To see this, assume by contradiction that the nearest neighbor of an external vertex in a star of size larger than 2 is not the internal vertex. It is thus either another external vertex of the same star or an internal or external vertex of another star. In each of these cases, we can connect the external vertex to its nearest neighbor, remove the edge connecting it to the internal vertex, and potentially remove further edges as well. It is thus always possible to decrease the weight and increase the likelihood of such an error net.

Let us define two of the vertices from each star, one internal and one external, to be a pair. All other external vertices are defined to be 'tag-alongs' to that pair.

The MWM algorithm can then be used to decompose the anyons into pairs and tag-alongs. The tag-alongs are those anyons that are not paired by the algorithm. They can be considered to be tagging-along with any of their nearest neighbours.

We use

$$d_j = \min_k d_{j,k} \,. \tag{8.21}$$

to denote the nearest neighbour distance of an anyon. The weight that MWM assigns to each pair will be the pairing weight of Eq. (8.17). For the tag-along weight, note that the decoder only combines the two anyons (or non-neutral clusters) within each pair to form new clusters. The tag-alongs are not included. It is thus not the most likely decomposition of the errors into stars that is most important, but the most likely decomposition into pairs and tag-alongs. The tag-along weight should therefore incorporate information about the number of nearest neighbours it can tag-along with. To do this we define the tag-along multiplicity of an anyon to be

$$\mu_j = \sum_{k \in \mathrm{nn}(j)} \mu_{j,k} \,. \tag{8.22}$$

Here $\mathrm{nn}(j)$ denotes the nearest neighbours of j, and so μ_j is the sum of all possible minimum distance error strings to nearest neighbours. The tag-along weight is then defined as

$$W^T_j = d_j - (\log \mu_j)/\beta \,, \tag{8.23}$$

for each anyon, j.

Abstaining weight

The true error model does not restrict to the error nets considered above, where strings meet only at anyons. Instead it can have more general structures, such as a triskelion with an anyon at each foot. Such error nets can cover the anyons using less errors than when only strings meeting at anyons are considered. The tag-along weights considered above are thus often an overestimate.

In order to deal with this, we will consider an alternative definition of the vertex weights which will be an underestimate in general. The final vertex weight will then be formed by combining the two.

For the underestimate, we choose the vertex weights such that only pairs of nearest neighbors will pair with each other. Let us define the minimum pairing weight for a vertex j,

$$W_j^{\min} = \min_k W_{jk} \,. \tag{8.24}$$

In order to ensure that only mutual nearest neighbors pair with each other, we set the vertex weight to be the 'abstaining' weight

$$W_j^A = \frac{W_j^{\min}}{2} + \epsilon \,. \tag{8.25}$$

Here, a small $\epsilon > 0$ is used to break the degeneracy between mutual nearest neighbors pairing and both abstaining.

Vertex weight

The tag-along weight is often an overestimate of the ideal vertex weight, and the abstaining weight is an underestimate. A linear interpolation between the two will thus be used:

$$W_j = W_j^A + \lambda \left(W_j^T - W_j^A \right) \,, \tag{8.26}$$

This gives W_j^T at $\lambda = 1$ and W_j^A at $\lambda = 0$. In general we are free to choose the λ for any given p, L and N that gives the best compromise between these two methods. In the following, we set $\lambda = 0.3$ throughout, which leads to better results than both $\lambda = 0$ and $\lambda = 1$.

However, note that the build-up of degeneracies will sometimes lead W_j^T to become lower than W_j^A. This means that W_j becomes smaller than the abstaining weight W_j^A, which means that no clusters will pair any more. In this case, we resort to the abstaining weight and set $W_j = W_j^A$.

Note that in the limit $\lambda \to 0$ the decoder introduced here is similar to the expanding diamonds decoder using shortcuts, in that only mutual nearest neighbors will be fused. However, unlike expanding diamonds, the MWM HDRG decoder can pair mutual nearest neighbors of different distances during the same iteration of the algorithm.

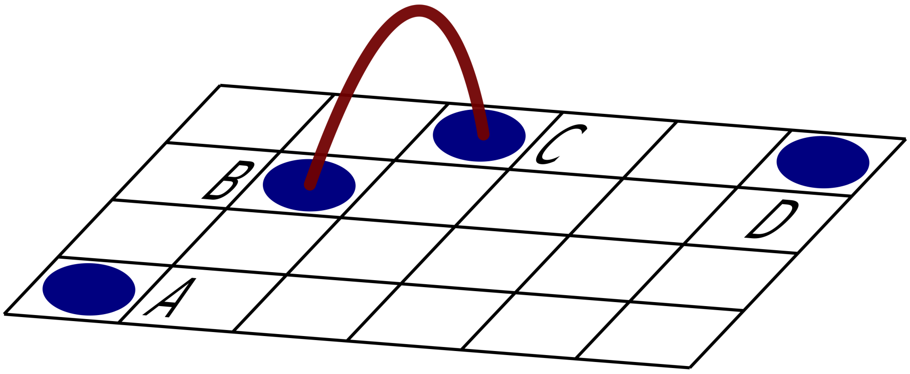

Figure 8.2: An example configuration involving four anyons (blue circles). After fusing anyon B with C, we add a "wormhole" to the lattice (red arc), which allows other anyons to take shortcuts.

Example

Fig. 8.2 shows an example configuration of four anyons. Assuming that no fusions have happened so far, we have $W_{AB} = 3 - \log\binom{3}{1})/\beta$, with β as defined in Eq. (8.13), $W_A = \frac{1+\lambda}{2} W_{AB}$, etc.. With $d = 3$ and $p = 10\%$, we have $W_A + W_{BC} + W_D < W_{AB} + W_{CD}$ for $\lambda < 0.37$, meaning that the algorithm will fuse anyons B and C in a first round, while anyons A and D refrain from matching at the cost of their vertex weight. After fusing B with C, other anyons are allowed to take shortcuts over the resulting cluster (irrespective of its anyonic charge). This can be thought of as adding a "wormhole" to the lattice (the red arc in Fig. 8.2). Taking the shortcut into account, the weight for connecting anyons A and D is updated from $W_{AD} = 8 - \log\binom{8}{3}/\beta \approx 6.61$ to $W_{AD} = 6 - \log\binom{2}{1}/\beta \approx 5.76$. For $\lambda > 0.37$, anyon A will be paired with anyon B in the first round, as well as C with D.

8.6 Numerical results for $D(\mathbb{Z}_d)$ models

Results for perfect syndrome measurements

In this section, we present the results achieved with our MWPM HDRG decoder. Fig. 8.3 shows logical error rates for various values of p and L for the case of $d = 3$. We find a cross-over point at $p_c = 12.3\%$, indicating the threshold error rate of our decoder.

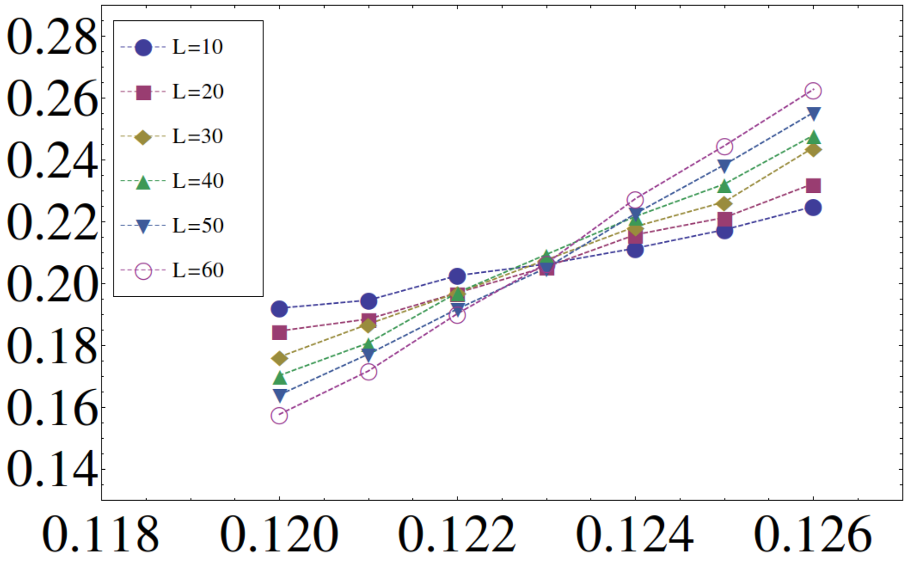

Figure 8.3: Error rate p (horizontal axis) versus logical error rate p_L (vertical axis) for the $D(\mathbb{Z}_3)$ model. Each data point represents 10^4 logical errors.

The cross-over point is obtained from Fig. 8.3 and similar figures by linear interpolation between the logical error rates obtained for equally-sized codes and visual inspection. More sophisticated fittings are used in Refs. [135, 140, 146].

We have produced similar plots for low prime dimensions $d = 3, 5, 7, 11$ and $d = 4$. The corresponding thresholds are displayed in Fig. 8.4. We find these thresholds to be higher than those achieved by HDRG methods in Ref. [146], yet lower than those achieved with a soft-decision renormalization group (SDRG) decoder in Ref. [135].

We also compare our thresholds with the hashing bound threshold, which provides an entropic estimate for the threshold error rates. Indeed, it has recently been shown [155] that the maximal threshold error rates for the $D(\mathbb{Z}_d)$ models achievable using computationally inefficient methods are very close to the hashing bound threshold values. The hashing bound threshold value for the model $D(\mathbb{Z}_d)$ is given by the solution of

$$-p \log\left(\frac{p}{d-1}\right) - (1-p)\log(1-p) = \frac{1}{2}\log(d)\,. \tag{8.27}$$

The solutions are compared with the threshold values achieved by our

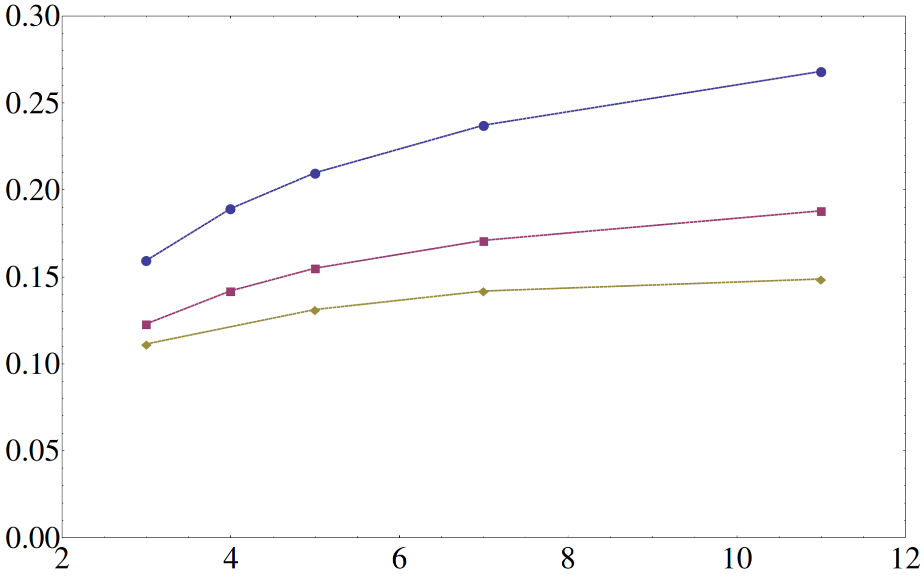

Figure 8.4: Thresholds error rates p_c for the $D(\mathbb{Z}_d)$ quantum double models for $d = 3, 4, 5, 7, 11$. We show the hashing bound threshold (circles), the threshold achieved with our HDRG decoder (squares), and the threshold achieved by ABCB (diamonds). Hashing bound values (circles) are obtained by solving Eq. (8.27). Our threshold values (squares) are obtained to accuracy 10^{-3} by comparing the logical error rates for various values of p and $L = 10, 20, \ldots, 60$, as illustrated in Fig. 8.3 for the case $d = 3$.

algorithm in Fig. 8.4.

For $d = 7919$ (the 1000-th prime), we find a threshold value of $p_c = 21.9\%$, which is significantly above the threshold value for p beyond which the error syndromes start to percolate the code [146]. It is higher than the threshold value achieved by previous HDRG methods [146].

Another important benchmark of a decoder is the minimum system size required such that the logical error rate, p_L is less than the physical error rate, p. This value, denoted $L^*(p)$, is the minimum code size for which the error correction yields a positive effect. These sizes were found for extreme cases of $d = 3$ and $d = 7919$ and are shown in Fig. 8.5. For $p < p_c/2$, system sizes of $L = 3$ are sufficient to demonstrate error correction for $d = 3$ and $L \leq 5$ is sufficient for $d = 7919$. Small values of $L^*(p)$ are odd since the minimal number of errors needed to break an $L = 2n - 1$ code is the same as for an $L = 2n$ code. At the point of syndrome

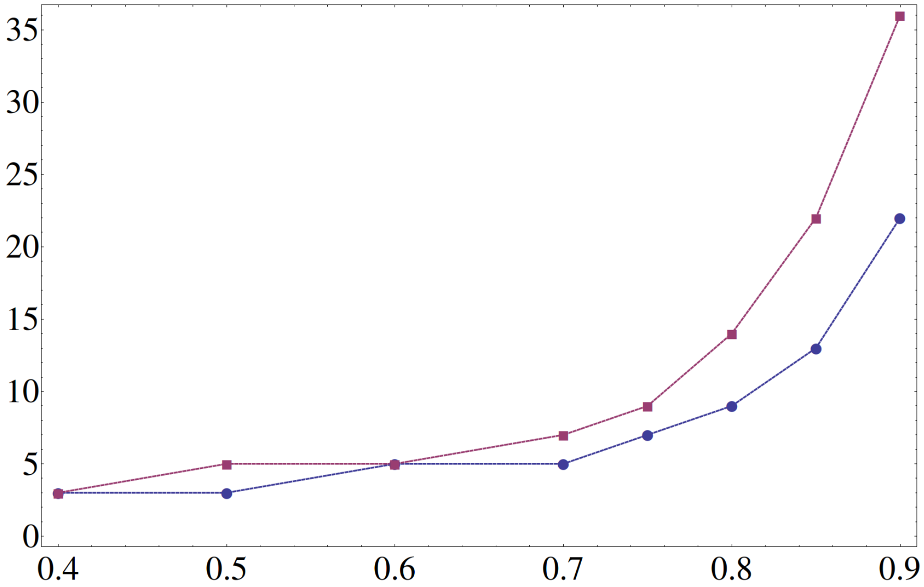

Figure 8.5: Minimal sizes $L^*(p)$ (vertical axis) such that $p_L < p$ for both $d = 3$ (circles) and $d = 7919$ (squares) for perfect stabilizer measurements. The horizontal axis shows p/p_c for the threshold values p_c provided in Fig. 8.4. We have $L^*(p) = 3$ for all $p/p_c < 0.4$.

percolation for $d = 7919$, which occurs at around $p = 18\%$, a system size of $L = 17$ is sufficient to demonstrate error correction.

Results for imperfect syndrome measurements

If syndrome measurements can fail with non-vanishing probability, error correction needs to be performed in a continuous fashion to allow the measurement errors to be detected. Non-trivial syndromes then persist through time, as long as no (data or syndrome measurement) error happens. The vertices in the graph entering our HDRG algorithm (which is now three-dimensional) are thus no longer given by non-trivial syndromes, but rather by non-trivial syndrome *changes*. Fusing two vertices with equal temporal coordinate means presuming data qudit errors, while fusing two vertices with equal spatial coordinates means presuming syndrome measurement errors.

We perform error correction for L rounds and assume that an error-free syndrome measurement is possible after the final round of syndrome measurement. The same assumption has been made for the qubit case in

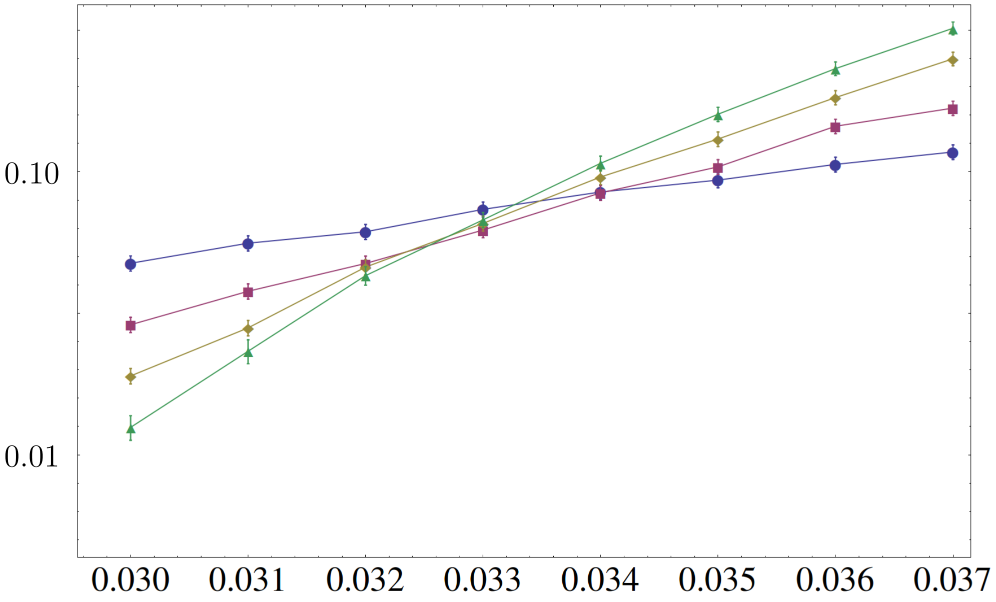

Figure 8.6: Error rate p (horizontal axis) versus logical error rate p_L (vertical axis) for $L = 8, 16, 24, 32$ (from top to bottom at $p = 0.030$) for the $D(\mathbb{Z}_3)$ model. Each data point represents 10^3 logical errors, or at least 400 for $L = 32$ and low p. Error bars are taken to be 2σ. We notice considerable finite-size effects for $L = 8$.

e.g. Ref. [126]. An alternative would be to assume periodic boundary conditions in temporal direction [137]. While both of these assumptions cannot be justified on physical grounds, they are necessary in order to observe a threshold error rate without explicitly modelling a measurement of the non-locally stored quantum information. In reality, the logical quantum state would have to be measured in a fault-tolerant way, and we avoid explicit modelling of such a measurement process for simplicity.

We model syndrome measurement errors by adding with probability p one of the $d-1$ non-trivial values $1, \dots, d-1$ to the actual syndrome value (modulo d). This generalizes the modelling of syndrome measurement errors used for the qubit case in Refs. [137, 140]. The distance between two non-trivial syndrome changes is then given by the 3D Manhattan distance $d_{jk} = d^x_{jk} + d^y_{jk} + d^t_{jk}$, and the number of possible

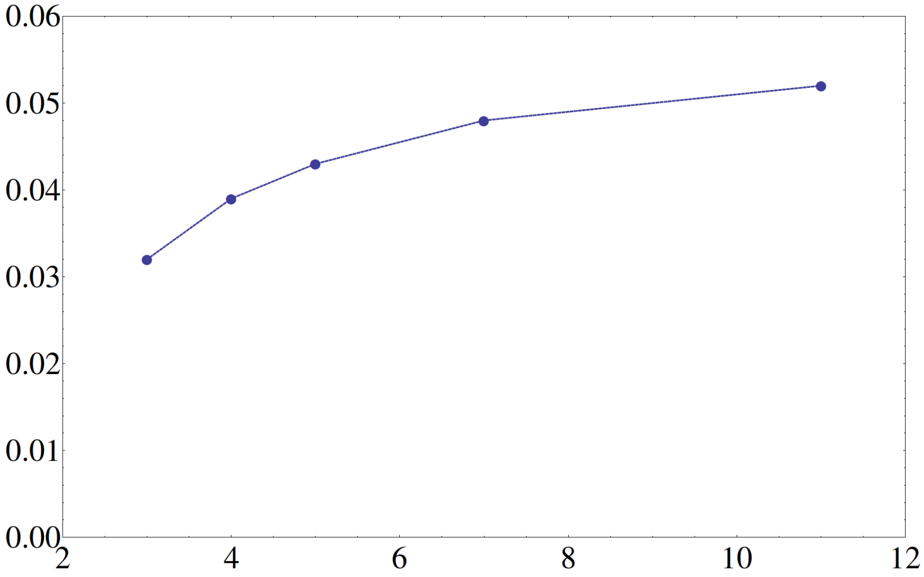

Figure 8.7: Thresholds p_c achieved with our HDRG decoder for $d = 3, 4, 5, 7, 11$ when errors affect both data qudits and syndrome measurements with a rate p.

minimum-weight error paths connecting them is

$$\mu_{jk} = (d-1)\binom{d_{jk}}{d^t_{jk}}\binom{d^x_{jk} + d^y_{jk}}{d^x_{jk}}. \tag{8.28}$$

Since the logical errors in our Monte Carlo simulations follow a binomial distribution, the standard deviation in the logical error rates are given by $\sigma = \sqrt{p_L(1-p_L)/N}$, where N is the number of experiments. Fig. 8.6 shows 2σ error bars. From Fig. 8.6, we estimate a threshold value of 3.2% for the $d = 3$ case. This is larger than the thresholds obtained with an analogous error model for the qubit ($d = 2$) case. Minimum-weight perfect matching achieves in this case a threshold of 2.9% [140], while an SDRG decoder achieves 1.9% [137].

Finally, Fig. 8.7 shows the thresholds obtained by comparing logical error rates as in Fig. 8.6 for different values of d. Note that for the imperfect measurement case, there is no obvious generalization of the Hashing bound with which our thresholds could be compared. For $d = 7919$, we obtain a threshold of $p_c = 6.1\%$.

We have again determined the minimal code sizes $L^*(p)$ which are necessary to achieve $p_L < p$ for some p for $d = 3$ and $d = 7919$. The

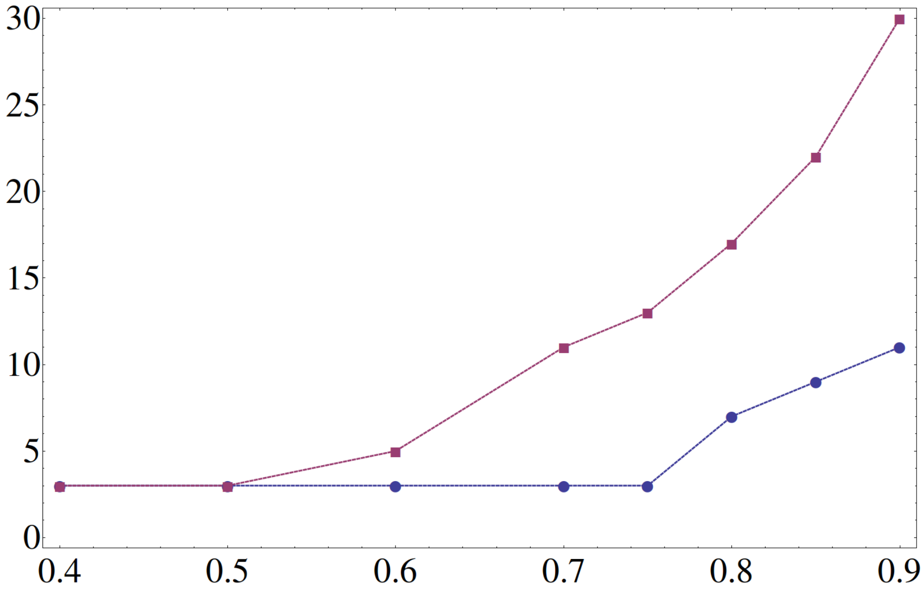

Figure 8.8: Minimal sizes $L^*(p)$ (vertical axis) such that $p_L < p$ for both $d = 3$ (circles) and $d = 7919$ (squares) for imperfect stabilizer measurements. The horizontal axis shows p/p_c for the threshold values p_c provided in Fig. 8.4. We have $L^*(p) = 3$ for all $p/p_c < 0.4$.

results are given as a function of p/p_c in Fig. 8.8.

8.7 Decoding Non-Abelian anyons

Due to the way HDRG decoders have been defined in this work, they are directly applicable to the case of non-Abelian anyons. This can be demonstrated by using them to decode the $\Phi - \Lambda$ model, a non-Abelian model whose anyons have fusion behaviour similar to that of the Fibonacci model [148]. Specifically, they have the fusion rules

$$\Lambda \times \Lambda = 1\,, \quad \Lambda \times \Phi = \Phi\,, \quad \Phi \times \Phi = 1 + \Lambda + \Phi\,. \tag{8.29}$$

Note that the Φ and Λ anyons are their own antiparticles.

Except for the fusion channel to a Φ in the last fusion rule, the fusion rules of the $\Phi - \Lambda$ model are identical to those for Ising anyons:

$$\psi \times \psi = 1\,, \quad \psi \times \sigma = \sigma\,, \quad \sigma \times \sigma = 1 + \psi\,. \tag{8.30}$$

Decoding of this model was studied both with the BH decoder and using MWPM methods in Ref. [149]. In order to understand decoding by means of MWPM, note that σ anyons can only be created and destroyed in pairs. It is thus possible to temporarily treat ψ particles as vacuum and use MWPM to pair all σ particles. In a second round, MWPM can be used to pair all ψ particles.

Similarly, it is possible to decode the $\Phi - \Lambda$ model by first fusing all Φ anyons and then pairing all remaining Λ particles by use of MWPM. However, in contrast to the Ising model, we can no longer use MWPM for the first round of decoding. Two Φ anyons can fuse both to a non-Φ outcome (1 or Λ) or to another Φ particle, exhibiting Fibonacci-like behavior. (In particular, the number of Φ anyons need not be even, as required for MWPM.) It is thus necessary to apply HDRG methods for this first round of decoding.

We consider the case of non-Abelian decoding with perfect syndrome measurements. In this case the $\Phi - \Lambda$ model can be efficiently simulated by the Abelian $D(\mathbb{Z}_6)$ model [148]. A Λ thereby corresponds to a charge m_3, while a Φ corresponds to charges m_1, m_2, m_4, and m_5. The simulation requires that the decoder cannot distinguish between the different charges of the $D(\mathbb{Z}_6)$ model that correspond to a Φ. Any more information would correspond to the decoding accessing the internal fusion space of the Φ anyons in an illegal way, and so no longer provides a good simulation of the non-Abelian model.

When applying the MWPM algorithm for pairing the Λ particles, the pairing weights between two of them would ideally incorporate knowledge about the initial location of all Φ anyons that fused into a particular Λ. However, for simplicity we ignore knowledge about the fusion history of the Λ particles during MWPM.

We consider an error model in which $p_\Phi = p_\Lambda = p/2$. In terms of the $D(\mathbb{Z}_6)$ model used for the simulation, we have $p_1 = p_2 = p_4 = p_5 = p_\Phi/4$, while $p_3 = p_\Lambda$. Here, p_g denotes the probability of a $(\sigma^x)^g$ error in the $D(\mathbb{Z}_6)$ model. Ref. [148] employed the expanding diamonds decoder for this error model and found a threshold error rate of $p_c = 7.0\%$. Figs. 8.9 and 8.10 show that our decoder achieves a threshold of $p_c = 15.0\%$, more than twice as high as the one achieved by previous HDRG methods. Fig. 8.9 suggests a scaling of the form $p_L \sim \exp[-\alpha(p)L^1]$. Recall from our discussion in Sec. 8.4 that this improvement over the $p_L \sim \exp[-\alpha(p)L^{2/3}]$ scaling achieved by previous HDRG decoders is due to the use of shortcuts. We point out again that even when using the shortcuts, there will be sub-polynomial corrections to the linear-in-L exponent.

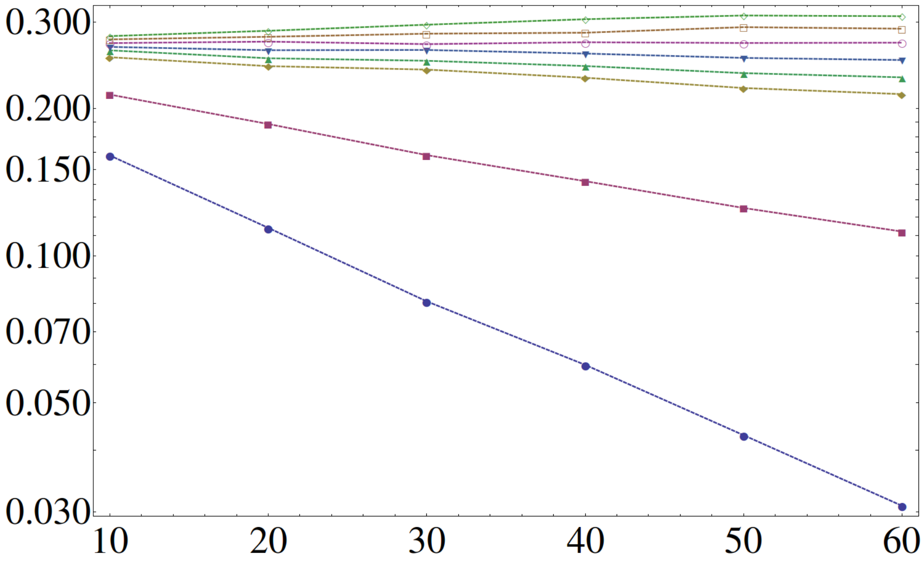

Figure 8.9: Logical error rate p_L as a function of L for various error rates p. From top to bottom, we have $p = 0.152, 0.151, 0.150, 0.149, 0.148, 0.147, 0.140, 0.130$. A threshold at $p_c = 15.0\%$ and exponential suppression of p_L for $p < p_c$ are clearly recognizable. Data points represent 10^4 logical errors.

Fig. 8.11 provides logical error rates in the low-p, low-L regime and shows that our decoding indeed allows the code to use its whole distance. Recall that the use of shortcuts makes $\lfloor (L+1)/2 \rfloor$ errors necessary for a logical error for $L < 9$, leading to a suppression $p_L \sim p^{\lfloor (L+1)/2 \rfloor}$ for low enough p.

The case of imperfect syndrome measurements for non-Abelian anyons is more complex than Abelian ones, and so cannot be done simply through the case of noisy syndrome measurements in $D(\mathbb{Z}_6)$. This will be addressed in future work.

8.8 Runtime of our algorithm

In this section, we provide a heuristic estimate of the parallelized runtime of our algorithm, for both the case with perfect and imperfect syndrome measurements.

Recall that in our algorithm each vertex has the possibility to "self-match" at the cost of the vertex-weight given in Eq. (8.26), which is upper-

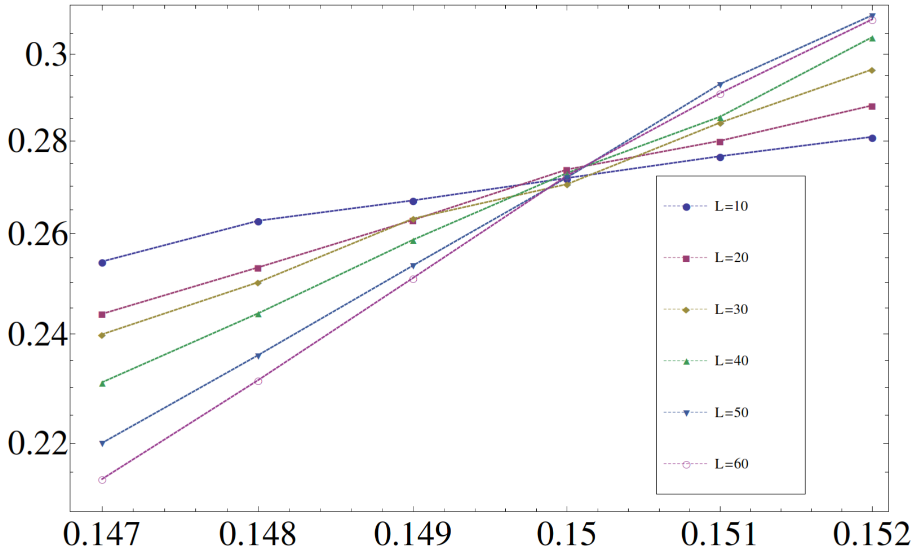

Figure 8.10: Logical error rate p_L as a function of p close to the threshold for various L.

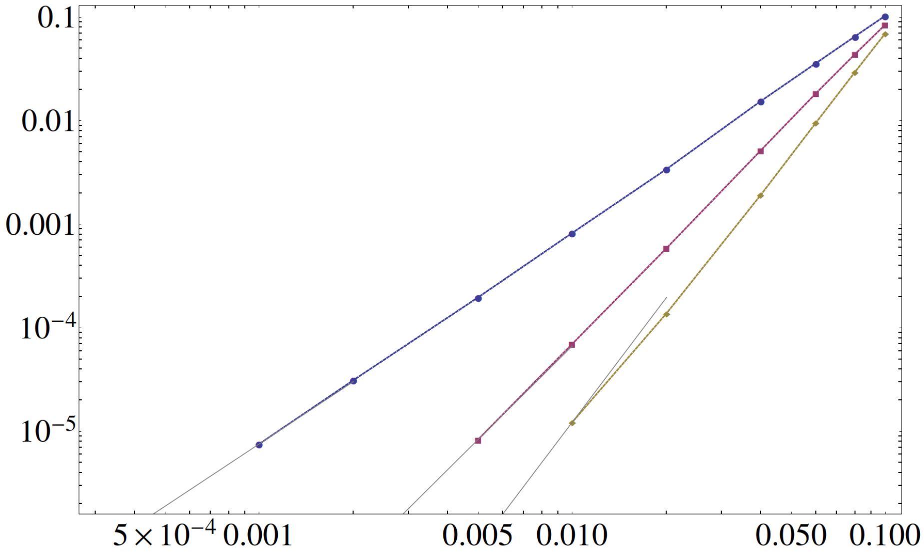

Figure 8.11: Logical error rate p_L as a function of p for small-distance codes $L = 3, 5, 7$ (top to bottom). Gray lines are fittings of the form $ap^{(L+1)/2}$ through the lowest data point for each L, showing that for $L = 3, 5$ we are already well in the regime where most likely error chains dominate the logical error rate.

bounded by the Manhattan distance to its nearest neighbor. Two vertices will thus only ever be matched by the algorithm if their distance is smaller than the sum of their respective nearest-neighbor distances. If their distance is larger, it is thus unnecessary to add an edge between them. For low enough p, the typical nearest-neighbor distance is $O(1)$ (an anyon can only be created from the anyonic vacuum together with another anyon), while the typical next-to-nearest-neighbor distance is $O(p^{-1/2})$. Each vertex is thus typically only connect to one other vertex for low enough p. This means that the graph given to the perfect matching algorithm decays into subgraphs of average size $O(1)$. The threshold value above which one of the subgraphs obtained this way percolates the entire code is estimated for the $D(\mathbb{Z}_3)$ case with perfect measurements in Fig. 8.12. It is significantly higher than the threshold error rate of our algorithm. Our algorithm thus lends itself nicely to parallelization. Note that the shortcuts discussed in Sec. 8.4 lead to local deformations of the lattice geometry only.

If p is below the aforementioned threshold, the propability of a subgraph involving n vertices is exponentially small in n. Correspondingly, the maximal number of vertices we expect to find in a subgraph is for a code of linear size L given by $O(\log L)$, as is well-known from percolation theory. For a graph with n vertices and $O(n^2)$ edges, the perfect matching algorithm `Blossom V` [69] finds a MWPM in time $O(n^3 \log n)$. In conclusion, one iteration of our MWPM HDRG algorithm takes in the perfect measurement case a time which grows like poly$(\log L)$.

The lower λ in the vertex-weight Eq. (8.26) is, the cheaper it is for an anyon to self-match and refrain from fusing with another anyon. The smallest number of fusions occurs for $\lambda = 0$, where two anyons are only fused if they are mutual nearest neighbors. Since we expect the number of mutual nearest neighbor pairs among all anyons not to fall below a certain fraction, at least a certain fraction of anyons will fuse during each iteration of the algorithm, such that $O(\log L)$ iterations will be sufficient even for $\lambda = 0$. The inset of Fig. 8.12 shows the average number of iterations of our algorithm for $d = 3$ and $\lambda = 0.3$, clearly following a logarithmic trend. With an average of $O(\log L)$ iterations, the total expected runtime of our algorithm is poly$(\log L)$.

For the more realistic case with imperfect measurements, where error correction is performed in a continuous fashion, the relevant quantity is the classical processing time per round of error correction. We assume that the error rate p is the same for data qubit errors and for syndrome measurement errors, and that we perform error correction for L

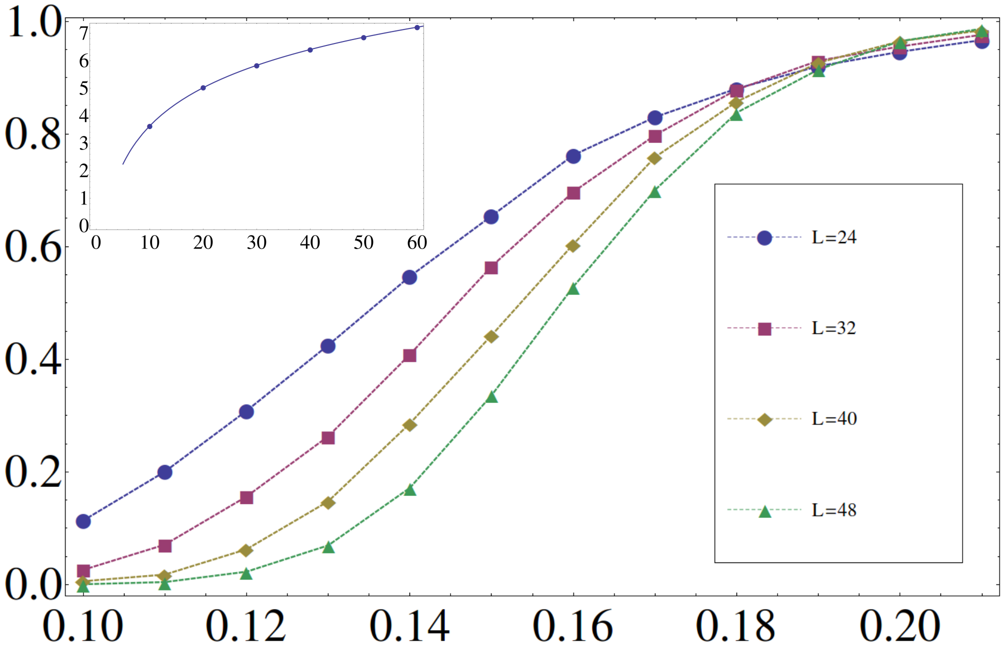

Figure 8.12: Propability that a subgraph wraps around the entire code for various error rates p (horizontal axis) and code sizes L for the $D(\mathbb{Z}_3)$ case with perfect measurements. Two vertices (non-trivial syndrome measurements) are connected by an edge if their distance is strictly smaller than the sum of their nearest-neighbor distances. The Manhattan distance is used for simplicity. A crossover point is observed at roughly $p = 19\%$, below which the probability of a code-spanning subgraph vanishes as $L \to \infty$. The inset shows the average number of iterations of our algorithm necessary for $p = 12\%$ as a function of L. The line is a fit of the form $a \log L + b$.

time-steps. After including measurement errors, three-dimensional clusters of syndrome changes will still be of average size $O(1)$ and maximal size $O(\log L)$. If the *local* processing speed of the classical computing devices performing the error correction algorithm can be temporarily increased by a factor of 2, larger than average sized clusters can still be dealt with in constant average time, as they are exponentially unlikely. Such an approach to error correction with constant average processing time per round of error correction has been described in much more detail in Ref. [156].

8.9 Conclusions

In conclusion, we have discussed strengths and weaknesses of existing HDRG decoders, and have proposed a new minimum-weight matching based algorithm which does not force us to compromise between the advantages of the different algorithms. Indeed, we have shown that in the perfect measurement case for the $D(\mathbb{Z}_d)$ quantum double models our algorithm achieves higher thresholds than previous HDRG decoders. Furthermore, we have used it to perform the first study of error correction for these qudit topological codes for which the possibility of syndrome measurement failure is taken into account.

The defining feature of non-Abelian systems is that the outcome of fusing two defects cannot be predicted when given local properties of the two defects only. The information about the fusion outcome is stored in non-local degrees of freedom, which are used to store and process quantum information. Since our decoder uses only the geometrical location of defects as inputs, and then updates based on whether or not two defects can be brought to annihilation, the methods discussed in this work are straightforwardly applicable to non-Abelian systems. We have employed them to achieve a drastically increased error threshold for a particular non-Abelian model, and anticipate their application in the open problem of continuous error correction for non-Abelian systems.

8.10 Acknowledgements

The authors would like to thank Benjamin Brown for critical reading of the manuscript and sharing data, and the Swiss NF and NCCR QSIT for support

Note. While this work was in preparation, the authors learnt of other forthcoming results for noisy syndrome measurements on the qudit codes [157]. This provides non-HDRG methods that could be used in conjunction with our decoder to boost performance.

CHAPTER 9

Parafermions in a Kagome Lattice of Qubits for Topological Quantum Computation

Adapted from:
Adrian Hutter, James R. Wootton, and Daniel Loss
"Parafermions in a Kagome lattice of qubits for topological quantum computation",
ArXiv:1505.01412 (2015)

Engineering complex non-Abelian anyon models with simple physical systems is crucial for topological quantum computation. Unfortunately, the simplest systems are typically restricted to Majorana zero modes (Ising anyons). Here we go beyond this barrier, showing that the $\mathbb{Z}_4$ parafermion model of non-Abelian anyons can be realized on a qubit lattice with only nearest neighbor interactions. Our system additionally contains the Abelian $D(\mathbb{Z}_4)$ anyons as low-energetic excitations. We show that braiding of these parafermions with each other and with the $D(\mathbb{Z}_4)$ anyons allows the entire $d = 4$ Clifford group to be generated. The error correction problem for our model is also studied in detail, guaranteeing fault-tolerance of the topological operations. Crucially, since the non-Abelian anyons are engineered through defect lines rather than as excitations, non-Abelian error correction is not required. Instead the error correction problem is performed on the underlying Abelian model, allowing high noise thresholds to be realized.

9.1 Introduction

Non-Abelian anyons exhibit exotic physics that would make them an ideal basis for topological quantum computation [16, 18, 158]. It has recently become apparent that truly scalable quantum computation with non-Abelian anyons can only be achieved when invoking active error correction, despite the protection provided by a finite anyon gap [148, 149, 159]. The development of practical systems in which non-Abelian anyons may be created, manipulated, and detected is therefore highly important. Systems in which non-Abelian anyons arise typically suffer from one of two drawbacks: either they are experimentally extremely challenging to realize (as is the case for quantum double [16] or string-net models [160]), or it is not clear how they can be made compatible with the active error correction required for fault-tolerance (as is the case for FQH systems).

A particularly attractive approach for building a fault-tolerant quantum computer is to use a system of physical qubits (spin-$\frac{1}{2}$ particles). A number of technologies allow for precise qubit control, such as superconducting qubits [45], trapped atomic ions [161], spin qubits [9], or cold atoms or polar molecules in optical lattices [162]. A qubit lattice with two-body nearest neighbour interactions would therefore be an ideal system to realize non-Abelian anyons. We therefore restrict ourselves to these.

Thus far, the only non-Abelian model known to be supported by a qubit system are Majorana zero modes, also known as Ising anyons [64, 163, 164]. A variety of proposals for experimental realization of Majorana zero modes in solid state systems have also been developed [165]. These anyons can be used to perform universal quantum computation when enhanced by non-topological operations [24, 166]. However, these additional operations are highly resource intensive. Anyon models with a richer set of topological operations would therefore be much more practical for the realization of topological quantum computation. Here we solve this by introducing a model composed of two-qubit Hamiltonian interactions that can realize a more complex model of non-Abelian anyons, known as $\mathbb{Z}_4$ parafermions. The error correction problem for these is studied in detail.

Parafermion modes are generalizations of Majoranas whose fusion and braiding behavior is more complex and computationally more powerful. This has led to a quest in recent years for systems that could host them. Numerous proposals for their experimental implementation in condensed matter systems such as fractional quantum Hall systems, nanowires, or topological insulators have recently appeared [167–180].

Extrinsic defects in *Abelian* topological states can behave like non-Abelian anyons [181]. The idea of non-Abelian anyons at the ends of defect lines, first introduced for FQH states [182], has been adapted to the $D(\mathbb{Z}_d)$ quantum double models in Refs. [183, 184]. These anyons are Majorana zero-modes for $d = 2$ and more powerful parafermions for $d > 2$. Unfortunately, the generalized Pauli operators appearing in the $D(\mathbb{Z}_d)$ quantum double models models coincide with the physically relevant spin-operators only for $d = 2$. Otherwise, their structure makes them highly difficult to realize experimentally. The case $d = 4$, however, allows us to combine the best of both worlds. The joint Hilbert space of two qubits allows the 4-dimensional generalized Pauli operators to be expressed in terms of two-qubit operators. Using this, we show how $\mathbb{Z}_4$ parafermions can emerge in a lattice of qubits with nearest-neighbor interactions only. This allows the computational power of $\mathbb{Z}_4$ parafermions to be harnessed in a qubit system.

The fact that our system is built on top of a system supporting Abelian anyons (the $D(\mathbb{Z}_4)$ quantum double model) proves very useful. The non-Abelian parafermion modes can not only be braided with each other, but also with Abelian excitations of the quantum double model, allowing us to generate the entire Clifford group for $d = 4$ by quasi-particle braiding. This extends beyond the limited set of gates found using the same parafermions in previous work [169]. Furthermore, we do not have to perform non-Abelian error correction (a still poorly understood problem [148, 149, 185, 186]) to guarantee fault-tolerance, but can correct the underlying Abelian model. This Abelian error correction problem is nevertheless more involved than the well-studied error correction problem for the standard $D(\mathbb{Z}_d)$ models, and we study it in detail.

The rest of this paper is organized as follows. In Sec. 9.2 we show how $\mathbb{Z}_4$ parafermion operators can be expressed in terms of qubit operators. Sec. 9.3 introduces a qubit Hamiltonian whose low-energetic excitations correspond to the $D(\mathbb{Z}_4)$ quantum double model. In Sec. 9.4 we discuss how $\mathbb{Z}_4$ parafermion modes appear at the ends of defect strings in our model. We demonstrate in Sec. 9.5 how the non-Abelian braiding statistics of these modes can be used to perform logical gates. Appendix 9.D contains a proof that the set of gates which can be performed this way generates the entire Clifford group $\mathcal{C}_4$, which may be of independent interest. In Sec. 9.6 we study the error correction problem of our model in detail and conclude in Sec. 9.7.

9.2 $\mathbb{Z}_4$ parafermion operators in terms of qubit operators

We consider d-dimensional generalizations of the Pauli matrices X and Z. These are unitary operators satisfying $X^d = Z^d = \mathbb{1}$ and $ZX = \omega XZ$, where $\omega = e^{2\pi i/d}$ with integer $d > 1$. If we define $Y = \omega^{(d+1)/2} X^\dagger Z^\dagger$, we also have $Y^d = \mathbb{1}$, $XY = \omega YX$, and $YZ = \omega ZY$. Operators X_i and Z_i act on qudit i and hence $[X_i, X_j] = [Z_i, Z_j] = [X_i, Z_j] = 0$ if $i \neq j$.

These operators are related to those of parafermions. Given a total ordering on the qudits $\{i\}$, one can obtain parafermion operators via a non-local transformation [187]

$$\gamma_{2i-1} = (\prod_{j<i} X_j) Z_i \,, \quad \gamma_{2i} = \omega^{(d+1)/2} (\prod_{j\leq i} X_j) Z_i \,. \tag{9.1}$$

These satisfy the $\mathbb{Z}_d$ parafermion relations,

$$\gamma_j^d = \mathbb{1} \,, \quad \gamma_j \gamma_k = \omega^{\mathrm{sgn}(k-j)} \gamma_k \gamma_j \,. \tag{9.2}$$

The operators X, Y, and Z can be represented as d-dimensional matrices. It is thus natural to seek a representation of these operators for the case $d = 4$ on the Hilbert space of two qubits (spins-$\frac{1}{2}$). Indeed, given two qubits 1 and 2, one easily verifies that the operators

$$\begin{aligned} X &= \frac{1}{2}(\sigma_1^x + \sigma_2^x - i\sigma_1^z\sigma_2^y + i\sigma_1^y\sigma_2^z) \\ Y &= \frac{1}{2}e^{i3\pi/4}(\sigma_1^y + i\sigma_2^y + i\sigma_1^x\sigma_2^z + \sigma_1^z\sigma_2^x) \\ Z &= \frac{1}{\sqrt{2}}e^{i\pi/4}(\sigma_1^z - i\sigma_2^z) \end{aligned} \tag{9.3}$$

are 4-dimensional generalized Pauli operators, and $\mathbb{Z}_4$ parafermions can be obtained from these via Eq. (9.1). We also note that $X^2 = \sigma_1^x\sigma_2^x$, $Y^2 = \sigma_1^y\sigma_2^y$, and $Z^2 = \sigma_1^z\sigma_2^z$.

9.3 Model

We consider a two-dimensional Kagome (trihexagonal) lattice as in Fig. 9.1. Each vertex of the lattice hosts one 4-dimensional qudit (one pair of $\mathbb{Z}_4$

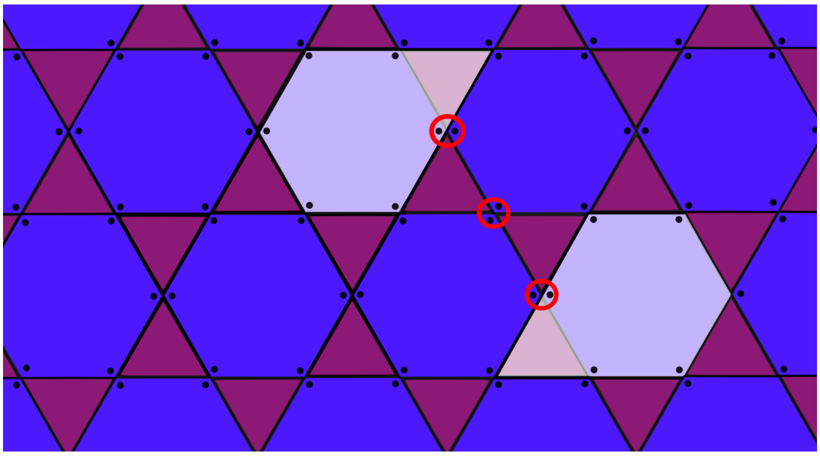

Figure 9.1: Two qubits are located at each vertex of a Kagome lattice. Each pair of qubits hosts two $\mathbb{Z}_4$ parafermions. To unlock their potential for non-Abelian braiding, two such parafermions need to become unpaired, which is achieved by adding a defect line to the lattice. These are strings of strong local operators acting on qubit pairs (encircled). They create unpaired parafermion modes located at their ends (light pentagon-shaped regions consisting of a hexagon and a triangle).

parafermions) or, in other words, two qubits. The Hamiltonian of our model is given by

$$H = \sum_{\triangle} H_{\triangle} + h \sum_{i} (\sigma^x_{i1} + \sigma^x_{i2})\,. \tag{9.4}$$

Here, the first term is a sum of equivalent terms for each triangle in the Kagome lattice. We label the vertices around one triangle a, b, and c, and the two qubits which are present at vertex a are called a_1 and a_2, etc. The triangle terms in the Hamiltonian are then given by

$$\begin{aligned} H_{\triangle} = {} & \frac{J}{2}(\sigma^z_{a1}\sigma^z_{b1}\sigma^z_{c1} + \sigma^z_{a2}\sigma^z_{b2}\sigma^z_{c2}) \\ & - \frac{J}{2}(\sigma^z_{a1}\sigma^z_{b1}\sigma^z_{c2} + \sigma^z_{a1}\sigma^z_{b2}\sigma^z_{c1} + \sigma^z_{a2}\sigma^z_{b1}\sigma^z_{c1} \\ & + \sigma^z_{a2}\sigma^z_{b2}\sigma^z_{c1} + \sigma^z_{a2}\sigma^z_{b1}\sigma^z_{c2} + \sigma^z_{a1}\sigma^z_{b2}\sigma^z_{c2})\,. \end{aligned} \tag{9.5}$$

The second sum $\sum_i$ in Eq. (9.4) runs over all vertices in the lattice. The two qubits located at vertex i are called $i1$ and $i2$. This second sum thus represents a uniform magnetic field in x-direction.

Our Hamiltonian involves three-qubit terms of the form $\sigma_a^z\sigma_b^z\sigma_c^z$. It is in principle straightforward to generate these from one-body terms and two-body interactions by use of perturbative gadgets [74, 115, 116]. Consider a "mediator qubit" u coupled to qubits a, b, and c. Starting from a Hamiltonian

$$H_{\text{gadget}} = -\frac{\Delta}{2}\sigma_u^z + \alpha(\sigma_a^z + \sigma_b^z)\sigma_u^x + \beta\sigma_c^z\sigma_u^z + \gamma\sigma_a^z\sigma_b^z + \delta\sigma_c^z\,, \tag{9.6}$$

and consider the perturbative regime $\Delta \gg |\alpha|, |\beta|$. In this regime, it is possible to integrate out qubit u. Taking up to third-order terms into account, one finds an effective Hamiltonian

$$H_{\text{eff}} = (\beta + \delta)\sigma_c^z + (-2\frac{\alpha^2}{\Delta} + \gamma)\sigma_a^z\sigma_b^z - 4\frac{\alpha^2\beta}{\Delta^2}\sigma_a^z\sigma_b^z\sigma_c^z\,. \tag{9.7}$$

Choosing $\delta = -\beta$ and $\gamma = 2\frac{\alpha^2}{\Delta}$ produces the desired three-qubit term without any undesired one- or two-qubit terms.

The generation of three-body interactions in optical lattices has been discussed in detail in Refs. [188, 189]. These proposals would make the perturbative gadgets unnecessary. A "toolbox" for generating spin-lattice models such as ours in optical lattices has also been developed [109].

The spin-Hamiltonian in Eq. (9.4) can be exactly rewritten as

$$H = -J\sum_{\triangle}(Z_aZ_bZ_c + \text{H.c.}) + h\sum_i(X_i + X_i^\dagger)\,. \tag{9.8}$$

Here again the first sum runs over all triangles in the lattice and the corners of a triangle are labeled a, b, and c. The second sum runs again over all vertices of the lattice.

We now consider the perturbative limit $h \ll J$ and regard the second sum in Eq. (9.8) as a perturbation to the first term. Note that all terms in the first sum in Eq. (9.8) commute, so the unperturbed Hamiltonian is trivially solved. The lowest-order non-vanishing terms appear in sixth-order perturbation theory. We find an effective Hamiltonian

$$\begin{aligned} H_{\text{eff}} = &-J\sum_{\triangle}(Z_aZ_bZ_c + \text{H.c.}) \\ &-\frac{63}{8}\frac{h^6}{(2J)^5}\sum_{\hexagon}(X_rX_s^\dagger X_tX_u^\dagger X_vX_w^\dagger + \text{H.c.})\,, \end{aligned} \tag{9.9}$$

where the second sum runs over all hexagons in the Kagome lattice and r, s, t, u, v, w label the six vertices around each hexagon. The effective Hamiltonian in Eq. (9.9) is derived in Appendix 9.A.

We note that all summands in H_{eff} commute, so the system is exactly solvable. The excitations of this system are Abelian anyons corresponding to the $D(\mathbb{Z}_4)$ quantum double model. The topological degeneracy of the model can be made manifest by studying non-local loop degrees of freedom that commute with all stabilizers $Z_aZ_bZ_c$, $X_rX_s^\dagger X_tX_u^\dagger X_vX_w^\dagger$, and their Hermitian conjugates, and fullfil themselves $\mathbb{Z}_4$ relations. A possible choice of operators is illustrated in Fig. 9.2.

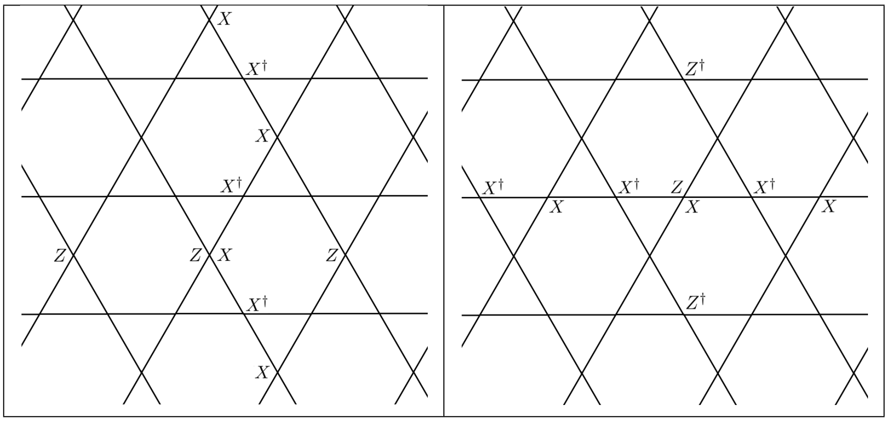

Figure 9.2: Two sets of logical operators $\tilde{X}_1 = XX^\dagger XX^\dagger \ldots$, $\tilde{Z}_1 = ZZZZ\ldots$ (left figure) and $\tilde{X}_2 = XX^\dagger XX^\dagger \ldots$, $\tilde{Z}_2 = ZZ^\dagger ZZ^\dagger \ldots$ (right figure) that satisfy the commutation relations of 4-dimensional generalized Pauli operators.

In passing, we note that the $\mathbb{Z}_2$ version of Eq. (9.8), in which the $\mathbb{Z}_4$ operators X and Z are replaced by Pauli operators σ^x and σ^z, leads to an effective Hamiltonian analogous to Eq. (9.9) and thus provides a very simple model with topological order. While this model requires three-body operators $\sigma^z\sigma^z\sigma^z$ as opposed to Kitaev's honeycomb Hamiltonian [64] which involves two-body interactions only, all of these interactions connect the same spin-component, which may provide a significant practical simplification over the honeycomb model.

9.4 Parafermion modes and defect lines

The model is constructed from the cyclic qudit operators Z and X, which are related to parafermion operators. It is therefore natural to seek an interpretation of the model in terms of parafermionic modes.

To do this we must first fix the exact form of the stabilizers, which define the anyonic charge carried by each excitation. Let us use E_p (M_p) to denote the stabilizer for a hexagonal (triangular) plaquette, p. For hexagonal plaquettes we use the convention that $E_p = X_r X_s^\dagger X_t X_u^\dagger X_v X_w^\dagger$, where r refers to the top-right corner and the other corners are labelled in an anti-clockwise fashion. For triangular plaquettes we use $M_p = Z_a Z_b Z_c$ for all triangles of the form $\triangle$ and $M_p = Z_a^\dagger Z_b^\dagger Z_c^\dagger$ for all triangles of the form $\bigtriangledown$. The stabilizer operators E_p and M_p are unitary operators with eigenvalues ω^k, $k \in \{0,1,2,3\}$, where here and in the following $\omega = i$ for $d = 4$. An eigenvalue ω^g of the E_P corresponds to a charge anyon of the form e_g, while M_P similarly detects flux anyons m_h. Fusion of charge anyons forms a representation of $\mathbb{Z}_4$, as does that of fluxes. The convention for the stabilizer operators chosen before ensures that the anyonic charge of both charge and flux type anyons is independently conserved (modulo 4). A full clockwise monodromy of an e_g around an m_h, or *vice versa*, yields a phase ω^{gh}, see Fig. 9.3 for illustration.

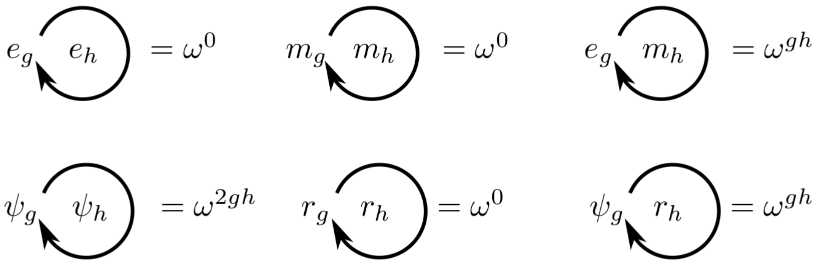

Figure 9.3: Phases obtained by braiding the e- and m-excitations of the $D(\mathbb{Z}_4)$ model around each other (top), and by braiding the excitations ψ and r of the transformed stabilizers around each other (bottom).

Just as Majorana modes (Ising anyons) in the qubit toric code [163, 184], parafermions appear in our system at the ends of defect strings. For the interpretation in terms of parafermions, it will be useful to introduce a new set of composite anyons defined as $\psi_g = e_g \times m_g$. These also obey $\mathbb{Z}_4$ fusion with each other, and their braiding behavior can be inferred from the behavior of the constituent charge and flux particles. The particles $\{\psi_0, \psi_1, \psi_2, \psi_3\}$ form a chiral Abelian anyon model with Chern number $\nu = 2$ [64].

Note that

$$e_g \times m_h = \psi_g \times m_{h-g} \,. \tag{9.10}$$

We now perform a local transformation from the set of stabilizer generators $\{E_p, M_p\}$, detecting the charges on the left-hand-side of Eq. (9.10), to a new set $\{S_p, R_p\}$ which detects the two charges on the right-hand-side. Let H denote the set of hexagonal plaquettes and T denote the set of triangular plaquettes. Note that $|T| = 2|H|$. Consider an injective map $\varphi : H \to T$, which to each hexagonal operator E_p assigns one of the six adjacent triangular operators $M_{\varphi(p)}$. Typically, we choose $M_{\varphi(p)}$ to be the top-right neighbor of E_p, while other choices become necessary next to defect lines. The transformation from the old to the new set of stabilizers reads $S_p = E_p$ for $p \in H$ and

$$R_p = \begin{cases} M_p E^{\dagger}_{\varphi^{-1}(p)} & \text{if } p \in \mathrm{Im}(\varphi) \\ M_p & \text{if } p \notin \mathrm{Im}(\varphi) \end{cases} \tag{9.11}$$

for $p \in T$. Here, $\mathrm{Im}(\varphi)$ denotes the image of the map φ.

Since $\prod_{p\in H} S_p = \prod_{p \in T} R_p = \mathbb{1}$, the charges detected by the new stabilizers are separately conserved (modulo 4). Just like the ψ_g anyons detected by the S_p stabilizers, the R_g charges detected by the R_p stabilizers also form an anyon model obeying $\mathbb{Z}_4$ fusion. However, while these two anyon models have the same fusion rules, they are not equivalent, as they exhibit different braiding behavior. A full clockwise monodromy of a ψ_g around a ψ_h gives a phase of ω^{2gh}, a monodromy of a r_g around an r_h gives a phase of 1, and a monodromy of a ψ_g around a r_h gives a phase of ω^{gh}, see again Fig. 9.3. Just like the e_g and m_h charges, the ψ_g and r_h particles correspond to a way of decomposing the $D(\mathbb{Z}_4)$ model into two submodels which are closed under fusion, but have non-trivial mutual braiding behavior,

$$\begin{aligned} D(\mathbb{Z}_4) &= \{e_0, e_1, e_2, e_3\} \times \{m_0, m_1, m_2, m_3\} \\ &= \{\psi_0, \psi_1, \psi_2, \psi_3\} \times \{r_0, r_1, r_2, r_3\} \,, \end{aligned} \tag{9.12}$$

where the three particle models other than $\{\psi_0, \psi_1, \psi_2, \psi_3\}$ correspond to the simple $\mathbb{Z}_4$ model.

The stabilizer operators S_p detect the presence of ψ_g anyon which are pinned to a pentagon-shaped double plaquette, made up of a neighbouring pair of triangular and hexagonal plaquettes. These anyons can be regarded as generalizations of Dirac fermions to the group $\mathbb{Z}_4$ (rather than

$\mathbb{Z}_2$). Just as Dirac modes can be decomposed into two Majorana modes, so too can the ψ modes be decomposed into two parafermion modes. Two parafermion modes, P_a and P_b, are therefore associated with each double plaquette, P. These are described using parafermion operators satisfying Eq. (9.2). The parity operator for the ψ mode associated with a pair (j,k) is defined $\omega^{(d+1)/2}\gamma_j\gamma_k^\dagger$ for $j<k$, and so $S_P=\omega^{5/2}\gamma_{P_a}\gamma_{P_b}^\dagger$.

For a stabilizer state, the system is within a definite eigenstate of all S_P. The parafermion modes are therefore all paired, with the pairs corresponding to the two within each double plaquette. In order to use the parafermion modes as non-Abelian anyons, some must be allowed to become unpaired. The creation and transport of unpaired parafermion modes can be done by adapting the method of Ref. [184] to the Kagome lattice. The method can be interpreted in terms of anyonic state teleportation [106,190], as explained for the Majorana case in Ref. [192].

The method introduces unpaired parafermion modes at the endpoints of defect lines. These are lines on which additional single qudit terms are added to the Hamiltonian, of one of the two following forms

$$\begin{aligned} Y+\text{H.c.} &= -\frac{1}{\sqrt{2}}(\sigma_1^y+\sigma_2^y+\sigma_1^x\sigma_2^z+\sigma_1^z\sigma_2^x)\,, \\ \omega^{5/2}XZ^\dagger+\text{H.c.} &= \frac{1}{\sqrt{2}}(\sigma_1^y-\sigma_2^y+\sigma_1^x\sigma_2^z-\sigma_1^z\sigma_2^x)\,. \end{aligned} \tag{9.13}$$

Specific examples are shown in Fig. 9.4.

The single qudit terms added along defect lines are much stronger than any other interactions, and thus effectively remove the qudits on which they act from the code. This means that the E_P and M_P operators for the double plaquettes along these lines no longer commute with the Hamiltonian, and so can no longer be used as stabilizer generators. Their pentagon-shaped product, R_P, is used instead. The pentagons in Fig. 9.4 show how next to a defect line the mapping φ needs to pick the bottom-left triangular-shaped stabilizer of a hexagon-shaped stabilizer to ensure that their product still commutes with the Hamiltonian.

This change of the stabilizer generators of the code has a drastic effect. Consider an e_g anyon moved towards a point along a defect line from one direction, and an m_g moved towards the same point from the other direction. Both of these are detected by R_P type stabilizers. When they meet on the same double plaquette, they will fuse to form a ψ_g, and so not be detected by the R_P stabilizers anymore. In fact, since the S_P stabilizer is removed for double plaquettes along a defect line, they will

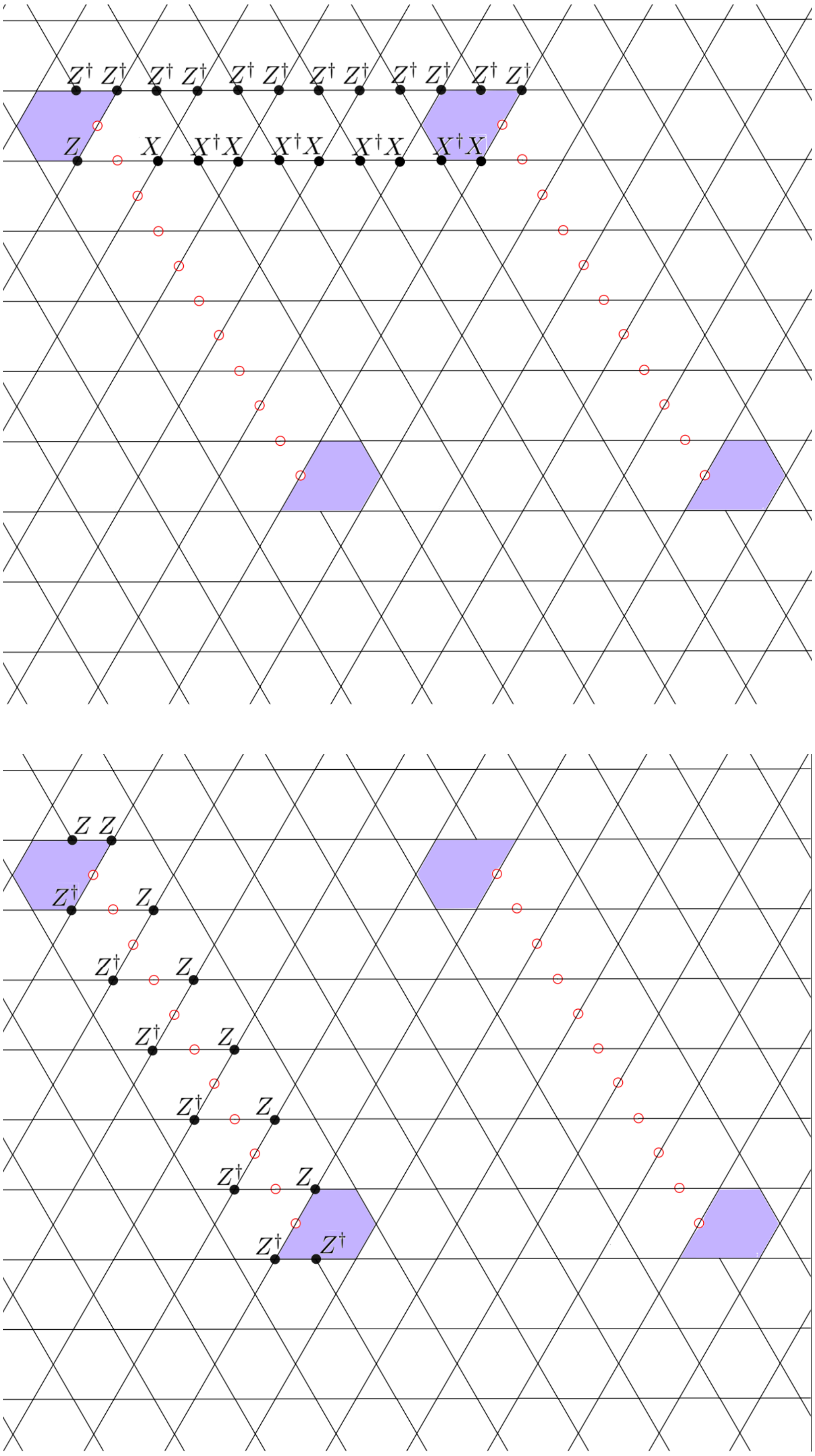

Figure 9.4: Strings of alternating single-qudit operators of the form $\omega^{5/2}Y_i$ + H.c. or $\omega^{5/2}X_iZ_i^\dagger$ + H.c. (encircled) are added to the Hamiltonian. These effectively eliminate the qudits on which they act from the code, leading to enlarged, pentagon-shaped stabilizers along the defect string. Parafermion modes reside on the pentagons at the ends of the defect strings (shaded). A possible choice for two logical operators $\tilde{X}_L$ (top) and $\tilde{Z}_L$ (bottom) satisfying $\tilde{Z}_L\tilde{X}_L = \omega\tilde{X}_L\tilde{Z}_L$ is illustrated.

not be detected by any stabilizer operator. The ψ_g occupancy of a defect line corresponds to an increased groundstate degeneracy of the system, referred to as a *synthetic topological degeneracy* [184].

In the following section, the $\{\psi_g, r_h\}$ decomposition of the $D(\mathbb{Z}_4)$ model will prove more convenient than the $\{e_g, m_h\}$ decomposition. A process in which a defect line converts an m_g into an e_{-g} can equivalently be described as one in which a r_g passes a defect line which emits a ψ_{-g}.

9.5 Parafermions as non-Abelian anyons

Since unpaired parafermion modes reside at the endpoints of defect strings, it is natural to use them to explain the properties of the modified stabilizer. Parafermion modes are described by a non-Abelian anyon model with particle species $\{\psi_0, \psi_1, \psi_2, \psi_3, \sigma\}$. Here $\psi_0 \equiv 1$ corresponds to the anyonic vacuum and σ is an unpaired parafermion mode. The fusion rules of this anyon model are

$$\begin{aligned} \sigma \times \sigma &= \psi_0 + \psi_1 + \psi_2 + \psi_3\,, \\ \psi_g \times \psi_h &= \psi_{g\oplus h}\,, \\ \psi_g \times \sigma &= \sigma\,, \end{aligned} \tag{9.14}$$

where $\oplus$ denotes addition modulo 4. A pair of parafermions (or the defect line between them) may therefore collectively hold any of the four types of ψ anyon.

As in the Majorana/Ising case, we use four parafermion modes (two defect strings) for which the total fusion sector is vacuum to store one logical qudit. The natural logical operators are parity operators for the pairs of parafermions. An eigenvalue ω^g corresponds to a ψ_g occupancy for the pair, and so the specific result $\sigma \times \sigma = \psi_g$ if they would be fused. We associate the Z basis of the logical qudit with the ψ occupancy of vertical pairs (connected by defect lines).

Specific choices of logical operator are illustrated in Fig. 9.4. The $\tilde{Z}_L$ corresponds to a clockwise loop of an e_1 around a defect line. The braiding of this e_1 around the ψ_g held in the pair yields the required phase of ω^g. The $\tilde{X}_L$ corresponds to clockwise loop of an e_{-1} anyon which is converted to an m_1 through one defect line and back to an e_{-1} through the other. Equivalently, we can describe it as a clockwise loop of a r_1 and a transfer of a ψ_1 from the right to the left defect line.

Let us denote a state in which the left defect line holds a mode ψ_g and the right defect line holds a mode ψ_h by $|\psi_g, \psi_h\rangle$. Two defect lines create a 4×4-fold synthetic topological degeneracy. For computational purposes, we restrict to the 4-dimensional subspace of states of the form $|g\rangle_L \equiv |\psi_g, \psi_{-g}\rangle$. This is the set of states which can locally be created from the anyonic vacuum. The effect of the logical operators on these states is $\tilde{X}_L|g\rangle_L = |g \oplus 1\rangle_L$ and $\tilde{Z}_L|g\rangle_L = \omega^g|g\rangle_L$.

In addition to the logical operators $\tilde{X}_L$ and $\tilde{Z}_L$, which can be performed in our model by braiding the *Abelian* $D(\mathbb{Z}_4)$ anyons around the parafermion modes (ends of defect strings), we can perform further topologically protected single-qudit and two-qudit gates by braiding the parafermion modes themselves. Defect lines used for braiding are shown in Appendix 9.B. Crucially, braiding parafermions allows one to perform an entangling gate by topological means, which is in contrast to Majorana fermions [169]. What is more, exploiting the fact that our non-Abelian system is built on top of an Abelian $D(\mathbb{Z}_4)$ system allows us to generate the entire 4-level Clifford group by braiding quasi-particles, as we discuss in the following.

For the rest of this section, X and Z refer to the logical operators called $\tilde{X}_L$ and $\tilde{Z}_L$ before, respectively. The first column in Fig. 9.5 illustrates how braiding of $D(\mathbb{Z}_4)$ charges and fluxes can be used to perform logical X and Z gates. Whether an e_1 or an m_1 anyon is used to perform the logical Z gate is irrelevant.

Consider two parafermion modes storing a ψ_g particle. A full clockwise monodromy of one parafermion around the other can be understood as a monodromy of the constituent e_g around the m_g, yielding an ω^{g^2} phase. We can thus expect a single exchange of the two parafermion modes storing a ψ_g to yield a square root of this phase, such as $\omega^{g^2/2}$. This is demonstrated directly by studying the necessary microscopic operations in App. 9.C.

For a logical qudit stored in four parafermion modes, let S denote a clockwise exchange of a vertical pair of parafermion modes, and T an exchange of a horizontal pair, see Fig. 9.6. As discussed, we have $S = \sum_g \omega^{g^2/2}|g\rangle\langle g|$, while T is diagonal in the logical X basis. In the logical Z basis, T reads (for $d = 4$)

$$T = \frac{1}{2}e^{-i\pi/4}\sum_{gh} e^{i\frac{\pi}{4}(g-h)^2}|g\rangle\langle h|\,. \tag{9.15}$$

Again, in contrast to Majorana fermions, parafermions support an entangling gate between two logical qudits by braiding operations [169]. The controlled phase-gate Λ is defined by its action on a logical two-qudit

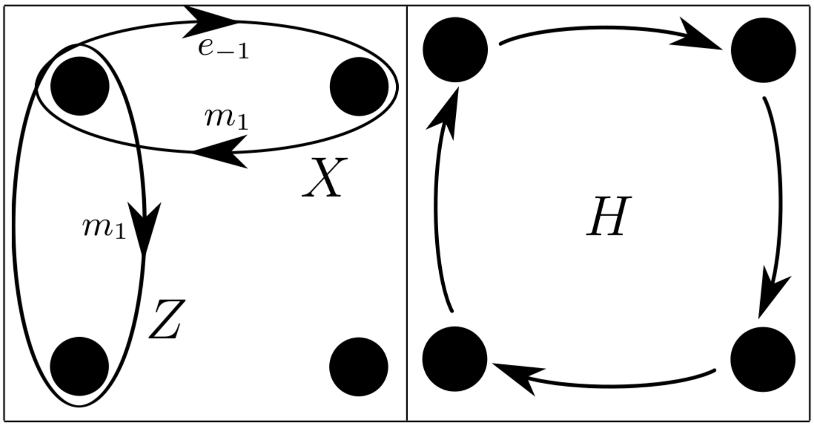

Figure 9.5: All generators of the single-qudit Clifford group can be performed by braiding quasi-particles. The four circles correspond to the four parafermion modes which are used to store one logical qudit. The left part of the figure illustrates how to perform the logical operators X and Z by braiding the Abelian excitations of the $D(\mathbb{Z}_4)$ model around the parafermions. The right part demonstrates a logical Hadamard gate H, which is performed by braiding the parafermion modes themselves.

Figure 9.6: Generators S and T of all gates that can be performed on a qudit stored in the fusion space of four parafermions by braiding them.

basis state, $\Lambda|g,h\rangle = \omega^{gh}|g,h\rangle$. In our parafermion scheme, an entangling gate can be performed by braiding of a pair of parafermions from one qudit with a pair from the other. Let us consider, for example, the braiding of the left vertical pair for both qudits. For an initial logical product state $|g,h\rangle$, the process corresponds to braiding a ψ_g clockwise around a ψ_h, which yields a phase of ω^{2gh}. The resulting operation is therefore the squared controlled phase-gate Λ^2. For $d = 2$, corresponding to the

Ising/Majorana case, $\Lambda^2 = \mathbb{1}$, and so this operation is trivial. For $d > 2$, however, it is a non-trivial entangling gate, akin to the one proposed in Ref. [169].

Clearly a more powerful entangling gate would be Λ itself. This can be achieved for $\mathbb{Z}_d$ parafermions for odd d by taking the $(d + 1)/2$-th power of Λ^2. However these do not admit the simple decomposition into qubits that we have used in defining the model. Fortunately, we can make use of the underlying charge and flux anyons to realize Λ despite the even qudit dimension.

The defect line may be interpreted as a hole for ψ type anyons: an area in which they may be placed such that their state becomes delocalized along the line and they are no longer detected by the stabilizers [44, 48, 196]. Similar holes can also be engineered for the constituent charge and flux anyons. A defect line is therefore a special case of the combination of a charge and flux hole, in which only $\psi_g = e_g \times m_g$ type anyons may reside rather than general $e_g \times m_h$ anyons. Nevertheless, we can consider a process in which a defect line is transformed into a separate charge and flux hole. Details on these holes and the transformations between them can be found in Appendix 9.E.

When only the charge hole of one qubit is braided around the defect line of another, the process for an initial state $|g, h\rangle$ corresponds to braiding an e_g around a ψ_h, which would yield the phase ω^{gh}. The charge and flux holes can then be recombined into a defect line. The net effect of the entire process is to apply the controlled phase gate Λ. Such a process is illustrated in Fig. 9.7.

One process which could split the defect line in this way is simply to intersect it with two others. One would be a line along which charge anyons are hopped by high-strength terms. The other would similarly hop flux anyons. The stabilizers that detect charges and fluxes, respectively, along these lines would then be suppressed. By adiabatically removing the defect line which delocalizes ψ modes, its ψ_g anyon occupation would be transferred to these two lines. The recombination of the defect line would be done by the reverse process.

For a tensor product of d-level systems, the Clifford group $\mathcal{C}_d$ consists of gates that map tensor products of d-level Pauli operators to other such tensor products under conjugation. In Appendix 9.D, we prove the following theorem.

Theorem. *The single-qudit gates S, T, and Z, and nearest-neighbor controlled phase-gates Λ generate the entire Clifford group $\mathcal{C}_4$.*

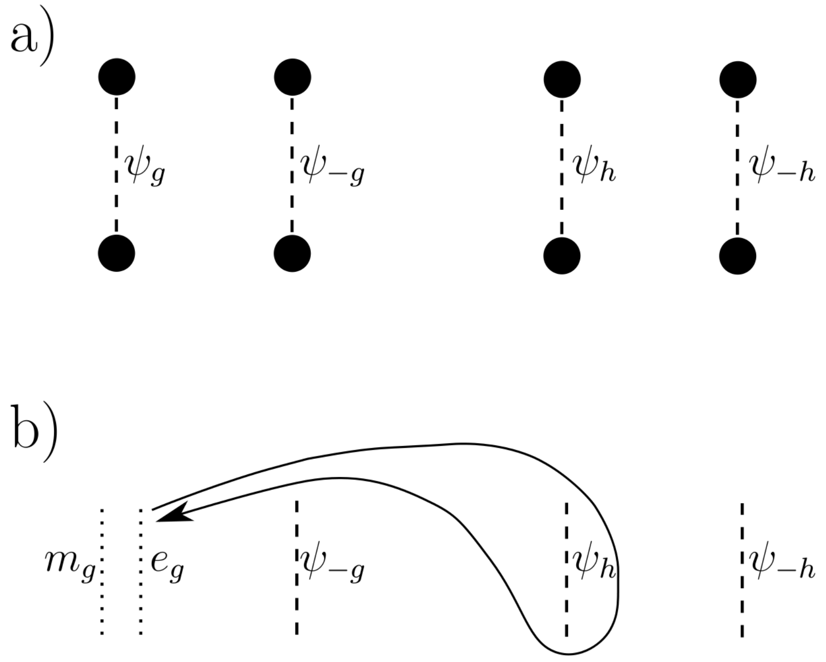

Figure 9.7: Performance of a controlled phase-gate. The a) part of the figure shows a logical product state $|g, h\rangle$ stored in the fusion space of eight parafermions. The defect line storing a mode ψ_g can be split into two defect lines storing $D(\mathbb{Z}_4)$ charges e_g and m_g, respectively. Braiding both endpoints of one of these lines clockwise around the defect line storing the ψ_h mode, as shown in the b) part, produces a phase ω^{gh}, as required.

As an example, $\tilde{H} = STS = TST$ satisfies $\tilde{H}X\tilde{H}^\dagger = Z$ and $\tilde{H}Z\tilde{H}^\dagger = X^\dagger$, so it can be identified with the logical Hadamard gate, up to a phase. Indeed, using the standard definition

$$H = \frac{1}{\sqrt{d}} \sum_{gh} \omega^{gh} |g\rangle\langle h| \,, \tag{9.16}$$

one verifies that $\sqrt{\omega}H = \tilde{H}$.

One possible implementation of H (up to a phase) is a cyclic permutation of the four parafermion modes, as in Fig. 9.5. This can be pictorially understood as follows. An X corresponds to a transfer of a ψ_1 from the right to the left defect line, accompanied by a clockwise loop of a r_1 around a horizontal pair. A Z corresponds to a clockwise loop of a r_1 around a vertical pair. A $\pi/2$ rotation as performed by H thus maps these two operations onto each other, up to the fact that we do not perform a vertical ψ_1 transfer, as the ψ occupancy of the vertical pair is delocalized along the defect line.

9.6 Error correction

For any system with a finite energy gap at finite temperature, excitations will appear with a finite density. This corresponds to finite length scale on which quantum computation can be performed before errors are almost certain to appear. This length scale can be increased by increasing the gap or lowering the temperature. However, neither of these methods is truly scalable. Error correction is therefore required if scalable quantum computation is to be performed.

For non-Abelian systems, the first studies of the corresponding error correction problem have recently appeared [148, 149, 185, 186]. Error correction for non-Abelian anyons is still poorly understood and its feasibility has not been demonstrated for the (realistic) time-continuous case. It comes thus very welcome that while our system provides the computational power of non-Abelian parafermions, its physical excitations still are Abelian $D(\mathbb{Z}_4)$ anyons, and the error correction problem for $D(\mathbb{Z}_n)$ quantum double models (including the time-continuous case) is well-studied [135, 146, 157, 185, 186]. However, when correcting these $D(\mathbb{Z}_4)$ anyons, we face a number of difficulties not considered in previous studies [135, 146, 157, 185]:

(i) Our stabilizer operators are products of $\mathbb{Z}_4$ qudit operators X, $X^\dagger$, Z, $Z^\dagger$, while an error model is realistically expressed in terms of single-qubit operators σ^x, σ^y, σ^z. These do not map eigenstates of the stabilizer operators to other eigenstates and one single-qubit operator can produce a product of up to three qudit operators (see below).

(ii) We consider quantum information stored in a synthetic topological degeneracy, which involves a defect line allowing anyons to change from one sublattice to the other (stars to hexagons and *vice versa*). We thus cannot decode each sublattice separately, as usually done for the toric code and other $D(\mathbb{Z}_d)$ quantum double models, but have to correct both of them simultaneously while taking the possibility of transferring anyons from one to the other into account.

(iii) Besides simplistic i.i.d. error models (such as depolarizing noise), we are particularly interested in Hamiltonian protection of a quantum state subject to thermal errors.

(iv) We do not consider a square lattice, but a trihexagonal one, which makes moving anyons and defining their distance more involved.

Error model

Since our 4-level qudits are composed of two qubits, it is natural to consider an error model in terms of single-qubit operations σ^x, σ^y, and σ^z. For a qudit hosted in two qubits 1 and 2, single-qubit Pauli operators can be expressed in terms of $\mathbb{Z}_4$ operators by inverting Eq. 9.3. We find

$$\begin{aligned}
\sigma_1^x &= \frac{1}{2}X(1-Z^2) + \text{H.c.}\,,\\
\sigma_2^x &= \frac{1}{2}X(1+Z^2) + \text{H.c.}\,,\\
\sigma_1^y &= \frac{1}{2}e^{i5\pi/4}Y(1+Z^2) + \text{H.c.}\,,\\
\sigma_2^y &= \frac{1}{2}e^{i3\pi/4}Y(1-Z^2) + \text{H.c.}\,,\\
\sigma_1^z &= e^{-i\pi/4}Z + \text{H.c.}\,,\\
\sigma_2^z &= e^{i\pi/4}Z + \text{H.c.}\,.
\end{aligned} \tag{9.17}$$

If we start from an eigenstate of all stabilizer operators, applying single-qubit Pauli operators will generate a superposition of states corresponding to different syndrome outcomes. By measuring all stabilizer operators, we can project again into a subspace with definite syndrome values. Each single-qubit Pauli operator thereby translates into a product of up to three qudit operators. Table 9.1 summarizes (up to irrelevant phases) into which qudit operators a certain single-qubit Pauli operator will translate with equal probability.

As a first simple error model, which does not involve a notion of Hamiltonian protection, we consider depolarizing noise. That is, for each qubit of the code we apply a Pauli operator with some probability p (the *depolarization rate*), where each of the three Pauli operators is chosen with equal probability.

More interesting from a physical perspective is a thermal error model. We consider a quantum state stored in the degenerate groundstates of the Hamiltonian given in Eq. (9.9), and assume that the system is weakly

σ_1^x, σ_2^x	$X, X^\dagger, XZ^2, X^\dagger Z^2$
σ_1^y, σ_2^y	$XZ, X^\dagger Z, XZ^\dagger, X^\dagger Z^\dagger$
σ_1^z, σ_2^z	$Z, Z^\dagger$

Table 9.1: Conversion from single-qubit Pauli operators to 4-dimensional generalized Pauli operators. When a syndrome measurement is performed, a Pauli operator is converted to each of the generalized Pauli operators in the right-hand column with equal probability.

coupled to a heat bath at some temperature T. Following e.g. Ref. [149], we assume that evolving the system according to the Metropolis algorithm provides a reasonable approximation of the thermalization process, since the evolution obtained by means of the Metropolis algorithm is local, Markovian, and has the thermal state as its unique fixed point.

During our simulation, we proceed as follows. We first pick one of the spins-$\frac{1}{2}$ of the system at random, then pick one of the three single-qubit opertors acting on that qubit at random, and convert that to a 4-dimensional generalized Pauli operator according to Table 9.1. We then calculate the energy cost Δ_{tot} of applying that generalized Pauli operator (or products thereof). This energy cost is of the form

$$\Delta_{\text{tot}} = m\Delta_{\triangle} + n\Delta_{\hexagon}\,, \tag{9.18}$$

where $\Delta_{\triangle}$ and $\Delta_{\hexagon}$ are the energy costs of creating a single triangle/hexagon-type anyon with charge 1 or 3 in Eq. (9.9), respectively. (That is, $\Delta_{\triangle} = 2J$ and $\Delta_{\hexagon} = 2\frac{63}{8}\frac{h^6}{(2J)^5}$.) Creating an anyon with charge 2 will have an energy cost $2\Delta_{\triangle}$ or $2\Delta_{\hexagon}$. The coefficients m and n are elements of $\{0, \pm 2, \pm 4\}$, depending on the change in anyonic charge. The proposed error is then accepted with probability $\min\{1, e^{-\Delta_{\text{tot}}/k_B T}\}$. If the proposal is accepted, we copy the current state of the system and try to correct it. If correction is successful, we continue our simulation with the uncorrected version of the system. If correction fails (for at least one logical operator), we interpret this as the quantum information having survived for a time which is given by the number of Metropolis steps divided by the number of spins in the system.

The thermal error model has three relevant energy scales $k_B T$, $\Delta_{\hexagon}$, and $\Delta_{\triangle}$. Since $\Delta_{\hexagon}$ appears in higher-order perturbation theory than $\Delta_{\triangle}$, we expect $\Delta_{\triangle} > \Delta_{\hexagon}$. Furthermore, effective protection requires $k_B T < \Delta_{\hexagon}, \Delta_{\triangle}$. We introduce a parameter λ which quantifies the separation of these three energy scales, i.e., $\Delta_{\hexagon} = \lambda k_B T$ and $\Delta_{\triangle} = \lambda^2 k_B T$. Very high values of λ are uninteresting, since they exponentially suppress errors from occurring.

Without defects

If there are no defect lines present, the anyonic charge of both types of anyons is conserved (modulo 4), and they can be corrected separately. Various techniques have been developed for correcting general $D(\mathbb{Z}_n)$ quantum double models [135, 146, 157, 185]. However, correcting the $D(\mathbb{Z}_4)$ case is particularly easy, since we can exploit the relation $\mathbb{Z}_4/\mathbb{Z}_2 \simeq \mathbb{Z}_2$. Specifically, we can first fuse all oddly-charged anyons in pairs. In a second round, the remaining anyons, which are all of charge 2, are fused in pairs. In order to find these pairings, we use the library `Blossom V` [69], which is the latest implementation of the efficient minimum-weight perfect matching algorithm due to Edmonds [70]. The weight between two equal-type anyons is thereby defined as the minimal number of generalized Pauli operators that need to be applied to create a pair of anyons at the two given locations.

Fig. 9.8 shows our results for the depolarizing noise model, i.e., the logical error rates of the the logical operators $\tilde{X}_1$ and $\tilde{Z}_1$ illustrated in Fig. 9.2 as a function of the depolarization rate p. One clearly recognizes threshold error rates $p_c \approx 24\%$ and $p_c \approx 10\%$, respectively. The equivalent figures for the logical operators $\tilde{Z}_2$ and $\tilde{X}_2$ look very similar and yield equivalent threshold error rates p_c.

These thresholds are best compared with those for an equivalent code based on $\mathbb{Z}_2$ anyons, and so with only a single qubit on each vertex. For independent bit and phase flips, the thresholds for $\tilde{X}_1$ and $\tilde{Z}_1$ are $p_c \approx 16.4\%$ and $p_c \approx 6.7\%$, respectively [40, 193]. When the hexagonal and triangular plaquettes are decoded separately, these correspond to thresholds of $p_c \approx 24.6\%$ and $p_c \approx 10.5\%$ for depolarizing noise. The similarity of these $\mathbb{Z}_2$ values with those of $\mathbb{Z}_4$ is remarkable. This qudit code is therefore just as adept at suppressing qubit noise as its qubit counterpart.

It is well-known that the finite-temperature lifetime of a two-dimensional quantum memory with local interactions only is upper-bounded by a constant independent of the system size, see e.g. Ref. [31]. Fig. 9.9 shows the lifetime of a logical qudit with logical operators X_1 and Z_1 subject to the thermal error model. We notice lifetimes that decrease to an asymptotic value for large L and considerable finite-size tails. These tails correspond to the regime in which the breakdown of error correction is not

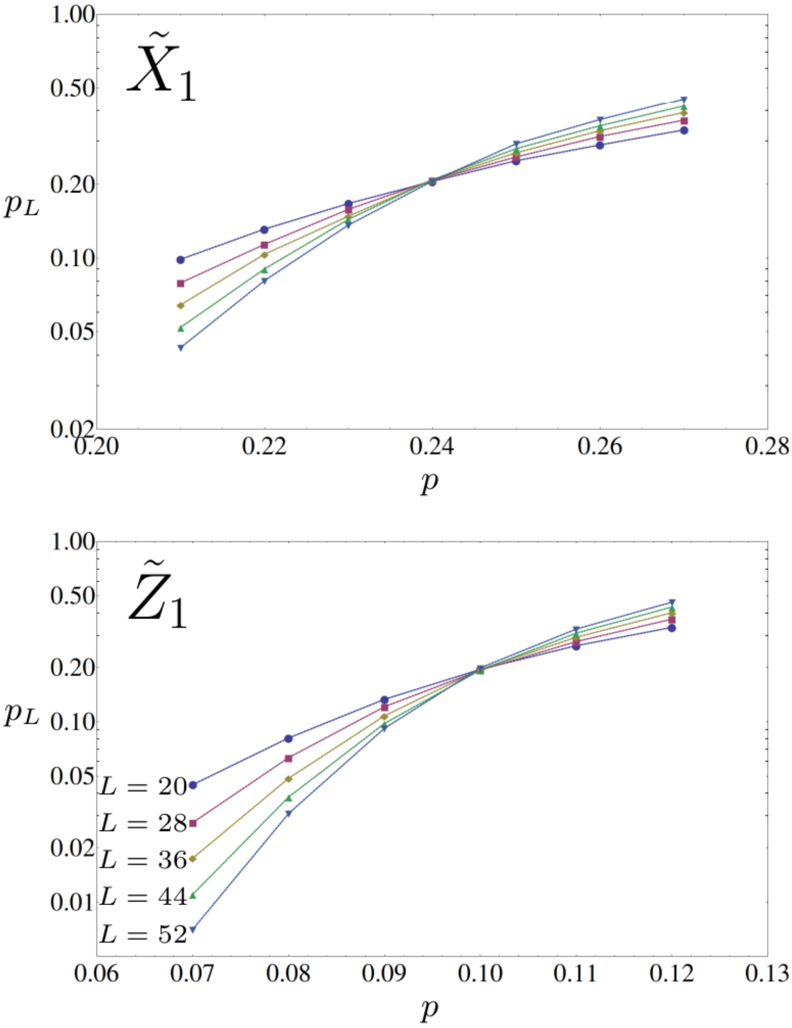

Figure 9.8: Error rates p_L of the logical operators $\tilde{X}_1$ and $\tilde{Z}_1$ illustrated in Fig. 9.2 as a function of the qubit depolarization rate p for code sizes $L = 20, 28, 36, 44, 52$. Each data point represents 10^4 logical errors, such that error bars are negligible. We recognize a threshold error rate $p_c \approx 24\%$ for $\tilde{X}_1$ and $p_c \approx 10\%$ for $\tilde{Z}_1$.

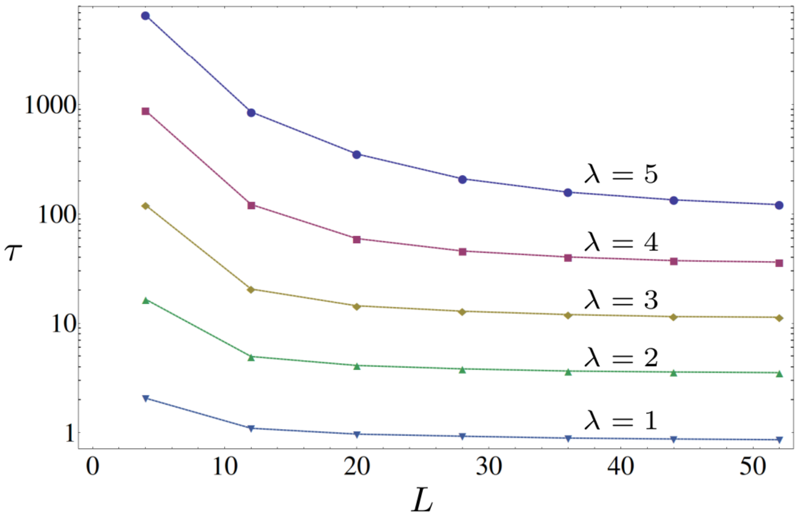

Figure 9.9: Average lifetimes τ of the logical qudit with logical operators $\tilde{X}_1$ and $\tilde{Z}_1$ as a function of code size L for $\lambda = 1, 2, 3, 4, 5$. Each data point represents 10^4 experiments. The lifetime is defined as the number of Metropolis steps until the first logical operator detects an error, divided by the number of spins in the code.

due to the density of anyons becoming so high that pairing them becomes ambiguous, but where the breakdown is caused by one of the first pairs wandering along a topologically non-trival path around the torus. The smaller the system, the longer it takes to produce an anyon pair, leading to the observed tails for small enough L and T (large enough λ).

With defects

When defect lines as in Fig. 9.4 are present, the error correction problem becomes more involved. It is no longer possible to correct the two anyon types (hexagons and triangles in our case) separately, as is usually done for the $D(\mathbb{Z}_n)$ models [135, 146, 157, 185]. Instead, error correction needs to take the possibility of converting between different anyon types into account. We thus pair all oddly-charge anyons of both types in a first round and all remaining charge 2 anyons of both types in a second round. Pairings can involve anyons which are of equal or of different type. The weight for connecting two anyons is defined as the minimal number of generalized Pauli operators needed to create a pair of anyons at their respective positions from the vacuum. For equal-type anyons, this will be an error string that crosses an even number of defect lines, while for different-type anyons this will be an error string that crosses an odd number of defect lines. This can mean, for instance, that connecting two equal-type anyons can have a large weight despite them being geometrically nearby, if there is a defect line between them.

For a code of linear size L in both dimensions, with periodic boundary conditions and L even, we choose defect lines involving $L/2+1$ qudits, as shown in Fig. 9.4 for $L = 20$. The logical operators $\tilde{X}_L$ and $\tilde{Z}_L$ then have a distance $L+2$ and $L/2+4$, respectively.

For the depolarizing error model, we find the threshold error rates p_c for both of the logical operators $\tilde{X}_L$ and $\tilde{Z}_L$ given in Fig. 9.4. The results are given in Fig. 9.10. For the defect operator $\tilde{X}_L$, we find a threshold error rate $p_c \approx 24\%$, as for the operators $\tilde{X}_1$ and $\tilde{X}_2$ in the defect-free case (Figs. 9.2 and 9.8), while for the defect operator $\tilde{Z}_L$ we find a threshold error rate $p_c \approx 10\%$, as for the operators $\tilde{Z}_1$ and $\tilde{Z}_2$ in the defect-free case.

The fact that these values coincide with the defect free case is not unexpected. The introduction of the defects essentially corresponds to a change in the boundary conditions. However, the vast majority of errors have large support within the bulk. The value of the threshold is therefore dominated by bulk effects rather than boundary effects.

Fig. 9.11 shows the average lifetime of the qudit stored in the synthetic topological degeneracy in Fig. 9.4 for the thermal error model. We note that for a given parameter λ, the asymptotic lifetimes ($L \to \infty$) are close to those in the defect-free case given in Fig. 9.9.

9.7 Conclusions

We have proposed a system which, on the physical level, involves only nearest-neighbor two-qubit interactions, allows one to perform all Clifford gates through quasi-particle braiding, and has a well-understood error correction problem.

We have greatly benefitted from the fact that our non-Abelian system is built on top of a system whose excitations correspond to an Abelian anyon model. This allows us to perform the logical operators X, Z, and Λ through quasi-particle braiding. It also makes our error correction problem manageable, despite some subtleties such as the fact that single-spin Pauli operators generate superpositions between different syndrome out-

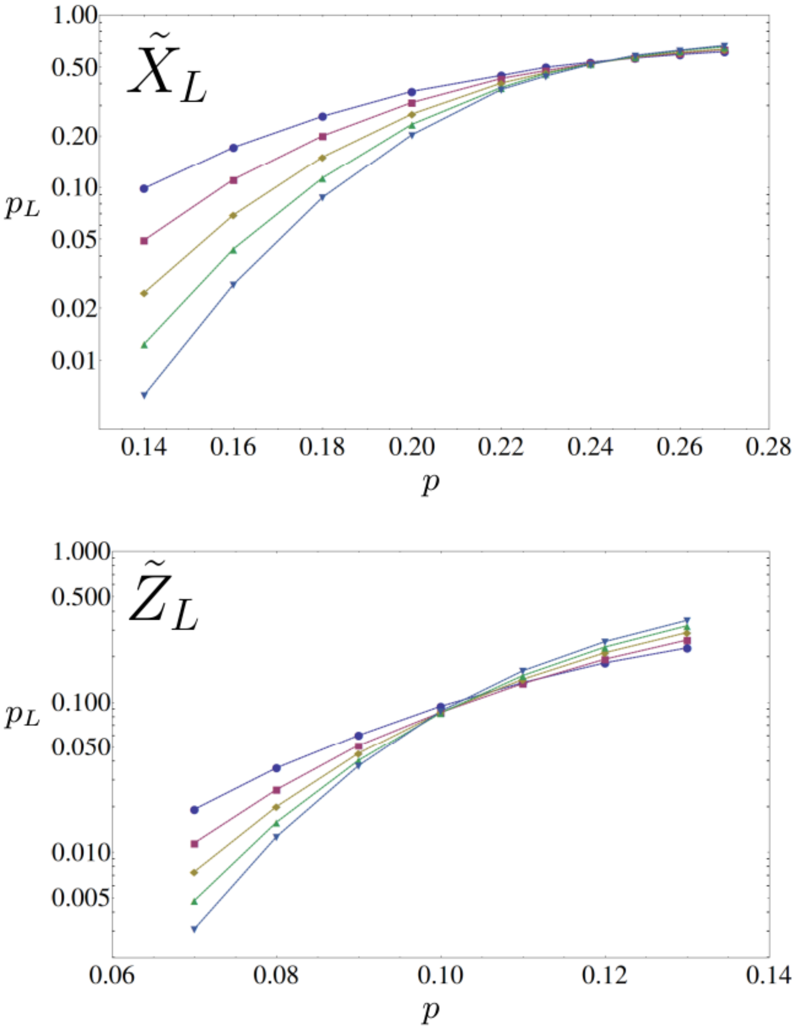

Figure 9.10: Error rates p_L of the logical operators $\tilde{X}_L$ and $\tilde{Z}_L$ illustrated in Fig. 9.4 as a function of the qubit depolarization rate p for code sizes $L = 20, 28, 36, 44, 52$. Each data point represents 10^4 logical errors, such that error bars are negligible. We recognize a threshold error rate $p_c \approx 24\%$ for $\tilde{X}_L$ and $p_c \approx 10\%$ for $\tilde{Z}_L$.

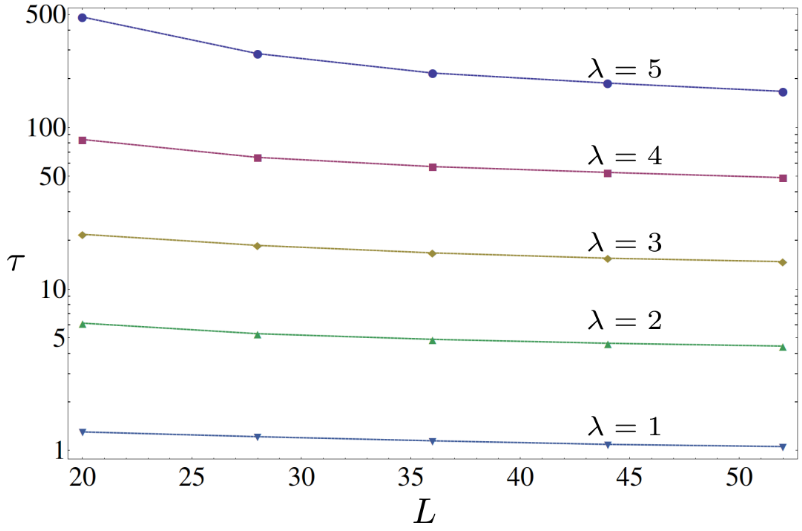

Figure 9.11: Average lifetimes τ of the logical qudit stored in the defect logical operators $\tilde{X}$ and $\tilde{Z}$ illustrated in Fig. 9.4 as a function of code size L for $\lambda = 1, 2, 3, 4, 5$. Each data point represents 10^4 experiments. The lifetime is defined as the number of Metropolis steps divided by the number of spins in the code.

comes and the ability to convert between different anyon species during error correction.

Universal quantum computation requires the ability to perform non-Clifford gates, such as "small-angle" unitaries. While it is not difficult to perform a non-Clifford operation by non-topological means in our system, this abandons fault-tolerance. The technique of magic state-distillation [46] is typically used to restore fault-tolerance. While research on magic state distillation has so far focused on prime qudit dimensions d [151, 152], qudit codes with the right transversality properties to perform magic state distillation in non-prime dimensions, including $d = 4$, also exist [200]. Unfortunately, for non-prime d it is not known whether Clifford gates plus an arbitrary non-Clifford gate are sufficient to achieve universality [201]. It is our hope that our work fuels interest in the $d = 4$ case, being a power of 2 and thus allowing to employ qubits, as demonstrated in our work, while being the smallest power of 2 that allows one to go beyond the Ising/Majorana case.

Alternatively, one could imagine energetically penalizing one of the degrees of freedom of a two-qubit Hilbert space to obtain a synthetic qutrit ($d = 3$). Magic state distillation for qutrits is well-studied [150], potentially allowing to perform fault-tolerant universal quantum computation with $\mathbb{Z}_3$ parafermions in a qubit system.[1]

The authors thank M. Barkeshli for elaborations on the development of the idea of generating non-Abelian defects in topological systems. This work was supported by the SNF, NCCR QSIT, and IARPA.

---

[1] This is indeed a route we have tentatively followed. Unfortunately, the Hamiltonians necessary to generate $D(\mathbb{Z}_3)$ quantum double models in a qubit system turned out to be much more involved than Eq. (9.4).

9.A Sixth-order degenerate perturbation theory

For our perturbation theory, we employ a Schrieffer-Wolff transformation [117], as formalized in Ref. [95].

Consider an unperturbed Hamiltonian H_0 whose spectrum can be separated into a low- and a high-energy subspace, which are energetically separated by a gap. Given a perturbation V, we want to find an effective Hamiltonian H_{eff} describing the "effective" physics on the low-energy subspace. The effective Hamiltonian can be developed in a perturbative series

$$H_{\text{eff}} = H_{\text{eff}}^{(0)} + H_{\text{eff}}^{(1)} + H_{\text{eff}}^{(2)} + \dots \tag{9.19}$$

in powers of some small expansion parameter.

Let P denote the projector onto the low-energy subspace and $Q = \mathbb{1} - P$ the projector onto the high-energy subspace. We define $V_{\text{d}} = PVP + QVQ$ and $V_{\text{od}} = V - V_{\text{d}} = PVQ + QVP$. For some operator A, we define the superoperator $\hat{A}$ via $\hat{A}(O) = [A, O]$. Let $H_0 = \sum_i E_i |i\rangle\langle i|$ be the spectral decomposition of H_0 and define the superoperator $\mathcal{L}$ via

$$\mathcal{L}(O) = \sum_{i,j} \frac{\langle i|QOP|j\rangle}{E_i - E_j} |i\rangle\langle j| - \text{H.c.}\,. \tag{9.20}$$

We employ the convention that unless indicated otherwise by use of brackets, a superoperator $\mathcal{L}$ acts on all operators to its right.

For the sixth-order effective Hamiltonian, one derives from Ref. [95] the expression

$$\begin{aligned} H_{\text{eff}}^{(6)} = {} & \frac{1}{2} P\hat{S}_5(V_{\text{od}})P \\ & - \frac{1}{24} P(\hat{S}_1^2\hat{S}_3 + \hat{S}_1\hat{S}_3\hat{S}_1 + \hat{S}_3\hat{S}_1^2 + \hat{S}_2^2\hat{S}_1 + \hat{S}_2\hat{S}_1\hat{S}_2 + \hat{S}_1\hat{S}_2^2)(V_{\text{od}})P \\ & + \frac{1}{240} P\hat{S}_1^5(V_{\text{od}})P\,, \end{aligned} \tag{9.21}$$

where

$$\begin{aligned}
S_1 &= \mathcal{L}(V_{\mathrm{od}}) \\
S_2 &= -\mathcal{L}\hat{V}_{\mathrm{d}}(S_1) \\
S_3 &= -\mathcal{L}\hat{V}_{\mathrm{d}}(S_2) + \frac{1}{3}\mathcal{L}\hat{S}_1^3(V_{\mathrm{od}}) \\
S_4 &= -\mathcal{L}\hat{V}_{\mathrm{d}}(S_3) + \frac{1}{3}\mathcal{L}(\hat{S}_1\hat{S}_2 + \hat{S}_2\hat{S}_1)(V_{\mathrm{od}}) \\
S_5 &= -\mathcal{L}\hat{V}_{\mathrm{d}}(S_4) + \frac{1}{3}(\hat{S}_2^2 + \hat{S}_1\hat{S}_3 + \hat{S}_3\hat{S}_1)(V_{\mathrm{od}}) \\
&\quad - \frac{1}{45}\mathcal{L}\hat{S}_1^4(V_{\mathrm{od}})\,.
\end{aligned} \tag{9.22}$$

In our case, the low-energy subspace onto which P projects is given by the space in which all triangle operators in Eq. (9.8) have minimal energy, i.e., $Z_aZ_bZ_c \equiv 1$ for all triangles (a, b, c). This subspace is fully degenerate. The lowest-energetic excitations change the eigenvalue of a stabilizer $Z_aZ_bZ_c$ from 1 to $\pm i$. Since the eigenvalue of $-(Z_aZ_bZ_c + \mathrm{H.c.})$ is thereby changed from -2 to 0, this has an energy cost $\Delta = 2J$. Note, however, that stabilizer eigenvalues can only be changed in pairs, such that the gap between the low-energetic (groundstate) subspace and the space of excited states is in fact given by 2Δ.

A crucial property of our Hamiltonian is that there is no lower-than-sixth-order perturbation that acts within the groundstate space. Therefore, we are only interested in terms of the form $PV_{\mathrm{od}}(V_{\mathrm{d}})^4V_{\mathrm{od}}P$, which allows to greatly simplify the effective Hamiltonian. Namely, only the first summand in all expressions in Eqs. (9.21) and (9.22) is relevant in our case. We find

$$H_{\mathrm{eff}}^{(6)} = \frac{1}{2}P\left[(\mathcal{L}\hat{V}_{\mathrm{d}})^4(\mathcal{L}V_{\mathrm{od}}), V_{\mathrm{od}}\right]P\,. \tag{9.23}$$

Using now that in our case $V_{\mathrm{d}}P = 0$, this can be further simplified to

$$\begin{aligned}
H_{\mathrm{eff}}^{(6)} &= \frac{1}{2}P\mathcal{L}\left(\mathcal{L}\left(\mathcal{L}\left(\mathcal{L}\left(\mathcal{L}\left(V_{\mathrm{od}}\right)V_{\mathrm{d}}\right)V_{\mathrm{d}}\right)V_{\mathrm{d}}\right)V_{\mathrm{d}}\right)V_{\mathrm{od}}P \\
&\quad - \frac{1}{2}PV_{\mathrm{od}}(\mathcal{L}V_{\mathrm{d}})^4(\mathcal{L}V_{\mathrm{od}})P \\
&= -PV_{\mathrm{od}}(\mathcal{L}V_{\mathrm{d}})^4(\mathcal{L}V_{\mathrm{od}})P\,.
\end{aligned} \tag{9.24}$$

There are $6! = 720$ possibilities for applying the six factors $X_rX_s^\dagger X_tX_u^\dagger X_vX_w^\dagger$ around one hexagon which leads the system back to the groundstate. Table 9.2 lists all possible routes the excitation energy above the groundstate can take, together with their numbers of possibilities.

$0 \to 2\Delta \to 2\Delta \to 2\Delta \to 2\Delta \to 2\Delta \to 0$	96
$0 \to 2\Delta \to 4\Delta \to 2\Delta \to 2\Delta \to 2\Delta \to 0$	48
$0 \to 2\Delta \to 2\Delta \to 4\Delta \to 2\Delta \to 2\Delta \to 0$	48
$0 \to 2\Delta \to 2\Delta \to 2\Delta \to 4\Delta \to 2\Delta \to 0$	48
$0 \to 2\Delta \to 4\Delta \to 4\Delta \to 2\Delta \to 2\Delta \to 0$	96
$0 \to 2\Delta \to 2\Delta \to 4\Delta \to 4\Delta \to 2\Delta \to 0$	96
$0 \to 2\Delta \to 4\Delta \to 4\Delta \to 4\Delta \to 2\Delta \to 0$	192
$0 \to 2\Delta \to 4\Delta \to 2\Delta \to 4\Delta \to 2\Delta \to 0$	24
$0 \to 2\Delta \to 4\Delta \to 6\Delta \to 4\Delta \to 2\Delta \to 0$	72

Table 9.2: Possible routes the excitation energy above the groundstate can take (left column), together with their respectiv multiplicities (right column). Note that the number of multiplicities adds up to $6! = 720$.

In conclusion, we find the sixth-order effective Hamiltonian

$$H_{\text{eff}} = -q\frac{h^6}{\Delta^5}(X_r X_s^\dagger X_t X_u^\dagger X_v X_w^\dagger + \text{H.c.}), \tag{9.25}$$

where the dimensionless prefactor

$$\begin{aligned} q &= \frac{96}{32} + \frac{48}{64} + \frac{48}{64} + \frac{48}{64} + \frac{96}{128} + \frac{96}{128} \\ &\quad + \frac{192}{256} + \frac{24}{128} + \frac{72}{384} \\ &= \frac{63}{8} \end{aligned} \tag{9.26}$$

is given by the multiplicities in Table 9.2, divided by the product of all excitation energies (in multiples of Δ) along the virtual process.

9.B Moving unpaired parafermion modes

To consider the creation and braiding of unpaired parafermionic modes, we must first decide on the double plaquettes with which we will work. Let us consider those of Fig. 9.12. To visualize the two parafermion modes within each double plaquette we use light blue circles. The one to the right of a double plaquette P is labelled P_1, and that to the left is P_2.

Parity operators for ψ modes are defined on pairs of parafermion modes. We are primarily concerned with two types of pairing: those

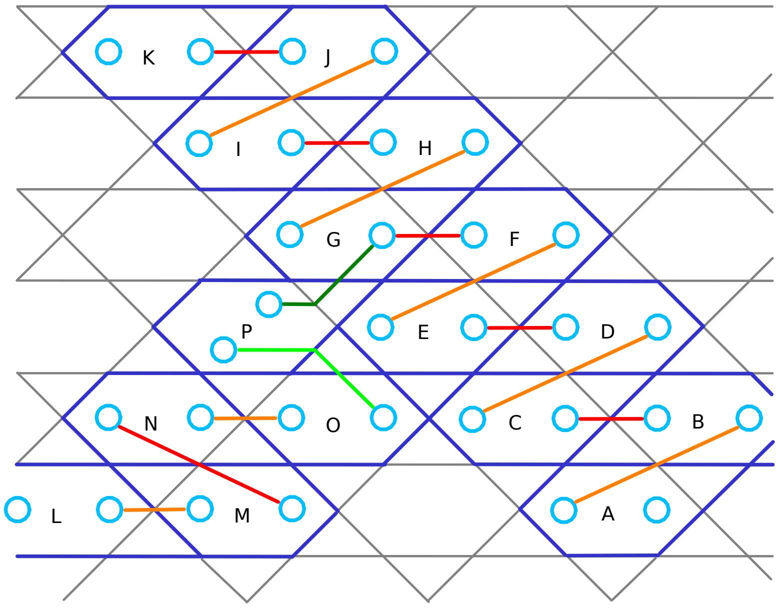

Figure 9.12: A selection of double plaquettes used in a braiding operation. Each double plaquette corresponds to two parafermion modes. For a double plaquette P, the parafermion to the right is labelled P_1, and that to the left is P_2.

of the two modes within the same double plaquette, and those of two modes from neighbouring double plaquettes. Relevant examples of the latter type are shown in Fig. 9.12 by red, orange and green lines connecting the corresponding modes.

For the two modes within each double plaquette, the parity operator $\omega^{5/2}\gamma_{P_1}\gamma^\dagger_{P_2}$ corresponds to the stabilizer S_P. The orange and red lines connecting modes P_2 to $(P+1)_1$ denote the parity operators $\omega^{5/2}\gamma_{P_2}\gamma^\dagger_{(P+1)_1}$. For orange lines, these correspond to the operator Y on the vertex through which the line passes. For red lines they correspond to the operator $X^\dagger Z$.

Consider a state initially within the stabilizer space. The parity operators for the pairs of parafermion modes within each double plaquette are therefore part of the stabilizer. The state therefore corresponds to this definite pairing of the modes.

Let us now consider the removal of the operator S_A from the set of stabilizer generators (while R_A remains). The corresponding parafermion modes are now, in some sense, unpaired. This contributes a factor of four to the ground space degeneracy.[2] However, due to the fact that the 'unpaired' parafermions are not well separated, it is not difficult for local perturbations to lift the degeneracy of this space. To become truly unpaired, and benefit from topological protection, they must be separated.

To do this, we can add a term $K(Y + Y^\dagger)$ to the Hamiltonian, which corresponds to the parity operator $\omega^{5/2}\gamma_{A_2}\gamma^\dagger_{B_1}$. This acts on the vertex through which the orange line connecting these modes passes.

For $K \gg J$, this new term will overwhelm the S_B term. The pairing of B_1 and B_2 will then be broken, and B_1 will become paired with A_2 instead. The unpaired mode originally at A_2 is therefore effectively moved to B_2. If the new term is introduced adiabatically, the degenerate subspace associated with the unpaired parafermion modes will remain in the same state during this process.

Similar processes can be used to move the unpaired modes further. The Hamiltonian term $K(X^\dagger Z + X^\dagger Z)$ corresponding to $\omega^{5/2}\gamma_{B_2}\gamma^\dagger_{A_1}$ can then be used to move the parafermion at B_2 to C_2, for example. Unpaired parafermion modes can therefore be separated by arbitrary distances, at the endpoints of lines on which single qudit terms are added to the Hamiltonian. In terms of qubits, these correspond to two-body interactions between qubits in the same site.

In order to unlock the potential of parafermions for quantum computation, it must be possible to braid the parafermion modes. Let us consider a specific example of this, using the system of Fig. 9.12. Consider an initial state within the stabilizer space of all S_P except A and L. At these two points, we have the unpaired parafermion modes A_1, A_2, L_1 and L_2. Let us now consider operations such as those described above to move A_1 and L_2 away, beyond the bottom of the figure. All four parafermion modes are then well separated, and so the ground state degeneracy is topological protected.

We will now consider the exchange of A_2 with L_1. We do this by first moving A_2 to K_2, then L_1 to A_2, and finally K_2 to L_1. The two modes have then swapped places. An exchange of opposite chirality would correspond to first moving L_1 to K_1, and so on. Note that all modes are kept well separated during the exchange, and so topological protection is always maintained.

During the exchange, the movement of the modes is mostly achieved using Hamiltonian terms that correspond to the red and orange pairings

---

[2] Note that, for closed boundary conditions, this added degeneracy does not arise for the first pair to be unpaired.

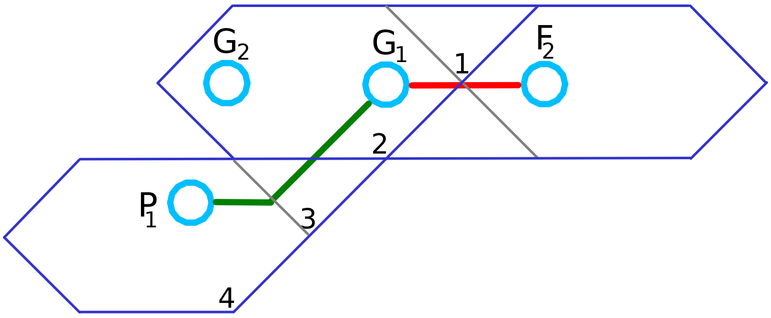

Figure 9.13: Double plaquettes used in the worked example of a single exchange.

in Fig. 9.12. These are all single qudit terms. At the junction, however, terms corresponding to the green pairings are used. We must therefore consider these in detail.

For the pairing show by the light green line, the parity operator is $\omega^{5/2}\gamma_{P_2}\gamma^\dagger_{O_1}$. This has the effect of creating an ψ_g, ψ_{-g} pair on the double plaquettes O and P. This requires the two qudit operator $X^\dagger_3 X_4 Z^\dagger_4$. For the dark green pairing, the $\omega^{5/2}\gamma_{P_1}\gamma^\dagger_{G_2}$ parity operator similarly requires the three qudit operator $\omega^{5/2}X_1 X^\dagger_2 Z_2 Z_3$. These terms correspond to four- and six-body quasi-local interactions on the corresponding qubits, respectively. They can be realized by standard methods of perturbative gadgets. However, note that they need only be implemented while an exchange is in progress.

9.C Exchange of two parafermion modes

To determine the effects of a single clockwise exchange we consider the smallest possible implementation. This involves the double plaquettes labelled F, G and P in Fig. 9.12, which are shown in more detail in Fig. 9.13. We consider a state in which the modes at P_1 and F_2 are unpaired, and those at G_1 and G_2 are paired by the Hamiltonian term S_G. Using this, we determine the effects of exchanging the unpaired modes. The method used to exchange the two modes is similar to previous methods proposed in order to perform anyon braiding [106, 190].

The results of the exchange are most easily understood in terms of the ψ mode formed by this pair. The parity operator, Γ for this mode is an operator that creates a ψ_1, ψ_{-1} pair and places them in double plaquettes P and F, respectively. Also it must have eigenvalues of the form ω^g, and so $\Gamma^4 = 1$. These conditions are satisfied by

$$\Gamma = \omega^{(1+2a)/2} Z_1 X_2^\dagger Z_2 Z_3. \tag{9.27}$$

We similarly require operations that can move parafermions between the relevant plaquettes. These correspond to the green line between G and P and the red line between F and G. These are

$$\Pi = \omega^{(1+2b)/2} X_1 X_2^\dagger Z_2 Z_3, \quad \Phi = \omega^{(1+2c)/2} X_1^\dagger Z_1, \tag{9.28}$$

respectively. In these relations a, b and c are all elements of $\mathbb{Z}_4$.

We have freedom in choosing the values $a, b, c \in \mathbb{Z}_4$ for these relations. The corresponding freedom also exists for all operators used to move parafermion modes, as well as the logical operators. The values used do not simply correspond to differences in a global phase. Instead they determine which eigenspace of these operators has eigenvalue $\omega^0 = 1$, and so which one corresponds to the vacuum occupancy ψ_0 of the ψ mode. These phases therefore cannot be chosen entirely arbitrarily, since the overall conservation constraint of ψ modes must be maintained. However, since here we do not explicitly consider the operations that placed unpaired parafermion modes at P_1 and F_2, we can assume that their phases are chosen in a way that maintains this conservation. We will therefore consider a free choice of a, b, and c.

The first step in exchanging the parafermions is to move the one at P_1 to G_2. This is done by adiabatically changing the Hamitonian to one in which the term $\Pi + \Pi^\dagger$ is present and stronger than S_G. This causes the modes at G_1 and P_1 to pair, moving the mode once at P_1 to G_2. The mode at F_2 is then moved to that at P_1 by adiabatically changing the Hamitonian to one in which the $\Phi + \Phi^\dagger$ term is present and stronger than S_G, and the $\Pi + \Pi^\dagger$ term is removed, pairing F_2 with G_1. The mode at G_2 is then moved to P_1 by adiabatically removing the $\Pi + \Pi^\dagger$ term and so allowing S_G to become dominant and G_1 and G_2 to pair. This process then results in the clockwise exchange of the modes.

The first step of this transformation takes a state that is initially in the ω^0 eigenspace of S_G and projects it to one in the ω^0 eigenspace of Π. The next step projects the state into the ω^0 eigenspace of Φ. The final step projects back into the ω^0 eigenspace of S_G. The end effect is then $P_G P_\Phi P_\Pi P_G$. Here P_G is the projector onto the ω^0 eigenspace of S_G, etc.

The rightmost P_G simply reflects the fact that the initial state lies within this eigenspace.

The parity operator Γ for the pair of unpaired modes commutes with S_G, and so can be mutually diagonalized with the above operator. We can therefore interpret its effects in terms of the phase factor assigned to each of the possible ψ_g eigenspaces of the ψ mode of the pair.

When doing this, different values of a, b, and c will result in different operations. This may seem to contradict the standard notion of a topological protected operation. However, these differences can be most easily understood by considering movement of parafermion modes implemented by measurement rather than adiabatic Hamiltonian manipulation. This method forces pairing of parafermion modes by measuring the occupancy of their corresponding ψ mode, and so forcing it to have a definite value. Ideally, this measurement will give the vacuum result ψ_0. The effect is then the same as the adiabatic manipulation. If a different ψ_g results, it must be removed by fusing it with the unpaired parafermion mode being moved. The different values used for the phases when moving unpaired modes, such as a, b and c here, determine how the measurement results are interpreted in terms of ψ anyons, and so determine the net ψ_g fused with the modes being moved. As such, differences in the conventions used for an exchange will change the resulting operation only by a factor of Γ^g, for some value of g that depends on a, b, and c.

For the standard convention used throughout this paper, with $a = b = c = 2$, the phase assigned to a ψ_g occupation by the exchange is $\omega^{g^2/2}\omega^{g(g+1)}$. These are indeed all square roots of ω^{g^2}, as predicted in the main text. However, they are not of the elegant form $\omega^{g^2/2}$ that would be more conducive for the proofs of Appendix 9.D.

For an exchange operation that does have the required form, consider $a = 1$ and $b = c = 2$. The phase assigned to ψ_g is $\omega^{-g^2/2}$ in this case, up to a global phase of $\omega^{1/2}$. The required phases $\omega^{g^2/2}$ would therefore be obtained from an anticlockwise exchange.

The fact that we obtain the phase $\omega^{-g^2/2}$ for a clockwise exchange in this case means we would get ω^{-g^2} for a full clockwise monodromy. This would seem to contradict the arguments of the main text, which predict a phase of ω^{g^2}. However, note that these phases differ only by a factor of $\omega^{2g^2} = \omega^{2g}$, and so are equivalent up to a factor of Γ^2. Since such factors are to be expected for different choices of a, b and c, this monodromy does not contradict our expectations.

Note that the arguments above do not assume anything about the initial state of the exchanged parafermions. Only their initial positions and the operations used to move them are required. The effect of the braiding is expressed in terms of Γ, the parity operator for their shared ψ mode, which can be defined for any pair of parafermions. It therefore does not matter what state the fusion space of the parafermions was initially in, and it does not matter whether or not they exist at the end of the same defect line. The effect of the braiding is the same in all cases.

9.D Generators of the Clifford group

For a tensor product of n d-level systems $(\mathbb{C}^d)^{\otimes n}$, the Pauli group $\mathcal{P}_d$ is defined as the group generated by the generalized Pauli operators X_i and Z_i, and the Clifford group $\mathcal{C}_d$ is defined as the normalizer of $\mathcal{P}_d$ in the unitary group on $(\mathbb{C}^d)^{\otimes n}$. That is, elements in $\mathcal{C}_d$ map tensor products of d-level Pauli operators to other such tensor products under conjugation.

We start with some general remarks on the action of $\mathcal{C}_d^{\otimes n}$ on $\mathcal{P}_d^{\otimes n}$ for $d = 4$. For $d = 4$, an operator $X^a Z^b$ has eigenvalues $\{1\}$ if $a = b = 0$, $\{1, -1\}$ if both a and b are even and at least one of them is non-zero, $\{i^{1/2}, i^{3/2}, i^{5/2}, i^{7/2}\}$ if both a and b are odd, and $\{1, i, -1, -i\}$ if $a+b$ is odd. Since the number of distinct eigenvalues is preserved under conjugation, this implies that the Pauli group $\mathcal{P}_d^{\otimes n}$ decays into distinct orbits when $\mathcal{C}_d^{\otimes n}$ acts on it by conjugation. This is in stark contrast to the case where d is an odd prime, which is studied in Ref. [194], where there is only one non-trivial orbit. The orbit containing the elements X_1, Z_1, …, X_n, Z_n consists of elements of the form

$$\omega^{k+p/2} Z_1^{a_1} X_1^{b_1} \dots Z_n^{a_n} X_n^{b_n}\,, \tag{9.29}$$

where $k, a_1, b_1, \dots, a_n, b_n \in \mathbb{Z}_4$, at least one of the exponents a_1, b_1, …, a_n, b_n is odd, and $p = \sum_{i=1}^n a_i b_i$ determines whether integer or half-integer powers of ω appear as phases (we sometimes write ω for i to avoid confusion with indices).

The following proof is an adaption of the proof in Appendix A of Ref. [194], where it is shown that a certain set of gates generate the Clifford group $\mathcal{C}_d^{\otimes n}$ for the case where d is an odd prime. The general structure of our proof is identical to the one in Ref. [194], while the generating set and individual lemmas and their proofs are different. After completion of this work, we became aware of the more general proof in Ref. [195].

Let us define the single-qudit unitaries

$$H = \frac{1}{2} \sum_{j,k=0}^{3} \omega^{jk} |j\rangle\langle k| \tag{9.30}$$

$$S = \sum_{j=0}^{3} \omega^{j^2/2} |j\rangle\langle j| \, , \tag{9.31}$$

and

$$\begin{aligned} T &= \frac{1}{2} e^{-i\pi/4} \sum_{j,k=0}^{3} e^{i\frac{\pi}{4}(j-k)^2} |j\rangle\langle k| \\ &= \frac{1}{2} \begin{pmatrix} \sqrt{i} & 1 & -\sqrt{i} & 1 \\ 1 & \sqrt{i} & 1 & -\sqrt{i} \\ -\sqrt{i} & 1 & \sqrt{i} & 1 \\ 1 & -\sqrt{i} & 1 & \sqrt{i} \end{pmatrix} . \end{aligned} \tag{9.32}$$

Lemma 1. *The gates $S^\dagger$, $T^\dagger$, $Z^\dagger$, X, $X^\dagger$, and $\sqrt{i}H$ can all be generated from S, T, and Z.*

Proof. As $S^8 = T^8 = \mathbb{1}$, we have $S^\dagger = S^7$ and $T^\dagger = T^7$. We have $\sqrt{i}H = STS = TST$ and $X = H^\dagger Z H = (\sqrt{i}H)^\dagger Z(\sqrt{i}H)$. Finally, $X^4 = Z^4 = \mathbb{1}$, so $X^\dagger = X^3$ and $Z^\dagger = Z^3$. □

If for some Clifford gate $U \in \mathcal{C}_d^{\otimes n}$ we have

$$U(Z_1^{a_1} X_1^{b_1} \ldots Z_n^{a_n} X_n^{b_n})U^\dagger = \alpha Z_1^{a_1'} X_1^{b_1'} \ldots Z_n^{a_n'} X_n^{b_n'} \, , \tag{9.33}$$

with $|\alpha| = 1$, we write

$$M(U)(a_1, b_1, \ldots, a_n, b_n)^T = (a_1', b_1', \ldots, a_n', b_n')^T \, . \tag{9.34}$$

The matrices $M(U) \in \mathbb{Z}_d^{2n\times 2n}$ form a representation of $\mathcal{C}_d^{\otimes n}$, as $M(UV) = M(U)M(V)$.

Lemma 2. *The gates S, T, and Z generate the entire single-qudit Clifford group $\mathcal{C}_4^{\otimes 1}$.*

Proof. For some $U \in \mathcal{C}_4^{\otimes 1}$, let $M(U) = \left(\begin{smallmatrix} a & c \\ b & d \end{smallmatrix}\right)$. Preserving the commutation relations of the single-qudit Pauli operators requires that $ad - bc = 1 \pmod 4$. One verifies that there are only 48 matrices M in the matrix ring $\mathbb{Z}_4^{2\times 2}$ satisfying the requirement $\det M = 1 \pmod 4$. We have $SXS^\dagger = \sqrt{\omega}XZ$ and $TZT^\dagger = \sqrt{\omega}ZX^\dagger$, such that $M(S) = \left(\begin{smallmatrix} 0 & 1 \\ 1 & 1 \end{smallmatrix}\right)$ and $M(T) = \left(\begin{smallmatrix} -1 & 1 \\ 1 & 0 \end{smallmatrix}\right)$. Once can verify by brute force that products of at most 9 factors $M(S)$ and $M(T)$ generate all of the aforementioned 48 matrices. Finally, since $XZX^\dagger = \bar{\omega}Z$ and $ZXZ^\dagger = \omega X$, we can generate arbitrary phases compatible with Eq. (9.29) (for $n = 1$). $\square$

We define the controlled Pauli-operators

$$C_X = \sum_{j=0}^{3} |j\rangle\langle j| \otimes X^j \tag{9.35}$$

and

$$C_Z = \sum_{j=0}^{3} |j\rangle\langle j| \otimes Z^j = \sum_{j,k=0}^{3} \omega^{jk} |j\rangle\langle j| \otimes |k\rangle\langle k| \,. \tag{9.36}$$

Note that C_Z has been called Λ in the main part of this work. We write $A \mapsto_U B$ as a shorthand for $UAU^\dagger = B$.

We have

$$\begin{aligned} Z_1 &\mapsto_{C_X} Z_1 \\ X_1 &\mapsto_{C_X} X_1X_2 \\ Z_2 &\mapsto_{C_X} Z_1^\dagger Z_2 \\ X_2 &\mapsto_{C_X} X_2 \end{aligned} \tag{9.37}$$

and

$$\begin{aligned} Z_1 &\mapsto_{C_Z} Z_1 \\ X_1 &\mapsto_{C_Z} X_1Z_2 \\ Z_2 &\mapsto_{C_Z} Z_2 \\ X_2 &\mapsto_{C_Z} Z_1X_2 \,, \end{aligned} \tag{9.38}$$

showing that $C_X, C_Z \in \mathcal{C}_4^{\otimes 2}$.

Lemma 3. *The gate C_X can be generated from S, T, and C_Z.*

Proof. We note that

$$HXH^\dagger = Z \qquad \text{and} \qquad HZH^\dagger = X^\dagger\,. \tag{9.39}$$

Thus

$$C_X = H_2^\dagger C_Z H_2 = (\sqrt{i}H_2)^\dagger C_Z(\sqrt{i}H_2)\,, \tag{9.40}$$

which together with Lemma 1 completes the proof. □

Let us define a more general controlled operator as

$$C_{st} = S_1^{-st}(C_X)^s(C_Z)^t\,. \tag{9.41}$$

It acts by conjugation as

$$\begin{aligned} &Z_1 \mapsto_{C_{st}} Z_1 \\ &X_1 \mapsto_{C_{st}} \omega^{st/2}X_1X_2^sZ_2^t \\ &Z_2 \mapsto_{C_{st}} Z_1^{-s}Z_2 \\ &X_2 \mapsto_{C_{st}} Z_1^tX_2\,. \end{aligned} \tag{9.42}$$

Up to the phase $\omega^{st/2}$, this action is identical to the one of the conditional Pauli gate $C_{X^sZ^t}$ studied in Ref. [194]. We point out again that such a phase is unavoidable for $\mathbb{Z}_4$, as there is, for instance, no unitary U such that $X_1 \mapsto_U X_1X_2Z_2$, since these two operators are not isospectral.

Let us define the SWAP gate $\mathcal{S}$ via $\mathcal{S}|j\rangle|k\rangle = |k\rangle|j\rangle$. Evidently, it acts as

$$X_1 \mapsto_{\mathcal{S}} X_2\,, \quad Z_1 \mapsto_{\mathcal{S}} Z_2\,, \quad X_2 \mapsto_{\mathcal{S}} X_1\,, \quad Z_2 \mapsto_{\mathcal{S}} Z_1\,. \tag{9.43}$$

The gate $\mathcal{S}$ thus allows to generate non-local entangling gates from nearest-neighbor ones.

Lemma 4. *The gate $i\mathcal{S}$ can be generated from S, T, and C_Z.*

Note that the gates $\mathcal{S}$ and $i\mathcal{S}$ act identically by conjugation.

Proof. Let

$$C_{X(1,2)} = \sum_{j=0}^{3} |j\rangle\langle j| \otimes X^j\,, \quad C_{X(2,1)} = \sum_{j=0}^{3} X^j \otimes |j\rangle\langle j|\,. \tag{9.44}$$

One verifies that

$$C_{X(1,2)}C^\dagger_{X(2,1)}C_{X(1,2)}(\sqrt{i}H_2)^2 = i\mathcal{S}\,, \tag{9.45}$$

which together with Lemmas 1 and 3 completes the proof. □

Let

$$\begin{aligned} P &= \alpha_P Z_1^{a_1} X_1^{b_1} \dots Z_n^{a_n} X_n^{b_n} \\ Q &= \alpha_Q Z_1^{c_1} X_1^{d_1} \dots Z_n^{c_n} X_n^{d_n} \,. \end{aligned} \tag{9.46}$$

All arithmetics involving the exponents a_j, b_j, c_j, and d_j that follow are to be understood modulo 4. It follows from the commutation relation $ZX = \omega XZ$ that $PQ = \omega^{(P,Q)} QP$ where

$$(P, Q) = \sum_{i=1}^{n} a_i d_i - b_i c_i \,. \tag{9.47}$$

Lemma 5. *Given $P, Q \in \mathcal{P}_4^{\otimes n}$ with $(P, Q) = 1$, we can generate $U \in \mathcal{C}_4^{\otimes n}$ from S, T, and nearest-neighbor C_Z such that*

$$\begin{aligned} P &\mapsto_U \alpha_P Z^{a'_1} X^{b'_1} \dots Z^{a'_n} X^{b'_b} \\ Q &\mapsto_U \alpha_Q Z^{c'_1} X^{d'_1} \dots Z^{c'_n} X^{d'_n} \,, \end{aligned} \tag{9.48}$$

with $|\alpha_P| = |\alpha_Q| = 1$, and there exists $j \in \{1, \dots, n\}$ such that $a'_j d'_j - b'_j c'_j = 1$.

Proof. Let P and Q be as in Eq. (9.46). Since

$$\sum_{i=1}^{n} a_i d_i - b_i c_i = 1 \tag{9.49}$$

by assumption, there exists j such that

$$r_j = a_j d_j - b_j c_j \in \{+1, -1\} \,. \tag{9.50}$$

If $r_j = 1$, we are done. If $r_j = -1$, then there is $k \neq j$ with $r_k = 2$ or $r_k = -1$. From Lemma 2, we know that from S_i and T_i we can generate single-qudit unitaries that change $\left(\begin{smallmatrix} a_i & c_i \\ b_i & d_i \end{smallmatrix}\right)$ in arbitrary ways as long as $r_i = a_i d_i - b_i c_i$ is preserved. So up to gates that can be generated from S_j and T_j, we can assume that $a_j = 0$, $b_j = c_j = 1$, and $d_j = 0$. If $r_k = 2$ then, up to gates that can be generated from S_k and T_k, we can assume that $a_k = 1$, $b_k = c_k = 0$, and $d_k = 2$. Finally, if $r_k = -1$ then, up to gates that can be generated from S_k and T_k, we can assume that $a_k = 1$, $b_k = 1$, $c_k = -1$, and $d_k = 2$. We note that application of a phase-gate $C_{Z(j,k)}$ changes r_j to $r'_j = r_j + (b_k d_j - b_j d_k)$, and recall that non-local phase gates $C_{Z(j,k)}$ can be generated from nearest-neighbor ones and SWAP gates, which we can generate according to Lemma 4. In both cases ($r_k = 2$ and $r_k = -1$), we find that application of a phase-gate $C_{Z(j,k)}$ gives $r'_j = 1$. $\square$

Lemma 6. *Given $P, Q \in \mathcal{P}_4^{\otimes n}$ with $(P, Q) = 1$, we can generate $U \in \mathcal{C}_4^{\otimes n}$ from S, T, and nearest-neighbor C_Z such that*

$$P \mapsto_U Z \otimes P' \qquad \textit{and} \qquad Q \mapsto_U X \otimes Q' \,, \tag{9.51}$$

with $P', Q' \in \mathcal{P}_4^{\otimes n-1}$.

Proof. Let P and Q be as in Eq. (9.46). By Lemma 5, we can assume that there is j with $a_j d_j - b_j c_j = 1$. Employing Lemma 4, we can perform a SWAP between qudits 1 and j. Finally, we perform a single-qudit unitary L on qudit 1 which is such that $M(L) = \left(\begin{smallmatrix} d_j & -c_j \\ -b_j & a_j \end{smallmatrix}\right)$. As $\det M(L) = 1$ (mod 4), such a unitary L can be constructed from S and T according to Lemma 2. We note that

$$Z^{a_j} X^{b_j} \mapsto_L \alpha_Z Z \qquad \text{and} \qquad Z^{c_j} X^{d_j} \mapsto_L \alpha_X X \,, \tag{9.52}$$

with $|\alpha_X| = |\alpha_Z| = 1$, which completes the proof. $\square$

Lemma 7. *For any $V \in \mathcal{C}_4^{\otimes n}$ we can construct U from S, T, Z, and nearest-neighbor C_Z such that $UX_1U^\dagger = VX_1V^\dagger$ and $UZ_1U^\dagger = VZ_1V^\dagger$.*

Proof. Clearly,

$$(VZ_1V^\dagger, VX_1V^\dagger) = (Z_1, X_1) = 1 \,, \tag{9.53}$$

so by Lemma 6, we can assume that $VX_1V^\dagger = X \otimes P'$ and $VZ_1V^\dagger = Z \otimes Q'$, up to gates that can be constructed from S, T, and nearest-neighbor C_Z.

Now let

$$\begin{aligned} P' &= \alpha_P Z_2^{a_2} X_2^{b_2} \dots Z_n^{a_n} X_n^{b_n} \\ Q' &= \alpha_Q Z_2^{c_2} X_2^{d_2} \dots Z_n^{c_n} X_n^{d_n} \,. \end{aligned} \tag{9.54}$$

We define

$$C_{st,i} = S_1^{-st} (C_{X(1,i)})^s (C_{Z(1,i)})^t \,, \tag{9.55}$$

with $i \in \{2, \dots, n\}$. The gate

$$U = (\sqrt{i} H_1) U_Q (\sqrt{i} H_1)^\dagger U_P \,, \tag{9.56}$$

with

$$U_P = \prod_{i=2}^{n} C_{b_n a_n, i} \quad \text{and} \quad U_Q = \prod_{i=2}^{n} C_{d_n c_n, i} \,, \tag{9.57}$$

can be constructed from S, T, and nearest-neighbor C_Z according to Lemmas 1, 3 and 4.

Using Eqs. (9.39) and (9.42), we find the sequences of mappings

$$\begin{aligned} X_1 &\mapsto_{U_P} X \otimes P' \mapsto_{(\sqrt{i}H_1)^\dagger} Z^\dagger \otimes P' \\ &\mapsto_{U_Q} Z^{-1-\sum_{i=2}^n (a_i d_i - b_i c_i)} \otimes P' \\ &\mapsto_{\sqrt{i}H_1} X^{1+\sum_{i=2}^n (a_i d_i - b_i c_i)} \otimes P' \,, \end{aligned} \tag{9.58}$$

and

$$Z_1 \mapsto_{U_P} Z_1 \mapsto_{(\sqrt{i}H_1)^\dagger} X_1 \mapsto_{U_Q} X \otimes Q' \mapsto_{\sqrt{i}H_1} Z \otimes Q' \,, \tag{9.59}$$

up to phases. Using again that $XZX^\dagger = \bar{\omega} Z$ and $ZXZ^\dagger = \omega X$, and that X can ge generated according to Lemma 1, allows us to generate arbitrary phases compatible with Eq. (9.29). Since

$$\begin{aligned} 1 &= (Z_1, X_1) = (VZ_1V^\dagger, VX_1V^\dagger) = (Z \otimes Q', X \otimes P') \\ &= 1 + \sum_{i=2}^{n} (a_i d_i - b_i c_i) \,, \end{aligned} \tag{9.60}$$

we finally conclude that

$$\begin{aligned} X_1 &\mapsto_U X \otimes P' = VX_1V^\dagger \\ Z_1 &\mapsto_U Z \otimes Q' = VZ_1V^\dagger \,, \end{aligned} \tag{9.61}$$

as required. □

Theorem 1. *Any Clifford gate $V \in \mathcal{C}_4^{\otimes n}$ can be constructed from S, T, Z, and nearest-neighbor C_Z.*

Proof. The proof is done by induction over n. The case $n = 1$ is given by Lemma 2. For $n > 1$, let U be as in Lemma 7. Since $U^\dagger V$ commutes with X_1 and Z_1, we have $U^\dagger V = \mathbb{1} \otimes V'$, where $V' \in \mathcal{C}_4^{\otimes n-1}$ acts on qudits $\{2, \ldots, n\}$. Assuming that the induction hypothesis holds for $n - 1$, V' and hence V can be constructed from S, T, and nearest-neighbor C_Z. □

9.E Defect lines and holes

Quantum computation in surface codes often uses the concept of 'hole' defects [44, 48, 196]. These are extended areas in which a single anyon can reside. Their large size makes it difficult to measure their anyon occupancy, and also to change it without leaving a trace nearby. This allows them to store an additional logical qubit in a topologically protected manner. The code distance is given by the size of the hole (for Z errors) and the distance to the nearest to its neighbour (for X errors), and so can be made arbitrarily large. They are primarily considered in systems without a background Hamiltonian, where they are created and moved using measurements [44, 48, 196]. However, they can also be created by adiabatic means when a Hamiltonian is present [197–199]. We now discuss this in detail for our system.

Enlarging and shrinking holes

The stabilizer is generated by the plaquette operators M_p and E_p for all triangular and hexagonal plaquettes. Let us consider, however, removing some of these operators from the stabilizer. In terms of the Hamiltonian, this means removing their corresponding terms.

Specifically, let us remove the plaquette operators E_p and E_q for two triangular plaquettes p and q. This will open up a new fourfold degeneracy in the stabilizer space. Corresponding Z basis states $|g\rangle$ can be labelled by the ω^g eigenstates of E_p. These states are therefore distinguished by the type of e_g anyon residing in the hole. Due to conservation of anyons, the antiparticle e_{-g} must reside in q. A further fourfold degeneracy will arise from each additional triangular plaquette removed from the plaquette. This is because only one removed plaquette, such as q, needs to have its occupation determined by the conservation of anyons.

For a logical qudit encoded in the additional stabilizer space, an X type operation corresponds to creating a particle/antiparticle pair of e anyons. One is placed on p and the other on q. The number of sites on which this process has support, and so the number of sites on which noise must act in order to cause a logical X error, is the distance between the two plaquettes. The qudit will therefore be topologically protected against such errors as long as the plaquettes are well separated.

The logical Z of the logical qubit corresponds exactly to the operator E_p, and E_q corresponds to $Z^\dagger$. Since these are three-body operators, this type of logical error requires action on only three qubit pairs. The stored qudit is therefore clearly not topologically protected against Z type errors.

To address this problem, we can deform the lattice by making the plaquettes p and q larger. By making them arbitrarily large, logical Z

errors can be arbitrarily suppressed.

To enlarge p, consider a neighbouring triangular plaquette p'. Let us use j to denote the single site shared by these. If the stored qudit holds an arbitrary state $|g\rangle$, the state of the code will be a ω^g eigenstate of E_p. It will also be an ω^g eigenstate of $E_pE_{p'}$, since the state is a $+1$ eigenstate of the stabilizer $E_{p'}$.

Consider the adiabatic introduction of the term $X_j + X_j^\dagger$ to the Hamiltonian. This term should be much stronger than the adjacent plaquette operators, and so will effectively force j into an eigenstate of X and remove it from the code. Since this term does not commute with E_p or $E_{p'}$, the resulting state will not be an eigenstate of these operators. However, the term does commute with the product $E_pE_{p'}$ since the support of the two plaquette operators on j cancels in this product. It therefore remains the same ω^g eigenstate as it was for the initial state. The qudit state $|g\rangle$ has therefore been effectively transferred from the single plaquette p to the combined plaquette pp'. The operator $E_pE_{p'}$ becomes the logical Z, and has support on four qubit pairs rather than three. This is further extended as more plaquettes are added using more $X_j + X_j^\dagger$ terms. As long as this is done for both p and q, the qudit will become topologically protected against Z errors as well as X.

The process used to extend holes can be reversed in order to shrink them. Consider a set of triangular plaquettes p, p', p'', ... that have been combined into a single hole. The basis state $|g\rangle$ of the qubit stored in this hole is associated with the ω^g eigenstate of $E_pE_{p'}E_{p''}\ldots$ We wish to shrink this hole so that p is no longer a part of it. The state will then have a $+1$ eigenvalue for E_p, and the qudit state $|g\rangle$ will be associated with the ω^g eigenstate of $E_{p'}E_{p''}\ldots$

To achieve this, recall that the combination of the plaquettes in the hole is is enforced by the strong $X_j + X_j^\dagger$ terms on their shared sites. To remove p from the hole, the term $E_p + E_p^\dagger$ should be added to the Hamiltonian, and the $X_j + X_j^\dagger$ term incident on p should be removed. Doing this adiabatically will result in a final state with the E_p term in its ground state, which is its $+1$ eigenspace. Due to conservation of anyon charge, the e_g anyon that was held in the larger hole must still be held in the smaller hole. The qudit state therefore remains $|g\rangle$.

As well as this being true for each basis state $|g\rangle$, we must also be sure that the process preserves coherent superpositions. Any process that causes decoherence in this basis will correspond to measurement (by the environment) in the Z basis. Any unitary that introduces unwanted relative phases can be expressed as a sum of powers of Z. As such, these processes must have support on all sites on which Z has support, which are all sites around the hole. Since the shrinking (and expansion) of holes does not have such support, it cannot cause any decoherence.

Corresponding processes can also be applied to hexagonal plaquettes. In that case, a logical qudit can be stored in the m_g occupations of plaquettes. Such qudits can be topologically protected by using lines of $Z_j + Z_j^\dagger$ terms to combine neighbouring horizontal plaquettes.

Using the processes of extending and shrinking holes, it is possible to move them. Gates can then be implemented through braiding. Braiding an e-type hole of triangular plaquettes in state $|g\rangle$ around an m-type hole of hexagonal ones in state $|h\rangle$ corresponds to braiding the e_g anyon held by the former around the m_h of the latter, yielding a phase ω^{gh}. This is a qudit generalization of the controlled phase gate.

Fusing holes into defect lines

By considering the alternative stabilizer generators S and R discussed in Sec. 9.4, holes can also be created which hold ψ_g anyons. These are formed by similarly combining the double plaquettes. Indeed, these are exactly the defect lines considered in the bulk of this paper. These have the property that anyons crossing the defect line undergo an automorphism that preserves the structure of the underlying Abelian state: it maps e anyons to their dual, the m anyons, and *vice versa*. This property is not shared by the e- and m-type holes. In these cases, the lines form a boundary along which one type of anyon can condense, but the other cannot cross. It is this difference that gives the ψ-holes additional properties, namely the localized parafermion modes at their endpoints, that the e- and m-holes do not possess. The topological degeneracy and protection, however, is a property shared by all three.

An e-type hole and an m-type hole together correspond to a two-qudit space. However, let us consider the subspace spanned by states $|g, g\rangle$. These are such that the e-type hole carries an e_g anyon whenever the m-type hole carries an m_g. A single qudit can be stored in this subspace

Since $\psi_g = e_g \times m_g$, two holes as described above hold a net ψ_g. Similar fusion can also be applied to holes, as we will now show. Specifically an e-type and an m-type hole can be combined into a ψ-type hole, and a ψ-type hole can be split into an e-type and m-type one.

These processes are in fact a simple generalization of the hole extension and shrinking processes described above. Suppose we have a defect line along double plaquettes P, P', P'', ... This stores a qudit whose basis states $|g\rangle$ are ω^g eigenstates of $W_P W_{P'} W_{P''} \dots$ Let us now extend this line. However, rather than adding another double plaquette, we instead add a triangular plaquette p. This can be done by adiabatically introducing the strong term $X_j + X_j^\dagger$ to the Hamiltonian on a site shared by p and the triangular part of P. This term does not commute with either E_p or W_P. However, it does commute with their product. The final state will then have the qudit basis states defined by the operator $E_p W_P W_{P'} W_{P''} \dots$. Further such processes can be used to extend the e-type part of the defect line. Corresponding processes on the hexagonal plaquettes can be used to grow an m-type part of the defect line. An illustration is given in Fig. 9.14.

When both e-type and m-type parts have been added, the original ψ-type defect line can be removed. This is done simply by removing the parity operator terms along its length and allowing the S_P terms to again dominate. The end result is that the ψ_g originally stored in the defect line now resides in the e-type hole as an e_g and the m-type hole as an m_g, corresponding to the state $|g, g\rangle$ of their individual qudits. As for the shrinking of holes, this process does not have sufficient support to distinguish between different basis states. The process therefore does not decohere any superpositions of these states, nor does it assign any relative phases.

To recombine the two holes into a single defect line, the process is simply reversed. This will be straightforward if the two holes are in a state of the form $|g, g\rangle$, since the state of the defect line will simply become $|g\rangle$. However some processes, such as mistakes during error correction, could result in holes whose states are not of this form. This will introduce frustration that will not allow all of the involved triangular and hexagonal plaquettes to return to their ground state after recombination.

As an example, consider a state of the form $|g, h\rangle$. This corresponds to an e_g and an m_h, and could arise from an initial state $|g, g\rangle$ if an m_{h-g} were added in error to the m-type hole, or from $|h, h\rangle$ with an e_{g-h} error on the e-type hole.

The anyons e_g and an m_h can combine either to a ψ_g and m_{h-g}, or a ψ_h and e_{g-h}. The former will be energetically favourable, due to the weaker strength of the M_p terms. The adiabatic process will therefore result in ψ_g being stored on the defect line and an m_{h-g} anyon present as an excitation on one of the triangular plaquettes that was once part of the holes. Syndrome measurement will then detect the m_{g-h}. However,

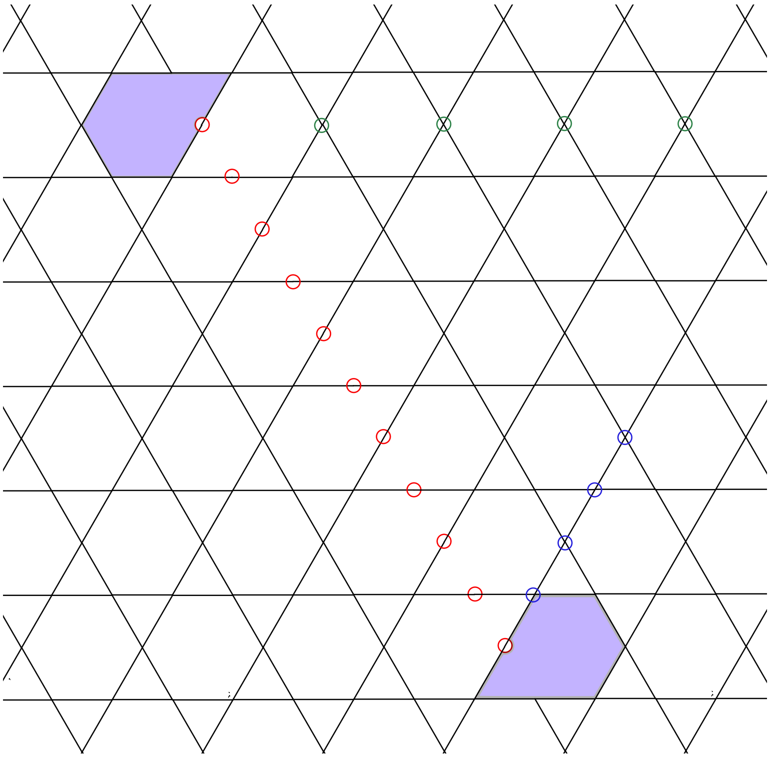

Figure 9.14: Red circles denote defects as in Eq. (9.13), with a pair of parafermions (purple) emerging at the ends of the defect line. Blue circles correspond to terms of the form $X_j + X_j^\dagger$, while green circles correspond to terms of the form $Z_j + Z_j^\dagger$. These grow the e- and m-part of the defect line, respectively. Once both the blue and green defect lines have been added, the red defect line can be removed. The ψ_g particle initially stored in the red defect line has then been split into its e_g and m_g components.

since the value $g-h$ gives information only about the error that occurred, and not the value of g or h, this does not extract any information about the stored qudit.

CHAPTER 10

Active Error Correction for Abelian and Non-Abelian Anyons

Adapted from:
James R. Wootton and Adrian Hutter
"Active error correction for Abelian and non-Abelian anyons",
ArXiv:1506.00524 (2015)

We consider a class of decoding algorithms that are applicable to error correction for both Abelian and non-Abelian anyons. This class includes multiple algorithms that have recently attracted attention, including the Bravyi-Haah RG decoder. They are applied to both the problem of single shot error correction (with perfect syndrome measurements) and that of active error correction (with noisy syndrome measurements). For Abelian models we provide a threshold proof in both cases, showing that there is a finite noise threshold under which errors can be arbitrarily suppressed when any decoder in this class is used. For non-Abelian models such a proof is found for the single shot case. The means by which decoding may be performed for active error correction of non-Abelian anyons is studied in detail. Differences with the Abelian case are discussed.

10.1 Introduction

The possibility of using anyonic quasiparticles for quantum computation has inspired a great deal of research [18]. This is due in part to the idea of 'topological protection', which promises inherent fault-tolerance for anyonic systems. Nevertheless, this protection still comes at a price. Without active error correction [148], or additional passive protection [31], the fault tolerance will fail after a system size independent lifetime [78, 148, 159]. Though one can hope to extend this through means such as lowering temperature, such an approach is not consistent with the scalability required for quantum computation. It is therefore important to study how error correction may be performed in anyonic systems.

For Abelian anyons the problem of error correction has been, and continues to be, studied in great detail [54, 146, 156, 185]. Many good decoding algorithms are known, and proofs that these allow exponential suppression of logical errors below a finite noise threshold have been found in multiple cases [62, 126]. For non-Abelian anyons, however, this study is in its infancy [148, 149, 185, 202]. The only case considered so far is a 'single shot' scenario. This assumes an initial burst of noise, with all measurements and manipulations performed perfectly thereafter. The more realistic problem of dealing with continuously occurring noise through active error correction has hardly been considered [148].

In this work we specifically consider a certain class of decoders. These can correspond to quite different methods, and yet have shared properties that allow them to be studied collectively. Examples of such decoders have recently been considered for multiple problems in Abelian and non-Abelian error correction [62, 145–149, 157, 185, 203] We provide a general proof of a finite noise threshold for these decoders, applicable to single shot error correction for Abelian and non-Abelian anyons, as well as active error for Abelian anyons.

For active error correction of non-Abelian anyons, we study the way in which syndrome measurements must be interpreted in order for the decoders to be applied. Differences between the Abelian and non-Abelian cases are found and discussed. Specifically, it is shown that these prevent the proof used for Abelian active correction from being adapted to the non-Abelian case.

10.2 Definitions

Code and Syndrome Lattice

The proof concerns error correcting codes defined on a two-dimensional lattice with quasilocal syndrome operators, such that their eigenspaces can be identified with anyonic occupations.

For concreteness we consider models based on a two-dimensional $L \times L$ lattice with periodic boundary conditions which we call the 'code lattice'. Anyons are associated with plaquettes, P, and the errors that affect a pair of neighbouring plaquettes are associated with the edge between them. The errors for each edge are assumed to act independently for analytical convenience.

A model of this form can be constructed for any anyon model. This framework may therefore be used to study general properties of anyonic decoding, when there is no need to specify the actual physical system used. They have especially been used to construct toy models for non-Abelian anyons. [149,202].

Error correction first requires the anyonic occupancy of the plaquettes to be measured. If the code is Abelian and the syndrome measurements are without noise, these results provide sufficient information for error correction to be performed. The input to the decoder in this case is therefore a two-dimensional syndrome composed of these measurement results. This is the single shot case for Abelian anyons.

For non-Abelian anyons the single shot case is more contrived. As well as perfect syndrome measurements, a lack of any noise while anyon fusions are performed must also be assumed. The problem therefore has little physical relevance, beyond providing a first glimpse into non-Abelian decoding. As for the Abelian case, the syndrome given to the decoder is two-dimensional [148,149,185,202].

When measurement results are noisy, a single measurement of each plaquette is no longer sufficient for good error correction. Instead, each syndrome operator must be measured periodically. Let us use T to denote the total number of measurement rounds. The measurement results at each time step can then be used to generate a three-dimensional syndrome, of size L in each spacial direction and T in the time direction.

Let us now construct a lattice on which the syndrome can be analyzed, which we call the 'syndrome lattice'. Consider the code lattice stacked upon itself T times to form a three-dimensional structure. We then define a set of points labelled (P, t) to lie directly between the copies of the plaquette P at timeslices t and $t+1$. These points are taken to be the vertices of the syndrome lattice. So-called 'time-like' edges are placed between each pair of vertices (P, t) and $(P, t+1)$. 'Space-like' edges are placed between each (P, t) and (P', t) for neighbouring plaquettes P and P'. This generalizes a well-known procedure for surface codes [57].

A syndrome value is assigned to each vertex of the syndrome lattice. These values reflect the difference between the measured anyon occupancy for the plaquette at these times. The exact details of how this is done depends on whether the anyons are Abelian or non-Abelian, and so will be specified in their respective sections.

Changes in anyon occupancy, as detected by this syndrome, are caused by errors. An error on the code between times t and $t+1$ that changes the anyon occupancies of P and P' is associated with the space-like edge between (P, t) and (P', t). A measurement error for a plaquette P during the round t is associated with the time-like edge between $(P, t-1)$ and (P, t).

We assume a toric or planar variant of the topological codes, for which logical information is stored within the degenerate vacuum states of the anyons. For this case, the code distance is L. Our results also apply to other means of storing logical information, such as holes [113], defects [163, 204] or using non-Abelian anyons themselves [18]. In these cases the code distance $L' < L$ reflects the distance between these structures. Our results apply straightforwardly to these cases, with the simple substitution $L \to L'$.

Code Lattice for Quantum Double Models

For concreteness let us consider the quantum double models [16], a specific class of topological codes based on explicit spin lattice models that can realize both Abelian and no-Abelian anyons. These models are based on a two-dimensional lattice, however, it does not correspond exactly to the code lattice as defined above. This is because syndrome operators are defined on both the vertices and the plaquettes.

For Abelian models, the set of anyons living on plaquettes and vertices are independent of one another in terms of their creation and fusion. They may therefore be decoded independently. One could therefore consider a two independent code lattices: one for which the plaquettes correspond to quantum double plaquettes, and one for which they correspond to quantum double vertices.

This property does not hold for general quantum double models, though. In the non-Abelian case, it is possible for plaquette anyons to fuse to vertex ones. They are therefore no longer independent. We must therefore reinterpret these models in order to find a code lattice in the simple form we desire.

Let us consider a quantum double model defined on a square lattice. A spin is associated with each edge of this lattice. To each plaquette, p, we assign the vertex v to its top right. This results in six spins around each combined (p, v). A hexagonal lattice can then be drawn such that these spins lie on the vertices. This will be used as the code lattice. Each combined (p, v) from the original lattice then corresponds to a single plaquette, P, in the code lattice. Each plaquette, P, has both kinds of stabilizer operator associated with it, and so can hold all possible kinds of anyon in the model. This lattice is shown in Fig. 10.1.

Note that each pair of neighbouring plaquettes, P and P', share two spins. For one of these, the only errors that would affect P and P' are those that affect flux anyons. For the other, only the errors for charge anyons affect P and P'. When using the code lattice, errors are associated with edges rather than vertices. These errors from different spins are therefore associated with the single edge that lies between P and P'. The independence of errors on each edge of the code lattice therefore requires not only that errors on each spin are independent of each other, but also independence of flux and charge errors on the same spin. We therefore assume such noise when considering quantum double models.

Clusters and Chunks

We use E to denote the set of errors that occur, including both spin and measurement errors. This is therefore a set of edges on the syndrome lattice. We use $S = S(E)$ to denote the corresponding set of non-trivial syndrome elements, which is a set of syndrome lattice vertices. Here $S(E)$ refers to 3D syndrome based on changes in measurement results, rather than the measured anyon occupancies themselves.

Any subset of the vertices of the syndrome lattice is called a cluster. Typically the clusters considered are those for which all vertices are occupied by an element of S. When this is not true, the cluster is called a vertex cluster.

Any subset of the edges of the syndrome lattice is called a chunk. We will only consider chunks made up of edges associated with an element of E. Chunks are therefore also subsets of E.

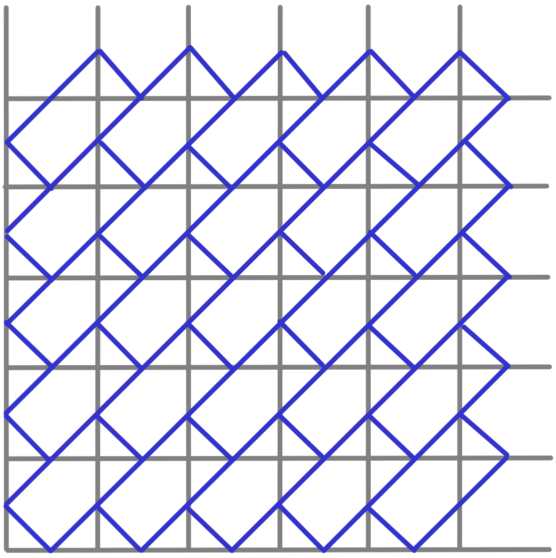

Figure 10.1: Square lattice on which a quantum double model is defined is shown in grey. The corresponding hexagonal code lattice is shown in blue. Spins are located on the edges of the former, and vertices of the latter.

The decoders we consider use the distance between non-trivial syndrome elements to determine how to best correct the errors that caused them. A sensible choice for the distance $d(k, k')$ between two vertices k and k' of the syndrome lattice is therefore the minimum number of edges required to connect them. This will be the metric that we primarily consider. However, any metric for which all distances are integers could also be used.

Two clusters, C and C', are said to overlap if there exists $k_1, k_2 \in C$ and a $k' \in C'$ such that $d(k_1, k') \leq d(k_1, k_2)$. The cluster C' is said to be inside C if the above is true for all $k' \in C'$.

The width of a cluster, C, is defined to be the distance between its extremal points,

$$W(C) = \max_{k,k' \in C} d(k, k'). \tag{10.1}$$

The distance between two overlapping clusters is defined to be zero. For non-overlapping clusters it is the distance between their closest points

$$d(C, C') = \min_{k \in C, k' \in C'} d(k, k'). \tag{10.2}$$

Note that this distance does not satisfy the triangle inequality. If clusters C and C' are separated by a finite distance, but both overlap with a cluster C'', then $d(C, C') > d(C, C'') + d(C'', C')$. This fact will not present a problem for the proof, but should be kept in mind.

To define widths and distances for a chunk ε, we consider the vertex cluster $C(\varepsilon)$ composed of all vertices adjacent to elements of the chunk. The width of the chunk is then defined to be the width of $C(\varepsilon)$. The distance between two chunks is the distance between their corresponding vertex clusters.

A cluster, C, is called neutral if there exists a chunk ϵ such that $C = C(\epsilon)$. Note that this ϵ need not be present in the actual error, E. The neutrality of C simple means that it is possible for it to have been created by some set of errors without otherwise affecting the syndrome. This means that it is also possible to correct the cluster independently of the rest of the syndrome. Finding neutral clusters is therefore an important part of decoding.

We call a chunk, ε, 'disconnected' if it generates its own syndrome cluster that does not depend on the rest of E, i.e.

$$S(E \setminus \varepsilon) \cup S(\varepsilon) = S, \quad S(E \setminus \varepsilon) \cap S(\varepsilon) = \emptyset. \tag{10.3}$$

A sufficient condition for this is clearly that the vertex clusters $C(\varepsilon)$ and $C(E \backslash \varepsilon)$ are disjoint, and so $d(\varepsilon, E \backslash \varepsilon) \geq 1$. Note that the syndrome cluster $S(\varepsilon)$ created by a disconnected chunk will be neutral by definition.

Error Model

To continue with our analysis, the error model must be specified. As stated earlier, we assume that the errors associated with each edge of the syndrome lattice occur with an independent probability distribution. This requires there to be no correlations between errors on different spins, and no correlations between charge and flux errors on each spin for quantum double models. However, it will be allowed for the error probability to depend on the occupancy of the two plaquettes adjacent each the spin. This occurs when there is an energy gap for anyon creation, for example.

For the measurement errors, we consider a model in which the measurement simply reports an incorrect value. This is the simplest model that allows us to study the nature of decoding when measurement errors are present, and is often used for benchmarking. More realistically one should consider all elements of the process, such as a quantum circuit, performing the measurements and include realistic errors in each.

However, since this will be very specific to each individual code, it is not compatible with our general approach.

We will quantify the strength of the noise using an upper bound on the probability that any kind of error will occur. Let us first consider this for the case of a charge error occurring on a spin during the time between two measurement rounds. Using j to denote a possible error type for a spin and k_P and $k_{P'}$ to denote the occupancies of the adjacent plaquettes, we define p_z to be

$$p_z = \max_{k_P, k_{P'}} \sum_j \mathrm{Prob}(j | k_P, k_{P'}). \tag{10.4}$$

It is therefore the total probability that an error of any kind will occur, for the anyon occupancies for which an error is most likely. The corresponding probability, p_x, for flux errors is defined in the same way. The maximum probability for any kind of error associated with any space-like edge of the syndrome lattice is then $p_s = p_x + p_z - p_x p_z$.

The probability for measurement errors, and hence time-like edges is

$$p_m = \max_k \sum_{j \neq k} \mathrm{Prob}(j|k). \tag{10.5}$$

Here j denotes a possible outcome reported by the measurement, and k denotes the true value. The probability p_m is therefore the total probability that the measurement reports any wrong value, for the true value for which an error is most likely.

We now combine this error rates into a single value $p = \max(p_s, p_m)$. This is an upper bound for the error probability for any kind of error event associated with any edge of the syndrome lattice.

Chunk decomposition

Let us now follow [62] by using the concept of level-n chunks. The definition of these depends upon a constant Q whose value can be chosen arbitrarily.

A level-0 chunk is defined to be a single error. A level-n chunk is a union of two disjoint level-$(n-1)$ chunks such that the width is at most Q^n. A level-n chunk therefore contains exactly 2^n errors.

We use E_n to denote the union of all possible level-n chunks. Note that this is not a disjoint union: the same errors could be involved in multiple possible level-n chunks. Clearly $E = E_0$, and

$$E_0 \supseteq E_1 \supseteq \ldots \supseteq E_m. \tag{10.6}$$

Here m is the highest level for which $E_m \neq \emptyset$, given the error E.

It is useful to reflect upon the meaning of the sets E_n. For the following two lists, 'within a distance' is used to mean 'such that the union has a width no greater than'.

- E_0 is the set of all errors.
- E_1 is the set of all errors within a distance Q of another.
- E_2 is the set of all errors within a distance Q of another for which there is another such pair within a distance Q^2.
- E_3 is the set of all errors within a distance Q of another, for which there is another such pair within a distance Q^2, for which there is another such quadruple with a distance Q^3.
- ...

Using the sets E_n, we define the sets $F_n = E_n \setminus E_{n+1}$. These are the errors that form part of E_n but not E_{n+1}, so

$$E = F_0 \cup F_1 \cup \ldots \cup F_m. \tag{10.7}$$

This is a disjoint union, which is called the 'chunk decomposition' of E. Again it is useful to reflect upon the meanings of these sets.

- F_0 is the set of all errors further than Q from any other.
- F_1 is the set of all errors for within a distance Q of another for which there is no other such pair within a distance Q^2.
- F_2 is the set of all errors for within a distance Q of another for which there is another such pair within a distance Q^2 but no other such quadruple within a distance Q^3.
- ...

10.3 Greedy HDRG decoders

Decoders based on greedy algorithms, in which syndrome elements attempt to neutralize themselves with near neighbours without considering the rest of the syndrome, will typically lead to a logical error rate that decays exponentially with L^β for $\beta < 1$. This is less than the optimal

$\beta = 1$ scaling, and is due to greedy algorithms being fooled by Cantor like error chains [145, 185]. However, such algorithms do typically have nice properties for analytical treatment. Specifically, any neutral cluster that is sufficiently far from the rest of the syndrome will typically be corrected independently of the rest.

Let us make this more rigorous. Decoders take a syndrome S as an input and yield a correction operator $E_c(S)$ as an output. A cluster C is called 'independent' if

$$E_c(S) = E_c(C) \times E_c(S \setminus C). \tag{10.8}$$

Note that here $E_c(S)$ is an operator acting on the Hilbert space of the code, and so the multiplication should be interpreted accordingly.

A disconnected chunk is similarly called independent if its syndrome cluster $S(\varepsilon)$ is independent. Note that since an independent cluster is disconnected by definition, and a disconnected cluster is neutral by definition, independent clusters will always be neutral.

Greedy HDRG decoders are then defined such that the following two properties hold.

Property 1. *For an independent chunk of width W, the width of the correction operator is no greater than $W + O(1)$.*

Property 2. *Any chunk ε of width W is independent as long as there is a distance of greater than $\lambda W/2$ from it to $E \setminus \varepsilon$. Here λ is a decoder dependent constant.*

Such decoders have recently been considered in References [62, 145, 146, 148, 149, 157, 185].

10.4 Threshold proof for greedy decoders

A decoder is only truly useful for fault-tolerance if there exists a threshold p_c such that the probability of a logical error vanishes for $p < p_c$ and $L \to \infty$. The nature of the decay with L is also important. Here we prove bounds for these for any decoder of the type described above. Here we formulate the proof in a way that can be applied to both the single shot and active error correction problems. The only difference is the dimension of the syndrome lattice, with $D = 2$ for the former case and $D = 3$ for the latter.

For the proof we require a value of Q such that the following holds true. For any $u \in F_n$, let ε denote the chunk composed of all errors no further than Q^n from u. For any $v \in E_n$ we then require that either:

- $v \in \varepsilon$;
- v is further than λQ^n from any element of ε.

A necessary and sufficient condition for the former is $d(u, v) \leq Q^n$. For the latter, the condition $d(u, v) > (\lambda + 1)Q^n$ is sufficient. We will define Q such that both of these will always hold.

Lemma 8. *For any $u \in F_n$ there is no $v \in E_n$ that satisfies*

$$Q^n < d(u, v) \leq (\lambda + 1)Q^n. \tag{10.9}$$

as long as $Q \geq \lambda + 3$.

Proof. Let us consider a pair of errors $u, v \in E_n$ that *do* satisfy Eq. 10.9. Since both errors are in E_n, both are contained within level-n chunks. Let us denote these C_u and C_v, respectively. Since chunks must have a width no greater than Q^n by definition, the condition that $d(u, v) > Q^n$ means that C_u and C_v must be disjoint chunks.

Despite the non-applicability of the triangle inequality, the width of the combined chunk $C_u \cup C_v$ will clearly satisfy

$$W(C_u \cup C_v) \leq W(C_u) + W(C_v) + d(u, v). \tag{10.10}$$

Again using the width restriction, as well as the condition that $d(u, v) \leq (\lambda + 1)Q^n$, we find

$$W(C_u \cup C_v) \leq 2Q^n + (\lambda + 1)Q^n. \tag{10.11}$$

The combined chunk will form a valid level-$(n + 1)$ chunk if its width is no greater than Q^{n+1}. Clearly this will be satisfied for all $Q \geq \lambda + 3$. Since both u and v will be contained within a level-$(n + 1)$ chunk in this case, neither will be an element of F_n. It therefore follows that, whenever either u or v is an element of F_n, Eq. 10.9 cannot hold.

□

With the chunk decomposition so defined, it can allow us to easily identify independent chunks of errors.

Lemma 9. *For any error u and the corresponding set F_n, let ε denote the chunk composed of all errors no further than Q^n from u. For $Q \geq \lambda + 3$, all such ε will be independent for any decoder that satisfies Property 2.*

Proof. Clearly the maximum width of any such chunk is $W \leq 2Q^n$. By Lemma 8 we know that such chunks are a distance of at least $\lambda Q^n \geq \lambda W/2$ from any other element of E_n. Any errors within this distance must therefore be elements the sets $E_{n'}$ for lower levels $n' < n$.

There are no lower levels than E_0, so let us proceed by induction. Any such ε based around a $u \in F_0$ will have no errors within a distance λW, and so will be independent for any decoder that satisfies Property 2. Since all errors in F_0 will be corrected independently, the decoder will treat the remaining errors in the same way as if the original error was $E \setminus F_0 = E_1$.

Similarly, none of the remaining errors E_1 will be within a distance $\lambda W/2$ of any ϵ based around a $u \in F_1$. All errors in F_1 are therefore also corrected independently, and the decoder act on the remaining errors as if the original error was $E \setminus F_0 \setminus F_1 = E_2$. Continuing this process, we find that all $\varepsilon(u)$ for $u \in F_n$ are independent chunks, as required.

□

The chunk decomposition therefore forms a decomposition of the errors into independently correctable chunks. This allows us to identify those errors that will cause the decoder to fail.

Lemma 10. *A necessary condition for a logical error is that the highest level in the chunk decomposition satisfies $m \geq \gamma \log(L/2)/\log(Q)$.*

Proof. By Property 1, any independent chunk is neutral and so can be corrected by a operator whose width is (essentially) no greater than that of the chunk. For an independent chunk to cause a logical error, its correction operator must have a width as large as L, the code distance. This requires independent chunks with width $W = 2Q^n \geq L$. The lowest value of m for which these can occur is $m \geq \log(L/2)/\log(Q)$, giving the required result. □

Now we can analyse the probability that a level-m chunk arises, for a given m. For this, consider the D-dimensional boxes Σ_n and Σ_n^+, centred on the same point. The former is sufficiently large to contain a chunk of width Q^n, and the latter can contain one of width $3Q^n$. Using these, consider the following events.

- $A_n : \Sigma_n$ contains at least part of a level-n chunk.
- $B_n : \Sigma_n^+$ contains a level-n chunk.
- $C_n : \Sigma_n^+$ contains a level-$(n-1)$ chunk.

Due to the width restriction on chunks, A_n is a sufficient condition for B_n. Their probabilities are therefore related by

$$P_{B_n} \geq P_{A_n}. \tag{10.12}$$

Note that B_n requires Σ_n^+ to contain two disjoint level-$(n-1)$ chunks. Two independent occurrences of event C_n are a necessary condition for this, so

$$P_{B_n} \leq P_{C_n}^2. \tag{10.13}$$

Note that Σ_n^+ is composed of $q = (3Q)^D$ disjoint boxes Σ_{n-1}. The event A_{n-1} on at least one Σ_{n-1} is therefore a necessary condition for the event C_n on Σ_n^+, and so

$$P_{C_n} \leq qP_{A_{n-1}}. \tag{10.14}$$

Putting this all together, we obtain the recursive relation

$$P_{A_n} \leq (qP_{A_{n-1}})^2. \tag{10.15}$$

The event P_{A_0} is that of a single error, which is upper bounded by p by definition. Repeatedly applying the recursive relation then allows us to express the probability of a level-m chunk in terms of p,

$$P_{A_m} \leq (q^2 p)^{2^m}. \tag{10.16}$$

For the single shot case, as well as that of active error correction when $T = L$, we consider a syndrome of size L^D. Since a chunk of size $m \geq \log(L/2)/\log(Q)$ is a necessary condition for a logical error, the logical error rate is upper bounded by,

$$P \leq \left[(3Q)^{2D} p\right]^{(L/2)^\beta}, \quad \beta \geq \frac{1}{\log_2 Q}. \tag{10.17}$$

Note that P decays exponentially in $(L/2)^\beta$ when

$$p < (3Q)^{-2D}. \tag{10.18}$$

This therefore gives a lower bound on the threshold, p_c, for this decoding problem and decoder.

For $T > L$, a necessary condition for a logical error is for a chunk of size $m \geq \log(L/2)/\log(Q)$ to intersect at least one of the (T/L) boxes of size $L \times L \times L$ that make up the $L \times L \times T$ syndrome. The probability for this will clearly share the exponential factor of Eq. 10.17. The same threshold applies therefore applies for arbitrary $T > L$.

The combined bounds are then

$$p_c \geq (3Q)^{-2D}, \;\; \beta \geq \frac{1}{\log_2 Q} \tag{10.19}$$

Note that the threshold and the exponent β both depend on Q.

10.5 Application to Abelian models

Let us now consider the specific case of a quantum double model is based on an Abelian group. The results of the syndrome measurements can therefore be interpreted in terms of Abelian anyons [16]. Any finite Abelian group is a product of cyclic groups Z_d. The resulting quantum double model is then the corresponding tensor product of the models based on each of these factors. As such we restrict to cyclic groups without loss of generality.

The way to analyse changes in the measured syndrome in order to perform active error correction is well known for these models [137,157, 185]. Nevertheless, we explain it here in detail.

We specifically consider error correction for the case in which the logical information is being stored in the code, and not manipulated. As such, though syndrome readout is being performed constantly, error correction can be delayed until readout.

The quantum double model $D(Z_n)$ has n^2 different species of anyons that can live in each of the plaquettes, P. These can be denoted $e_g m_h$ for $g, h \in Z_d$, and have the fusion rules

$$e_g m_h \times e_{g'} m_{h'} = e_{g+g'} m_{h+h'}. \tag{10.20}$$

Here addition is taken modulo n. The anyon $e_0 m_0$ is identified with the vacuum.

Without errors, the syndrome measurements would never change. As such, changes in the measurement results are signatures of errors. Such changes will not necessarily occur adjacent to every error. Instead, they are found at the endpoints of error chains. The type of error chain that can terminate at any syndrome change depends on the nature of the change.

In order to correct the errors we must consider what error chains are consistent with the syndrome measurements. We therefore need to determine exactly what syndrome changes have occurred, where they occurred and when. The details of the changes can then be placed on the three dimensional syndrome lattice (with two dimensions for space and one for time). If the outcome of the measurement of P at $t-1$ is $e_g m_h$, and that of the same plaquette at t is $e_{g'} m_{h'}$, the corresponding vertex (P, t) of the syndrome lattice is assigned the value $e_{g'-g} m_{h'-h}$. This gives the trivial value $e_0 m_0$ if the two results are the same, signalling that no error has been detected. Otherwise a non-trivial syndrome element is present at (P, t). We refer to these as 'defects'. Note the syndrome lattice of defects contains the same information as the list of all measurement results. However, it presents the information in a form that is more convenient for analysing error chains.

The first step towards determining a likely error chain for an Abelian model could be to choose defects that are likely joined by an error chain, and draw an error chain between them. Let us use $e_{g_1} m_{h_1}$ to denote the type of one of these defects, and $e_{g_2} m_{h_2}$ to denote that of the other. If

$$g_1 + g_2 = m_1 + m_2 = 0 \mod n, \tag{10.21}$$

this pair of defects can be said to be neutral. This means that no further error chains are required to explain this pair of syndrome changes. Otherwise the pair is non-neutral. In this case we can cease to regard the two points as being defects individually. Instead they collectively make up a single defect, along with the error chain that connects them. This must be connected with error chains to further defects in order to be resolved. Once such a cluster of syndrome changes, C, satisfies

$$\sum_j g_j = \sum_j h_j = 0 \mod n, \tag{10.22}$$

where $e_{g_j} m_{h_j}$ is the syndrome value for each $j \in C$, it can be said to be neutral. The set of error chains connecting the syndrome changes is then sufficient to explain their presence without being dependent on any other part of the syndrome.

Correction of a neutral cluster is done by moving its defects together. These obey the same fusion rules as the anyons, and so the effect of moving all the defects together is to annihilate them. Moving a defect along a time-like interval implies that the measurement results along the interval were incorrect. The movement is done by correcting the results by changing their values. Moving along a space-like interval implies that errors occurred on the spins along the interval, and is done by applying the inverse of the corresponding errors. In both cases the required operations are applied to edges of the syndrome lattice.

Note that the defects created by a chunk ε are always inside $C(\varepsilon)$. The movement of defects by a decoder can always be implemented such that they always remain inside $C(\varepsilon)$. As such, we can always assume that the decoder satisfies Property 1.

Bravyi-Haah and ABCB Decoders

The Bravyi-Haah decoder [62, 157] runs an iterative process to find neutral clusters. In the nth iteration, all defects within a distance 2^n of each other are placed in the same cluster. Neutral clusters are then identified and removed from the syndrome. If defects remain, the process is repeated for $n+1$.

The minimum n required to cover an independent chunk ε of width W is $n = \lceil \log_2 W \rceil$. In order for no defects from $E \setminus \varepsilon$ to be included within the same cluster, they must be more than a distance 2^n away.

Note that the same n covers distances from $2^{n-1}+1$ to 2^n. The minimum W that requires a distance of 2^n to other chunks is therefore $2^{n-1}+1$. This means that a chunk of width W requires a distance of greater than $2(W-1)$ to be independent. This decoder is therefore a greedy HDRG decoder with $\lambda = 4$.

The ABCB decoder [146] is based on the same principle as that above. However, the distance used for iteration n is simply n rather than 2^n. As such $\lambda = 2$ for this decoder.

Expanding Diamonds

The expanding diamonds decoder [145,205] is based on a similar iterative process to the above. Initially, the syndrome is decomposed into clusters such that each defect corresponds to its own cluster. During iteration n, each cluster checks whether another exists at a distance n away. If so, the clusters can be paired. Each pair is removed from the syndrome if neutral. Once no more pairs are possible for the distance n, the distance $n+1$ is considered.

The largest distance required for all defects within an independent cluster to see each other is its width. In order for none to see any defects outside the independent cluster before they become neutral, the distance to other defects simply needs to be greater than this. As such $\lambda = 2$ for this decoder.

MWM based decoder

This decoder is based on the graph theoretic problem of finding matchings [185]. Though it is an HDRG decoder, it is not greedy in general. Instead it uses techniques that perform optimzation of the correction operator over long ranges.

One such technique is the use of 'shortcuts'. These are modifications made to the distances between clusters when any neutral cluster is removed. It is a modification that is also possible for the above decoders, and has been found to allow better decoding [145,185]. However, for the applicability of the proof, we consider this decoder without the use of shortcuts.

This decoder uses a tunable parameter, Λ, that can vary between 0 and 1. For any given code, system size and noise model, Λ can be set at whatever value gives the best results. Proving a threshold for any value of Λ therefore proves it also for the decoder in general. The decoder can only be regarded as greedy for $\Lambda = 0$, and so we focus on this.

For the case of $\Lambda = 0$, this decoder works in a similar way to expanding diamonds, building clusters by pairing existing clusters. Clusters are only ever paired when they are mutual nearest neighbours, i.e. neither has a neighbour closer than the other.

This means that, like expanding diamonds, the largest distance required for all defects within an independent cluster to see each other is its width. In order for none to see any defects outside the independent cluster before they become neutral, the distance to other defects simply needs to be greater than this. As such $\lambda = 2$ for this decoder.

10.6 Application to non-Abelian models

We now consider models for which the syndrome can be interpreted in terms of non-Abelian anyons, such as quantum double models based on a non-Abelian group [16].

Single shot error correction

Single shot error correction of non-Abelian anyons has previously been studied numerically [148,149,185,202]. These studies provided evidence of a finite threshold, but no formal proof has yet been presented. However, such a proof follows immediately from the discussions of the Abelian case above.

In the single shot case, errors create an anyon configuration. To correct a chunk, the anyons it creates simply need to be fused to annihilate them. In general, moving a non-Abelian anyon requires a controlled operation on all the spins on which its syndrome operator has support. The size of the correction operation will therefore be slightly bigger for the non-Abelian case than the Abelian one to account for this. Specifically, moving the anyons generated by a chunk of width W together requires a correction operator of width at most $W+2$. Greedy HDRG decoders will therefore certainly satisfy Property 1 for this case.

Decoders will also satisfy Property 2 for the single shot non-Abelian case in exactly the same way as for the Abelian. As long as the anyons within each chunk see each other before they see those of other chunks, they will mutually annihilate without affecting or being affected by the anyons of other chunks.

The non-trivial braiding of the non-Abelian anyons will not have any effect on either property. This can be simply seen by the same induction as in Lemma 9. Chunks centred around elements of F_0 are spatially separated from all others, and so the anyons created by such chunks will not have braided around those of others. Nor will the correction operator that fuses the anyons cause such braiding. The anyons for such such chunks will therefore still annihilate, even if the braiding causes changes in intermediate fusion results. Chunks centred around elements of F_1 will similarly remain independent of all remaining errors, and so on for higher levels.

Single shot non-Abelian decoding can therefore be performed by the decoders discussed above, and will have the same values of λ. The decoding will lead to the threshold noise rates of Eq. (10.19).

Syndrome for active error correction

Though there may be many types of anyon possible in any given anyon model, from henceforth we will not distinguish between them for the sake of simplicity. We are therefore only concerned with whether each position in the code is occupied or unoccupied by an anyon according to the measurement results. For the Fibonacci model, in which there is only one non-trivial anyon type, this is the most detailed case possible.

For codes with Abelian anyons, decoding can be postponed until final readout. Furthermore, errors can be corrected effectively by a basis change for the affected spins. This removes the need to physically apply correction operators. Unfortunately, non-Abelian codes share neither of these useful traits. Measurement of anyon occupation alone does not extract sufficient information for good decoding. Fusion of the anyons must also be performed continuously through the process [148]. These attempted operations performed by the decoder must therefore be taken into account when interpreting the measurement results. Note also that this action will, in general, lead to higher error rates on the spins involved in the anyon transport. However, this can simply be incorporated into the maximum error rate p_s for spins.

Using the measurement results we must construct the syndrome, which will be used as an input for the decoder. For the Abelian case, this was done by assigning a defect to the syndrome lattice wherever there is a change in this measured syndrome. This is because such points are necessarily the endpoints of error chains, and so can be used to determine a likely set of errors that could have caused the measured syndrome. The defects, and hence the anyons, are then removed using this as a guide. The same approach should be taken for the non-Abelian case: points that are necessarily the endpoints of error chains must be identified, and used to remove the anyons.

For the non-Abelian case, it is not true that the measurement result for a given plaquette will only change due to errors. Since the decoder needs to move anyons in order to fuse them, some changes will be expected. For example, if an anyon was measured at $(P, t-1)$ and then moved, it would be expected that no anyon would be measured at (P, t). In fact, it would be unexpected if an anyon was measured at (P, t), and so a lack of change would be the signature of an error in this case. The measurement results at $t-1$, along with the set of movements attempted by the decoder between $t-1$ and t, should then be used to determine the expected set of measurement results at t. Any point at which the measurement results at t differ from this are a signature of an error, and so should be associated with a defect.

A plaquette P is expected to be empty if it was empty at $t-1$ and no anyon was moved to it, or if it held an anyon at $t-1$ but it was moved away. It is expected to be full if it held an anyon at $t-1$ but no attempt was made to move it, or if it was empty and a single anyon was moved to it. There are two remaining cases, both of which correspond to fusion of anyons: at least one anyon is moved onto a plaquette holding another, or several are moved onto the same plaquette. In these cases there is no expectation either way, since either result could be due to fusion rather than the effects of adjacent errors. As such, no defect will be assigned to such a (P, t).

If no attempts to move the anyons are ever made, a plaquette P will be measured to hold an anyon from the time t at which it was unexpectedly measured for the first time, and the time t' at which it unexpectedly disappeared. A defect will be assigned to both (P, t) and (P, t'), since these are necessarily endpoints of error chains. However, note that error chains for the non-Abelian case can terminate anywhere there is an anyon. Such errors chains will not necessarily change the anyon occupancy, and so cannot always be detected by a defect. The 'world line' between the defects at (P, t) and (P, t') should therefore also be included in the syndrome given to the decoder. If an anyon is still present at the most recent time slice, the world lines will terminate on these present time anyons rather than defects.

When attempts to move anyons are made, the corresponding world lines should be dragged along with the intended movements. These will combine at fusion events, creating larger 'world nets'.

The decoder must find a set of errors that could explain the configuration of defects on the syndrome lattice. In order to do this, error chains can be proposed which connect each defect to another point at which an error chain can end: another defect, a present time anyon or a net.

Any valid error chain corresponds to a proposal for how the missing portions of anyon world nets (corresponding to creation, movement, etc) should be filled in. Once such a chain has been proposed, the corresponding portion can then be added to the world net, and the related defects can be removed from the syndrome lattice. When the error chain connects a defect to a present time anyon, this anyon should also be removed from the syndrome. This is because such an error chain proposes that these apparent anyons are in fact due to measurement errors.

When proposing error chains, one must be careful to determine whether the resulting error net will have portions that are connected to the rest only by a single time-like world line. Such structures would imply that an anyon has been created from vacuum, violating their conservation laws. Such structures must therefore be avoided.

Note that the above is not necessarily true if some part of the structure braids around another world net. This is due to the effects of braiding non-Abelian anyons. However, even in this case, an error chain directly connecting the two nets would correspond to a simpler error, and so could be considered instead. Otherwise, two nets that are braided should be considered to be a single net, just as if they had been connected by an error chain.

When a world net does not contain defects, its neutrality can be considered. If the net contains no present time anyons, the proposed error chain is sufficient to explain the observed defects without otherwise affecting the syndrome. Such a net may therefore be considered to be neutral. If it terminates in multiple present time anyons, it could be that fusion of these will lead to annihilation, and hence neutrality. These anyons should therefore be moved together by the decoder to determine whether this is indeed the case. If the net terminates in a single present time anyon, at least one further error chain is required to explain the presence of this anyon. Such world nets are therefore not neutral, and should be considered to be defects themselves. Note that these defects can be paired with their own present time anyon, reflecting the possibility of a chain of measurement errors between the time of fusion and the present time, as well as being paired with other defects, nets or present time anyons.

For an error chain connecting a defect with a present time anyon, the removal of the defect from the syndrome should not be considered permanent. This is because further timeslices might show that this proposed error chain was, in fact, unlikely. Any such defects should be reinstated after the movement performed at each timeslice, along with the rest of their net.

Decoding for active error correction

The syndrome for non-Abelian anyon models above is largely the same as that for Abelian ones. The main difference is the need to consider world lines at which error chains can end in an undetected manner. This difference does not prevent the greedy HDRG decoders discussed above from being straightforwardly applied to the non-Abelian case. As such, one might expect that the threshold proof straightforwardly applies also.

Unfortunately, this is not the case. The differences between the Abelian and non-Abelian decoding problems prevent any decoder from satisfying Property 2, even in general. This prevents the application of the proof, and demonstrates a significant difference between the decoding of Abelian and non-Abelian models.

To see why Property 2 does not hold, consider a chain of spin errors of length l, which create a pair of anyons located at the endpoints. Annihilating these requires moving them together. Assuming that each anyon can only be moved to a neighbouring plaquette in each time step, this means that the anyons will still be present for at least a time $l/2$ after their creation. If a single error occurs adjacent to one, it can cause it to move. This error is therefore certainly not independent of the string. However, the width of the single error is $W = 1$, and the distance from it to any other error is can be up to $l/2$. Its lack of independence therefore implies $l/2 < \lambda/2$ for any $l = \Theta(L)$. As such $\lambda = \Theta(L)$, which contradicts Property 2.

To remove this effect, one could assume that a non-Abelian decoder can move anyons arbitrarily far in each time step. Though an unphysical assumption, it could be used to make progress towards a threshold proof. Unfortunately, even this is not enough. Consider again the above chain of errors. If measurement errors are as likely as spin ones, until a time $l/2$ has passed it is more likely that the anyons are a result of measurement errors than the chain of l spin errors. Proposed error chains will therefore pair them with their present time anyons, and so they will not be moved. They will therefore still present for at least a time $l/2$ after their creation, and so the above arguments apply even when anyons can be moved arbitrarily quickly.

Note that these issues do not imply a lack of threshold for error correction of non-Abelian anyons. Instead it simply shows that chunks that would be independent in Abelian codes can still interact with each other if the code is non-Abelian. However, this still requires them to be sufficiently close. A logical error would therefore require a collection of chunks that would cause these effects to percolate across the lattice. This percolation is likely to be highly suppressed for low enough p, and so a threshold proof for the non-Abelian case is likely to be possible. However, such a proof of the threshold theorem for non-Abelian anyons is yet to be found.

10.7 Conclusions

Here we have provided a very general threshold proof, applicable to both Abelian and non-Abelian decoding problems for general anyon models. The proof also applies to a general class of decoders. However, the threshold theorem for active error correction of non-Abelian anyons still remains to be proven. We have made contributions in this direction, by studying how active error correction may be performed in this case. Numerical and analytical verification of a threshold, either for general models and decoders or for specific cases, is left to future work.

10.8 Acknowledgements

JRW would like to thank Fern Watson for discussions of the proof in [62]. The authors acknowledge the SNF and QSIT for support.

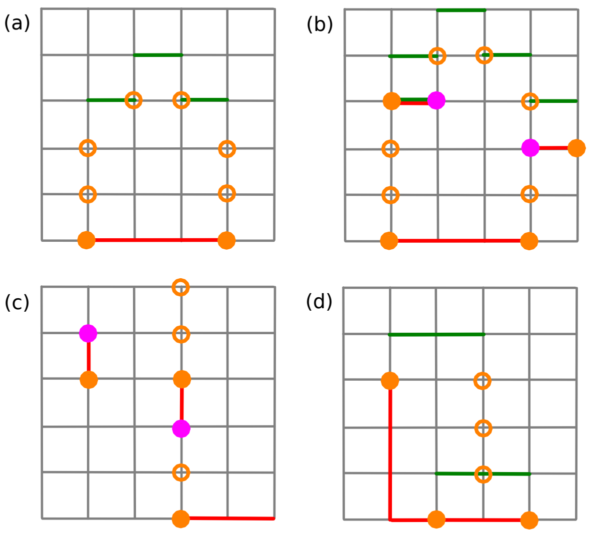

Figure 10.2: Examples of errors, and how these may be dealt with by a decoder. Here only a one dimensional slice of the spatial plane is considered, represented horizontally. Time corresponds to the vertical direction, with time flowing in the upwards direction. Points at which anyons are measured are denoted by orange circles. These are filled if the anyon is unexpected, and so correspond to a defect. Points at which no anyon was measured when one was expected, another defect, are denoted by pink circles. Red lines denote errors (horizontal for spin and vertical for measurement) while green lines denote attempted anyon movement by the decoder. (a) A chain of three spin errors creates a pair of anyons. For a few time steps it is most likely that the anyons are simply due to measurement errors. After this they are most likely to have been created in a pair, and so are moved towards each other until annihilation. (b) Same as before, except that an additional spin error moves the right anyon. This creates an additional pair of defects. The first movement operation applied to the left anyon also fails, meaning that the anyon does not move as expected. This also creates an additional pair of defects. Nevertheless, these effects are accounted for, and the anyons are finally annihilated. (c) Two examples of measurement errors, one where no anyon is expected and one where one is. Both lead to a pair of defects. (d) A chain of spin errors create three anyons, though one is hidden for a time by measurement errors. The decoder first pairs those it can see, but they do not annihilate. The final anyon, once visible, is annihilated with the fusion product.

CHAPTER 11

Continuous error correction for Ising anyons

Adapted from:
Adrian Hutter and James R. Wootton
"Continuous error correction for Ising anyons",
ArXiv:1508.04033 (2015)

Quantum gates in topological quantum computation are performed by braiding non-Abelian anyons. These braiding processes can be performed with very low error rates. However, to make a topological quantum computation architecture truly scalable, even rare errors need to be corrected. Error correction for non-Abelian anyons is complicated by the fact that it needs to be performed on a continuous basis and further errors may occur while we are correcting existing ones. Here, we provide the first study of this problem and prove its feasibility, establishing non-Abelian anyons as a viable platform for scalable quantum computation. We thereby focus on Ising anyons as the most prominent example of non-Abelian anyons and show that for these a finite error rate can indeed be corrected continuously. There is a threshold error rate $p_c > 0$ such that for all error rates $p < p_c$ the probability of a logical error per time-step can be made exponentially small in the distance of a logical qubit.

11.1 Introduction

Besides revealing spectacular features of quantum physics, non-Abelian anyons are sought for their potential application in topological quantum computing [16–18, 158, 206]. Ising anyons are the most well-studied non-Abelian anyon model, since they describe the exchange statistics of localized Majorana fermions and are expected as elementary excitations of the $\nu = \frac{5}{2}$ fractional quantum Hall state [15]. A variety of condensed-matter systems have been proposed as potential hosts of Majorana fermions [207–226], including topological insulators, p-wave superconductors, nanowires with strong spin orbit interaction, and graphene-like systems, see Refs. [165, 227–229] for reviews. Using nanowire hybrid systems, an approach inspired by the so-called Kitaev wire [230, 231], seems especially promising as experimental evidence for the existence of Majorana fermions in these systems has appeared in recent years [21–23, 232–236]. A network of such wires would allow the Majorana fermions to be braided [237]. Ising anyons also appear as excitations [64, 160, 238, 239] or ends of defect lines [163, 164, 183, 204] in several spin-lattice models.

The set of quantum gates that can be performed topologically, i.e. by braiding anyons, depends on how qubits are encoded into the fusion space of a number of anyons. However, the gate set will not allow for universal quantum computation for any encoding [240]. The standard way of encoding a logical qubit $\{|0\rangle, |1\rangle\}$ into Ising anyons is to employ the two possible ways in which four Ising anyons can fuse to the anyonic vacuum as logical states. With this choice of basis, the only gates that can be performed through topological (braiding) operations are single-qubit Clifford gates – neither "small angle" single-qubit unitaries (such as the $\frac{\pi}{8}$ gate) nor entangling gates are available [24]. In order to perform a universal quantum computation by use of Ising anyons, these gates need to be performed in a non-topological way [24, 166, 241, 242]. Assuming that all topological operations are error-free, these non-topological operations have a very high error threshold [24].

Here, we want to focus on the assumption of error-free topological operations. It is often said that topological operations are "inherently fault-tolerant". However, even a mass gap which is significantly higher than temperature will still lead to a finite density of accidental excitations, and these need to be corrected if a *scalable* quantum computation architecture is to be built. Plausible error mechanisms for quantum information stored in Majorana fermions include the injection of parity-changing excitations from the environment [243–247] and tunnelling of virtual quasiparticles [248].

The field of error correction for non-Abelian anyons is still relatively young. Error correction algorithms for Ising anyons [149] and other non-Abelian anyon models [148, 185] have been benchmarked using Monte Carlo simulations. Ref. [202] demonstrated that even error correction for Fibonacci anyons can be simulated on a classical computer, despite them being universal for quantum computation. These references assume that we are able to detect all anyonic charges at some time, and then are able to fuse as many anyons as we like without any further errors occurring. This picture, however, is highly idealized. In reality, further errors may occur while we are moving existing anyons in order to bring them to fusion. Ref. [186] provides a threshold proof for arbitrary anyon models and a wide class of decoders assuming the idealized picture describe above. In toric (or surface) code models, which support an Abelian anyon model, it is possible to record all syndrome measurements for some time and only correct the net error on each qubit at the final time step [57]. This is a possibility we do not have with non-Abelian anyons: errors need to be corrected on a continuous basis. Ref. [159] recently pointed out that even performing error correction after the completion of each Majorana braid is not sufficient, since the braiding procedure will turn local errors into non-local ones.

This work thus investigates the thus far unexplored problem of *continuous error correction for non-Abelian models*, where we focus on Ising anyons as a concrete example of high practical relevance. We restrict our study to the most trivial topological gate, the identity – i.e., on the task of preserving a topologically stored quantum state. It is generally assumed that the thresholds for quantum information processing are identical to those for quantum information storage. Our main result is that a sufficiently low rate of errors can indeed be corrected continuously, allowing in principle to preserve a topologically stored quantum state indefinitely in a sufficiently large system.

Sec. 11.2 discusses continuous error correction for Ising anyons and states our main result, the proof of which can be found in Sec. 11.3.

11.2 Continuous error correction for Ising anyons

We consider a square lattice of size $L \times L$ with periodic boundary conditions which hosts *Ising anyons*. Each cell can carry either *vacuum* 1, a *fermion* ψ, or a (non-Abelian) *anyon* σ. These satisfy the well-known fusion rules

$$\psi \times \psi = 1\,, \quad \psi \times \sigma = \sigma\,, \quad \sigma \times \sigma = 1 + \psi\,. \tag{11.1}$$

This setting is adapted from Ref. [149], which studied the idealized case of a single round of errors affecting the system with numerical simulations.

All $L \times L$ charges are measured periodically at times $0, 1, 2, \ldots$. We assume that these measurements can be performed flawlessly. We study the question of whether it is possible to preserve a quantum state stored in this system despite a constant rate of errors affecting it. More specifically, we consider whether it is possible to preserve a certain state of the degenerate vacuum of the system. Transitions between different vacuum states can be induced by dragging fermions or anyons around the torus. More realistically, one would consider storing a quantum state in the fusion space of a set of well-separated anyons [149]. However, we focus on the task of preserving a certain vacuum state of the torus for simplicity. Following Ref. [149], we assume that at sufficiently large length-scales, the question of correctability is independent of the particular encoding scheme chosen.

Let us assume that between any two rounds of charge measurement a pair of fermions and a pair of anyons are created on each pair of adjacent cells of the lattice with probability p each ($2p < 1$). Error events can thus be associated with edges of the square lattice. Note that the case of both a pair of anyons and a pair of fermions being created on the same edge is indistinguishable from only a pair of anyons being created. We thus restrain from considering this case explicitly. Finally, we assume that we are able to move an anyon or a fermion to an adjacent cell over the course of one measurement period.

The basic idea behind our error correction approach is that according to the fusion rules Eq. (11.1) it is always possible to first fuse all σ anyons in pairs, and then fuse all ψ fermions in pairs in order to obtain a vacuum state [149]. A crucial difference between error correction for Abelian and non-Abelian anyons is that for the former, it is possible to record the outcomes of all charge measurements and postpone the actual act of fusing them to perform correction arbitrarily; while for the latter, errors need to be corrected "on the fly". The results of their non-Abelian braiding would be impossible to unwind later on.

In our case, the ψ fermions are Abelian while the σ anyons are non-Abelian. Note that according to the second of the fusion rules in Eq. (11.1), if a fermion and an anyon move to the same cell, they will fuse to an anyon. If that anyon is further moved around, it will carry with it the additional fermionic charge. We will refer to this informally as the anyon "swallowing" the fermion. The fermion will be recovered if the anyon is brought to fusion with an other anyon, as the fermionic parity is conserved. We will thus continuously fuse the anyons in pairs, recovering any "swallowed" fermions, while error correction for the fermions is postponed. If we are moving two anyons towards each other in an attempt to fuse them, further errors may happen along their path that make one of them disappear. We will shortly discuss how we deal with this. As we will discuss in the following, anyons that are moved around and brought to fusion during error correction can not only "swallow" fermions, but can actually create fermions, without any fermionic errors happening. This makes the the error correction problem for the fermions much more involved than for the anyons.

In order to formally discuss error correction, we consider a $2+1$-dimensional cubic lattice, in which time flows "upwards", and with periodic boundary conditions in horizontal (spatial) direction. Charge measurements correspond to horizontal faces. It will prove convenient to identify error events and paths along which we move anyons with edges of the *dual* lattice of this cubic lattice. Error events happen between consecutive rounds of charge measurement and affect two adjacent cells. They can thus naturally be identified with vertical faces of the primal lattice, and, in turn, horizontal edges of the dual lattice. We will call the one-cell-per-time-step paths along which we move the anyons during error correction their *world-lines*. Error events are not considered to be part of a world-line. Horizontal faces of the primal lattice (charge measurements) are naturally identified with vertical edges of the dual lattice. For every charge measurement which detects an anyon, we consider the associated vertical edge of the dual lattice to be part of the anyon's world-line. If an anyon is moved to an adjacent cell, the horizontal edge connecting the old and new vertical edge is also considered to be part of the anyon's world-line. Note that error events always correspond to horizontal edges of the dual lattice, while anyon world-lines include both horizontal (intentional movements) and vertical (charge measurements) edges.

Let A denote the set of all anyonic (as opposed to fermionic) error events and F the set of all fermionic error events. These are disjoint. Both of these are subsets of the horizontal edges of the dual of the $2+1$-dimensional cubic lattice. Let ∂A denote the set of cells of the cubic lattice which have an *odd* number of elements of A incident upon them. Elements in ∂A correspond to *unexpected changes in the anyonic charge*, i.e., those which are not due to us intentionally moving an anyon to an adjacent cell. The set ∂A is known to us with certainty.

Let A_t and ∂A_t denote the subsets of A and ∂A, respectively, that happen between charge measurements $t-1$ and t. Since the fusion rules in Eq. (11.1) preserve the parity of the number of anyons that exist at any given time, the sets ∂A_t always have even cardinality (for any t). We note that the sets A_t with different time-coordinates are independent from each other. It is the task of a classical error correction algorithm to form a hypothesis about the set A_t that is compatible with the given set ∂A_t. This problem is in fact exactly isomorphic to the well-studied problem of correcting bit-flip errors in the toric code with perfect syndrome measurements [57]. We can thus employ the standard algorithm used to find such a pairing in the toric code case, namely an efficient minimum-weight perfect matching (MWPM) algorithm [69]. The weight of a path connecting two lattice cells is thereby given by the 2-dimensional L_1-norm, i.e., the Manhattan distance in the $L \times L$ lattice with periodic boundary conditions. We stress that despite the fact that we deal with anyon world-lines in $2+1$ dimensions, the algorithmic part of the error correction problem for the anyons is a 2-dimensional one. This is in contrast to the error correction problem for the fermions, as we shall see.

Let us call a subset of the edges of the dual lattice a *string* if there are exactly two cells of the cubic lattice which have exactly one of the edges incident upon them, and all other cells have either zero or two edges incident upon them. (Note that a string can consist of a single edge.) The MWPM algorithm will return strings that connect the elements in ∂A_t in pairs. The union of these strings, which we call H_t, forms our hypothesis about what anyonic errors have happened between charge measurements $t-1$ and t. Let $H = \bigcup_t H_t$ denote the union of these hypotheses. We note that A_t can in general not be decomposed into strings ending at elements of ∂A_t – it can contain *loops*. These are defined as sets of edges of the dual lattice such that each cell of the cubic lattice has zero or two edges of the set incident upon them. However, H_t will never contain loops, as they increase the weight of the hypothesis without explaining elements in ∂A_t.

Each currently existing anyon is connected through a world-line consisting of horizontal and vertical edges (intentional movements and charge measurements which detected an anyonic charge) of the dual lattice to an element of ∂A, its creation event. World-lines are always strings. Each element in ∂A is connected by a string which is a subset of H to a contemporaneous element of ∂A. Furthermore, each element in ∂A is the beginning or the end of an anyon world-line. This world-line connects the element either to another element in ∂A, which has a different time-coordinate, or to a currently existing anyon. Each currently existing anyon is thus connected through a chain consisting of strings which are alternately subsets of W and H to another currently existing anyon. If two currently existing anyons are connected this way, we move them towards each other, one cell per time-step, along the shortest possible path which is homologically equivalent to the chain that connects them. If they are already adjacent, it suffices to move one of them to the location of the other in order to bring them to fusion.

Let W denote the union of all world-lines. We note that H and W are not necessarily disjoint: it can happen that we attempt to move an anyon to an adjacent cell and, between the same two rounds of charge measurement, an anyonic error affecting the same two cells happens. Let us thus study the disjoint union

$$H \sqcup W = \{(e,h) : e \in H\} \cup \{(e,w) : e \in W\}\,. \tag{11.2}$$

Here, the index i in the ordered pair (e,i) tells us which of the two sets H and W the edge e belongs to. If an edge is an element of both H and W, there will thus be two corresponding edges in $H \sqcup W$. The set $H \sqcup W$ decays into loops (meaning that all involved anyons have already be brought to fusion) and strings which end at pairs of currently existing anyons. Very rarely, it may happen during error correction that, according to our hypothesis, anyonic errors have happened which fused two anyons in a way which is not equivalent to the way we have foreseen. In this case, we need to *create* these two anyons again in order to finish error correction in a way that is equivalent to our hypothesis.

The difficulty with correcting the fermions is that they are not only created and moved by elements of F, but also by elements of A and W. Fig. 11.1 illustrates a process in which two fermions are created while correcting two pairs of anyons, and a process in which a fermion is "swallowed" during anyon error correction. The second process illustrates that it is possible to create pairs of fermions which do not appear in the same measurement period. For this reason, the error correction problem for the fermions is $2 + 1$-dimensional. Similarly to the case when error correction is performed for Abelian systems with imperfect syndrome measurements, we need to pair unexpected changes of the fermionic charge which may have different time-coordinates. (Since before the final time-step we never attempt to move fermions, any change in fermionic charge is unexpected.) Unexpected appearances of fermions are due to fermion error events, or due to fusion of two anyons. Unexpected disappearances are due to an anyon "swallowing" a fermion, or due to an appearance event at a location where a fermion has already been present. When applying MWPM to the fermionic problem, the weight we assign to connecting two spatio-temporally separated events is the $2 + 1$-dimensional L_1-norm. Clearly, a more sophisticated weight would take knowledge about anyon world-lines into account. This would be similar to the idea of introducing "shortcuts" in Ref. [185]. It may also help to weight spatial and temporal distances differently. However, we restrict to the L_1 norm for simplicity.

Our main result is the following theorem.

Theorem. *If error correction is performed as described above, there is a finite threshold* $p_c > 0$ *such that for* $p < p_c$ *the error rate on the stored quantum information is exponentially small in* L.

In the following section, we prove this theorem with $p_c \approx 3 \times 10^{-17}$. Given the crudeness of our arguments, we expect this lower bound to be rather pessimistic. A better estimate of the true threshold value p_c could be obtained by numerical simulations, extending the work of Ref. [149] to the continuous case. Such simulations could employ more involved distance measures than the $2 + 1$-dimensional L_1-norm on which we rely in our proof, taking entropic contributions and "shortcuts" due to already performed fusion processes into account [185].

11.3 Proof

Our proof is similar in nature to the proofs for the correctability of the toric code by means of MWPM. The basic idea is the following. In a lattice of size L, the number of errors which are necessary for error correction to fail grows linearly with L, so the probability of any given set of errors that could cause the failure of error correction is $\sim p^{aL}$. However, the number

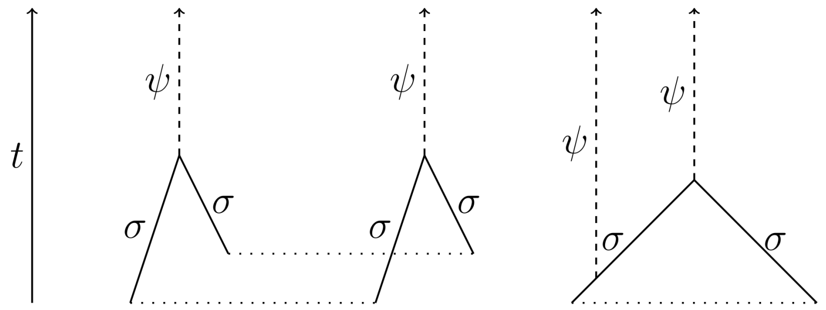

Figure 11.1: Two possible processes illustrating how creation and fusion of σ anyons can produce or "swallow" ψ fermions. Anyonic errors are dotted, anyonic world-lines are solid, and fermionic world-lines are dashed. Left process: Two error strings produce two pairs of anyons, which are incorrectly paired and correspondingly brought to fusion. This process creates a pair of fermions with probability $\frac{1}{2}$. Right process: An error string creates a pair of anyons which are brought to fusion. Along one of the anyonic world-lines, a pair of fermions is created and one of the two fermions is "swallowed" by the nearby anyon (cf. the second of the fusion rules Eq. (11.1)). The second fermion is recovered only when the two anyons are fused.

of possible sets of errors that could lead to the failure of error correction is exponentially large in L, say $\sim b^L$. The probability of a logical error occurring is thus exponentially suppressed with L if $p^a b < 1$, leading to $p_c = b^{-1/a}$. For the case of the toric code with perfect syndrome measurements, such a proof was given in Ref. [57] while Ref. [126] proved a threshold for the fully fault-tolerant case, with circuit-based syndrome extraction. As long as we only consider the (non-Abelian) anyons, the error model for them is isomorphic to the one for the toric code [16,57] with bit-flip rate p and perfect syndrome measurements. The correctabiliy of the anyons thus follows from the correctability of this (very well-studied) error model. Indeed, Ref. [57] contains an analytical proof that for this problem $p_c \geq 3.7\%$.

Our main difficulty is correcting the fermions which may be produced or "swallowed" during the continuous correction of the anyons, leading to a more involved, correlated effective error model for the fermions. Fig. 11.1 shows two examples of such processes. The rest of the proof is devoted to showing how to deal with the influence that correction of the anyons can have on the fermions.

For the rest of this proof, we consider the *hypothetical completion* of $H \sqcup W$. That is, we consider the *hypothetical* world-lines W that we would obtain if we could complete error correction in accordance with our hypothesis H at a given time and bring all anyons to fusion, without any further errors occurring. There is thus no longer a notion of "currently existing anyons". Each string in W (anyon world-line) begins and ends at an element of ∂A (unexpected change in anyonic charge).

We have remarked that the set A can be decomposed into loops and strings which connect elements in ∂A in pairs. We choose this decomposition such that each element in ∂A has exactly one string incident upon it. Let $A = A^s \cup A^l$ be such a decomposition. (This decomposition is in general not unique. Consider for instance two contemporaneous elements of ∂A which are connected by three strings in A. The decomposition will consider the union of two of these strings to form a loop.) The sets A^s, H, and W can then all be decomposed into strings, each of which ends at an element of ∂A. Conversely, each element of ∂A has three strings incident upon it, which are respectively subsets of A^s, H, and W. Consider the disjoint union

$$\begin{aligned}&A^s \sqcup H \sqcup W = \\ &\quad \{(e,a) : e \in A^s\} \cup \{(e,h) : e \in H\} \cup \{(e,w) : e \in W\}\,. \end{aligned} \tag{11.3}$$

It forms a trivalent graph, with each vertex corresponding to an element of ∂A, and having an A^s, an H-, and a W-string incident upon it. Let us study minimal connected components of this graph. Let A^s_i, H_i, and W_i denote the union of all strings in A^s, H, and W, respectively, that belong to connected component i. Finally, let W^h_i denote the set of horizontal edges (i.e., intentional anyon movements) and W^v_i the set of vertical edges (i.e., charge measurements which detect an anyon) in W_i. Recall that A^s_i and H_i consist of horizontal edges only.

From the way our error correction procedure is defined, we have the inequalities

$$|W^h_i| \leq |H_i| \leq |A^s_i|\,. \tag{11.4}$$

The first inequality is due to us moving anyons along the shortest path which is homologically equivalent with H_i. We could always choose $|W^h_i| = |H_i|$ by undoing exactly the errors that happened according to our hypothesis. The second inequality is due to using MWPM for error correction. Assume by contradiction that $|H_i| > |A^s_i|$. Then, replacing H_i with A^s_i would yield a perfect matching of the unexpected changes in anyonic charge which is of lower weight than the one returned by the MWPM algorithm, which contradicts its definition.

Now consider the loops $O_i = A_i^s \sqcup W_i$. The following lemma is the main technical tool that we use in order to deal with the loops O_i.

Lemma 11. *All loops O_i satisfy*

$$|O_i| \leq 4|A_i^s|\,. \tag{11.5}$$

Note that for the simplest possible process, a single anyon error event that is immediately corrected ($|A_i^s| = 1$, $|H_i| = 1$, $|W_i^h| = 1$, $|W_i^v| = 2$, $|O_i| = 4$), the bound is tight.

Proof. Let f_i denote the number of fusion events of a pair of anyons in O_i. An anyon needs to be moved away from each location at which it appears. However, before fusion two anyons may be adjacent so that we need to move only one of them. We thus have

$$|W_i^h| \geq |W_i^v| - f_i\,. \tag{11.6}$$

Furthermore, each error event can create at most two anyons, so

$$f_i \leq |A_i^s|\,. \tag{11.7}$$

Combining these with Eq. (11.4), we find

$$|W_i^v| \leq 2|A_i^s|\,. \tag{11.8}$$

For the total length of the loop, we find, using Eqs. (11.4) and (11.8),

$$|O_i| = |A_i^s| + |W_i^h| + |W_i^v| \leq 4|A_i^s|\,. \tag{11.9}$$

□

The following lemma provides a necessary condition for the failure of error correction.

Lemma 12. *A failure of error correction requires a homologically non-trivial closed path P (a loop) satisfying*

$$7|P \cap A| + |P \cap F| \geq |P|/2\,. \tag{11.10}$$

Proof. Let us first study the possibilities for error correction failing for the anyons (as opposed to the fermions). Recall that we have decomposed the set of anyonic errors A into loops A^l and strings A^s. If one the loops in A^l is homologically non-trivial, Eq. (11.10) will obviously be satisfied, as we can choose P to be the corresponding loop and have $|P \cap A| = |P|$. The second possibility for error correction for the anyons failing is that one of the loops O_i is topologically non-trivial. In this case, we choose $P = O_i$ and are done, since by use of Lemma 11 we have

$$7|O_i \cap A| = 7|A_i^s| \geq \frac{7}{4}|O_i|\,. \tag{11.11}$$

So assume from now on that all loops which are subsets of A^l and all loops O_i are homologically trivial, and that error correction failing is due to the fermionic part of the problem.

Clearly, MWPM failing to correct the fermions requires that there be a homologically non-trivial closed path P containing at least $|P|/2$ edges that have been affected by an event that can possibly have created or moved fermions, for otherwise the minimum-weight correction of the fermions will never move a fermion around the torus. We assume pessimistically that each edge in A^l and in $O = \bigcup_i O_i$ (anyon error event or anyon world-line) counts as a potential fermion error event. So formally, we need a path P with

$$|P \cap (A^l \cup O \cup F)| \geq |P|/2\,. \tag{11.12}$$

We will prove that if there is such a path P, there is a (possibly identical) path P' which is homologically equivalent to P and satisfies the inequality in the lemma, i.e., $7|P' \cap A| + |P' \cap F| \geq |P'|/2$.

Given a loop O_i with $O_i \cap P \neq \emptyset$, we can consider the "deformed" path $D_i(P) = (P \backslash O_i) \cup (O_i \backslash P)$. The path P' is obtained by applying a (possibly empty) set of deformation operations D_i to P. Since all of the loops O_i are homologically trivial, the deformed path P' will be homologically equivalent to P. We define the path P' such that the number of A events in the path is maximized; i.e., such that

$$|P' \cap A_i^s| = \max\{|P \cap A_i^s|, |D_i(P) \cap A_i^s|\}\,, \tag{11.13}$$

for all loops with $O_i \cap P \neq \emptyset$. Equivalently, the path P' is defined such that

$$|A_i^s \setminus P'| \leq |A_i^s \cap P'|\,. \tag{11.14}$$

Let us define $\tilde{A}^l = A^l \setminus O$ and $\tilde{F} = F \setminus O$. By assumption, we have

$$\begin{aligned}
0 &\leq |P \cap (A^l \cup O \cup F)| - |P|/2 \\
&= |P \cap \tilde{A}^l| + |P \cap O| + |P \cap \tilde{F}| - |P|/2 \\
&= |P \cap \tilde{A}^l| + |P \cap O| + |P \cap \tilde{F}| \\
&\quad - (|P \cap O|/2 + |P \setminus O|/2) \,. \qquad (11.15)
\end{aligned}$$

Note that $P \setminus O$ is not affected by deformation operations, i.e. $P \setminus O = P' \setminus O$. Since $P \cap \tilde{F} \subseteq P \setminus O$, we also have $P \cap \tilde{F} = P' \cap \tilde{F}$ and similarly $P \cap \tilde{A}^l = P' \cap \tilde{A}^l$. Therefore

$$\begin{aligned}
0 &\leq |P' \cap \tilde{A}^l| + |P \cap O|/2 + |P' \cap \tilde{F}| - |P' \setminus O|/2 \\
&= |P' \cap \tilde{A}^l| + (|P \cap O| + |P' \cap O|)/2 + |P' \cap \tilde{F}| \\
&\quad - (|P' \setminus O|/2 + |P' \cap O|/2) \\
&= |P' \cap \tilde{A}^l| + \sum_i (|P \cap O_i| + |P' \cap O_i|)/2 \\
&\quad + |P' \cap \tilde{F}| - |P'|/2 \,. \qquad (11.16)
\end{aligned}$$

If $\underline{P \cap O_i = P' \cap O_i}$ we find

$$\begin{aligned}
&(|P \cap O_i| + |P' \cap O_i|)/2 \\
&\quad = |P \cap O_i| \\
&\quad = |P \cap A_i^s| + |P \cap O_i \setminus A_i^s| \,. \qquad (11.17)
\end{aligned}$$

Since $P \cap O_i \setminus A_i^s \subseteq O_i \setminus A_i^s$ and $A_i^s \subseteq O_i$ we have

$$|P \cap O_i \setminus A_i^s| \leq |O_i \setminus A_i^s| = |O_i| - |A_i^s| \,. \qquad (11.18)$$

Combining Eqs. (11.17) and (11.18) with Lemma 11, we arrive at

$$(|P \cap O_i| + |P' \cap O_i|)/2 \leq |P \cap A_i^s| + 3|A_i^s| \,. \qquad (11.19)$$

Using Eq. (11.14), we obtain

$$|A_i^s| = |A_i^s \cap P'| + |A_i^s \setminus P'| \leq 2|A_i^s \cap P'| = 2|A_i^s \cap P| \,. \qquad (11.20)$$

We finally find

$$(|P \cap O_i| + |P' \cap O_i|)/2 \leq 7|P' \cap A_i^s| \,. \qquad (11.21)$$

If, on the other hand, $\underline{P \cap O_i \neq P' \cap O_i}$, we find, using Lemma 11 for the first inequality,

$$(|P \cap O_i| + |P' \cap O|_i)/2 = |O_i|/2 \leq 2|A_i^s| \leq 4|P' \cup A_i^s|\,. \tag{11.22}$$

So in both cases Eq. (11.21) holds and we find from Eq. (11.16) that

$$\begin{aligned} 0 &\leq |P' \cap \tilde{A}^l| + 7\sum_i |P' \cap A_i^s| + |P' \cap \tilde{F}| - |P'|/2 \\ &\leq 7|P' \cap A| + |P' \cap F| - |P'|/2\,. \end{aligned} \tag{11.23}$$

□

Lemma 13. *The probability per time-step of a path as in Lemma 12 is exponentially suppressed with L if* $p < 15^{-14} \approx 3 \times 10^{-17}$.

Proof. Consider two lines of length L looping in homologically non-equivalent ways around the torus. Path P needs to cross at least one of them. Since the two lines can be crossed at $O(L)$ locations, and a path in a three-dimensional cubic lattice can at each step turn into 5 directions, there are at most $5^{\ell+O(\log(L))}$ closed paths of length ℓ in the lattice crossing any of the two lines at a given time. Let $n = |P \cap A| + |P \cap F|$ be the number of error events along the path, and let $\ell = |P|$. For a path satisfying $7|P \cap A| + |P \cap F| \geq |P|/2$, we need $14n \geq \ell$. With fixed locations of the n errors, the probability of such a path is at most $p^n \leq p^{\ell/14}$. In a path of length ℓ, there are no more than 3^ℓ possibilities for picking the locations of A and F events. The probability per time-step of a path satisfying $7|P \cap A| + |P \cap F| \geq |P|/2$ is thus upper-bounded by

$$\sum_{\ell=L}^{\infty} 5^{\ell+O(\log(L))} 3^\ell p^{\ell/14}\,, \tag{11.24}$$

which is exponentially suppressed with L if $15p^{1/14} < 1$. □

11.4 Conclusions

In recent years, experimental results have appeared that allow to be cautiously optimistic about the prospects of topological quantum computing [21–23,232–236]. One can hope that the first proof-of-principle experiments involving non-Abelian braiding will be performed in the not-too-distant future. These would unambiguously demonstrate the potential for quantum information processing with hardware which has intrinsically low error rates. Still, these error rates would presumably not be low enough to allow for a truly large-scale computation, as is necessary for, say, breaking RSA-cryptography, without invoking error correction. Here, we have demonstrated the feasibility of this task under the realistic assumption that errors keep happening as we correct those from previous rounds.

Our result can potentially be extended in several directions. First, one could think about extending it to the case where measurements of the anyonic charge can fail, similar to syndrome measurements in surface codes. This leads to several new complications, such as cases where during error correction we need to change our judgement about which anyon needs to be paired with which one. This will lead to changes in the "direction" along which we move an anyon during error correction, making it much harder to analyze anyon world-lines. Second, one would hope for a threshold proof for further non-Abelian anyon models, including those for which MWPM cannot be applied to perform error correction [148, 185, 202]. Unfortunately, the highly general proof in Ref. [186] does not allow for straightforward generalization to the continuous case.

Finally, it would be valuable to get a better idea of the "true" threshold for our setup. This could be done via a more ingenious analytical approach, or by use of Monte Carlo simulations. For qubit-based quantum computing, analytically proved fault-tolerance thresholds increased from $p_c \approx 10^{-6}$ [**?**, 42] to $p_c \approx 10^{-3}$ [126] over the course of more than a decade, while numerical simulations indicate even higher thresholds of $p_c \approx 10^{-2}$ [44]. It will be interesting to see whether the fault-tolerance thresholds for quantum information processing by means of non-Abelian anyons undergo a similar development. If they do not, the very low error rates that one hopes to achieve with anyon-based quantum computing may actually be a necessity. The "true" thresholds for Abelian models can often be assessed by finding the phase-transition in a related classical statistical mechanics model [57, 131, 155]. Whether something similar can be done for non-Abelian models remains an open problem.

11.5 Acknowledgements

The authors gratefully acknowledge Courtney Brell and Daniel Loss for careful reading of the manuscript and helpful comments. This work was supported by the SNF and NCCR QSIT.

Bibliography

[1] A. Einstein, B. Podolsky, and N. Rosen, Phys. Rev. **47**, 777 (1935).

[2] X.-S. Ma, T. Herbst, T. Scheidl, D. Wang, S. Kropatschek, W. Naylor, B. Wittmann, A. Mech, J. Kofler, E. Anisimova, V. Makarov, T. Jennewein, R. Ursin, and A. Zeilinger, Nature **489**, 269 (2012).

[3] R. P. Feynman, Int. J. Theor. Phys. **21**, 467 (1982).

[4] P. W. Shor, *Proceedings of the Symposium on the Foundations of Computer Science*, 124 (1994).

[5] L. K. Grover, Phys. Rev. Lett. **79**, 325 (1997).

[6] A. W. Harrow, A. Hassidim, and S. Lloyd, Phys. Rev. Lett. **103**, 150502.

[7] P. Rebentrost, M. Mohseni, and S. Lloyd, Phys. Rev. Lett. **13**, 130503 (2014).

[8] D. Loss and D. P. DiVincenzo, Phys. Rev. A **57**, 120 (1998).

[9] Ch. Kloeffel and D. Loss, Annu. Rev. Condens. Matter Phys. 4, 51 (2013).

[10] H. Bluhm, S. Foletti, I. Neder, M. Rudner, D. Mahalu, V. Umansky, and A. Yacoby, Nat. Phys. **7**, 109 (2011).

[11] J. M. Leinaas and J. Myrheim, Il Nuovo Cimento B **37**, 1 (1977).

[12] J. Bell, Physics **1**, 195 (1964).

[13] A. Aspect, P. Grangier, and G. Roger, Phys. Rev. Lett. **49**, 91 (1982).

[14] F. Wilczek, Phys. Rev. Lett. **49**, 957 (1982).

[15] G. Moore and N. Read, Nucl. Phys. B 360, **362** (1991).

[16] A. Y. Kitaev, Ann. Phys. **303**, 2 (2003).

[17] M. H. Freedman, A. Y. Kitaev, M. J. Larsen, and Z. Wang, arXiv:0101025 (2001).

[18] J. K. Pachos, *Introduction to Topological Quantum Computation*, Cambridge University Press (2012).

[19] S. Bravyi, M. Hastings, and S. Michalakis, J. Math. Phys. **51**, 093512 (2010).

[20] J. Preskill, Lecture Notes for Physics 219: Quantum Computation. `http://www.theory.caltech.edu/~preskill/` (2004).

[21] V. Mourik, K. Zuo, S. M. Frolov, S. R. Plissard, E. P. A. M. Bakkers, and L. P. Kouwenhoven, Science, **336**, 1003 (2012).

[22] A. Das, Y. Ronen, Y. Most, Y. Oreg, M. Heiblum, and H. Shtrikman, Nat. Phys. **8**, 887-895 (2012).

[23] S. Nadj-Perge, I. K. Drozdov, J. Li, H. Chen, S. Jeon, J. Seo, A. H. MacDonald, B. A. Bernevig, and A. Yazdani, Science **346**, 602 (2014).

[24] S. Bravyi, Phys. Rev. A **73**, 042313 (2006).

[25] S. Clancy, Nat. Edu. **1**, 103 (2008).

[26] R. Landauer, IBM Journal of Research and Development **5**, 183 (1961).

[27] R. Peierls, Mathematical Proceedings of the Cambridge Philosophical Society **32**, 477 (1936).

[28] E. Ising, Z. Phys. **31**, 253 (1925).

[29] R. Alicki, Open Systems & Information Dynamics **19**, 1250016 (2012).

[30] C. G. Brell, arXiv:1411.7046 (2014).

[31] B. J. Brown, D. Loss, J. K. Pachos, C. N. Self, and J. R. Wootton, arXiv:1411.6643 (2014).

[32] B. Yoshida, Ann. Phys. **326**, 2566 (2011).

[33] R. Alicki, M. Fannes, and M. Horodecki, J. Phys. A: Math. Theor. **42**, 065303 (2009).

[34] R. Alicki, M. Horodecki, P. Horodecki, and R. Horodecki, Open Syst. Inf. Dyn. **17**, (2010).

[35] S. Bravyi and B. Terhal, New J. Phys. **11**, 043029 (2009).

[36] A. Blais, R.S. Huang, A. Wallraff, S. M. Girvin, and R. J. Schoelkopf, Phys. Rev. A **69**, 062320 (2004).

[37] A. Imamoglu, D. D. Awschalom, G. Burkard, D. P. DiVincenzo, D. Loss, M. Sherwin, and A. Small, Phys. Rev. Lett. **83**, 4204 (1999).

[38] S. Chesi, B. Röthlisberger, and D. Loss, Phys. Rev. A **82**, 022305 (2010).

[39] F. L. Pedrocchi, S. Chesi, and D. Loss, Phys. Rev. B **83**, 115415 (2011).

[40] B. Röthlisberger, J. R. Wootton, R. M. Heath, J. K. Pachos, and D. Loss, Phys. Rev. A **85**, 022313 (2012).

[41] O. Landon-Cardinal, B. Yoshida, D. Poulin, and J. Preskill, Phys. Rev. A **91**, 032303 (2015).

[42] E. Knill, R. Laflamme, and W. Zurek, arXiv:quant-ph/9610011 (1996).

[43] D. Aharonov and M. Ben-Or, arXiv:quant-ph/9611025 (1996).

[44] R. Raussendorf and J. Harrington, Phys. Rev. Lett. **98**, 190504 (2007).

[45] R. Barends, J. Kelly, A. Megrant, A. Veitia, D. Sank, E. Jeffrey, T. C. White, J. Mutus, A. G. Fowler, B. Campbell, Y. Chen, Z. Chen, B. Chiaro, A. Dunsworth, C. Neill, P. OMalley, P. Roushan, A. Vainsencher, J. Wenner, A. N. Korotkov, A. N. Cleland, and J. M. Martinis, Nature **508**, 500 (2014).

[46] S. Bravyi and A. Kitaev, Phys. Rev. A **71**, 022316 (2005).

[47] A. G. Fowler, A. M. Stephens, and P. Groszkowski, Phys. Rev. A **80**, 052312 (2009).

[48] A. G. Fowler, M. Mariantoni, J. M. Martinis, and A. N. Cleland, Phys. Rev. A **86**, 032324 (2012).

[49] N. C. Jones, R. Van Meter, A. G. Fowler, P. L. McMahon, J. Kim, T. D. Ladd, and Y. Yamamoto, Phys. Rev. X **2**, 031007 (2012).

[50] C. Horsman, A. G. Fowler, S. Devitt, and R. Van Meter, New J. Phys. **14** 123011 (2014).

[51] H. Bombin and M. A. Martin-Delgado, Phys. Rev. Lett. **97**, 180501 (2006).

[52] A. J. Landahl and C. Ryan-Anderson, arXiv:1407.5103 (2014).

[53] D. Nigg, M. Mueller, E. A. Martinez, P. Schindler, M. Hennrich, T. Monz, M. A. Martin-Delgado, R. Blatt, Science **345**, 302 (2014).

[54] S. Bravyi, M. Suchara, and A. Vargo, Phys. Rev. A **90**, 032326 (2014).

[55] Z. Nussinov and G. Ortiz, arXiv:cond-mat/0702377 (2007).

[56] Z. Nussinov and G. Ortiz, Phys. Rev. B **77**, 064302 (2008).

[57] E. Dennis, A. Kitaev, A. Landahl, and J. Preskill, J. Math. Phys. **43**, 4452 (2002).

[58] A. Kay and R. Colbeck, arXiv:0810.3557v1 (2008).

[59] J. Haah and J. Preskill, Phys. Rev. A 86, 032308 (2012).

[60] J. Haah, Phys. Rev. A **83**, 042330 (2011).

[61] S. Bravyi and J. Haah, Phys. Rev. Lett. **107**, 150504 (2011).

[62] S. Bravyi and J. Haah, Phys. Rev. Lett. **111**, 200501 (2013).

[63] Jeongwan Haah, private communication, Jan. 2012.

[64] A. Y. Kitaev, Ann. Phys. **321**, 2 (2006).

[65] A. Hamma, C. Castelnovo, and C. Chamon, Phys. Rev. B **79**, 245122 (2009).

[66] S. Bravyi and A. Kitaev, arXiv:9811052v1 (1998).

[67] David J. C. MacKay, *Information Theory, Inference & Learning Algorithms*, Cambridge University Press, New York, NY, USA, (2002).

[68] J. R. Shewchuk, *Applied Computational Geometry: Towards Geometric Engineering*, vol 1148 of *Lecture Notes in Computer Science*, Springer (1996).

[69] V. Kolmogorov, Math. Prog. Comp. **1**, 43 (2009).

[70] J. Edmons, Can. J. Math. **17**, 449 (1965).

[71] E. B. Davies, Comm. Math. Phys. **39**, 91 (1974).

[72] A. J. Leggett, S. Chakravarty, A. T. Dorsey, M. P. A. Fisher, A. Garg, and W. Zwerger, Rev. Mod. Phys. **59**, 1 (1987).

[73] D. P. DiVincenzo and D. Loss, Phys. Rev. B **71**, 035318 (2005).

[74] J. Kempe, A. Kitaev, and O. Regev, SIAM J. Comput. **35**, 1070 (2006).

[75] J. Vidal, K. P. Schmidt, and S. Dusuel, Phys. Rev. B **78**, 245121 (2008).

[76] J. R. Wootton, J. Phys. A: Math. Theor. **45**, 395301 (2012).

[77] C. Castelnovo and C. Chamon, Phys. Rev. B **76**, 184442 (2007).

[78] R. Alicki, M. Fannes, and M. Horodecki, J. Phys. A: Math. Theor. **40**, 6451 (2007).

[79] D. Bacon, Phys. Rev. A **73**, 012340 (2006).

[80] K. P. Michnicki, Phys. Rev. Lett. **113**, 130501 (2014).

[81] A. Hutter, J. R. Wootton, B. Röthlisberger, and D. Loss, Phys. Rev. A **86**, 052340 (2012).

[82] F. L. Pedrocchi, A. Hutter, J. R. Wootton, D. Loss, Phys. Rev. A **88**, 062313 (2013).

[83] H. Weimer, M. Müller, I. Lesanovsky, P. Zoller, and H. P. Büchler, Nat. Phys. **6**, 382 (2010).

[84] J. T. Barreiro, M. Müller, P. Schindler, D. Nigg, T. Monz, M. Chwalla, M. Hennrich, C. F. Roos, P. Zoller, and R. Blatt, Nature **470**, 486 (2011).

[85] M. Mueller, K. Hammerer, Y. L. Zhou, C. F. Roos, and P. Zoller, New. J. Phys. **13**, 085007 (2011).

[86] H. Weimer, Mol. Phys. **111**, 1753 (2013).

[87] A. V. Gorshkov, K. R. A. Hazzard, and A. M. Rey, arXiv:1301.5636 (2013).

[88] T. Tanamoto, V. M. Stojanovi, C. Bruder, and D. Becker, Phys. Rev. A **87** 052305 (2013).

[89] L. Viola and S. Lloyd, Phys. Rev. A **58**, 2733 (1998).

[90] L. Viola, E. Knill, and S. Lloyd, Phys. Rev. Lett. **82**, 2417 (1999).

[91] P. Zanardi, Phys. Lett. A **258**, 77 (1999).

[92] R. R. Ernst, G. Bodenhausen, and A. Wokaun, *Principles of Nuclear Magnetic Resonance in One and Two Dimensions*, Oxford Univ. Press, London/New York (1990).

[93] W. Magnus, Comm. Pure Appl. Math **7**, 649 (1954).

[94] H. Tal-Ezer and R. Kosloff, J. Chem. Phys. **81**, 3967 (1984).

[95] S. Bravyi, D. P. DiVincenzo, and D. Loss, Ann. Phys. **326**, 2793 (2011).

[96] Z. Nussinov and J. van den Brink, arXiv:1303.5922 (2013).

[97] O. Landon-Cardinal and D. Poulin, Phys. Rev. Lett. **110**, 090502 (2013).

[98] B. J. Brown, A. Al-Shimary, and J. K. Pachos, Phys. Rev. Lett. **112**, 120503 (2014).

[99] J. R. Wootton and J. K. Pachos, Phys. Rev. Lett. **107**, 030503 (2011).

[100] C. Stark, L. Pollet, A. Imamoglu, and R. Renner, Phys. Rev. Lett. **107**, 030504 (2011).

[101] P. Simon, B. Braunecker, and D. Loss, Phys. Rev. B **77**, 045108 (2008).

[102] W. Nolting and A. Ramakanth, *Quantum Theory of Magnetism*, Springer, Berlin, (2009).

[103] G. D. Mahan, *Many-Particle Physics*, Plenum (1990).

[104] S. Chesi, D. Loss, S. Bravyi, and B. M. Terhal, New J. Phys. **12**, 025013 (2010).

[105] H. Mori and K. Kawasaki, Prog. Theor. Phys. **27**, 529 (1962).

[106] P. Bonderson and C. Nayak, Phys. Rev. B **87**, 195451 (2013)

[107] S. Gladchenko, D. Olaya, E. Dupont-Ferrier, B. Doucot, L. B. Ioffe, and M. E. Gershenson, Nat. Phys. **5**, 45 (2009).

[108] X.-C. Yao, T.-X. Wang, H.-Z. Chen, W.-B. Gao, A. G. Fowler, R. Raussendorf, Z.-B. Chen, N.-L. Liu, C.-Y. Lu, Y.-J. Deng, Y.-A. Chen, and J.-W. Pan, Nature **482**, 489 (2012).

[109] A. Micheli, G. K. Brennen, and P. Zoller, Nat. Phys. **2**, 341 (2006).

[110] R. Koenig, Quant. Inf. Comp. **10**, oN. 3, 292(2010).

[111] C. G. Brell, S. T. Flammia, S. D. Bartlett, and A. C. Doherty, New J. Phys. **13**, 053039 (2011).

[112] B. M. Terhal, F. Hassler, and D. P. DiVincenzo, Phys. Rev. Lett. **108**, 260504 (2012).

[113] J. R. Wootton, J. Mod. Opt. **59**, 1717 (2012).

[114] Y.-C. Zheng and T. A. Brun, Phys. Rev. A **89**, 032317 (2014).

[115] S. P. Jordan and E. Farhi, Phys. Rev. A **77**, (062329) (2008).

[116] R. Oliveira and B. M. Terhal, Quant. Inf. Comp. Vol. **8**, No. 10, 0900 (2008)

[117] J. R. Schrieffer and P. A. Wolff, Phys. Rev. **149**, 491 (1966).

[118] S. Bravyi, D. P. DiVincenzo, D. Loss, and B. M. Terhal, Phys. Rev. Lett. **101**, 070503 (2008).

[119] D. Forster, *Hydrodynamic Fluctuations, Broken Symmetry, and Correlation Functions*, Benjamin, MA (1975).

[120] N.D. Mermin and H. Wagner, Phys. Rev. Lett. **17**, 1133 (1966).

[121] H. B. Callen, Phys. Rev. **130**, 890 (1963).

[122] R. A. Tahir-Kheli and H. B. Callen, Phys. Rev. **135**, A679 (1964).

[123] D. P. DiVincenzo and F. Solgun, arXiv:1205.1910 (2012).

[124] S. E. Nigg and S. M. Girvin, Phys. Rev. Lett. **110**, 243604 (2013).

[125] G. Duclos-Cianci and D. Poulin, Phys. Rev. Lett. **104**, 050504 (2010)

[126] A. G. Fowler, A. C. Whiteside, and L. C. L. Hollenberg, Phys. Rev. Lett. **108**, 180501 (2012).

[127] J. R. Wotton and D. Loss, Phys. Rev. Lett. **109**, 160503 (2012).

[128] A. G. Fowler, arXiv:1310.0863 (2013).

[129] W. Dür, M. Hein, J. I. Cirac, and H.-J. Briegel, Phys. Rev. A **72**, 052326 (2005).

[130] J. Emerson, M. Silva, O. Moussa, C. Ryan, M. Laforest, J. Baugh, D. G. Cory, and R. Laflamme, Science **317**, 1893 (2007).

[131] H. Bombin, R. S. Andrist, M. Ohzeki, H. G. Katzgraber, and M. A. Martin-Delgado, Phys. Rev. X **2**, 021004 (2012).

[132] D. S. Wang, A. G. Fowler, A. M. Stephens, and L. C. L. Hollenberg, Quantum Inf. Comput. **10**, 456 (2010).

[133] H. N. Gabow, Proceedings 26th Annual Symposium of the Foundations of Computer Science, (1985).

[134] D. S. Wang, A. G. Fowler, and L. C. L. Hollenberg, Phys. Rev. A **83**, 020302(R) (2011).

[135] G. Duclos-Cianci and D. Poulin, Phys. Rev. A **87**, 062338 (2013).

[136] A. Hutter, J. R. Wootton, and D. Loss, Phys. Rev. A **89**, 022326 (2014).

[137] G. Duclos-Cianci and D. Poulin, Quant. Inf. Comp. **14**, 0721 (2014).

[138] E. Novais and E. R. Mucciolo, Phys. Rev. Lett. **110**, 010502 (2013).

[139] P. Jouzdani, E. Novais, and E. R. Mucciolo, Phys. Rev. A **88** 012336 (2013).

[140] J. W. Harrington, Ph.D. thesis, California Institute of Technology (2004).

[141] L. Trifunovic, F. L. Pedrocchi, and D. Loss, Phys. Rev. X **3**, 041023 (2013).

[142] A. G. Fowler and J. M. Martinis, Phys. Rev. A **89**, 032316 (2014) (2014).

[143] B. M. Terhal and G. Burkard, Phys. Rev. A **71**, 012336 (2005).

[144] E. Dennis, Ph.D. thesis, California Institute of Technology (2003).

[145] J. R. Wootton, Entropy **17**, 1946 (2015).

[146] H. Anwar, B. J. Brown, E. T. Campbell, and D. E. Browne, New J. Phys. **16** 063038 (2014).

[147] P. Sarvepalli, R. Raussendorf, Phys. Rev. A **85**, 022317 (2012).

[148] J. R. Wootton, J. Burri, S. Iblisdir, and D. Loss, Phys. Rev. X **4**, 011051 (2014).

[149] C. G. Brell, S. Burton, G. Dauphinais, S. T. Flammia, and D. Poulin, Phys. Rev. X **4**, 031058 (2014).

[150] H. Anwar, E. T. Campbell, and D. E. Browne, New J. Phys. **14**, 063006 (2012).

[151] E. T. Campbell, H. Anwar, and D. E. Browne, Phys. Rev. X **2**, 041021 (2012).

[152] E. T. Campbell, Phys. Rev. Lett. **113**, 230501 (2014).

[153] J. R. Wootton, J. K. Pachos, ENTCS **270**, 209–218 (2011).

[154] S. S. Bullock and G. K. Brennen, J. Phys. A.: Math. Theo. **40**, 3481, (2007).

[155] R. S. Andrist, J. R. Wootton, and H. G. Katzgraber, Phys. Rev. A **91**, 042331 (2015).

[156] A. G. Fowler, Quant. Inf. Comp. **15**, 0145–0158 (2015).

[157] F. Watson, H. Anwar, and D. Browne, arXiv:1411.3028 (2014).

[158] C. Nayak, S. H. Simon, A. Stern, M. Freedman, and S. Das Sarma, Rev. Mod. Phys. **80**, 1083 (2008).

[159] F. L. Pedrocchi and D. P. DiVincenzo, arXiv:1505.03712 (2015).

[160] M. A. Levin and X.-G. Wen, Phys. Rev. B **71**, 045110 (2005).

[161] C. Monroe and J. Kim, Science **339**, no. 6124, 1164 (2013).

[162] A. Negretti, P. Treutlein, and T. Calarco, Quantum Inf. Process. **10**, 721–753 (2011).

[163] H. Bombin, Phys. Rev. Lett. **105**, 030403 (2010).

[164] O. Petrova, P. Mellado, and O. Tchernyshyov, Phys. Rev. B **90**, 134404 (2014).

[165] J. Alicea, Rep. Prog. Phys. **75**, 076501 (2012).

[166] M. Freedman, C. Nayak, and K. Walker, Phys. Rev. B **73**, 245307 (2006).

[167] N. H. Lindner, E. Berg, G. Refael, and A. Stern, Phys. Rev. **X** 2, 041002 (2012).

[168] M. Cheng, Phys. Rev. B **86**, 195126 (2012).

[169] D. J. Clarke, J. Alicea, and K. Shtengel, Nat. Commun. **4**, 1348 (2013).

[170] A. Vaezi, Phys. Rev. B **87**, 035132 (2013).

[171] M. Burrello, B. van Heck, and E. Cobanera, Phys. Rev. B **87**, 195422 (2013).

[172] R. S. K. Mong, D. J. Clarke, J. Alicea, N. H. Lindner, P. Fendley, C. Nayak, Y. Oreg, A. Stern, E. Berg, K. Shtengel, and M. P.A. Fisher, Phys. Rev. **X** 4, 011036 (2014).

[173] M. Barkeshli and X.-L. Qi, Phys. Rev. X **4**, 041035 (2014).

[174] J. Klinovaja and D. Loss, Phys. Rev. Lett. **112**, 246403 (2014).

[175] F. Zhang and C. L. Kane, Phys. Rev. Lett. **113**, 036401 (2014).

[176] Y. Oreg, E. Sela, and A. Stern, Phys. Rev. B **89**, 115402 (2014).

[177] J. Klinovaja and D. Loss, Phys. Rev. B **90**, 045118 (2014).

[178] J. Klinovaja, A. Yacoby, and D. Loss, Phys. Rev. B **90**, 155447 (2014).

[179] M. Barkeshli, Y. Oreg, and X.-L. Qi, arXiv:1401.3750 (2014).

[180] C. P. Orth, R. P. Tiwari, T. Meng, and T. L. Schmidt, Phys. Rev. B **91**, 081406 (2015).

[181] M. Barkeshli, C.-M. Jian, and X.-L. Qi, Phys. Rev. B **87**, 045130 (2013).

[182] M. Barkeshli, X.-L. Qi, Phys. Rev. X **2**, 031013 (2012).

[183] Y.-Z. You and X.-G. Wen, Phys. Rev. B **86**, 161107(R) (2012).

[184] Y.-Z. You, C.-M. Jian, and X.-G. Wen, Phys. Rev. B **87**, 045106 (2013).

[185] A. Hutter, D. Loss, and J. R. Wootton, New J. Phys. **17**, 035017 (2015).

[186] J. R. Wootton and A. Hutter, arXiv:1506.00524 (2015).

[187] E. Fradkin and L. P. Kadanoff, Nucl. Phys. B **170**, 1 (1980).

[188] J. K. Pachos and M. B. Plenio, Phys. Rev. Lett. **93**, 056402 (2004).

[189] H. P. Büchler, A. Micheli, and P. Zoller, Nat. Phys. **3**, 726 (2007).

[190] P. Bonderson, M. Freedman, and C. Nayak, Phys. Rev. Lett. **101**, 010501 (2008).

[191] P. Bonderson, Phys. Rev. B **87**, 035113 (2013).

[192] J. R. Wootton, arXiv:1501.07779 (2015).

[193] A. Al-Shimary, J. R. Wootton and J. K. Pachos, New J. Phys. **15** 025027 (2013).

[194] S. Clark, J. Phys. A: Math. Gen. **39**, 2701 (2006).

[195] J. M. Farinholt, J. Phys. A: Math. Theor. **47**, 305303 (2014).

[196] J. R, Wootton, J. Mod. Opt. **59**, 20 (2012).

[197] J. R. Wootton, V. Lahtinen, B. Boucot, J. K. Pachos, Ann. Phys. **326**, 2307 (2011).

[198] C. Cesare, A. J. Landahl, D. Bacon, S. T. Flammia, A. Neels, Phys. Rev. A **92**, 012336 (2015).

[199] Y.-C. Zheng, T. A. Brun, Phys. Rev. A **91**, 022302 (2015).

[200] F. H. E. Watson, E. T. Campbell, H. Anwar, and D. E. Browne, Phys. Rev. A **92**, 022312 (2015).

[201] E. T. Campbell, private communication.

[202] S. Burton, C. Brell, and S. T. Flammia, arxiv:1506.03815 (2015).

[203] B. J. Brown, N. H. Nickerson, and D. E. Browne, arXiv:1503.08217 (2015).

[204] J. R. Wootton, J. Phys. A: Math. Theor. **48**, 215302 (2015).

[205] E. Dennis, Ph.D. thesis, California Institute of Technology, arXiv:quant-ph/0503169 (2005).

[206] A. Stern and N. H. Lindner, Science, **339**, 1179 (2013).

[207] C. Nayak and F. Wilczek, Nucl. Phys. B **479**, 529 (1996).

[208] N. Read and D. Green, Phys. Rev. B **61**, 10267 (2000).

[209] D. A. Ivanov, Phys. Rev. Lett. **86**, 268 (2001).

[210] L. Fu and C. L. Kane, Phys. Rev. Lett. **100**, 096407 (2008).

[211] Y. Tanaka, T. Yokoyama, and N. Nagaosa, Phys. Rev. Lett. **103**, 107002 (2009).

[212] M. Sato and S. Fujimoto, Phys. Rev. B **79**, 094504 (2009).

[213] J. D. Sau, R. M. Lutchyn, S. Tewari, and S. Das Sarma, Phys. Rev. Lett. **104**, 040502 (2010).

[214] R. M. Lutchyn, J. D. Sau, and S. Das Sarma, Phys. Rev. Lett. **105**, 077001 (2010).

[215] Y. Oreg, G. Refael, and F. von Oppen, Phys. Rev. Lett. **105**, 177002 (2010).

[216] J. Alicea, Phys. Rev. B **81**, 125318 (2010).

[217] P. Ghosh, J. D. Sau, S. Tewari, and S. Das Sarma, Phys. Rev. B **82**, 184525 (2010).

[218] L. Jiang, T. Kitagawa, J. Alicea, A. Akhmerov, D. Pekker, G. Refael, J. I. Cirac, E. Demler, M. D. Lukin, and P. Zoller, Phys. Rev. Lett. **106**, 220402 (2011).

[219] S. Sasaki, M. Kriener, K. Segawa, K. Yada, Y. Tanaka, M. Sato, and Y. Ando, Phys. Rev. Lett. **107**, 217001 (2011).

[220] J. R. Williams, A. J. Bestwick, P. Gallagher, S. S. Hong, Y. Cui, A. S. Bleich, J. G. Analytis, I. R. Fisher, and D. Goldhaber-Gordon, Phys. Rev. Lett. **109**, 056803 (2012).

[221] J. Klinovaja, S. Gangadharaiah, and D. Loss, Phys. Rev. Lett. **108**, 196804 (2012).

[222] J. Klinovaja, P. Stano, and D. Loss, Phys. Rev. Lett. **109**, 236801 (2012).

[223] J. Klinovaja, P. Stano, A. Yazdani, and D. Loss, Phys. Rev. Lett. **111**, 186805 (2013).

[224] B. Braunecker and P. Simon, Phys. Rev. Lett. **111**, 147202 (2013).

[225] J. Klinovaja and D. Loss, Phys. Rev. **X** 3, 011008 (2013).

[226] R. P. Tiwari, U. Zülicke, and C. Bruder, New J. Phys. **16**, 025004 (2014).

[227] M. Leijnse and K. Flensberg, Semicond. Sci. Technol. **27**, 124003 (2012).

[228] C. W. J. Beenakker, Annu. Rev. Con. Mat. Phys. **4**, 113 (2013).

[229] S. Das Sarma, M. Freedman, and C. Nayak, arXiv:1501.02813 (2015).

[230] E. Lieb, T. Schultz, and D. Mattis, Ann. of Phys. **16**, 407 (1961).

[231] A. Yu. Kitaev, Phys.-Usp. **44**, 131 (2001).

[232] M. Deng, C. Yu, G. Huang, M. Larsson, P. Caro, and H. Xu, Nano Lett. 12, 6414 (2012).

[233] L. P. Rokhinson, X. Liu, and J. K. Furdyna, Nat. Phys. **8**, 795 (2012).

[234] H. O. H. Churchill, K. G.-R. V. Fatemi, P. C. M. T. Deng, H. Q. Xu, and C. M. Marcus, Phys. Rev. B 87, 241401(R) (2013).

[235] A. Finck, D. V. Harlingen, P. Mohseni, K. Jung, and X. Li, Phys. Rev. Lett. 110, 126406 (2013).

[236] R. Pawlak, M. Kisiel, J. Klinovaja, T. Meier, S. Kawai, T. Glatzel, D. Loss, and E. Meyer, arXiv:1505.06078 (2015).

[237] J. Alicea, Y. Oreg, G. Refael, F. von Oppen, and M. P. A. Fisher, Nat. Phys. **7**, 412 (2011).

[238] E. Kapit and S. H. Simon, Phys. Rev. B **88**, 184409 (2013).

[239] G. Palumbo and J. K. Pachos, Phys. Rev. D **90**, 027703 (2014).

[240] A. Ahlbrecht, L. S. Georgiev, and R. F. Werner, Phys. Rev. A **79**, 032311 (2009).

[241] P. Bonderson, D. J. Clarke, C. Nayak, and K. Shtengel, Phys. Rev. Lett. **104**, 180505 (2010).

[242] P. Bonderson, S. Das Sarma, M. Freedman, C. Nayak, arXiv:1003.2856 (2010).

[243] G. Goldstein and C. Chamon, Phys. Rev. B **84**, 205109 (2011).

[244] J. C. Budich, S. Walter, and B. Trauzettel, Phys. Rev. B **85**, 121405(R) (2012).

[245] D. Rainis and D. Loss, Phys. Rev. B **85**, 174533 (2012).

[246] M. J. Schmidt, D. Rainis, and D. Loss, Phys. Rev. B **86**, 085414 (2012).

[247] F. Konschelle and F. Hassler, Phys. Rev. B **88**, 075431 (2013).

[248] A. A. Zyuzin, D. Rainis, J. Klinovaja, and D. Loss, Phys. Rev. Lett. **111**, 056802 (2013).

Curriculum Vitae

Adrian Hutter

Since Sept. 2015	**Postdoctoral associate in the Condensed Matter Theory group at the University of Basel.**
Dec. 2011 – Sept. 2015	**PhD student in the Condensed Matter Theory group at the University of Basel,** under the supervision of Prof. Daniel Loss. PhD degree with *summa cum laude*.
Sept. 2009 – July 2011	**Master studies in Physics at ETH Zurich.** Fellow of the *ETH Zurich Excellence Scholarship & Opportunity Programme*. Graduated with distinction. Master's thesis written at the National University of Singapore under the supervision of Prof. Renato Renner and Prof. Stephanie Wehner. Thesis title: *Understanding Equipartition and Thermalization from Decoupling*.
Sept. 2006 – July 2009	**Bachelor studies in Physics at ETH Zurich.**
June 2005	**Graduated from the Kantonsschule am Burggraben, St. Gallen,** majoring in physics and mathematics.